DISSERTATION

Atomistic Modeling in the Context of the Bias Temperature Instability

ausgeführt zum Zwecke der Erlangung des akademischen Grades

eines Doktors der technischen Wissenschaften

eingereicht an der Technischen Universität Wien

Fakultät für Elektrotechnik und Informationstechnik

von

FRANZ SCHANOVSKY

Wien, im März 2013

_____

Abstract

The bias temperature instability (BTI) is one of the most serious reliability concerns in state-of-the-art metal-oxide-semiconductor (MOS) field-effect transistors. It is observed when a large voltage is applied to the gate contact of the MOS transistor at elevated temperatures while all other terminals are grounded. The strongest effect is seen when a negative bias voltage is applied to a p-channel MOS transistor, the corresponding degradation is commonly termed *negative* bias temperature instability (NBTI). Bias-temperature degradation is generally ascribed to electrochemical reactions at point-defects in the oxide and at the semiconductor-oxide interface. Concerning the physical details of the degradation process, however, no general consensus has been found yet and a lively debate has been going on for several years.

For almost four decades, the *reaction diffusion model* has been the standard interpretation for NBTI. This model assumes the observed degradation to be primarily due to the depassivation of silicon dangling bonds at the Si-SiO$_2$ interface. These dangling bonds originate from the inherent lattice mismatch between the silicon substrate and the oxide layer and are passivated during the manufacturing process using hydrogen. The reaction diffusion model assumes that during NBT stress the hydrogen atoms leave the dangling bonds and diffuse into the oxide and that this diffusion process determines the transient behavior of the degradation.

As the reaction diffusion model is unable to give the experimentally observed recovery behavior, an alternative description has been developed by Grasser and coworkers. This *multi-state multi-phonon* model ascribes the BT degradation primarily to the capture and emission of holes at point defects inside the oxide. In this model, each point-defect can undergo a charge transition, which is understood as a non-radiative multi-phonon transition, or a structural reconfiguration, which is understood as a barrier hopping process. The multi-state multi-phonon model is able to explain complex BT experiments with very high accuracy and also links BTI to other oxide-defect-related effects. Unfortunately, the model has a large set of parameters that need to be calibrated and the atomic nature of the defect is still unknown.

The present work applies atomistic modeling techniques to both BTI models. The reaction-diffusion mechanism is studied at the stochastic chemistry level. Our results clearly show that the commonly employed mathematical description using rate equations is inappropriate for the reaction-diffusion mechanism. However, the physically more reasonable model developed in the present work fails to give both the experimentally observed degradation and recovery. This suggests that the reaction-diffusion model requires a revision at the microscopic level and that especially the diffusion-limitation of NBTI degradation is not a reasonable assumption.

For the multi-state multi-phonon model it is shown how the number of free parameters can be reduced using an atomistic representation of a point defect and an electronic structure method. For this purpose, the broad literature of multi-phonon transition theory is briefly reviewed. Methods are developed to extract line shape functions, which describe the non-radiative multi-phonon capture and emission of charge carriers, at different levels of physical detail from an atomistic model of a point defect. The oxygen vacancy and the hydrogen bridge in crystalline silicon dioxide are studied for their BTI behavior both as examples and as references for future defect studies.

Kurzfassung

Bei der *Bias Temperature Instabilität* (BTI) handelt es sich um einen Degradationseffekt in MOS-Feldeffekttransistoren, der stark thermisch aktiviert ist und bei hohen elektrischen Feldern im Oxid auftritt. BTI-Degradation wird meist erzeugt indem dem Gatekontakt des Transistors eine überhöhte Spannung zugeführt wird, während alle anderen Anschlüsse auf dem Massepotential liegen. Obwohl in allen Kombinationen von Spannungs- und Kanalpolaritäten beobachtbar, wird die mit Abstand stärkste Schädigung mit negativer Stressspannung in p-Kanal MOSFETs verursacht. Diese Situation wird als *Negative Bias Temperature Instabilität* (NBTI) bezeichnet. Nach gängiger Meinung liegt die Ursache der beobachteten Zerstörung in elektrochemischen Reaktionen an Punktdefekten die sowohl an der Oxid-Halbleiter-Grenzschicht wie auch im Oxid lokalisiert sind. Über den genauen physikalischen Vorgang der Schädigung konnte jedoch bisher keine Einigkeit erzielt werden.

Im Reaktions-Diffusions-Modell (RD-Modell) der NBTI ist die Degradation durch die fortschreitende Depassivierung von Siliziumatomen an der Oxid-Halbleiter Grenzfläche bestimmt. In dieser Region entstehen im Herstellungsprozess unabgesättigte Bindungen, die von den unterschiedlichen Strukturen im Oxid und im Substrat herrühren. In der Halbleiterbauteilfertigung werden diese offenen Bindungen durch Wasserstoffatome abgesättigt. Die Modellannahmen bestehen nun darin, dass die Anwesenheit von Defektelektronen in Kombination mit der erhöhten Temperatur die Si-H Bindungen brechen lässt und die Wasserstoffatome ins Oxid diffundieren, und dass diese Diffusion das zeitliche Verhalten der NBTI bestimmt.

Trotz seiner Beliebtheit ist weder das RD-Modell noch eine seine zahlreichen Erweiterungen in der Lage, alle experimentellen Beobachtungen konsistent zu erklären. So versagt dieser Ansatz beispielsweise völlig bei der Vorhersage der Ausheilung, die stattfindet sobald die Gatespannung reduziert wird. Das alternative *Mehrzustands-Multiphonon-Modell* von Grasser et al. versteht die BTI als dominiert vom Ladungsträgereinfang an Punktdefekten im Oxid. Der Ladungsaustausch mit dem Substrat wird in dem Modell als nicht strahlender vibronischer Übergang beschrieben. Zusätzlich zum Ladungsträgereinfang ist der Defekt in der Lage, zwischen zwei stabilen Konfigurationen zu wechseln, die durch eine thermische Barriere getrennt sind. Das Mehrzustands-Multiphonon-Modell ist in der Lage, das Verhalten von Bauteilen in einer Reihe von Komplexen BTI-Experimenten akkurat wiederzugeben. Aufgrund des großen Parametersatzes ist die Kalibrierung des Modells jedoch sehr aufwändig und oftmals uneindeutig. Weiters ist noch völlig unklar, welcher Punktdefekt für BTI verantwortlich ist.

In der vorliegenden Arbeit wurden beide Modelle mittels atomistischer Simulationstechniken näher untersucht. Der Reaktions-Diffusionsmechanismus wird hierbei auf Basis der Mastergleichung der stochastischen Chemie modelliert. Dabei wird deutlich, dass die übliche Beschreibung dieses Prozesses mittels Reaktionsgleichungen grob unzureichend ist. Mit dem hier präsentierten, physikalisch sinnvolleren Modell sind jedoch weder die experimentell beobachtete Degradation noch der Ausheilvorgang vorhersagbar. Dieser Umstand legt nahe, dass das RD-Modell auf physikalisch nicht haltbaren Annahmen basiert und dieses Konzept — im Speziellen die Annahme der diffusionslimitierten Degradation — einer Überprüfung auf mikroskopischer Ebene bedarf.

Mit Bezug auf das Mehrzustands-Multiphonon-Modell wird gezeigt wie einzelne Modellparameter auf Basis eines atomistischen Defektmodells mittels quantenchemischer Methoden berechnet werden können. Energieabhängige Übergangsquerschnitte werden mit unterschied-

lichen Näherungen extrahiert, und die Ergebnisse gegenübergestellt. Die gewählten Defekt-strukturen, die Sauerstoffvakanz und die Wasserstoffbrücke in kristallinem SiO_2, dienen dabei als Anwendungsbeispiel und als Referenzdefekte für zukünftige Studien. Die Anwendung der berechneten Querschnitte in einer makroskopischen Bauteilsimulation wird demonstriert.

Acknowledgment

This document owes its existence and quality to a large number of people and the following lines are solely devoted to adequately honor these extraordinary people.

Tibor Grasser's wonderful lecture on semiconductor modeling has brought me to this fascinating field. His tireless scientific commitment and his deep fascination with physics and applied numerics is a constant motivation for his students. I would like to thank Tibor for giving me both freedom and advice, for the patience during my descent into the realm of quantum physics, and for hours of stimulating discussions.

From the many interesting discussions I had on conferences, I enjoyed the ones with **Andreas Schenk** most because of his in-depth knowledge of both semiconductor device simulation and multi-phonon transitions. I feel honored and grateful that he agreed to partake in my examination committee despite his enormously busy schedule.

Erasmus Langer and **Siegfried Selberherr** have founded and shaped the institute for microelectronics and the high quality of our research as well as the unique atmosphere at the institute are a credit to their efforts.

For the past five years, **Paul-Jürgen Wagner** and **Phillipp Hehenberger** were the best company one could ask for, and I enjoyed every of the hundreds of longer and shorter discussions in our office, both scientific and personal. I would like to thank Phillipp for his assistance in the solution of several tricky physics problems. Paul has contributed to the quality of many publications at the institute (including this one) by sharing his comprehensive and detailed knowledge of circuit engineering, typesetting and english grammar. Also, his manifold contributions to my world view are highly appreciated.

The most important thing I have learned during my doctoral studies is that the discussion with a competent person can save a hundred pages of reading. I therefore thank my colleagues **Wolfgang Gös**, **Viktor Sverdlov**, **Oskar Baumgartner**, and **Zlatan Stanojevic** for the numerous times they shared their expertise with me.

I would have never found my way into the enormously broad field of multi-phonon transitions without the invaluable input from **Alex Shluger** and **Keith McKenna**. **Georg Kresse** and **Peter Blöchl** have provided a lot of practical tips for my electronic structure calculations.

As I have the bad habit of losing track of signs and symbols during longer derivations, I thank **Yannick Wimmer** for heroically checking the formulae in Chap. 2.

During my time at the institute for microelectronics, **Ewald Haslinger**, **Christoph Haslinger**, **Manfred Katterbauer**, and **Renate Winkler** have competently handled all administrative tasks. In this context, I also thank **Dietlinde Egger** for her wonderful and friendly help with the bureaucratic aspects of my studies, and for lots of pleasant conversations.

Finally, I would like to acknowledge all the love and support I have received from my family. I thank my wife **Nicole**, from whom I learned more than from anyone else in the past 16 years, my daughter **Lena**, the Kung-Fu fighting piano virtuoso who takes every opportunity to make her parents the proudest on Earth[1], and my daughter **Margarete**, who is the most amazing almost two years old stunt girl in the world. This work is dedicated to these three wonderful women.

---

[1] . . . and who was always at my side to fight pirates while riding flying horses at a time when this was still considered "cool".

*To Nicole, Lena, and Margarete*

Contents

1 Introduction

Point defects in solids have been in the focus of scientific interest since the very beginnings of solid state theory due to their large influence on the macroscopic mechanical, electrical, and optical properties of the host material. In semiconductor technology, which is itself largely based on the intentional introduction of impurities into a host material, defects affect the motion of the electrons and the holes by scattering, carrier trapping, or as recombination centers. Under certain operational or environmental conditions, or just over time, point defects in a given semiconductor device might be created, destroyed, repositioned, or modified in their ability to interact with the carriers. As these changes usually alter the characteristics of the device in an undesired manner, detailed knowledge of the defect physics is of utmost importance in the field of semiconductor device reliability, within which the present work has been carried out.

1.1 The Bias Temperature Instability

The main focus of interest for this thesis lies in the bias temperature instability (BTI) of metal-oxide-semiconductor (MOS) transistors. This instability is usually encountered during burn-in tests or high-performance operation of MOS devices [1, 2] at temperatures in the $100^{\circ}\mathrm{C}$–$250^{\circ}\mathrm{C}$ range, when a large voltage is supplied to the gate contact (≈ 7–$10\,\mathrm{MV/cm}$ oxide field) while all other terminals are grounded, see Fig. 1.1. BTI degradation shows as a shift of the threshold voltage and a degradation of the channel mobility. Bias temperature instabilities have been known for forty years [3, 4] and, due to their minor influence on early semiconductor technology, were mainly of academic interest. With the aggressive shrinking of feature sizes down to the nanometer regime, oxide fields need to be increased with every new technology generation, to keep the sub-threshold leakage of the transistors at reasonable values [5]. Additionally, the increasing concentration of currents during device operation into smaller and smaller volumes leads to an increase in the thermal power density due to Joule heating and thus raises the operating temperature of the MOS transistor. These effects brought bias temperature instabilities to the industrial agenda in the early 2000s. As the problem is getting worse with every new technology node, partially also because of the introduction of new materials to the

Figure 1.1: Schematic of a typical BTI measurement. During stress, a large negative gate voltage V_{g} is applied. The degradation is monitored through the drain current which is driven by applying a small voltage along the channel.

1
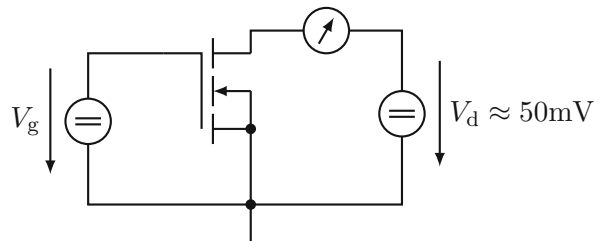
semiconductor process, BTI has evolved to a major reliability issue in modern, highly scaled MOS transistors [2]. Although present in both n- and p-channel devices with both polarities of the bias voltage, the most pronounced BTI is observed when negative bias stress is applied to p-channel MOS (pMOS) transistors. The corresponding instability is termed *negative* bias temperature instability (NBTI).

1.2 BTI Modeling

Lifetime predictions for BT instabilities are usually made based on accelerated (so-called burn-in) tests, where the devices are operated at temperatures and voltages that are beyond their specifications, aiming at the amplification of one specific degradation mechanism as much as possible without damaging the device otherwise. The degradation observed in these tests is then extrapolated to the normal operation conditions by using empirical *acceleration factors* [6] to predict the lifetime of the devices under these conditions. As the acceleration factors are purely empirical expressions, they bear large uncertainties, requiring equivalently large reliability margins, and tend to be overly pessimistic. An accurate and physics-based model could help to reduce reliability margins thus making more efficient circuit designs possible.

In order to obtain accurate long-term (ten years or more) predictions for the amount of degradation induced by a certain mechanism, a detailed physical understanding of this degradation process is required. The identification of the relevant physics, however, proves to be difficult in practice due to the limited experimental observability. These limitations arise from the small structural dimensions of the microelectronic devices together with the low density of defects present in the materials. The resulting number of defects generated during stress in a commercial device is below the detection limit of most measurement methods that give hints to the atomic structure involved, like electron spin resonance (ESR, also known as electron *paramagnetic* resonance EPR) or optical absorption. Additionally, the defects generated during BT stress recover fast, so any delay between the removal of the stress and the measurement of the generated defects influences the outcome of this measurement. As a consequence, BTI degradation models are quantitatively evaluated solely against electrical measurements. Other experimental data is considered only in a qualitative fashion.

1.3 The Reaction-Diffusion Model for NBTI

Because of its impact, most modeling has been done on the *negative* bias temperature instability. The first model for NBTI was put forward by Jeppson and Svensson in 1977 [7]. Their model was based on the following ideas, which are illustrated in Fig. 1.2. Due to the lattice mismatch between silicon and silicon dioxide, some of the silicon atoms do not have an oxygen neighbor. A silicon atom in this situation has one unpaired valence electron, which is called a dangling bond. This dangling bond is visible in electronic measurements as it gives rise to states within the band-gap [2]. During the manufacturing process the wafer is exposed to a hydrogen-rich atmosphere so that hydrogen atoms can penetrate through the oxide and passivate the silicon dangling bonds, leading to a removal of the band-gap states.

During stress, the presence of holes at the interface and the increased temperature leads to a liberation of the hydrogen atoms. The remaining silicon dangling bonds become electrically active carrier traps. According to the model, the depassivation and repassivation of dangling bonds at the interface reaches an equilibrium in a very short time [8, 9], and it is the constant flux of hydrogen atoms (or some hydrogenic species) away from the interface that determines

Figure 1.2: The basic concept behind the reaction-diffusion model for NBTI. **(a)** Silicon dangling bonds at the Si-SiO$_2$ interface are initially passivated by hydrogen atoms. **(b)** During stress, hydrogen atoms are liberated leaving behind the unpassivated silicon dangling bonds which degrade the device properties. **(c)** The time evolution is determined by the depopulation of the interface due to the flux of hydrogen into the oxide.
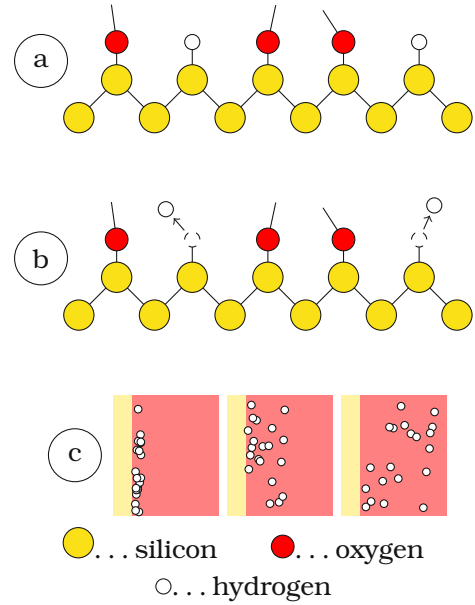
the temporal evolution of the degradation. Because of the two proposed stages — the electrochemical reaction at the interface and the subsequent diffusion of the hydrogenic species — this model bears the name *reaction-diffusion* (RD) model.

The mathematical framework the of model is based on a macroscopic description using a rate equation for the interface reaction and a Fickian diffusion equation for the motion of the hydrogen in the oxide. Central actors are the density of depassivated silicon dangling bonds at the interface $N_{\mathrm{it}} = [\mathrm{Si}^*]$, and the concentration of hydrogen in the oxide $H = [\mathrm{H}](x,t)$ and at the interface $H_{\mathrm{it}} = [\mathrm{H}](0,t)$. During degradation, a fraction N_{it} of the initially passivated silicon dangling bonds $N_0 = [\mathrm{SiH}]_0$ is depassivated according to

$$\frac{\partial N_{\mathrm{it}}}{\partial t} = k_{\mathrm{f}}(N_0 - N_{\mathrm{it}}) - k_{\mathrm{r}}N_{\mathrm{it}}H_{\mathrm{it}}, \tag{1.1}$$

with the depassivation (forward) rate k_{f} and the repassivation (reverse) rate k_{r}. The hydrogen liberated at the interface then diffuses into the oxide as

$$\frac{\partial H}{\partial t} = -D\frac{\partial^2 H}{\partial x^2} \tag{1.2}$$

with the diffusion coefficient D. The RD model became popular amongst reliability engineers as it features a simple mathematical description and a small set of parameters which have a sound physical interpretation. Most importantly, as shown in Fig. 1.3, this model predicts a constant-stress degradation that initially grows linearly with time and then follows a power-law of the form [8, 9]

$$N_{\mathrm{it}}(t) = \sqrt{\frac{k_{\mathrm{f}}N_0}{2k_{\mathrm{r}}}}(Dt)^{1/4}. \tag{1.3}$$

This power-law degradation corresponded well with experimental results of the seventies.

In later experiments, power-law exponents were found that differed from the $1/4$ prediction of the model. These findings led to a modification of the original RD model to account for different diffusing species such as H$_2$ [10]. For almost four decades, the reaction-diffusion idea was the unquestioned standard interpretation for NBTI until around 2005 NBT recovery moved into the focus of the scientific attention. The experiments showed that NBTI recovery

Figure 1.3: Basic features of the degradation predicted by the RD model for NBTI. In the initial phase, the depassivation reaction with rate k_f dominates, giving rise to a degradation that increases linearly with time. After the depassivation and repassivation reactions have reached an equilibrium, the degradation is determined by the flux of hydrogen away from the interface, which gives rise to a power-law with an exponent of $1/4$.
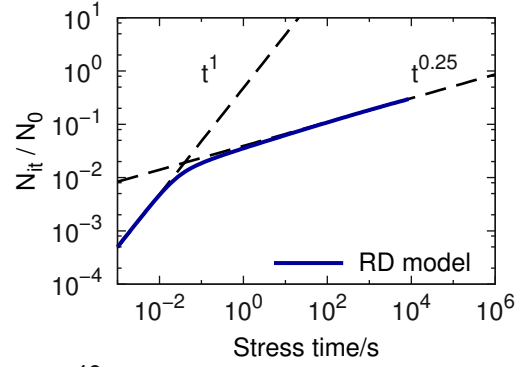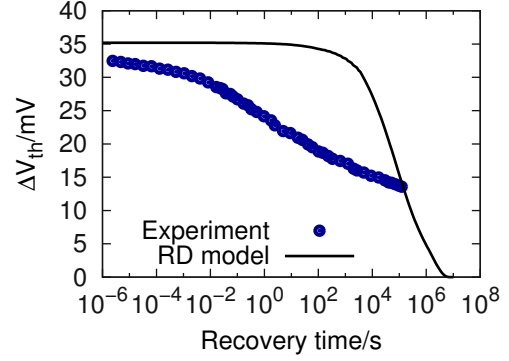

Figure 1.4: Typical recovery trace as predicted by the RD model for NBTI using equations (1.4)–(1.6), which is similar for all variants of the RD mechanism. The comparison with experimental data [12] shows that the RD predicted recovery occurs much too late and proceeds much too fast.

starts immediately (even before a microsecond) after the removal of stress and extended over several decades, continuing even after more than 10^5 s [11, 12]. This behavior stands in strong contrast to the predictions of the RD model, which predicts a recovery that proceeds within four decades, centering around the duration of the preceding stress phase [13, 14]. A comparison of a typical experimental NBT recovery trace and the corresponding prediction of the RD model is shown in Fig. 1.4. Several extensions to the RD model have been put forward, such as dispersive transport of the hydrogenic species [9, 11], but none could give the observed experimental behavior. The current state-of-the-art RD-based modeling supplements the RD theory with empirical hole-trapping expressions. It is assumed that short-time ($1\,\mathrm{s}$) degradation and recovery is dominated by hole trapping into oxide and interface defects, while the long-term degradation and recovery are determined by the RD mechanism [15–18]. The RD theory employed in these modeling efforts is the *modified* RD model [19–21] that has been developed as an extension of the classical RD models and explicitly considers diffusion of H and H_2 and their interconversion reactions. Classical models assume an instantaneous transition between the liberated interfacial hydrogen and the diffusing species, usually H_2 [10]. The reactions present in the modified RD model are the interface reaction $SiH \rightleftharpoons Si^* + H$, the dimerization reaction $2H \rightleftharpoons H_2$, and the diffusion of both species. The mathematical framework is an extension of (1.1) and (1.2) [20, 21],

$$\frac{\partial N_{\mathrm{it}}}{\partial t} = k_f(N_0 - N_{\mathrm{it}}) - k_r N_{\mathrm{it}} H_{\mathrm{it}}, \tag{1.4}$$

$$\frac{\partial H}{\partial t} = -D\frac{\partial^2 H}{\partial x^2} - k_H H^2 + k_{H_2} H_2, \tag{1.5}$$

$$\frac{\partial H_2}{\partial t} = -D_2\frac{\partial^2 H_2}{\partial x^2} + \frac{k_H}{2} H^2 - \frac{k_{H_2}}{2} H_2, \tag{1.6}$$

with the additional parameters k_H and k_{H_2} which are the reaction rates for dimerization and

atomization, respectively. Again the motion of H and H_2 is described by a simple diffusion law with the corresponding diffusion coefficients D and D_2 [22].

The combination of this modified reaction-diffusion model with empirical hole-trapping somewhat improves the match with experimental DC and AC stress data. The failure of the RD model to properly describe NBT recovery is shifted out of the time window of some experiments, but essentially remains.

Most recently, it has been argued that the shortcoming of the reaction-diffusion based model concerning the prediction of NBTI recovery comes from the one-dimensional description of the H and H_2 diffusion and that a proper description of the three-dimensional atomic motion would lead to the experimentally observed long recovery tails [16, 17]. Additionally, some groups are working towards a microscopic formulation of the reaction-diffusion model which would then be applicable to small-scale effects like random telegraph noise (RTN) and nano-scale devices in general [23].

We have also derived and implemented a microscopic formulation of the RD model [24, 25], in order to study the behavior of the RD mechanism on the atomic scale. Our calculations, which are more deeply explained in Chap. 3, have disproved the claims in [16, 17] and raise strong doubts of the validity of the proposed RD mechanism and its modeling using rate equations.

1.4 Defect-Centered Models

The obvious inability of the reaction-diffusion model and its variants to accurately predict NBTI recovery as well as other properties, such as the universal scaling of BTI degradation [27], led to increased interest in alternative descriptions. A promising approach was found in 2008 in BTI models based on dispersive reactions between two or three states [27, 28], termed double-well or triple-well models. Although the central actors were still believed to be hydrogen atoms, these models brought a fundamental reinterpretation of the physical process behind the BTI. The collective diffusion process that determines the degradation and recovery in the RD models was replaced with a dispersive hopping of isolated particles. Even better accordance with experimental data was found later that year with a model that coupled a two-state description of the 'hydrogen atom' with an also statistically distributed thermally activated hole capture process [29]. The introduction of more complex experimental techniques such as rapid gate voltage and device temperature switches created new testing-grounds for BTI modeling. Early 2009 a refined model could be devised that was also able to explain the more complex experimental data with striking accuracy [26]. This model brought along a complete reinterpretation of the degradation process that no longer assumes the hole capture to happen at the Si-SiO_2 interface, but instead at defects *within the gate-oxide*. Upon hole capture, these defects would undergo complicated reconfiguration, as explained in Fig. 1.5, and eventually offer a bonding state to a hydrogen atom. Interfacial hydrogen atoms would be thermodynamically more stable at this defect site than at the interfacial silicon dangling bond, thus creating an interface defect. In contrary to its predecessors this model is based on a concrete microphysical picture, where the structural reorganization is described as a transition over a barrier and the hole capture is understood as a field-accelerated multi-phonon process. This behavior was inspired by models for irradiation damage, which assume the oxygen vacancy defect in SiO_2 as the central actor [30]. In its neutral state, the oxygen vacancy is assumed to exist in a dimer position, where the silicon atoms adjacent to the vacancy form a bond. The positively charged variant of this defect structure is usually identified with the E'_δ paramagnetic center, which is visible in electron spin resonance (ESR) measurements of amorphous silica.

Figure 1.5: In the neutral oxygen vacancy, a strong bond is formed between the two silicon atoms adjacent to the vacancy. Upon hole capture, this bond is weakened and the defect eventually relaxes to the energetically more favorable 'puckered' configuration. The charged dimer position is usually identified with the E'_δ defect and the puckered position with the E'_γ defect visible in ESR measurements. The original two-stage model does not consider the charged dimer state of the oxygen vacancy and has an additional hydrogen component [26].
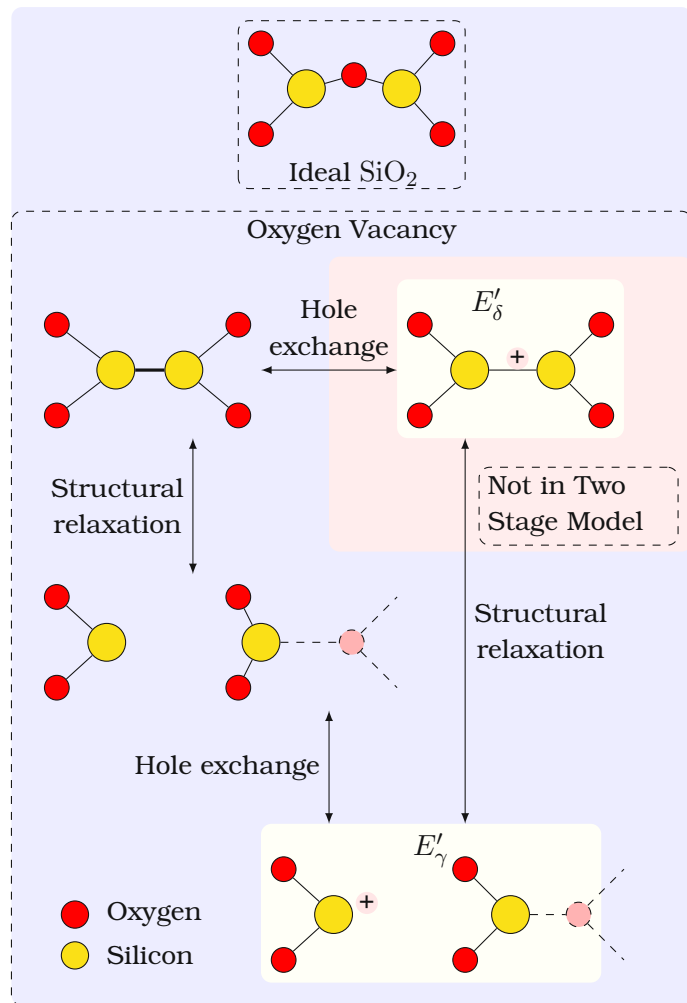
Upon hole capture the bond of the dimer is weakened and one of the silicon atoms eventually relaxes through the plane of its oxygen neighbors and forms a weak bond with a nearby oxygen atom, which is then threefold coordinated. The resulting position is called the 'puckered' state, which is also paramagnetic and usually identified with the E'_γ center.

While the microscopic picture behind the two-stage model was based on a broad and rigorous literature study, the mathematical description was formulated in a way that only captures the basic behavior arising from the microscopic theories but that did not fully implement the physical details of those theories.

1.5 A Multi-State Multi-Phonon Model for BTI and RTN

A further advance of the defect model was stimulated by experiments taken on small-area devices, where the recovery in response to NBT stress proceeds in discrete steps instead of a continuous curve [31]. The careful analysis of these steps led to the development of the time-dependent defect spectroscopy (TDDS) method [31–33], which makes a detailed investigation of the charging and discharging of single defects possible [32]. A typical TDDS spectral map is given in Fig. 1.6. The results of the TDDS experiments served as a testing ground of unprecedented detail for BTI models and allowed for the refinement of the physics in the
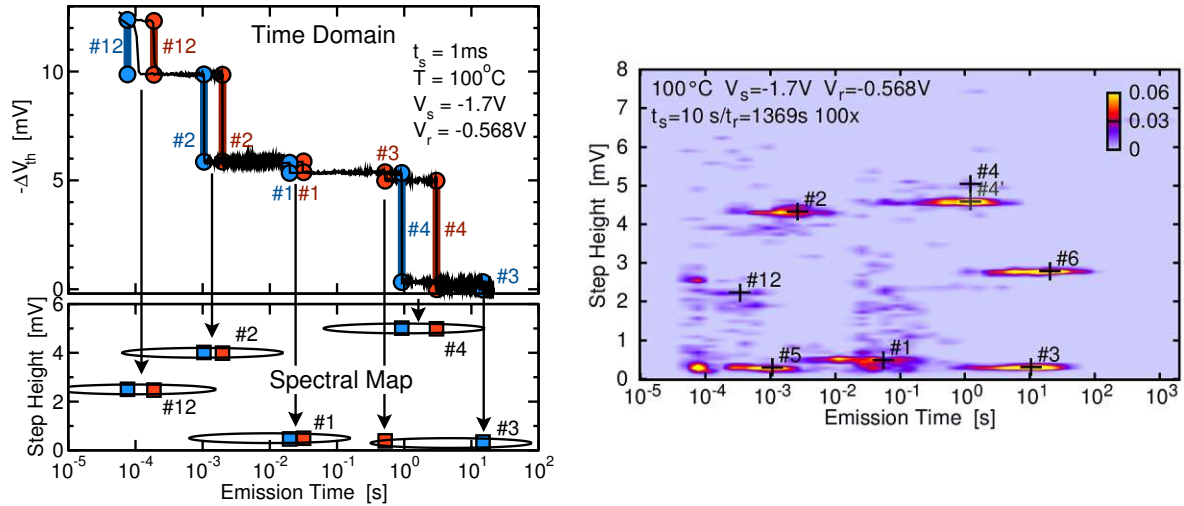
Figure 1.6: (left) In small-area devices, NBT recovery proceeds in discrete steps which is accounted to the discharge of single defects. The careful analysis of the step-curves has led to the development of the time-dependent defect spectroscopy (TDDS) method [31, 32]. In TDDS experiments a number of stress-recovery cycles are measured and the steps are detected. The times and magnitudes of those steps are binned into a two-dimensional histogram which is called the TDDS spectral map **(right)**. In these spectra, defects show up as isolated clusters. The variation of the stress and recovery conditions makes the experimental study of the trapping behavior of single defects possible.

two-stage model. The resulting multi-state defect model not only fits experimental data from BTI and TDDS experiments very well, it also links these phenomena to other phenomena such as random telegraph noise (RTN) and flicker noise [32, 34–37].

As an extension to the original two-stage model, the multi-state NMP model considers four states of the oxygen vacancy, as illustrated in Figures 1.5 and 1.7, and rests upon a more detailed physical theory for the hole capture and emission rates, which will be more deeply discussed later.

The mathematical formulation of the defect based model assigns a probability $p_\alpha(t)$ to every state α of a defect with $\sum_\alpha p_\alpha(t) = 1$. The dynamics of the defect state is then described using rate equations of the form

$$\frac{\partial p_\alpha}{\partial t} = \sum_{\beta \neq \alpha} k_{\beta\alpha} p_\beta(t) - k_{\alpha\beta} p_\alpha(t). \tag{1.7}$$

The transient behavior of a defect arises from the potential energy surfaces in its various charge states. The potential energy surface $E_i(\vec{R})$ corresponding to a certain charge state α of the defect assigns a total energy to each atomic configuration $\vec{R}$. In our model, the defect is assumed to have two relevant potential energy surfaces, corresponding to the neutral and the positive charge state of the defect. Fig. 1.7 shows the gradual change of the total energies as the system moves in configuration space and the resulting energetic minima which give rise to the states of the defect (denoted 1, $1'$, 2, and $2'$). The model knows two types of transitions: the transitions between the structural configurations ($1 \leftrightarrow 1'$ and $2 \leftrightarrow 2'$) and the transitions between the charge states of the defect ($1 \leftrightarrow 2'$, $2 \leftrightarrow 1'$). The former are treated as adiabatic
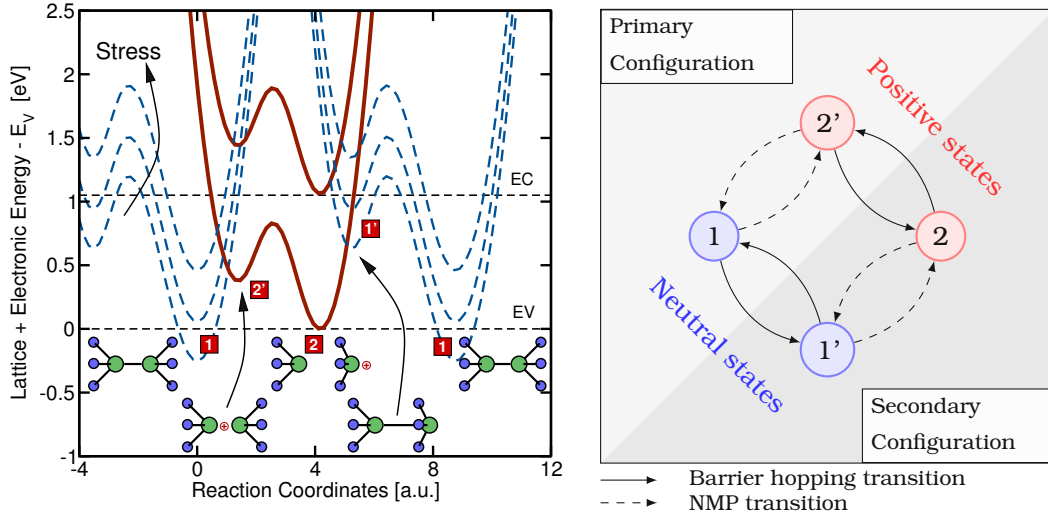
Figure 1.7: (left) Our model for BTI is based on potential energy surfaces for a defect in its neutral (dashed blue lines) and positive (solid red lines) charge state [32]. As explained in Chap. 2, the minima of the potential energy surfaces correspond to the stable and meta-stable states of the defect structure. The effects of stress and different reservoir energies are indicated [32]. **(right)** State-representation of the defect in our model for NBTI. The defect can exist in two different structural states, where each again can be either neutral or positively charged. The charged states affect the device characteristics of the MOS transistor, the neutral states are invisible to electrical measurements.

barrier-hopping transitions of the form

$$k_{\alpha\alpha'} = \nu_\alpha e^{-\frac{E_{\alpha\alpha'}}{k_B T}}, \tag{1.8}$$

where ν_α is the attempt frequency and $E_{\alpha\alpha'}$ is the activation energy associated with the transition. The charge state transitions are understood as non-radiative multi-phonon transitions and are modeled as

$$k_{\alpha\beta'} = \sigma v_{th} p e^{-\frac{E_{\alpha\beta'}}{k_B T}}, \tag{1.9}$$

where σ is the capture cross section of the defect, v_{th} is the thermal velocity of the carriers, p is the hole density at the defect site, and $E_{\alpha\beta'}$ is the energy barrier defined by the crossing of the potential energy surfaces.

In our model, the defect is initially in state 1, which is electrically neutral. During normal device operation, the defect will remain there due to the large energetic barriers separating state 1 from all other states. When large negative bias is applied, the relative energetic shift of the neutral potential energy surface to the positive ones changes as indicated in Fig. 1.7, resulting in a decrease of the transition barrier for hole capture from the silicon valence band. After the transition to the positive state $(1 \rightarrow 2')$, the defect undergoes structural relaxation and moves to state 2 by overcoming a small energetic barrier. In its new (secondary) structural configuration, even after the bias is removed, the defect can change its charge state much easier, due to the smaller barriers for interaction with the silicon. From the neutral secondary state $1'$, the defect can return to the initial configuration 1 by again overcoming a thermal barrier.

In electrical measurements of large area transistors one observes an ensemble of the de-scribed defects and, due to the amorphous nature of the gate oxide, every defect moves on a

different energetic landscape. This means that all the state energies and barrier energies are statistically distributed and thus each defect shows a different transient behavior. The macroscopically observed degradation is the superposition of a large number of defects changing their state from 1 to 2, e.g. due to electrical stress, as the charged state of these defects influence the charge carriers in the silicon substrate. Similarly, if an increased number of defects undergo the transition $1' \rightarrow 1$ or $2 \rightarrow 2' \rightarrow 1$, a recovery of the device characteristics will be observed macroscopically.

1.6 The Search for the BTI Defect

Although the central defect for BTI has been illustrated as an oxygen vacancy up to now, to date there is no direct experimental evidence of the actual microscopic nature of this defect. Defects in SiO_2 have been predominantly studied with electron spin resonance (ESR) measurements [38]. From these studies, two types of defects have been identified in the MOS system: P_b- and E'-centers [38–42].

Judging from the properties of their ESR-spectra the P_b-centers are located at the Si-SiO$_2$-interface. They have been identified with fast amphoteric interface states [2, 39, 43–46]. Their connection to NBTI is still actively debated, but the experimental evidence suggests that the P_b-centers are only generated after long-term bias-temperature stress [26], although the generation process is still unclear. A complete picture of BTI degradation will certainly involve the P_b-center dynamics in some form, most likely as a slowly recovering, or permanent damage component. The present work, however, concentrates on the defects that are dominant for BTI, which are described using the multi-state NMP model and show strong recovery. These defects have often been suggested to be E'-centers, which are paramagnetic centers inside the SiO_2. Several centers of this class have been detected in MOS structures, especially in experiments involving irradiation damage [40, 43, 46–53]. Atomistic models for many of the E'-centers have been put forward [50, 51, 54–62]. The best agreement between theory and experiment has been found between oxygen vacancy (V_O) models and the E'_γ-center, which is the most abundant dangling bond center in amorphous SiO_2 [40]. For this reason, a huge amount of literature exists that deals with oxygen vacancies in SiO_2 [50, 54–56, 58, 59, 62–72] spanning four decades of research. Apart from radiation damage, oxygen vacancies have been linked to 1/f-noise [73], high-field stress response [74], leakage currents [75], and time-dependent dielectric breakdown [76] in the context of MOS reliability. The most interesting property for our BTI modeling efforts, however, is the bistability of the oxygen vacancy [57–59, 63, 65, 77], which can be identified with the two structural states of our BTI defect. In the so-called dimer configuration, the two silicon atoms adjacent to the oxygen vacancy relax towards each other and form a strong bond. This configuration has been identified with the E'_δ-center by some authors [40, 59, 65]. The second stable configuration is the "puckered" position, where one of the oxygen atoms relaxes through the plane of its oxygen neighbors and bonds to a close oxygen atom. The puckered position has been associated with the important E'_γ-center in amorphous SiO_2 and to its crystalline counterpart, the E'_1-center in α-quartz [57, 59, 68, 78]. Due to its involvement in different types of degradation effects and its well-studied bistability, the oxygen vacancy has been viewed as a likely candidate for the BTI defect [26, 32].

In addition to oxygen vacancies, also defects involving silicon dangling bonds and hydrogen have received some attention. Studies showed that atomic hydrogen is produced in quartz under heavy irradiation conditions [79, 80]. Although hydrogen is routinely used in the production process of MOS structures to passivate dangling bonds, it has been shown that exposure to
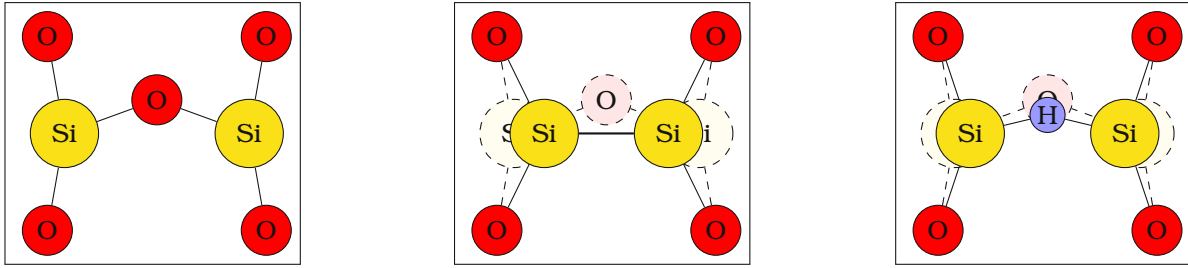
Figure 1.8: Schematic illustration of the defects investigated in the present work. **(left)** The ideal SiO_2-structure is a network of alternating silicon and oxygen atoms. **(center)** The oxygen vacancy has been associated with the paramagnetic centers E'_δ and E'_γ in ESR experiments and has been proposed as candidate defect for several degradation effects in MOS structures. **(right)** The hydrogen bridge has been less-intensely studied but is associated with the E'_2 and the E'_4 center in α-Quartz and has been proposed to play a role in SILC and hot-carrier degradation.

hydrogen can also induce degradation [80–82]. Particularly interesting for the present work is the hydrogen-complexed oxygen vacancy, which has been identified with the E'_2 and the E'_4 center in α-quartz [56, 59]. This defect, which is also sometimes called hydrogen bridge, has been linked to hot-carrier degradation [83] as well as stress-induced leakage currents [59, 84]. The hydrogen bridge is also the only hydrogen-containing defect described so far that has two stable structural configurations, which correspond to the two configurations of the oxygen vacancy [56, 59]. In the following, the states corresponding to the dimer and the puckered oxygen vacancy will be called closed and broken hydrogen bridge, respectively [85, 86]. Both the oxygen vacancy and the hydrogen bridge are illustrated in Fig. 1.8.

Unfortunately, electron spin resonance measurements can only give hints on the atomic structure of the defect and electrical measurements can only show the capture and emission behavior of the defects under different operation conditions. Thus from the experimental findings up to this point no conclusion can be drawn regarding the microscopic origin of the BTI. On the modeling side, the great success of the multi-state NMP model for BTI in the explanation of experimental data is somewhat spoiled by the large set of parameters and the unknown defect structure. The model parameters are usually determined by calibration to measurement data. Especially for the modeling of BTI and RTN, however, this method is somewhat unsatisfactory as the measurements show a broad spread in transition rates [31, 34, 87], which requires assumptions on the statistical distribution of the defect parameters. Some insight in the behavior of single defects is gained from the TDDS [31]. However, the measurement of TDDS spectral maps is a quite demanding task and few devices have been analyzed using this technique up to now. Thus, there is not yet enough data available to give an estimate about the statistics of the observed defects.

The goal of the present work is to extend our modeling efforts to the atomic scale, in order to make the prediction of the BTI-related parameters from an atomistic model of a point defect possible. The methods developed and described in this work can be used to evaluate atomistic models of defect candidates against parameters obtained from calibrations to experimental data. In order to find an atomistic model of the BTI defect, different defect candidates can then be evaluated against the available parameter sets. A suitably designed atomistic model of the amorphous MOS oxide could then be used to study the statistics of the BTI defect and make predictions on its stability and its dependence on processing conditions.

At first, we study the foundation of our BTI model in the framework of physical chemistry

to get a detailed understanding of the microscopic processes behind the states and transitions described above. This includes an attempt to shed some light on the huge amount of literature available for multi-phonon transitions. In Chap. 4, the microscopic description of the point-defect is put into the context of a semiconductor device and a multi-scale modeling method is developed, which combines the description of the defect at the microscopic level with a macroscopic model of the MOS structure. At the time this document is written, the search for a defect candidate that explains the behavior seen in BTI experiments is still ongoing. For the reasons stated above, we study the behavior of atomistic models of the oxygen vacancy and the hydrogen bridge in crystalline SiO_2 as an example. The discrepancies arising from these models with respect to BTI experiments are pointed out and possible directions for a future search of the BTI defect are given.

Erwin with his 'psi' can do
calculations quite a few.
But one thing has not been seen:
what does psi really mean?

(Erich Hückel)

2 Theory of States and Reactions

The degradation mechanisms discussed in this text proceed via chemical or electrochemical reactions at defects in the oxide or at the semiconductor-oxide interface. This chapter reviews the theories of theoretical and physical chemistry that are relevant for the applications presented in the later chapters, starting from the highest level of detail and moving to the less detailed but computationally more efficient macroscopic descriptions. Most of the concepts presented in this chapter are much more generally applicable than just to describe the dynamics of oxide defects. Examples are given to link those concepts to the context of the present application.

2.1 Problem Statement: The Molecular Hamiltonian

The theory employed in the present work rests upon the fundament of physical chemistry, sometimes also referred to as "low energy physics", which is applicable to the processes dominating our everyday experience like the dynamics of fluids and gases, electrical and thermal conduction, and chemical reactions. In contrast to high energy physics, where subatomic particles and at least three of the four fundamental interactions have to be considered, the central actors in physical chemistry are electrons and nuclei which only interact through electrostatic forces. The theoretical foundation of quantum chemistry thus lies in the Schrödinger equation of the system of electrons and nuclei. In the following, $\vec{R}$ and $\vec{r}$ denote the position vector of all nuclei and all electrons, respectively. For a system containing n electrons and N nuclei, $\vec{r}$ will be $3n$ dimensional and $\vec{R}$ will have $3N$ dimensions. The positions of the individual particles will be denoted $\vec{r}_a$ and $\vec{R}_A$ and the associated masses are m_e for the electrons (which is a fundamental constant) and M_A for the nuclei (which is different for each species). In the following, the term "vibrational" will be used for the nuclear degrees of freedom. This refers to the nature of the nuclear motion, which is usually oscillatory and confined to a potential well of some sort, as will be explained later. Especially in older works [88] and generally in works on molecules the nuclear degrees of freedom are split into vibrational and rotational parts, where the latter mean a total rotation of the molecule. As this thesis is concerned with phenomena in a solid-state context, the internal degrees of freedom (center-of-mass position and rotation) present in theories on molecules are omitted [89].

The Schrödinger equation for the system of electrons and nuclei is [88, 90, 91]

$$\hat{H}\Psi(\vec{r}, \vec{R}) = E\Psi(\vec{r}, \vec{R}), \tag{2.1}$$

where $\Psi(\vec{r}, \vec{R})$ is called the *vibronic* wave function as it expands over the electronic and the nuclear (vibrational) degrees of freedom, and

$$\hat{H} = \hat{T}_\mathrm{e} + \hat{T}_\mathrm{N} + \hat{V}_\mathrm{ee} + \hat{V}_\mathrm{NN} + \hat{V}_\mathrm{eN} \tag{2.2}$$

is the Hamiltonian of the system, which is sometimes also termed the *molecular* Hamiltonian. It consists of

$$\hat{T}_{e} = -\sum_{a=1}^{n} \frac{\hbar^2}{2m_e} \vec{\nabla}_a \qquad \text{kinetic energy operator for electrons} \qquad (2.3)$$

$$\hat{T}_{N} = -\sum_{A=1}^{N} \frac{\hbar^2}{2M_A} \vec{\nabla}_A \qquad \text{kinetic energy operator for nuclei} \qquad (2.4)$$

$$\hat{V}_{ee} = \frac{q_0}{4\pi\epsilon_0} \sum_{a<b} \frac{1}{|\vec{r}_a - \vec{r}_b|} \qquad \text{electron-electron repulsion} \qquad (2.5)$$

$$\hat{V}_{NN} = \frac{q_0}{4\pi\epsilon_0} \sum_{A<B} \frac{Z_A Z_B}{|\vec{R}_A - \vec{R}_B|} \qquad \text{nucleus-nucleus repulsion} \qquad (2.6)$$

$$\hat{V}_{eN} = -\frac{q_0}{4\pi\epsilon_0} \sum_{a=1}^{N} \sum_{A=1}^{M} \frac{Z_A}{|\vec{r}_a - \vec{R}_A|} \qquad \text{electron-nucleus attraction.} \qquad (2.7)$$

Despite the striking elegance of this equation, it is unsolvable in its pure form for all but the simplest molecules. However, a profound simplification can be drawn from a separation of the total Schrödinger equation into separate problems for the electronic and the nuclear degrees of freedom. The first theoretically well-founded approximation of this type was put forward by Max Born and Robert Oppenheimer in 1927.

2.2 The Born-Oppenheimer Approximation

The Born-Oppenheimer approximation relies on the fact that the mass of even the lightest nuclei exceeds the electron mass by orders of magnitude. In order to make use of this property, Born and Oppenheimer rewrote the molecular Hamiltonian as

$$\hat{H} = \hat{H}_0 + \kappa^4 \hat{H}_1 \qquad (2.8)$$

with

$$\kappa = \sqrt[4]{m_e/\bar{M}} \qquad (2.9)$$

$$\hat{H}_0 = \hat{T}_e + \hat{V}_{ee} + \hat{V}_{eN} + \hat{V}_{NN} \qquad (2.10)$$

$$\hat{H}_1 = -\frac{\hbar^2}{2m_e} \sum_{A=1}^{N} \vec{\nabla}_A, \qquad (2.11)$$

where $\overline{M}$ is the average ionic mass. The solution of the molecular Schrödinger equation is then expanded in powers of κ [88, 90]. The zero-order term of this expansion became known as the 'clamped nuclei' Hamiltonian. In this case, the problem reduces to the Schrödinger equation for the electrons with the nuclei fixed in their respective positions

$$\hat{H}_0 \varphi_i(\vec{r}; \vec{R}) = E_i(\vec{R}) \varphi_i(\vec{r}; \vec{R}). \qquad (2.12)$$

Although this is an eigenproblem in the electronic degrees of freedom, the results depend parametrically on the position of the nuclei. The higher order elements of the series expansion

Figure 2.1: Illustration of the dependence of different electronic states on the nuclear configuration. The adiabatically adjusting energies of the electronic states act as potential for the nuclei. Different electronic states may give rise to drastically different potentials. For example, while the potentials E_0 and E_1 in the figure show only a shift of the optimum position and a change of the curvature, E_2 does not show any optimum position in the shown configuration range. In a molecule, E_0 and E_1 correspond to bonding states, while E_2 leads to an antibonding (repulsive) behavior.
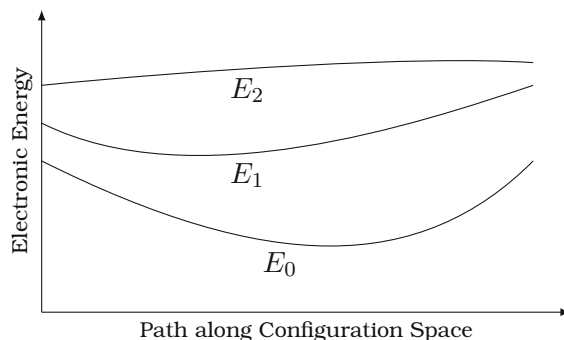
show that the expectation value of the energy $E_i(\vec{R})$ associated with the electronic state $\varphi_i(\vec{r}; \vec{R})$ will act as a potential energy on the nuclei. Thus, the molecular wave function is obtained as

$$\Psi_{iI}(\vec{r}, \vec{R}) = \varphi_i(\vec{r}; \vec{R})\eta_{iI}(\vec{R}), \tag{2.13}$$

where $\varphi_i(\vec{r}; \vec{R})$ is one of the solutions of (2.12) and $\eta_{iI}(\vec{R})$ is determined from

$$(\hat{T}_{\mathrm{N}} + E_i(\vec{R}))\eta_{iI}(\vec{R}) = E_{iI}\eta_{iI}(\vec{R}). \tag{2.14}$$

This approximation implicitly assumes that the electronic quantum number is not affected by the momentum of the nuclei, which means that the nuclei are assumed to move slowly enough that the electrons can adjust *adiabatically*, i.e. without any transfer of momentum from or to the nuclei. This approximation is consequently called the *adiabatic Born-Oppenheimer approximation*. The potential $E_i(\vec{R})$ is the *potential energy surface* of the molecule which is a central concept of chemistry and plays a significant role in the theory of chemical states and reactions. It is important to realize that different electronic states will give rise to different potential energy surfaces, as illustrated in Fig. 2.1. This difference between the potentials is at the heart of the electrochemical reactions discussed in this document. Especial importance is assigned to the potential energy surface $E_0(\vec{R})$ of the lowest electronic state $\varphi_0(\vec{r}; \vec{R})$, which is the dominant state in thermal equilibrium.

The original derivation of Born and Oppenheimer [88,90] was restricted to molecules in which the potential energy surface was essentially a quadratic function with the nuclei moving around the minimum. Interestingly, it also gives very accurate results for situations where these conditions are not even approximately fulfilled [90,92]. This behavior and also the breakdown of the approximation can be understood using an improved approach that is discussed later in Sec. 2.9.1.

In summary, the essence of the Born-Oppenheimer approximation is that due to the large difference in masses, the heavy nuclei are standing still from the perspective of the electrons. The electrons will thus adjust their orbit instantaneously to the motion of the nuclei and the energy of this orbit acts back as a potential on the nuclei. The resulting separation of the electronic and the nuclear degrees of freedom is, however, only a slight improvement from the perspective of solubility, as a typical solid or molecule still contains too many electrons and ions for an exact solution of (2.12) and (2.14). However, both the electronic as well as the nuclear problem can be greatly simplified by the exploitation of inherent symmetries and some well-defined approximations.
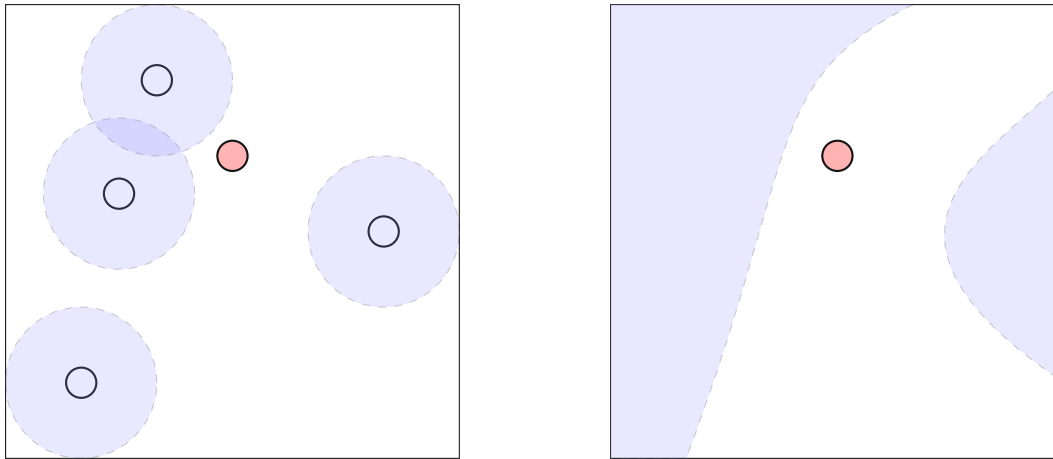
Figure 2.2: An intuitive picture of the self-consistent field approach. Instead of considering all the interactions between all particles (left), the problem is reformulated as a system of isolated particles moving in a mean field (right).

2.3 Electronic Structure Methods

The solution of the electronic many-particle problem arising from the Born-Oppenheimer approximation is a classic topic of quantum chemistry, and a multitude of approaches exist using different approximations. Depending on the size of the system and the available computational resources, different levels of sophistication can be employed to calculate the potential energy surface of a molecule or a solid. While the simplest approaches employ analytic potentials which try to mimic the shape of the electronic energy, the more sophisticated approaches actually attempt to solve the electronic Schrödinger equation (2.12) for its ground (and sometimes also for an excited) state. The latter methods are referred to as *electronic structure methods* or *quantum chemistry methods*. The term 'quantum chemistry method' may sometimes be a source of confusion, as especially in the materials science community this term is used for wave function based methods to distinguish them from density functional methods. However, in this document the term quantum chemistry method and electronic structure method are both used interchangeably for methods that calculate the potential energy surface based on a solution of the electronic Schrödinger equation.

2.3.1 Self-Consistent Field Methods: Hartree-Fock

For all but the smallest systems, an exact solution of the electronic Schrödinger equation is computationally unfeasible, as the dimensionality of the problem increases linearly with the number of particles, leading to an exponential increase in computational complexity. The first approach to the solution of the many-electron problem for isolated atoms was reported by Hartree in three papers in 1928 [93–95]. His approach, described in the second part of the series, was termed 'self-consistent field method' as it approximates the electron-electron interaction through an effective potential V_{H}, calculated from the total charge density less the charge density of the electron under consideration in order to avoid self-interaction (see Fig. 2.2).

$$\hat{H}_{\mathrm{H}} = \hat{T}_{\mathrm{e}} + \hat{V}_{\mathrm{eN}} + \hat{V}_{\mathrm{H}}(\varphi) \tag{2.15}$$

The formulation of Hartree's method initially followed physical intuition rather than a mathematical derivation. Its connection to the many-body Schrödinger equation was clarified later as a variational determination of the ground state using a product-wave function ansatz.

$$\varphi(\vec{r}_1, \vec{r}_2, \ldots) = \varphi_1(\vec{r}_1)\varphi_2(\vec{r}_2)\ldots \tag{2.16}$$

A central problem of this ansatz is that it does not have the required fermionic symmetries upon particle exchange [96–98]. An improved description was found by Fock using a properly symmetrized ansatz, which can be written in a compact form as determinant in which the single-particle wave function is the same along a column and the particle coordinate is the same along a row.

$$\varphi(\vec{r}_1, \vec{r}_2, \ldots) = \begin{vmatrix} \varphi_1(\vec{r}_1) & \varphi_2(\vec{r}_1) & \ldots \\ \varphi_1(\vec{r}_2) & \varphi_2(\vec{r}_2) & \ldots \\ \vdots & \vdots & \ddots \end{vmatrix} \tag{2.17}$$

Following the same basic steps as in the Hartree-method again leads to an effective single-particle problem, with an additional self-consistent non-local potential $\hat{V}_\mathrm{F}$.

$$\hat{H}_\mathrm{HF} = \hat{T}_\mathrm{e} + \hat{V}_\mathrm{eN} + (\hat{V}_\mathrm{H}(\varphi) - \hat{V}_\mathrm{F}(\varphi)) \tag{2.18}$$

The resulting method was named Hartree-Fock self-consistent field method, the new term in the equation is usually called exchange- or Fock-operator[1]. The Hartree-Fock self-consistent field method gives good results in many situations and is a standard method of quantum chemistry. The wave function resulting from the method as well as the total (ground state) energy are physically relevant within the bounds of the approximation, in contrary to the density functional approach which is discussed below. Although it is considered a reasonable starting point, the accuracy of the theory is limited due to the neglect of electronic correlation [96,97]. A popular method that improves on this situation is the Møller-Plesset perturbation series, which brings correlation into the Hartree-Fock-Hamiltonian using a perturbation approach that dramatically improves the accuracy for some systems [97,99].

Despite their sound theoretical foundation and the good accuracy of the perturbation approach, Hartree-Fock based methods are rarely used for large molecules or solid-state problems due to the large computational effort arising from the non-local exchange operator ($\mathcal{O}(N^4)$, where N is the number of basis functions). The sharp rise in computational demand for increasing number of basis functions results in the need for highly efficient basis sets for practical Hartree-Fock-type calculations. The employed basis sets are usually linear combinations of atomic orbitals (LCAO), most typically constructed using Gaussian functions for computational reasons [96,99]. These basis sets themselves require an appreciable amount of fine-tuning and are not to be considered general-purpose tools. For the study of defects, Hartree-Fock methods are sometimes used in embedded [66,77] or isolated [54,57] cluster models.

2.3.2 Self-Consistent Field Methods: Density Functional Theory

Density functional theory is a more mathematical approach to the many-body problem. It is based on the findings by Hohenberg and Kohn, which state that

---

[1] Interestingly, the Hartree potential in the Hartree-Fock-method is slightly different from the Hartree method as it arises from the charge density of *all* electrons, which would lead to self-interaction in the original method, but is compensated for by the Fock operator.

1. for a given external potential V_{ext} which acts equally on all of the electrons, there is a ground state electron density n_0. This density is unique to the external potential apart from a trivial constant energy.

2. there is a functional $E[n]$ of the electron density which, when minimized in n for a given V_{ext}, gives the ground state energy E_0 and the ground state electron density n_0 of the many-body system.

From these two findings it follows that the exact ground state energy of the ($3N$-dimensional) electronic system, i.e. the ground state potential energy surface, could be found by minimizing the Hohenberg-Kohn functional of the (three-dimensional) electron density, if this functional was known exactly [96, 100]. However, as the exact functional itself depends on the wave functions of the many-body system [96], additional approximations are necessary. To make the problem solvable, Kohn and Sham made the assumption that a non-interacting auxiliary system can be defined

$$\hat{H}_{\text{KS}} = \hat{T}_{\text{e}} + \hat{V}_{\text{eN}} + \hat{V}_{\text{H}} + \hat{V}_{\text{xc}} \tag{2.19}$$

that has the same ground state density and energy as the interacting system. All exchange and correlation effects of the interacting system are represented in the auxiliary system through the effective local potential $\hat{V}_{\text{xc}}$ that itself depends on the ground state electron density. Due to its favorable scaling properties ($\mathcal{O}(N^3)$) compared to the Hartree-Fock approach, and the remarkable accuracy of the method for a broad set of problems, DFT has become the standard approach in many fields of physical chemistry. The exchange-correlation potential has been a focus of active research for decades, yielding a manifold of different local and non-local potentials for different specific applications. A standard general-purpose functional that is also used extensively in the present work is the first-principles gradient-corrected functional by Perdew, Burke and Ernzerhof [101]. It is evident from the explanation above that, in contrary to the HF method, the wave functions in Kohn-Sham DFT do not have any physical relevance. Rather, the wave functions and eigenlevels are features of an auxiliary system that is only introduced as part of an approximation to the many-body problem. Nevertheless, it is common to draw conclusions from the Kohn-Sham eigenlevels, e.g. when calculating band structures [96] or defect levels [102]. Problems of the Kohn-Sham eigenspectrum, such as the underestimation of band-gaps, as well as errors in total energies are sometimes reduced by the application of so-called *Hybrid-functionals*. These functionals combine the original (semi-)local density functional of standard DFT approaches with a fraction of Hartree-Fock exchange. Hybrid functionals significantly improve the description of semiconductors and insulators, at the expense of increased computational complexity.

2.3.3 Explicit Many-Body Methods

The most accurate methods available today are the diffusion and variational quantum Monte Carlo methods, and the configuration-interaction (CI) or coupled-cluster (CC) methods [96, 97]. These methods are able to appropriately handle correlation effects and are often used as a high-accuracy reference to benchmark self-consistent field methods. However, due to their vast computational demand those methods are usually limited to very small molecules or require massively parallel computers with thousands of CPUs. For the present work, these methods are way too expensive and also more accurate than necessary, considering the various approximations that have to be made.

2.3.4 Empirical Methods

The broad class of empirical electronic structure methods offers inexpensive, yet accurate solutions to various problems, especially in the field of microelectronics research. The level of physical accuracy here ranges from the classic semi-empirical quantum chemistry methods (CNDO, MNDO, PM3, ...) [97] over tight-binding methods, which use a Hamiltonian that is built from analytic expressions [96], to the simplest empirical molecular dynamics potentials, which are based on analytical functions of the positions of the nuclei.

Semi-empirical quantum chemistry methods use a Hartree-Fock-based Hamiltonian, which replaces some of the more expensive integrals with parametrizable expressions. These methods have been under active development for decades, and are especially popular in the field of organic chemistry. The parameters for these methods are usually calibrated to small molecules, and the standard parametrizations have been shown to fail in the solid-state context [103, 104]. A comparison of semi-empirical methods for the calculation of the oxygen vacancy defect in α-quartz is given in [105], which shows a strong dependence of the predicted defect levels on the employed method.

Empirical tight-binding methods are often used for the study of the electronic structure of ideal bulk or surface structures [96]. They have also been employed in defect studies, primarily for defects in crystalline and amorphous silicon [106–108], but also for defects in SiO_2 [55]. Compared to semiempirical methods, the tight-binding Hamiltonians rely on even stronger simplifications which makes the parametrizations of this method even less transferable. Thus, when employing tight-binding methods one cannot rely on standard parametrizations as is usually done in semiempirical methods.

A review of different empirical molecular dynamics potentials applied to silicon or SiO_2 systems is found in [109]. Although empirical potentials are computationally very efficient and make calculations with millions of atoms possible [78], they have too little predictive power for defect calculations as those involve unpaired spins and charged states which are difficult to include in this formalism in a physically meaningful way. However, empirical potentials are used extensively for the generation of amorphous structures that are subsequently used for defect calculations [78, 110, 111].

The advantage of semiempirical methods is the inclusion of experimental input, to account efficiently for the physics neglected in the approximations. For the study of defects in SiO_2, the calibration of all discussed empirical methods requires an extensive training set. Unfortunately there is no reliable experimental data available that can be used as a reference for parametrization, so for the present work we are bound to ab-inito methods.

2.4 The Nuclear Problem: Chemical Microstates

For electronic structure problems it is reasonable to treat the correlated motion of the electrons as a second-order effect, which does not influence the basic behavior for most practical cases. For the motion of the nuclei, an approximation like this is not possible. Vibrational states are usually heavily correlated motions of nuclei like stretching or bending modes in molecules or phonons in a solid. A fully quantum-mechanical treatment is again impossible due to the large number of degrees of freedom and even a quantum Monte-Carlo-like treatment is unfeasible due to the computational effort required to calculate the potential energy surface. It is thus necessary to either approximate the quantum mechanical nuclear problem as a classical one or to approximate the potential energy surface as an essentially quadratic function of the position of the nuclei so that the atomic motion can be separated into uncoupled harmonic oscillations.

The former method is broadly applied throughout theoretical chemistry for molecules and solids and is well suited for situations where temperatures are high enough so that quantization effects may be neglected and where the adiabatic Born-Oppenheimer approximation holds. With respect to the BTI model introduced in Sec. 1.5, this concerns the structural transitions $1 \leftrightarrow 1'$ and $2 \leftrightarrow 2'$. For situations where the electronic state changes non-adiabatically, as in the charge transition reactions $1 \leftrightarrow 2'$ and $2 \leftrightarrow 1'$, or at very low temperatures the quantum-mechanical nature of the nuclei must be considered and the harmonic approximation, or a similar simplification, is necessary [91].

Once the potential energy surface for a given atomic system is known and a sufficiently accurate description of the nuclear dynamics has been found, it is possible to calculate observable quantities and predict the evolution of that system over time. The state of the atomic system under consideration is fully described by the state of the electronic system, which is usually identified by its potential energy surface, and the nuclear state, which is $\eta_{iI}(\vec{R})$ in a quantum-mechanical description and the instantaneous position in phase-space $(\vec{R}, \vec{P}) - \vec{P}$ denoting the momenta of all particles — in a classical description. In the following, these combinations of electronic and nuclear states will be called *microstates* in accord with the theory of statistical physics [112]. As will be explained in more detail in Sec. 2.9.1, the adiabatic Born-Oppenheimer approximation can be assumed to be valid for all regions of the nuclear configuration space in which the potential energy surfaces are sufficiently separated. The systems of interest for the present document spend most of their time inside these regions and the electronic transitions happen either through radiative transitions or non-radiatively in the vicinity of potential energy surface crossings. Both of these transitions are sufficiently described as occurring instantaneously. Consequently, the transitions between the microstates are governed by the dynamics of the nuclei and the transitions between different potential energy surfaces. Although in principle the dynamics of any molecule or solid can be described in this way, in practice it is usually tedious to describe the long-term evolution of even the simplest chemical system from the trajectories of its nuclei and transitions between electronic states. Fortunately, the time-evolution of chemical systems usually consists of longer time-periods of thermal quasi-equilibrium which are interrupted by transitional motions of very short duration. This behavior is exploited and formalized in the theory of chemical states and reactions.

2.5 Chemical States and Reactions

In order to understand chemical kinetics, it is first necessary to define in a physically meaningful way the *chemical states*, which are the central actors of chemistry, and the *chemical reactions*, which change the system under consideration from one chemical state to another. Quite generally, chemical states are groups of microstates. The microstates that belong to a certain chemical state could in principle be selected completely arbitrarily, but usually a chemical state is defined and receives its meaning from a certain observable[2]. In the case of a defect within a semiconductor device the corresponding observable may be for example its charge state, which is observed through its effects on the device characteristics, or its bonding state, which will give rise to different capture and emission times. The microstates belonging to a chemical state are consequently those which are indistinguishable from the viewpoint of the associated observable. It is the nature of these observables that they need to be stable for a sufficient amount of time, so that they can be measured by a human-made apparatus. As

---

[2]To avoid confusion, it has to be mentioned that the observables here are not the principal quantum-mechanical operators, but are elements of statistical mechanics, i.e. measurable properties.

Figure 2.3: The potential energy surface of an atomic system typically has several minima which are separated by energetic barriers. The nuclei will spend a significant amount of time oscillating randomly around those minima and will eventually pass the barriers at time scales that are too short to be observable. Along the barriers, the configuration space can be separated into chemical states, illustrated as grey/white region. The potential energy surface could for example arise from two different bonding states of a defect, as schematically shown in the boxes.
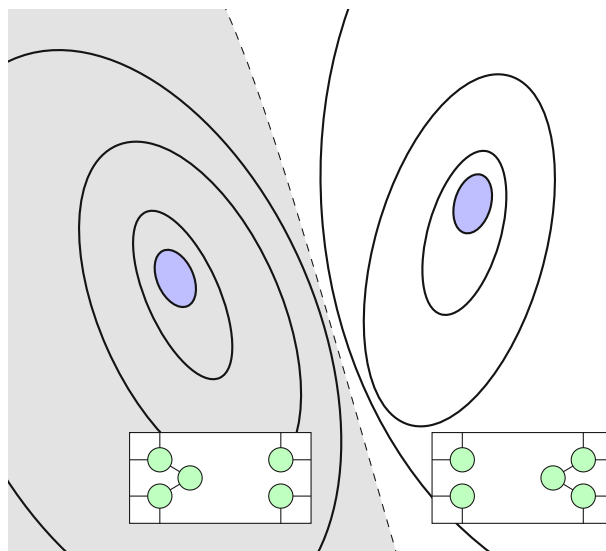
for the microstates, the electronic subsystem often defines its own chemical states as it tends to establish a stationary state on a very short time scale (femtoseconds) and this state is then quite stable in the absence of potential energy surface crossings or radiative transitions. For the vibrational subsystem, the requirement on stability over a certain time-range means that states are defined as the neighborhood of minima in the potential energy surface. This follows from the nature of the atomic motion, which is essentially random due to the permanent interaction with the environment. Usually within picoseconds after a change in state the momenta of the nuclei will assume the thermal equilibrium distribution induced by the heat-bath. Thus the momentum, or in the quantum mechanical view the vibrational quantum state, of the nuclei is not relevant in the definition of chemical states and the only relevant information comes from the shape of the region of the configuration space in which they are moving, which is defined by the energetic barriers of the potential energy surface, as illustrated in Fig. 2.3.

Once a chemical state is defined in terms of microstates, the measurable observables are obtained from thermal averages over those microstates belonging to this chemical state. If the nuclei are treated as classical particles, those thermal averages consist of integrals over a certain potential energy surface and over the momentum-space of the nuclei, which is commonly assumed to follow the behavior of the ideal gas [112].

As mentioned above, in practical calculations it is assumed that transitions between chemical states occur instantaneously and the thermal equilibrium of the microstates in the new chemical state is established immediately. This assumption is obviously justified for transitions of the electronic subsystem, as mentioned above. Transitions between the minima of a potential energy surface or between two different electronic states are usually followed by an equilibration phase where the momentum distribution of the nuclei returns to the ideal gas distribution. This equilibration usually proceeds at time-scales of picoseconds, which is also reasonably instantaneous for most observables. However, especially for the case of hydrogen-passivated dangling bonds at the silicon surface, long-term stable vibrational modes have been reported which lead to a considerably prolonged equilibration [113]. Thus, regarding the nuclear subsystem the assumption of instantaneous transitions needs to be applied cautiously.

For the sake of completeness it is mentioned here that, as chemical states may be arbitrarily defined, it is possible that certain microstates are part of more than one chemical state. Additionally, a chemical state may consist of an arbitrary number of lower-level chemical states.

To avoid confusion, in the following all chemical states and reactions are *elementary*, i.e. they are not further separable into long-term stable chemical states.

2.6 The Chemical Master Equation

Once the chemical states and reactions that comprise the chemical system under consideration are defined, their dynamics can be described as a random process that switches between states [114, 115]. For this purpose, the state of the chemical system is described as a vector $\vec{x}$. Additionally, a set of reaction channels is established, which cause the transitions between the discrete states of this vector. Due to the unpredictable nature of the dynamics of the microstates, the time at which a reaction takes place is not a deterministic quantity. Instead, if the chemical system is in a given state $\vec{x}_\alpha$ at time t, for every reaction channel γ a reaction rate c_γ can be defined, so that $c_\gamma \mathrm{d}t$ is the probability of the reaction taking place between t and $t + \mathrm{d}t$ [115]. Due to the assumed instantaneous equilibration of the microstates, c_γ is a constant in time. Different chemical states have different reaction rate constants for their reaction channels. Again due to the assumed instantaneous equilibration, these reaction rate constants depend only on the current state of the chemical system irrespective of the previous states of the system. In this case a function can be defined for every reaction channel that assigns a specific rate to a specific state $c_\gamma = a_\gamma(\vec{x}_\alpha)$. These functions are called the *propensity functions* [115]. The change induced by the reaction channel γ is described using the state change vector $\vec{\nu}_\gamma$. The thus formulated model describes a memory-less random process with discrete states, which is usually called a Markov process [37]. The removal of memory from the system occurs through the thermal equilibration, which is assumed to happen much faster than the chemical reactions. Examples for non-markovian behavior are correlated reactions as in the recombination-enhanced defect reaction (REDR) theory [116] or time-dependent propensity functions as suggested for reemission after the multi-phonon capture of carriers [117]. In the context of BTI, non-markovian behavior has been used to explain accelerated recovery observed in charge-pumping measurements [118]. Interestingly, in standard BTI experiments with constant or AC stress, even up to $5\,\mathrm{MHz}$, no memory-related behavior has been found yet. We thus assume that the accelerated recovery is a specific effect of the charge-pumping measurements, which requires deeper experimental investigation, and ignore non-markovian behavior in this work.

According to the theory of stochastic chemical kinetics [114, 115], the evolution of this system over time can then be described by a chemical master equation

$$\frac{\partial P(\vec{x}, t)}{\partial t} = \sum_{\gamma=1}^{\Gamma} [a_\gamma(\vec{x} - \vec{\nu}_\gamma)P(\vec{x} - \vec{\nu}_\gamma, t) - a_\gamma(\vec{x})P(\vec{x}, t)], \tag{2.20}$$

where $P(\vec{x}, t) = P(\vec{X} = \vec{x}, t | \vec{x}_0, t_0)$ is the probability that the stochastic process $\vec{X}(t)$ equals $\vec{x}$ at time t, given that $\vec{X}(t_0) = \vec{x}_0$.

The master equation approach can be illustrated using the simple example of a system with two states $\vec{x}_1$ and $\vec{x}_2$ [37], see Fig. 2.4. The system has two reaction channels 1 and 2, which connect the two states through the state change vectors $\vec{\nu}_1$ and $\vec{\nu}_2$ as

$$\vec{x}_1 + \vec{\nu}_1 = \vec{x}_2 \quad \text{and} \quad \vec{x}_2 + \vec{\nu}_2 = \vec{x}_1 \tag{2.21}$$

Figure 2.4: Illustration of the example system discussed in the text. The system exists in one of the two states $\vec{x}_1$ and $\vec{x}_2$. Transitions between these states are caused by two reaction channels with the state-change vectors $\vec{\nu}_1$ and $\vec{\nu}_2$, and the associated rates k_{12} and k_{21}.
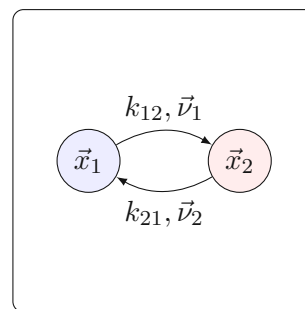
The propensity functions a_1 and a_2 assume the form

$$a_1(\vec{x}_1) = k_{12}, \qquad a_1(\vec{x}_2) = 0, \tag{2.22}$$

$$a_2(\vec{x}_1) = 0, \text{and} \quad a_2(\vec{x}_2) = k_{21}. \tag{2.23}$$

The master equation for this system consequently reads

$$\frac{\partial P(\vec{x}_1, t)}{\partial t} = k_{21} P(\vec{x}_2, t) - k_{12} P(\vec{x}_1, t) \tag{2.24}$$

$$\frac{\partial P(\vec{x}_2, t)}{\partial t} = k_{12} P(\vec{x}_1, t) - k_{21} P(\vec{x}_2, t) \tag{2.25}$$

As the system can only exist in one of the two states at a time, it follows that

$$P(\vec{x}_1, t) = 1 - P(\vec{x}_2, t) = p(t), \tag{2.26}$$

which reduces the master equation of the two-state system to

$$\frac{\partial p(t)}{\partial t} = k_{21}(1 - p(t)) - k_{12} p(t). \tag{2.27}$$

This is the rate-equation of the two-state system, which is equivalent to the master equation for this simple example.

Within the theoretical frame work of the chemical master equation, all the microphysical details elaborated in the previous section are now contained in the propensity functions a_γ and the state-change vectors $\vec{\nu}_\gamma$ for the Γ reaction channels. These can be either obtained from experiment, or calculated from microphysical theories, some of which are explained in the following.

2.7 The Calculation of Rates

The assumptions introduced above lay the foundation for the development of theoretical methods to calculate rates between chemical states. As mentioned in Sec. 2.4, the description of the nuclear state can either be classical with the full potential energy surface or quantum-mechanical with a highly idealized potential. Both approaches contain specific approximations and thus need to be cautiously applied to real-world situations. Quite generally, for reactions occurring at low temperatures the quantum-mechanical approach will be the most suitable as the effects of quantization and tunnelling may be pronounced, yet the nuclear system will be close to a minimum of the potential energy surface where idealizations are quite accurate. For reactions at higher temperatures, quantum mechanical effects will be less pronounced but the system will occupy states that are further away from the potential minima which are poorly described by the usually harmonic model Hamiltonians.

Figure 2.5: Illustrative example of a potential energy surface along a reaction path. The reaction path itself is the optimal path on the $3N$-dimensional potential energy surface between two minima. The point of maximum energy, which is a saddle-point of the potential energy surface, is sometimes called the transition state. Its energy with respect to the energetic minimum of the initial state is the activation energy E_{a}. The transition point is also the border which separates the initial and the final state in a classical picture.
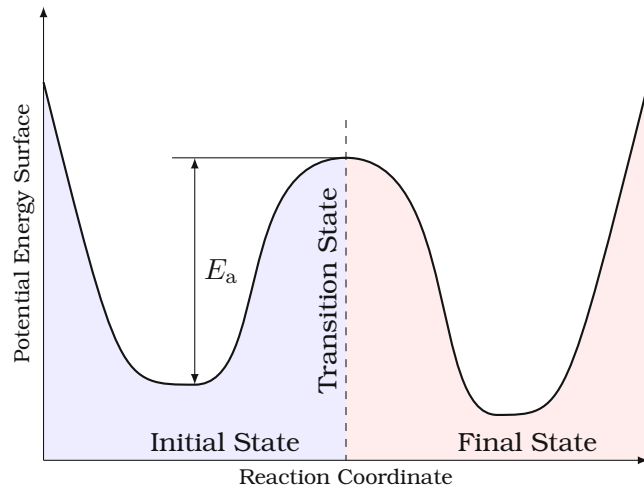
2.8 Barrier Hopping Transitions

Barrier hopping transitions such as the structural transitions in the BTI model are reactions which the electronic system follows adiabatically and thus only change the state of the nuclear system. For the temperature ranges relevant to this document these transitions are sufficiently described using classical nuclei. This is a common working-hypothesis in practical calculations [112, 119, 120] and is sometimes supplemented with quantum mechanical corrections [112] where necessary. The microstates consist of the electronic state, which is unchanged except for the adiabatic adjustment of the electronic wave functions, and the position of the nuclear system in phase-space [119], which follows classical mechanics.

As mentioned above, for a given defect model the barrier hopping processes can in principle be described by a propagation of the microstates, i.e. the phase-space position of the nuclei. Calculations of this type are called molecular dynamics simulations [119]. However, the time range that can be treated with molecular dynamics is in the picosecond regime and can only be extended to nanoseconds for classical molecular dynamics potentials, which are not usable in defect calculations. Usual defect reactions in BTI occur in and above the microsecond regime [26, 37], which makes them rare events from a microstate perspective.

The theory employed for the calculation of rates in this picture is the *transition state theory*. This theory is the mathematical formulation of the assumptions of Sec. 2.5. As in Fig. 2.3, the chemical states in the transition state theory are defined by regions $\mathcal{R}_{\alpha} \subset \mathbb{R}^{3N}$ in the configuration space of the N nuclei. These regions are non-overlapping and defined by the barriers of the potential energy surface. The transition from a region $\mathcal{R}_1$ to an adjacent region $\mathcal{R}_2$ is assumed to proceed as a flux $\mathcal{F}(\partial\mathcal{R}_{12})$ through the boundary surface $\mathcal{R}_{12}$, which is called the *transition state* [121].

In practice, one is usually only interested in the temperature activation for a certain transition. Also, the thermal integrals necessary to calculate the flux through the transition state, are quite tedious to calculate. Due to the assumption of thermal equilibrium, in which the system preferably occupies states of lower energy, the transition will be dominated by the point of lowest energy of the transition state. In practical calculations it is thus usually sufficient to find the energetically optimal path between the energetic minimum point of $\mathcal{R}_1$ and the energetic minimum point of $\mathcal{R}_2$, as illustrated in Fig. 2.5. This path is usually termed the *reaction path*. The maximum energy along this path is called the activation energy. Macroscopic theories usually model the temperature activation of hopping transitions using an Arrhenius law

that has the activation energy as parameter. However, one has to be aware that this neglects entropic properties which are only sufficiently described in the full transition state theory.

2.9 Multi-Phonon Transitions

The charge-state transitions in the multi-state multi-phonon transition model for BTI involve the trapping of holes from the silicon valence band. These trapping events are understood as non-radiative multi-phonon (NMP) transitions. Multi-phonon, or vibronic, transitions are transitions involving a change of the electronic and the vibrational state. They play significant roles in many domains of molecular and solid state physics and have been studied extensively from both the experimental and theoretical side [91, 122–125] especially for transitions at point-defects. The development of the theory of vibronic transitions is tightly linked to the development of the quantum mechanical theory of solids and molecules. As multi-phonon transitions at defects are inherently quantum-mechanical processes that are significantly influenced by a chaotic perturbation (i.e. the heat-bath), their theoretical description is a quite demanding task and usually involves strong idealizations.

2.9.1 Vibronic Coupling

The first theory capable of explaining the behavior of molecules on a well-founded quantum-mechanical level was the adiabatic Born-Oppenheimer approximation. This approximation, which is based on a power-series expansion with respect to the ratio of the electronic and nucleic masses, see Sec. 2.2, has some drawbacks that in principle limit its applicability to chemical processes. The first problem is that the potential energy surfaces arising from the power-series expansion are essentially harmonic functions with the equilibrium positions fixed at a certain configuration. In this form, the theory is unable to describe the adiabatic reactions discussed in the previous section. Nevertheless, the comparison with experimental studies showed that "the adiabatic model has a wider application than predicted by this theory" ([90], Appendix VII). Secondly, within the series expansion formulation there will always be an adiabatic adjustment of the electronic state to the vibrational degrees of freedom, i.e. there will be no transfer of kinetic energy from the nuclei to the electrons and thus no change in the electronic state can be induced from the vibrations of the molecule or solid.

A second approach to the derivation of a molecular wave function was presented by Born more than two decades later [92] (see also [90], Appendix VIII). Instead of a series expansion of the molecular Hamiltonian, this derivation starts with an ansatz-wave function of the form

$$\Psi(\vec{r}, \vec{R}) = \sum_i \varphi_i(\vec{r}; \vec{R})\eta_i(\vec{R}), \qquad (2.28)$$

where the $\varphi_i(\vec{r}; \vec{R})$ are the solutions of the electronic Hamiltonian $\hat{H}_0 = \hat{T}_e + \hat{V}_{ee} + \hat{V}_{NN} + \hat{V}_{eN}$ in (2.12), which are assumed to be known, and $\eta_i(\vec{R})$ can be seen as a weighting-factor for the electronic wave function i. In a way, this ansatz expands the molecular wave function using the adiabatic Born-Oppenheimer wave functions as a basis set. This expansion considers the correlation of the electronic motion to the motion of the nuclei, but neglects the effects on the nuclei induced by the instantaneous positions of the electrons. Thus, it is not exact although stated otherwise sometimes.

Before the ansatz is inserted into the molecular Schrödinger equation (2.1), it is useful to apply it to the constituent operators of the associated Hamiltonian (2.2) separately. The potential operators, which are mere functions of the degrees of freedom, are summed up as

$\hat{V} = \hat{V}_{\text{ee}} + \hat{V}_{\text{NN}} + \hat{V}_{\text{eN}} = V(\vec{r}, \vec{R})$ and are applied as

$$\hat{V}\Psi(\vec{r}, \vec{R}) = \sum_i V(\vec{r}, \vec{R})\varphi_i(\vec{r}; \vec{R})\eta_i(\vec{R}). \tag{2.29}$$

The electronic kinetic energy operator (2.3) acts only on the $\varphi_i(\vec{r}; \vec{R})$

$$\hat{T}_{\text{e}}\Psi(\vec{r}, \vec{R}) = \sum_i \eta_i(\vec{R})\hat{T}_{\text{e}}\varphi_i(\vec{r}; \vec{R}). \tag{2.30}$$

The application of the electronic Hamiltonian to $\Psi(\vec{r}, \vec{R})$ thus gives

$$\hat{H}_0\Psi(\vec{r}, \vec{R}) = (\hat{T}_{\text{e}} + \hat{V})\Psi(\vec{r}, \vec{R}) \tag{2.31}$$

$$= \sum_i \eta_i(\vec{R})\hat{T}_{\text{e}}\varphi_i(\vec{r}; \vec{R}) + V(\vec{r}, \vec{R})\varphi_i(\vec{r}; \vec{R})\eta_i(\vec{R}) \tag{2.32}$$

$$= \sum_i \eta_i(\vec{R})\left(\hat{T}_{\text{e}}\varphi_i(\vec{r}; \vec{R}) + V(\vec{r}, \vec{R})\varphi_i(\vec{r}; \vec{R})\right) \tag{2.33}$$

$$= \sum_i \eta_i(\vec{R})\left(\hat{H}_0\varphi_i(\vec{r}; \vec{R})\right) = \sum_i \eta_i(\vec{R})\left(E_i(\vec{R})\varphi_i(\vec{r}; \vec{R})\right) \tag{2.34}$$

where $E_i(\vec{R})$ is again the eigenvalue for $\varphi_i(\vec{r}; \vec{R})$ with respect to $\hat{H}_0$. The nuclear kinetic energy operator (2.4) acts on both the $\varphi_i(\vec{r}; \vec{R})$ and the $\eta_i(\vec{R})$. Using the definition

$$\hat{T}_{\text{N}} = \sum_{A=1}^{N} \frac{\hat{P}_A \cdot \hat{P}_A}{2M_A} \tag{2.35}$$

with

$$\hat{P}_A = -i\hbar\vec{\nabla}_A, \tag{2.36}$$

and the product rules for the gradient and the divergence, it is trivial to show that

$$\hat{T}_{\text{N}}\Psi = \sum_i \varphi_i\hat{T}_{\text{N}}\eta_i + \eta_i\hat{T}_{\text{N}}\varphi_i + \sum_{A=1}^{N} \frac{1}{M_A}\left(\hat{P}_A\varphi_i\right) \cdot \left(\hat{P}_A\eta_i\right). \tag{2.37}$$

Applying the Hamilton operator

$$\hat{H}\Psi(\vec{r}, \vec{R}) = (\hat{H}_0 + \hat{T}_{\text{N}})\Psi(\vec{r}, \vec{R}), \tag{2.38}$$

one arrives at

$$\hat{H}\Psi(\vec{r}, \vec{R}) =$$

$$\sum_i \eta_i E_i \varphi_i + \varphi_i\hat{T}_{\text{N}}\eta_i + \eta_i\hat{T}_{\text{N}}\varphi_i + \sum_{A=1}^{N} \frac{1}{M_A}\left(\hat{P}_A\varphi_i\right) \cdot \left(\hat{P}_A\eta_i\right) = E\sum_i \varphi_i\eta_i. \tag{2.39}$$

Finally, the equation is expanded in the electronic basis set. Therefore we multiply with φ_j^* from the left and integrate over the electronic degrees of freedom $\vec{r}$, yielding the system of equations

$$\left(\hat{T}_{\text{N}} + E_j(\vec{R})\right)\eta_j(\vec{R}) +$$

$$\sum_i \left(\int \varphi_j^*(\vec{r}; \vec{R})\hat{T}_{\text{N}}\varphi_i(\vec{r}; \vec{R})d\vec{r} + \sum_{A=1}^{N} \frac{1}{M_A}\int \varphi_j^*(\vec{r}; \vec{R})\hat{P}_A\varphi_i(\vec{r}; \vec{R})d\vec{r} \cdot \hat{P}_A\right)\eta_i(\vec{R})$$

$$= E\eta_j(\vec{R}) \tag{2.40}$$

for i running over all eigenstates of $\hat{H}_0$. This system of equations is conveniently rewritten into matrix form as

$$\mathcal{H}\vec{\eta}(\vec{R}) = E\vec{\eta}(\vec{R}) \tag{2.41}$$

with

$$\vec{\eta}(\vec{R}) = \begin{pmatrix} \eta_1(\vec{R}) \\ \eta_2(\vec{R}) \\ \eta_3(\vec{R}) \\ \vdots \end{pmatrix} \tag{2.42}$$

and

$$\mathcal{H} = \mathcal{H}^{\mathrm{A}} + \mathcal{H}^{\mathrm{NA}} \tag{2.43}$$

$$\mathcal{H}^{\mathrm{A}} = \begin{pmatrix} \hat{T}_{\mathrm{N}} + E_1(\vec{R}) & 0 & 0 & \cdots \\ 0 & \hat{T}_{\mathrm{N}} + E_2(\vec{R}) & 0 & \cdots \\ 0 & 0 & \hat{T}_{\mathrm{N}} + E_3(\vec{R}) & \cdots \\ \vdots & \vdots & \vdots & \ddots \end{pmatrix} \tag{2.44}$$

$$\mathcal{H}^{\mathrm{NA}} = \begin{pmatrix} \hat{L}_{11} & \hat{L}_{12} & \hat{L}_{13} & \cdots \\ \hat{L}_{21} & \hat{L}_{22} & \hat{L}_{23} & \cdots \\ \hat{L}_{31} & \hat{L}_{32} & \hat{L}_{33} & \cdots \\ \vdots & \vdots & \vdots & \ddots \end{pmatrix} \tag{2.45}$$

$$\hat{L}_{ij} = \int \varphi_j^*(\vec{r}; \vec{R})\hat{T}_{\mathrm{N}}\varphi_i(\vec{r}; \vec{R})d\vec{r} + \sum_{A=1}^{N} \frac{1}{M_A} \int \varphi_j^*(\vec{r}; \vec{R})\hat{P}_A\varphi_i(\vec{r}; \vec{R})d\vec{r} \cdot \hat{P}_A. \tag{2.46}$$

$\mathcal{H}^{\mathrm{A}}$ is now again the adiabatic Hamiltonian known from the Born-Oppenheimer approximation, the transfer of kinetic energy from the vibrational to the electronic system is described by the non-adiabatic part of the Hamiltonian $\mathcal{H}^{\mathrm{NA}}$. As one would expect, the adiabatic Hamiltonian is diagonal in the matrix representation and the coupling between the potential-energy surfaces $E_i(\vec{R})$ is solely due to $\mathcal{H}^{\mathrm{NA}}$, more specifically the off-diagonal matrix elements $\hat{L}_{ij}$.

If $\mathcal{H}^{\mathrm{NA}}$ is neglected, the original Born-Oppenheimer approximation is retained and the resulting eigenstates will be of the form (2.13)

$$\Psi_{iI}(\vec{r}, \vec{R}) = \varphi_i(\vec{r}; \vec{R})\eta_{iI}(\vec{R}), \tag{2.47}$$

i.e. the state of the system can be identified by a separate quantum number for the electronic and the vibrational state, respectively. In the more general case where the non-adiabatic part of the Hamiltonian cannot be neglected, the electronic and vibrational quantum numbers are not generally separable and the eigenstates will expand over several electronic states.

There seems to be no established name for the presented approach to the molecular Schrödinger equation. It is sometimes also refered to as Born-Oppenheimer approximation (which is misleading as it is using a completely different derivation), Born-Huang approximation, or Born-ansatz. The non-adiabatic theory not only makes it possible to describe vibronic coupling, but also gives an idea of the conditions under which the adiabatic approximation is reasonable. Following the expressions in [126] and Sec. 3.1.3 of [91], the adiabatic approximation is valid for systems with a large separation between the potential energy surfaces and a weak dependence of the electronic wave functions on the position of the nuclei.

For the derivations in the following sections it is convenient to use a Dirac notation for the Born-Oppenheimer states as

$$\left|\Psi_{iI}\right\rangle = \left|i(\vec{R})\right\rangle\left|iI\right\rangle\!\rangle. \tag{2.48}$$

Although one may be tempted to view this wave function as a simple tensor product of wave functions and employ the usual algebra, this is not possible here due to the parametric dependence of the electronic state on the vibrational coordinate $\vec{R}$. Nevertheless, this notation is often found in literature and will also be applied in this document where ever it may serve to improve readability. However, the reader is advised to handle vectors of the form (2.48) with care. To improve readability somewhat further this document uses a notation that distinguishes between integrals over the electronic degrees of freedom $\langle\,\cdot\,|\,\cdot\,\rangle$ and over the nuclear degrees of freedom $\langle\!\langle\,\cdot\,|\,\cdot\,\rangle\!\rangle$.

2.9.2 Quantum Mechanical Theory of Vibronic Transitions

Although in principle a diagonalization of the non-adiabatic Hamiltonian is possible, the resulting stationary states are not of interest for this work, as we assume transitions between well-defined electronic states. Indeed, in real-world situations the stationary states corresponding to the eigenstates of the non-adiabatic Hamiltonian will never be established due to the constant perturbation from the environment. The influence of the environment is a very complex random process in nature that cannot be treated, or even formulated, exactly. The theory of vibronic transitions therefore has to rely on physical intuition and defines the initial and final states of the transition somewhat heuristically as the initial and final Born-Oppenheimer states (2.13). It is assumed that initially the electronic subsystem is in a defined state, which is called $\left|i(\vec{R})\right\rangle$ in the following. The transition rate to a specific final state $\left|f(\vec{R})\right\rangle$ is to be calculated. The vibrational degrees of freedom assumingly have established an equilibrium with the surrounding lattice, i.e. the probability p of finding the vibrational subsystem in a state $\left|iI\right\rangle\!\rangle$, given that the electronic system is in state i depends on the energy E_{iI} as

$$p_{iI} = Z^{-1}e^{-\frac{E_{iI}}{k_{\mathrm{B}}T}}, \tag{2.49}$$

where Z is the canonical partition function

$$Z = \sum_{I} e^{-\frac{E_{iI}}{k_{\mathrm{B}}T}}. \tag{2.50}$$

The Born-Oppenheimer states, however, do not diagonalize the non-adiabatic Hamiltonian and thus will not give rise to stationary states but will decay over time and thus the system will move between different electronic states. As the off-diagonals in the non-adiabatic Hamiltonian are usually assumed to be small compared to the diagonal part, the transitions between the electronic states is treated using first-order time-dependent perturbation theory [98]. Thus, the rate of transition from $\left|\Psi_{iI}\right\rangle$ to $\left|\Psi_{jJ}\right\rangle$ reads

$$W_{iI\to jJ} = \frac{2\pi}{\hbar}\left|\left\langle\Psi_{iI}\right|\hat{L}\left|\Psi_{jJ}\right\rangle\right|^2\delta(E_{jJ} - E_{iI}), \tag{2.51}$$

where the perturbation $\hat{L}$ is the non-adiabacity operator (2.46).

The total rate from $\left|i(\vec{R})\right\rangle$ to $\left|f(\vec{R})\right\rangle$ is obtained by averaging (2.51) over all possible initial states $\left|iI\right\rangle\!\rangle$ and summing over all possible final states $\left|fF\right\rangle\!\rangle$

$$W_{\mathrm{i}\to\mathrm{f}} = \frac{2\pi}{\hbar}\mathop{\mathrm{avg}}_{I}\sum_{F}\left|\langle\!\langle fF\right|\left\langle f(\vec{R})\right|\hat{L}\left|i(\vec{R})\right\rangle\left|iI\right\rangle\!\rangle\right|^2\delta(E_{\mathrm{f}F} - E_{\mathrm{i}I}). \tag{2.52}$$

where avg_I is just a shorthand for an averaging over all states I, using (2.49) as the weighting factors.

2.9.3 Model Matrix Elements

Now that the basic theory of vibronic transitions is laid out, the next important step is the calculation of the matrix element $\langle\!\langle \mathrm{fF} | \langle \mathrm{f}(\vec{R}) | \hat{L} | \mathrm{i}(\vec{R}) \rangle | \mathrm{iI} \rangle\!\rangle$. The integration for this matrix element runs over all electronic and vibrational degrees of freedom and requires the quantum mechanical states of the electronic and the vibrational system to be known. Especially the latter requirement is impossible to fulfill exactly for real-world systems, so additional assumptions have to be made. These assumptions must lead to a model description that captures enough of the basic behavior of the real-world system to give accurate results yet include only so much complexity that a quantum-mechanical treatment is still feasible.

The published models for vibronic transitions [91, 127–130] contain several approximations that simplify the molecular Hamiltonian (2.2) and the corresponding Born-Oppenheimer states. These approximations are described in the following.

Unaffected Electrons

As stated above, the molecular Hamiltonian includes the interactions of all electrons and all nuclei. However, a vibronic transition will usually leave most of the electrons in their respective state thus it is not necessary to consider them explicitly in the calculation. What has to be considered is their interactions with the nuclei and with the explicitly treated electrons (usually only one). The former interactions together with the Coulomb repulsion $\hat{V}_{\mathrm{NN}}$ will give rise to a potential for the nuclei, the latter interactions are considered in the effective electronic Hamiltonian $\hat{H}_{\mathrm{e}}$. The resulting Hamiltonian is

$$\hat{H} = \hat{H}_{\mathrm{e}} + \hat{H}_{\mathrm{N}} + \hat{H}_{\mathrm{eN}}, \tag{2.53}$$

where $\hat{H}_{\mathrm{e}}$ only acts on the (considered) electronic degrees of freedom and

$$\hat{H}_{\mathrm{N}} = \hat{T}_{\mathrm{N}} + \hat{V}_{\mathrm{N}} \tag{2.54}$$

acts only on the nuclei. The details of $\hat{H}_{\mathrm{e}}$ and $\hat{H}_{\mathrm{eN}}$ depend heavily on the system under consideration and cannot be given in a general form.

Phonon Modes

Another important approximation concerns the potentials $\hat{V}_{\mathrm{N}}$ and $\hat{H}_{\mathrm{eN}}$. It is usually assumed that they are smooth enough so that a Taylor series expansion is suitable and this expansion is usually canceled after the second order for $\hat{V}_{\mathrm{N}}$. For a parabolic potential

$$V(\vec{R}) = V_0 + \vec{V}_1 \cdot \vec{R} + \vec{R}^{\mathrm{T}} \tilde{V}_2 \vec{R} \tag{2.55}$$

it is always possible to define a coordinate system $\vec{R}'$ which is shifted so that the linear part of the potential is zero. On top of this, a coordinate system $\vec{Q} = \sum_S Q_S \vec{e}_S$ is obtained from the diagonalization of the quadratic part as

$$\tilde{V}_2 \vec{e}_S = \Lambda_S \vec{e}_S. \tag{2.56}$$

28

The eigenvalue Λ_S is conveniently written as

$$\Lambda_S = \frac{M_S \omega_S^2}{2} \tag{2.57}$$

using the mass

$$M_S = \sum_A (e_{SAx}^2 + e_{SAy}^2 + e_{SAz}^2) M_A, \tag{2.58}$$

as in a classical picture this leads to a nuclear motion that is composed of uncoupled harmonic modes with the frequencies ω_S. The resulting coordinate system is called modal system, M_S is the modal mass, and the coordinates Q_S are called modal coordinates. The vibrational Hamiltonian thus assumes the form

$$\hat{H}_N = \sum_S -\frac{\hbar^2}{2M_S}\frac{\partial^2}{\partial Q_S^2} + \frac{M_S \omega_S^2}{2} Q_S^2. \tag{2.59}$$

An additional assumption that is always employed but rarely stated explicitly is that the electron-phonon interaction $\hat{H}_{eN}$ does not change the modal structure, i.e. it is also diagonal in $\vec{Q}$ [129, 131]. In this case the interaction Hamiltonian can be written as

$$\hat{H}_{eN} = \sum_S \hat{U}_S F_S(Q_S), \tag{2.60}$$

where $\hat{U}_S$ is a potential for the electrons which is coupled to the instantaneous nuclear position by $F_S(Q_S)$.

The transition rate is now determined from (2.52), with the wave functions in the modal coordinate system

$$\Psi_{iI}(\vec{x}, \vec{Q}) = \varphi_i(\vec{x}; \vec{Q}) \eta_{iI}(\vec{Q}) = \big|i(\vec{Q})\big\rangle |iI\rangle\!\rangle \tag{2.61}$$

and the non-adiabacity operator

$$\hat{L}_{ij} = \sum_S \hat{L}_{ijS} \tag{2.62}$$

$$\hat{L}_{ijS} = -\frac{\hbar^2}{2M_S}\big\langle j(\vec{Q})\big|\frac{\partial^2}{\partial Q_S^2}\big|i(\vec{Q})\big\rangle - \frac{\hbar^2}{M_S}\big\langle j(\vec{Q})\big|\frac{\partial}{\partial Q_S}\big|i(\vec{Q})\big\rangle\frac{\partial}{\partial Q_S}. \tag{2.63}$$

The $\big|i(\vec{Q})\big\rangle$ are the solutions of the equation

$$(\hat{H}_e + \hat{H}_{eN})\big|i(\vec{Q})\big\rangle = E_i(\vec{Q})\big|i(\vec{Q})\big\rangle, \tag{2.64}$$

Perturbation Theory

In addition to the *time dependent* perturbation theory employed to calculate the transition rates, nearly all published model matrix elements treat the dependence of the electronic wave functions and energies on $\vec{Q}$ using a perturbation expansion based on the ($\vec{Q}$-independent) solutions of the electronic Hamiltonian

$$\hat{H}_e|i\rangle = E_i|i\rangle. \tag{2.65}$$

An exception is the work of Kubo [128], which uses a highly idealized defect wave function. In the Condon approximation or adiabatic approximation (not to be confused with the adiabatic Born-Oppenheimer approximation), the $\vec{Q}$-dependence of the electronic wave functions is obtained from first-order perturbation theory, i.e.

$$\left|i(\vec{Q})\right\rangle = |i\rangle + \sum_{k \neq i} \frac{\langle k|\hat{H}_{\mathrm{eN}}|i\rangle}{E_i - E_k}|k\rangle$$

$$= |i\rangle + \sum_{k \neq i} \sum_S \frac{\langle k|\hat{U}_S|i\rangle F_S(Q_S)}{E_i - E_k}|k\rangle \tag{2.66}$$

$$E_i(\vec{Q}) = E_i + \langle i|\hat{H}_{\mathrm{eN}}|i\rangle$$

$$= E_i + \sum_S \langle i|\hat{U}_S|i\rangle F_S(Q_S). \tag{2.67}$$

This approximation was used initially by Huang and Rhys [127, 132] and was subsequently employed in many publications. The matrix element for a general operator $\hat{O}$ is

$$\langle j(\vec{Q})|\hat{O}|i(\vec{Q})\rangle = \langle j|\hat{O}|i\rangle$$

$$+ \sum_S \left(\sum_{k \neq i} \langle j|\hat{O}F_S(Q_S)|k\rangle\langle k|\frac{\hat{U}_S}{E_i - E_k}|i\rangle + \sum_{k' \neq j} \langle j|\frac{\hat{U}_S}{E_j - E_k}|k'\rangle\langle k'|F_S^*(Q_S)\hat{O}|i\rangle \right)$$

$$+ \text{ second order terms.} \tag{2.68}$$

Unfortunately, the matrix elements for non-radiative transition rates calculated using the Condon approximation were too small by orders of magnitude [132, 133] and so different approximations were developed. The most popular approaches are the static coupling scheme [89, 132, 134, 135] and the non-Condon approximations [130], which were based on an "infinite order" perturbation expansion. Both methods give transition rates closer to experiment and the relative advantages of each of the approximations have been discussed for more than two decades. In the early 1980s it was conclusively shown by several authors that in principle all three approximations are equivalent and that significant differences arise from the employed wave functions, which makes this part of the theory slightly arbitrary [132, 136–138]. In the remaining part of this document the standard Condon approximation is applied for its simplicity. The electronic matrix elements employed contain parameters that are calibrated to experimental data, which is assumed to properly account for the shortcomings of the approximation.

The perturbation expansion of the energy has an important consequence for the vibrational system, as in the employed Born-Oppenheimer approximation the energy levels act as a potential for the nuclei. The vibrational part of the problem now reads

$$(\hat{H}_{\mathrm{N}} + E_i(\vec{Q}))\left|iI\right\rangle\!\!\big\rangle = \left(E_i + \sum_S -\frac{\hbar^2}{2M_S}\frac{\partial^2}{\partial Q_S^2} + \frac{M_S\omega_S^2}{2}Q_S^2 + \langle i|\hat{U}_S|i\rangle F_S(Q_S) \right)\left|iI\right\rangle\!\!\big\rangle = E_{iI}\left|iI\right\rangle\!\!\big\rangle. \tag{2.69}$$

This Hamiltonian is a sum of independent operators for every phonon mode which is solved by the wave function [98]

$$\left|iI\right\rangle\!\!\big\rangle = \left|iI_1\right\rangle\!\!\big\rangle \otimes \left|iI_2\right\rangle\!\!\big\rangle \otimes \left|iI_3\right\rangle\!\!\big\rangle \otimes \cdots \left|iI_S\right\rangle\!\!\big\rangle \cdots \tag{2.70}$$

with the corresponding energy

$$E_{iI} = E_i + \sum_S E_{iI_S} \tag{2.71}$$

and the constituents $\left|iI_S\right\rangle\!\rangle$ and E_{iI_S} are obtained from

$$\left(-\frac{\hbar^2}{2M_S}\frac{\partial^2}{\partial Q_S^2} + \frac{M_S\omega_S^2}{2}Q_S^2 + \langle i|\hat{U}_S|i\rangle F_S(Q_S)\right)\left|iI_S\right\rangle\!\rangle = E_{iI_S}\left|iI_S\right\rangle\!\rangle. \tag{2.72}$$

In essence, this result makes the true separation of the phonons possible, which is of importance for the following considerations. The quantum state of the vibrational system I that belongs to the electronic state i now consists of the independent states of all phonon modes I_S.

Electron-Phonon-Coupling

In most publications, the coupling function $F(\vec{Q})$ is a linear expression in the modal coordinates [130]

$$\hat{H}_{\text{eN}} = \sum_S \hat{U}_S a_S Q_S, \tag{2.73}$$

where a_S is a normalization factor that is sometimes absorbed into the coupling potential. This approximation is known as the *linear coupling* approximation and is widely used throughout literature [127, 130, 132].

Inserting the linear relation for $F_S(Q_S)$ into (2.72) gives

$$\left(-\frac{\hbar^2}{2M_S}\frac{\partial^2}{\partial Q_S^2} + \frac{M_S\omega_S^2}{2}(Q_S + Q_{Si})^2 - E'_{Si}\right)\left|iI_S\right\rangle\!\rangle = E_{iI_S}\left|iI_S\right\rangle\!\rangle \tag{2.74}$$

with

$$Q_{Si} = \frac{\langle i|\hat{U}_S|i\rangle a_S}{M_S\omega_S^2} \text{ and } E'_{Si} = \frac{\langle i|\hat{U}_S|i\rangle^2 a_S^2}{2M_S\omega_S^2}. \tag{2.75}$$

The resulting modal wave functions are harmonic oscillator wave functions [139]

$$\left|iI_S\right\rangle\!\rangle = h_{\lambda_S}^{I_S}(Q_S - Q_{Si}) \tag{2.76}$$

$$\lambda_S = M_S\omega_S \tag{2.77}$$

$$h_\lambda^n(Q) = \frac{1}{\sqrt{2^n n!}}H_n(Q)h_\lambda^0(Q) \tag{2.78}$$

$$h_\lambda^0(Q) = \left(\frac{\lambda}{\pi\hbar}\right)^{1/4} e^{-\frac{Q^2\lambda}{2\hbar}}, \tag{2.79}$$

where $H_n(Q)$ are the Hermite polynomials [139]. Each mode S has an associated vibrational center Q_{Si} that is determined by the electronic state i. Upon a transition to a different electronic state, the vibrational wave functions are shifted to the new potential minimum as illustrated in Fig. 2.6.

In addition to the linear coupling approximation, some works also investigate systems with purely *quadratic* coupling which has the form [128, 129]

$$\hat{H}_{\text{eN}} = \sum_S \hat{U}_S b_S Q_S^2. \tag{2.80}$$

As shown in Fig. 2.7, contrary to the linear coupling, the quadratic coupling does not change the equilibrium coordinate of the mode but the oscillation frequency, leading to a vibrational Schrödinger equation of the form

$$\left(-\frac{\hbar^2}{2M_S}\frac{\partial^2}{\partial Q_S^2} + \frac{M_S\omega_{Si}^2}{2}Q_S^2\right)\left|iI_S\right\rangle\!\rangle = E_{iI_S}\left|iI_S\right\rangle\!\rangle \tag{2.81}$$
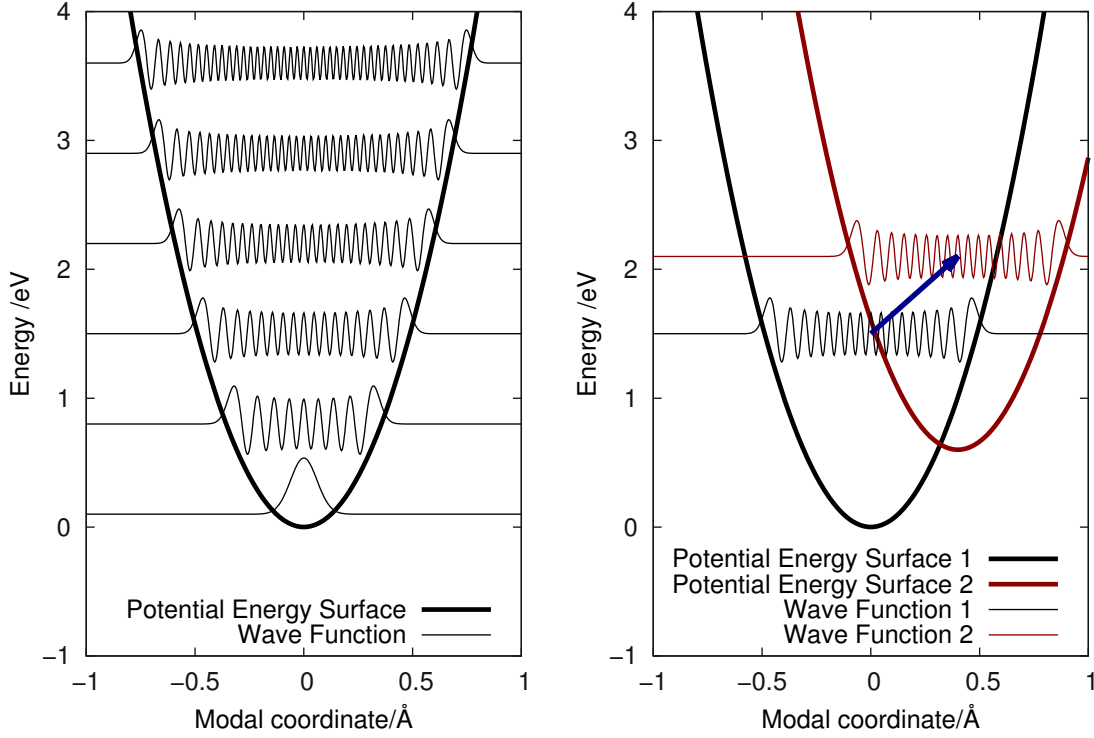
Figure 2.6: Potential energy surfaces and the corresponding vibrational wave functions for one mode in the linear coupling approximation. **(left)** Different electronic states give rise to harmonic potential energy surfaces that differ only in the energetic and spatial position of the minimum. The corresponding set of vibrational wave functions is shifted accordingly but remains unchanged otherwise. **(right)** The vibronic transition theory (2.51) describes the transition between two specific vibrational sub-states as indicated by the arrow. The total rate is computed by thermally averaging over all possible transitions.

with

$$\omega_{Si}^2 = \omega_S^2 + \frac{2b_S}{M_S}\langle i|\hat{U}_S|i\rangle. \tag{2.82}$$

The vibrational wave functions thus assume the form

$$|ia_S\rangle\!\rangle = h_{\lambda_{Si}}^{a_S}(Q_S) \tag{2.83}$$

$$\lambda_{Si} = M_S\omega_{Si}. \tag{2.84}$$

Both the linear coupling approximation and the quadratic approximation have been studied in numerous papers. As is shown in Chap. 4 and also described in our publications [86, 140], the defects that are considered relevant for MOS reliability need a combination of both couplings to even capture the basic features of the potential energy surfaces calculated from density functional theory. Thus we are dealing with an interaction of the form

$$\hat{H}_{\mathrm{eN}} = \sum_S \hat{U}_S(a_S Q_S + b_S Q_S^2) \tag{2.85}$$

and upon a transition between two electronic states both the equilibrium position and the os-
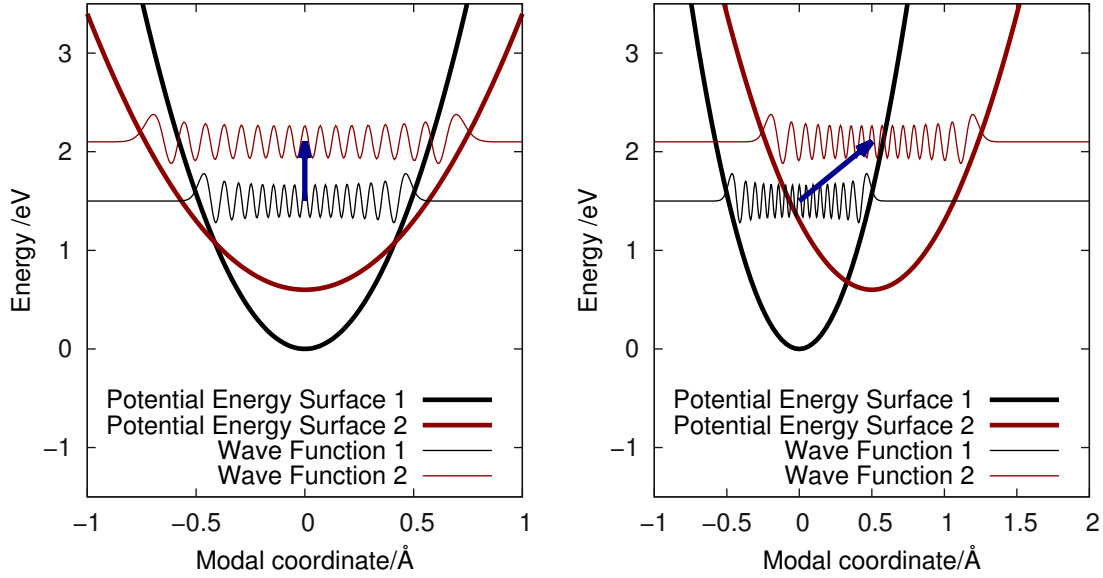
Figure 2.7: Potential energy surfaces and vibrational wave functions for a transition in the quadratic coupling **(left)** and in the combined linear and quadratic coupling approximation **(right)**. In the purely quadratic coupling approximation, there is no shift in the equilibrium position but a change in the oscillation frequency. In the combined version, both the equilibrium position and the oscillation frequency change.

cillation frequency of the phonon modes change, yielding the vibrational Schrödinger equation

$$\left(-\frac{\hbar^2}{2M_S}\frac{\partial^2}{\partial Q_S^2} + \frac{M_S\omega_{Si}^2}{2}(Q_S - Q_{Si})^2 + E'_{Si} \right)|iI_S\rangle\!\rangle = E_{iI_S}|iI_S\rangle\!\rangle \tag{2.86}$$

with

$$Q_{Si} = \frac{a_S}{2b_S + \frac{M_S\omega_S^2}{\langle i|\hat{U}_S|i\rangle}}, \tag{2.87}$$

$$E'_{Si} = -\frac{a_S^2\langle i|\hat{U}_S|i\rangle^2}{4b_S\langle i|\hat{U}_S|i\rangle + 2M_S\omega_S}, \text{ and} \tag{2.88}$$

$$\omega_{Si} = \sqrt{2}\sqrt{\frac{2b_S\langle i|\hat{U}_S|i\rangle}{M_S} + \omega_S^2} \tag{2.89}$$

2.9.4 The Line Shape Function

Line shapes are a concept originating from the field of optical spectroscopy. As an introduction to the concept, we take a look at the first quantitative theory for the multi-phonon transitions of a point-defect derived by Huang and Rhys [127] in 1952 for the F-Center in potassium bromide. The first part of that work is dedicated to a transition induced by incident radiation. In these transitions, the dominant perturbation arises from the polarization operator $\hat{M}$ and not from the non-adiabacity operator $\hat{L}$ in (2.52). It is safe to assume that $\hat{M}$ acts only on the electrons,

again due to the comparably large mass of the nuclei. In the Condon approximation (2.68) the corresponding matrix element reads

$$
\begin{aligned}
\langle j(\vec{Q})|\hat{M}|i(\vec{Q})\rangle = &\langle j|\hat{M}|i\rangle \\
&+ \sum_S \Bigg(F_S(Q_S) \sum_{k\neq i} \langle j|\hat{M}|k\rangle\langle k|\frac{\hat{U}_S}{E_i - E_k}|i\rangle \\
&\quad + F_S^*(Q_S) \sum_{k'\neq j} \langle j|\frac{\hat{U}_S}{E_j - E_k}|k'\rangle\langle k'|\hat{M}|i\rangle \Bigg)
\end{aligned}
\tag{2.90}
$$

where the first term represents the direct transition between the two electronic states due to the incident radiation, and the other two terms account for transitions mediated by electron-phonon interactions. It is commonly assumed that the indirect transitions are negligible compared to the direct matrix element $\langle j|\hat{M}|i\rangle$. Consequently the sums in (2.90) can be neglected and the electronic matrix element is approximately independent of the position of the nuclei.

$$
\langle j(\vec{Q})|\hat{M}|i(\vec{Q})\rangle \approx \langle j|\hat{M}|i\rangle
\tag{2.91}
$$

This is known as the quantum mechanical Franck-Condon principle [91, 127]. It is important to stress that the $\vec{Q}$-independence only concerns the matrix element but not its constituents. In this case, the electronic matrix element in (2.51) can be taken out of the integration over $\vec{Q}$, yielding

$$
\langle \Psi_{jJ}|\hat{M}|\Psi_{iI}\rangle = \langle\!\langle jJ|\langle j(\vec{Q})|\hat{M}|i(\vec{Q})\rangle|iI\rangle\!\rangle \approx \langle j|\hat{M}|i\rangle\langle\!\langle jJ|iI\rangle\!\rangle.
\tag{2.92}
$$

In essence, this describes the transition as an electronic matrix element with vibrational selection rules. The factors $\left|\langle\!\langle jJ|iI\rangle\!\rangle\right|^2$ arising from the quantum-mechanical Franck-Condon principle are usually called Franck-Condon factors.

Inserting this matrix element into (2.52) results in the expression [117]

$$
W_{\mathrm{i}\to\mathrm{f}}(h\nu) = \frac{2\pi}{\hbar}\left|\langle\mathrm{f}|\hat{M}|\mathrm{i}\rangle\right|^2 f(h\nu),
\tag{2.93}
$$

where $h\nu$ is the energy of the radiation and

$$
f(h\nu) = \operatorname*{avg}_I \sum_F \left|\langle\!\langle \mathrm{f}F|\mathrm{i}I\rangle\!\rangle\right|^2 \delta(E_{\mathrm{f}F} - E_{\mathrm{i}I} - h\nu)
\tag{2.94}
$$

is the *line shape function*. In optical spectroscopy line shape functions describe the thermal broadening of absorption peaks [91, 117, 127], but the concept is also applicable to non-radiative carrier capture at defects in semiconductors, as shown below.

2.9.5 Line Shapes for Non-Radiative Transitions

While the Franck-Condon principle is easy to justify for optical matrix elements using the Condon approximation, the above argument completely fails for the non-adiabacity operator (2.63) which contains the electronic matrix elements $\langle j(Q_S)|\frac{\partial}{\partial Q_S}|i(Q_S)\rangle$ and $\langle j(Q_S)|\frac{\partial^2}{\partial Q_S^2}|i(Q_S)\rangle$ that do not induce a direct transition. Using the interaction (2.85), the Condon approximation for these matrix elements gives with (2.66)

$$
\langle j(\vec{Q})|\frac{\partial}{\partial Q_S}|i(\vec{Q})\rangle = (a_S + 2b_S Q_S)\langle j|\frac{\hat{U}_S}{E_i - E_j}|i\rangle
\tag{2.95}
$$

and

$$\langle j(\vec{Q})|\frac{\partial^2}{\partial Q_S^2}|i(\vec{Q})\rangle = 2b_S\langle j|\frac{\hat{U}_S}{E_i - E_j}|i\rangle, \tag{2.96}$$

and the transition matrix element reads with (2.63)

$$\langle\!\langle jJ|\langle j(\vec{Q})|\hat{L}|i(\vec{Q})\rangle|iI\rangle\!\rangle = \sum_S \langle\!\langle jJ|\hat{L}_{ijS}|iI\rangle\!\rangle \tag{2.97}$$

$$\langle\!\langle jJ|\hat{L}_{ijS}|iI\rangle\!\rangle = -U_{ijS}S_{IJS} \tag{2.98}$$

$$U_{ijS} = \frac{\hbar^2}{M_S}\langle j|\frac{\hat{U}_S}{E_i - E_f}|i\rangle \tag{2.99}$$

$$S_{IJS} = b_S\langle\!\langle jJ|iI\rangle\!\rangle + a_S\langle\!\langle jJ|\frac{\partial}{\partial Q_S}|iI\rangle\!\rangle + 2b_S\langle\!\langle jJ|Q_S\frac{\partial}{\partial Q_S}|iI\rangle\!\rangle. \tag{2.100}$$

The matrix elements of the separate modal non-adiabacity operators again resemble the radiative matrix elements obtained from the Franck-Condon principle above as the expression consists of an electronic part and a vibrational part. Unlike the Frank-Condon expression above, however, this vibrational part contains both a dependence on the vibrational coordinates themselves as well as a dependence on their derivative.

Inserting (2.70) for the vibrational wave functions gives

$$S_{IJS} = \left(\prod_{S'\neq S}\langle\!\langle jJ_{S'}|iI_{S'}\rangle\!\rangle\right)\left(b_S\langle\!\langle jJ_S|iI_S\rangle\!\rangle + a_S\langle\!\langle jJ_S|\frac{\partial}{\partial Q_S}|iI_S\rangle\!\rangle + 2b_S\langle\!\langle jJ_S|Q_S\frac{\partial}{\partial Q_S}|iI_S\rangle\!\rangle\right). \tag{2.101}$$

This result is interesting as it shows that each mode contributes a Frank-Condon factor to the matrix element of every other mode. The vibrational part is determined by the change of the potential energy surface between the states, which is caused by the diagonal part of the electron-phonon coupling Hamiltonian $\langle i|\hat{U}_S|i\rangle$, see (2.67). The electronic matrix element, on the other hand, arises from the off-diagonal elements $\langle j|\hat{U}_S|i\rangle$. As the diagonals and the off-diagonals of the coupling operator need not be related to each other, there is no direct link between the contribution of a mode to the electronic matrix element and its contribution to the vibrational part. In the literature, modes contributing to the electronic matrix element are called *promoting modes* and those contributing to the vibrational part are called *accepting modes* [131]. Usually, every mode of a defect system will fall into both categories to some degree.

The target of the present work is to extract relevant parameters for the non-radiative transitions from atomistic calculations. Although the parameters a_S and b_S of the above expression can be extracted from a suitably designed atomistic model, as will be shown later in this document, this parameter extraction bears some ambiguity due to the anharmonicity of the potential energy surface from the electronic structure method. Also, the complicated structure of the investigated defects and the strong distortion of the host lattice around them makes the assumption of a constant mode-spectrum quite unlikely. Finally, there is no method available for the estimation of the cross-terms $\langle j|\hat{U}_S|i\rangle$ required for the promoting contribution due to the ill-defined or inaccurate wave functions in the available electronic structure methods. Under this viewpoint, an approach to calculate the non-radiative transition rate using the accurate operator (2.98) appears unreasonable due to the inaccuracy of the underlying model system. We therefore assume that all modes in our system are purely accepting modes, which enter the transition rate only through the Franck-Condon factors $\langle\!\langle jJ_{S'}|iI_{S'}\rangle\!\rangle$ and the conservation of energy. We assume a perturbation operator $\hat{L}'$ that contains the promoting contributions of
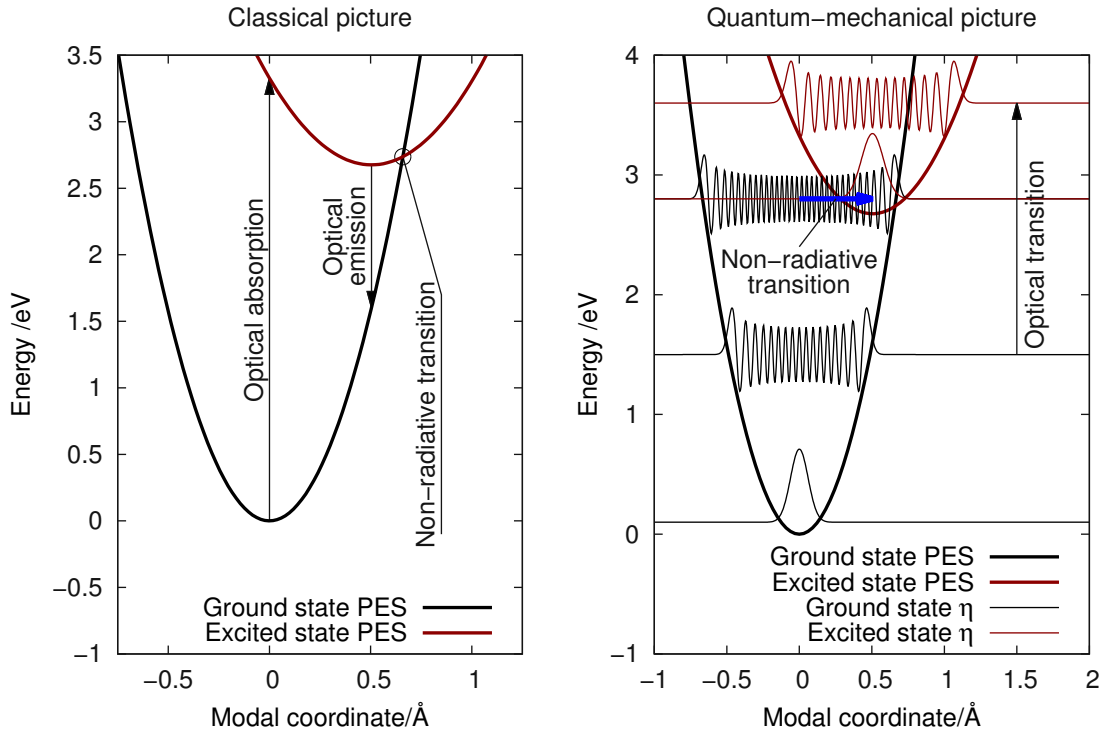
Figure 2.8: A schematic configuration-coordinate diagram illustrating vibronic transitions in a classical and a quantum mechanical picture. In the classical picture **(left)**, radiative as well as non-radiative electronic transitions occur with the nuclei fixed in their respective position (Franck-Condon principle). Thus, optical transitions occur vertically in this diagram and non-radiative transitions happen at the crossing-points of the potential energy surfaces. As the system most dominantly resides at the minima of the potential energy surfaces, different wavelengths are observed for absorption and emission of radiation. In the quantum-mechanical picture **(right)**, the transitions happen between the vibrational sub-states arising from the different potential energy surfaces.

the modal spectrum but acts like an optical matrix element $\hat{M}$. Just as $\hat{L}$, $\hat{L}'$ is assumed to couple the initial and final state elastically, i.e. it does not contribute to the conservation of energy. As $\hat{L}'$ is not known exactly, it will be approximated by a parametrizable expression. The resulting non-radiative transition rate can thus be based on the radiative transition rates (2.93) as the limit [86, 117, 123, 141]

$$W_{i \to f} = \lim_{h\nu \to 0} W_{i \to f}(h\nu) = \frac{2\pi}{\hbar} \left| \langle f | \hat{L}' | i \rangle \right|^2 f(0). \tag{2.102}$$

This approach is well compatible with published works which either apply the Frank-Condon principle directly to the non-adiabacity operator [117, 127, 131, 142] or where the perturbation does not arise from the non-adiabacity operator but instead from an applied field [143, 144].

36

2.10 Vibronic Transitions with Classical Nuclei

As for the barrier hopping transitions in Sec. 2.8, it is also possible to formulate a theory for vibronic transitions that treats the nuclei as classical particles [117, 129]. Several semi-classical approaches have been published over the years, especially for the estimation of reemission probabilities [117] or correlated hopping [116]. In the present work, non-Markovian behavior is not assumed to be relevant, so the theory is again derived using the assumption of thermal equilibrium.

As above, we derive the non-radiative transition from an optical transition by letting the optical energy approach zero. In this approach, the transition between the electronic Born-Oppenheimer wave functions $\left|i(\vec{R})\right\rangle$ and $\left|f(\vec{R})\right\rangle$ proceeds via the optical matrix element $\hat{M}$. For any position $\vec{R}$ of the nuclei, one can now again employ time-dependent perturbation theory to calculate the transition rate as

$$W_{i\to f}(h\nu, \vec{R}) = \frac{2\pi}{\hbar} \left|\left\langle f(\vec{R})\middle|\hat{M}\middle|i(\vec{R})\right\rangle\right|^2 \delta\left(h\nu - E_f(\vec{R}) - E_i(\vec{R})\right). \qquad (2.103)$$

Again following just the same considerations as before, we assume that the nuclear degrees of freedom are in thermal equilibrium and can be described by classical statistical physics. The probability to find the system in electronic state $\left|i\right\rangle$ at a certain configuration $\vec{R}$ is hence given by

$$P(\vec{R}) = Z^{-1} e^{-\frac{E_i(\vec{R})}{k_B T}} \qquad (2.104)$$

$$Z = \int_{\vec{R}} e^{-\frac{E_i(\vec{R}')}{k_B T}} d\vec{R}' \qquad (2.105)$$

and thus the total transition rate for a given optical energy can be computed from

$$W_{i\to f}(h\nu) = \int_{\mathbb{R}^N} P(\vec{R}') W_{i\to f}(h\nu, \vec{R}') \mathrm{d}\vec{R}' = \int_{\mathbb{R}^N} Z^{-1} e^{-\frac{E_i(\vec{R}')}{k_B T}} W_{i\to f}(h\nu, \vec{R}') \mathrm{d}\vec{R}' \qquad (2.106)$$

$$= \int_{\mathbb{R}^N} Z^{-1} e^{-\frac{E_i(\vec{R}')}{k_B T}} \frac{2\pi}{\hbar} \left|\left\langle f(\vec{R}')\middle|\hat{M}\middle|i(\vec{R}')\right\rangle\right|^2 \delta\left(h\nu - E_f(\vec{R}') - E_i(\vec{R}')\right) \mathrm{d}\vec{R}' \qquad (2.107)$$

Again assuming the electronic matrix element to be independent of the nuclear configuration one obtains

$$W_{i\to f}(h\nu) = \frac{2\pi}{\hbar} \left|\left\langle f\middle|\hat{M}\middle|i\right\rangle\right|^2 f(h\nu) \qquad (2.108)$$

$$f(h\nu) = \int_{\mathbb{R}^N} Z^{-1} e^{-\frac{E_i(\vec{R}')}{k_B T}} \delta\left(h\nu - E_f(\vec{R}') - E_i(\vec{R}')\right) \mathrm{d}\vec{R}'. \qquad (2.109)$$

This time the line shape function is only determined from the probability to find the system in a configuration that fulfills the conservation of energy for the optical energy $h\nu$. For the non-radiative transitions we again replace the optical matrix element by the quasi-optical non-adiabacity operator $\hat{L}'$ and let the optical energy go to zero as illustrated in Fig. 2.8. In summary, when calculating vibronic transitions with classical nuclei, we again employ (2.102), but use (2.109) as the line shape function. This classical line shape is determined from a transition-state theory like expression, where the transition state is defined by the conservation of energy. In comparison to (2.94), the classical line shape has the advantage that it can in principle use the potential energy surfaces from electronic structure methods in their full glory, i.e. without the necessity of a harmonic approximation.
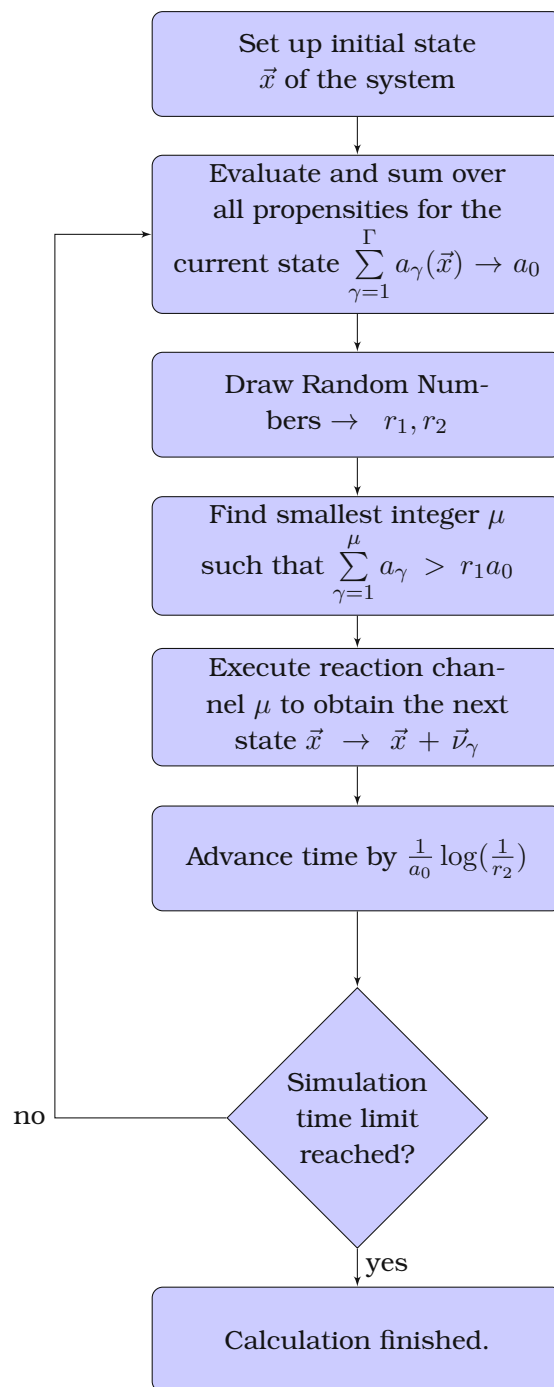
Figure 2.9: Sketch of the stochastic simulation algorithm (SSA) [114]. The algorithm generates a realization of the stochastic process described by the chemical master equation (2.20).

2.11 Solution of the Master Equation

Now that the chemical states and reactions are defined and we have obtained rates for the reactions from the explained microscopic theories, we can calculate the time evolution of the chemical system from the chemical master equation (2.20). As explained above, this equation

is a stochastic differential equation which assigns a probability to any state vector $\vec{x}$, given that $\vec{X} = \vec{x}_0$ at $t = t_0$. For a system with a small set of states $\{\vec{x}_1, \ldots, \vec{x}_\Omega\}$, a direct solution can be attempted, which results in a coupled system of Ω differential equations [37]. However, in many situations the number of states will be quite big or even infinite, rendering a direct solution of the master equation unfeasible or even impossible. A feasible alternative is the stochastic simulation algorithm (SSA) [114] explained in Fig. 2.9, which is also known as the kinetic Monte Carlo method. Instead of solving the differential equation (2.20), a realization of the stochastic process $\vec{X}$ is generated using pseudo-random numbers. The SSA does not have any algorithmic parameters and is a mathematically exact description of the system defined by the states and reaction channels [114]. The moments of the probability distribution $P(\vec{x}, t)$ are trivially calculated by averaging over several simulation runs, although care has to be taken to ensure the randomness of the pseudo-random numbers between two runs to avoid correlation effects.

2.11.1 Subsystems, Well-Stirredness, and Diffusion

Most chemical systems are constructed of a large number Θ of similar sub-systems with a small number of states Ω, for example a number Θ of well-separated doping atoms within a semiconductor device which can exist in a number Ω of different charge states. The chemical state of the total system can in principle be constructed from all the states of the subsystems, i.e.

$$\vec{x} = \begin{pmatrix} \vec{x}_1 \\ \vec{x}_2 \\ \vec{x}_3 \\ \vdots \\ \vec{x}_\Theta \end{pmatrix}, \ \vec{x}_\delta \in \{\vec{s}_1, \vec{s}_2, \ldots, \vec{s}_\Omega\}, \ \Theta \gg \Omega. \tag{2.110}$$

For every subsystem δ there is now a number Γ of reaction channels with associated state change vectors $\vec{\nu}_{\delta 1} \ldots \vec{\nu}_{\delta \Gamma}$ and propensity functions $a_{\delta 1}(\vec{s}_\delta) \ldots a_{\delta \Gamma}(\vec{s}_\delta)$.

In a situation like this a given observable will usually be unable to separate these sub-systems. For instance for the transport characteristics of a semiconductor device it is irrelevant *which* dopant has contributed a carrier but only *how many* of them have. As the sub-systems are similar enough that their propensity functions are the same

$$a_{\delta_i \gamma} = a_{\delta_j \gamma} = a_\gamma, \tag{2.111}$$

the chemical state of the total system can be reformulated, considering only the numbers of subsystems n_ω in a given state $\vec{s}_\omega$. The new total state vector will be

$$\vec{x}' = \begin{pmatrix} n_1 \\ n_2 \\ n_3 \\ \vdots \\ n_\Omega \end{pmatrix}, \tag{2.112}$$

the state change vectors will only operate on the numbers $n_1, \ldots, n_\Omega$, and the corresponding propensity functions will take the form

$$a'_{\omega \gamma} = n_\omega a_\gamma, \tag{2.113}$$

corresponding to the probability per unit time that *any* of the subsystems in state ω will take reaction channel γ. In theoretical chemistry these reactions in which an isolated sub-system undergoes a transition are termed *unimolecular reactions* [115]. Especially if the chemical system under consideration consists of diffusing species, such as atoms or molecules in a solvent, two of these subsystems may also interact and form new species, for example $2H_2 + O_2 \rightarrow 2H_2O$. In those reactions, the corresponding reaction channel changes two or more numbers of $\vec{x}'$ at the same time and the associated propensity function takes the form

$$a'_{\omega_1 \omega_2 \gamma} = n_{\omega_1} n_{\omega_2} a_\gamma, \tag{2.114}$$

which is the probability per unit time that any two of the n_{ω_1} specimens of species ω_1 and n_{ω_2} specimens of species ω_2 will undergo the reaction γ, where different species in the above context may refer to different types of sub-systems (e.g. different molecules) or different sub-systems of the same type in a different state. Reactions of this type are called *bimolecular* reactions. For bimolecular reactions which involve two specimens of the same species, the propensity function is

$$a'_{\omega \gamma} = \frac{n_\omega (n_\omega - 1)}{2} a_\gamma, \tag{2.115}$$

which corresponds to the probability that *any pair* of specimens of type ω will undergo the reaction γ. Any higher order reactions can be reduced to a series of bimolecular and unimolecular reactions [115].

Bimolecular reactions usually emerge in situations when at least one of the specimens is able to move, giving it access to different reaction partners. A mathematical description of the form (2.114) or (2.115) implies, that the reaction probability is the same for every pair of reactants, i.e. a homogeneous distribution of the reacting specimens within the volume associated with the chemical system. This condition is commonly referred to as the system being *well-stirred*. Different approaches exist for chemical systems where the intermixing is not fast enough, which are called *reactive-diffusive systems*. These approaches and their relevance for the reaction-diffusion model for NBTI will be discussed in Chap. 3.

2.12 Reaction Rate Equations

As stated above, it is quite common that observables only determine how many constituents of a chemical system have assumed a certain state, or equivalently how many specimens of a certain species exist in that system. Usually the most interesting quantities for a chemical system in number representation is thus the development of the *average* numbers of (2.112) over time. These averages are obtained as

$$\langle \vec{n} \rangle \, (t) = \sum_{\vec{n}} \vec{n} P(\vec{n}, t | \vec{n}_0, t_0), \tag{2.116}$$

which corresponds to the first moment of the probability distribution P.

To obtain these averages from the SSA one has to take the average of several simulation runs, which is usually a quite time-consuming task. Especially if there are very fast reactions or a large number of particles in the system, the simulation of longer time-ranges quickly becomes unfeasible using this approach. A computationally more efficient approach is to directly calculate the dynamics of the average values. For convenience we introduce the average number vector $\vec{N} = \langle \vec{n} \rangle$. The time evolution of $\vec{N}$ is calculated from

$$\frac{\partial \vec{N}}{\partial t} = \frac{\partial}{\partial t} \sum_{\vec{n}} \vec{n} P(\vec{n}, t | \vec{n}_0, t_0) = \sum_{\vec{n}} \vec{n} \frac{\partial}{\partial t} P(\vec{n}, t | \vec{n}_0, t_0). \tag{2.117}$$

The substitution of the right side of (2.20) for the derivative of P and a few trivial transformations yield [115]

$$\frac{\partial \vec{N}}{\partial t} = \sum_{\gamma} \vec{\nu}_{\gamma} \langle a_{\gamma} \rangle .$$

(2.118)

For the case of unimolecular reactions (2.113), whose propensity functions are linear in $\vec{n}$, it is trivial to show that $\langle a_{\gamma} \rangle = \vec{a}_{\gamma} \cdot \vec{N}$, which leads to the popular description using reaction rate equations

$$\frac{\partial \vec{N}}{\partial t} = \sum_{\gamma} \vec{\nu}_{\gamma} (\vec{a}_{\gamma} \cdot \vec{N}).$$

(2.119)

Due to their efficiency and simplicity, reaction rate equations are a popular method to describe reactive systems. However, one has to be aware that this description is only exact if all the reactions in the system are unimolecular. Nevertheless, reaction rate equations are also commonly used for systems with bimolecular reactions and even reactive-diffusive systems, as in the reaction-diffusion model for NBTI. The consequences and inadequacies of this approach are discussed in Chap. 3.

As a final remark, it is common not to use the number-representation of $\vec{N}$. Instead, the number of particles is usually normalized to the volume of the system, leading to a formulation based on *concentrations* instead. In this formulation, the particles within the system are understood as a continuum of a certain density. A formulation like this is usually termed a macroscale formulation.

3 A Microscopic Reaction-Diffusion Model for NBTI

As mentioned in Chap. 1, the reaction diffusion model has been mainly used for the interpretation of BTI experiments for almost four decades. Its apparent inability to explain NBTI recovery has led to several modifications of the concept, including trapping of the diffusing species and different types of diffusors [9, 11].

Quite recently it was claimed that the misprediction of recovery is due to the one-dimensional description of the diffusing species in the macroscopic model (1.5)–(1.6). As illustrated in Fig. 3.1, it was suggested that this formulation makes it too easy for the hydrogen atom to find a dangling bond to passivate because the one-dimensional diffusion considers only two options of motion: forward and backward jumping. In a higher-dimensional description the diffusion and reaction kinetics are much richer:

1. The atoms can move in all three dimensions equally likely, leading to a distribution of arrival times at the interface during recovery.

2. H_2-molecules dissociate at a dangling bond, creating a passivated dangling bond and a free hydrogen atom that does not immediately find another dangling bond to passivate.

3. Hydrogen atoms arriving later have to hover along the interface to find an unoccupied dangling bond.

A simple estimate of the recovery in the hypothetical three-dimensional model is given in [16]. This estimate mimics the different repassivation kinetics arising in the atomic description within the framework of the usual macroscopic RD model. To account for the longer "effective"
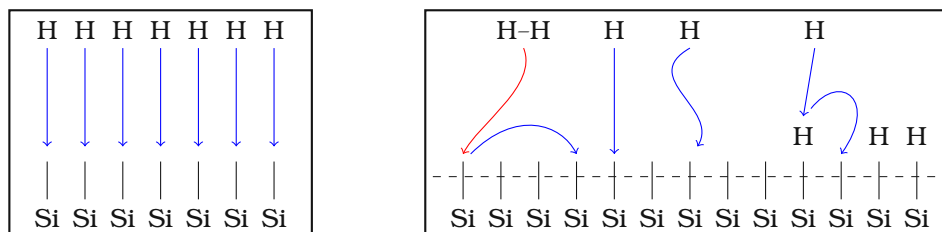

Figure 3.1: (left) According to Mahapatra et al. [16], the inability of the macroscopic reaction-diffusion model (1.4)–(1.6) to predict the experimentally observed NBTI recovery is due to the one-dimensional description of the diffusive motion which makes it too easy for the hydrogen to find its dangling bond. **(right)** A correct description of the three-dimensional atomic motion, so the argument, leads to much richer repassivation kinetics and thus to a distribution of repassivation times.

Figure 3.2: According to [16], the distribution of repassivation times arising from an accurate three-dimensional microscopic description can be approximately modeled by varying the diffusion coefficient during recovery in the macroscopic model. The plot shows the numerically calculated recovery traces for different diffusion coefficients during recovery and the average of these traces. Indeed, this average shows a recovery that proceeds over more time-scales.
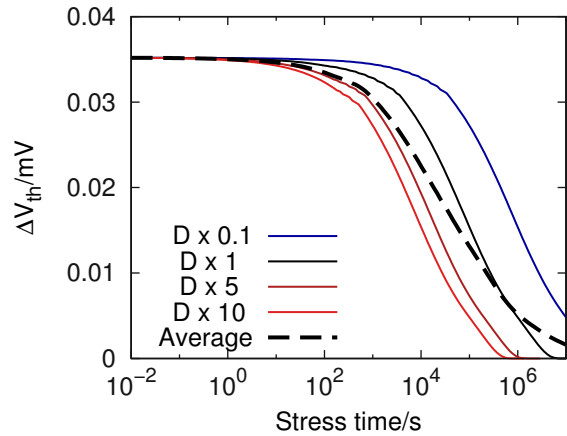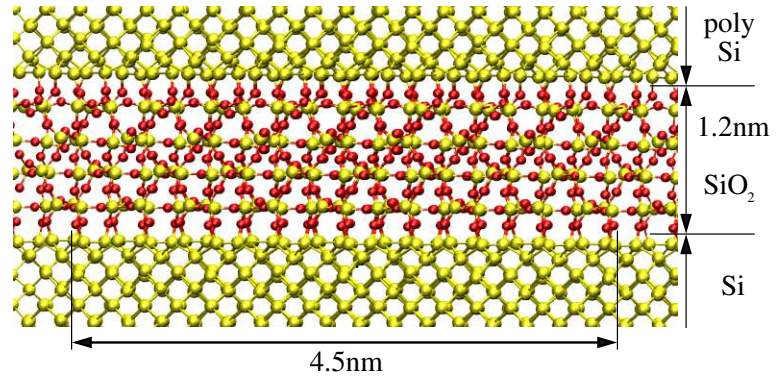

Figure 3.3: A random distribution of 10 dangling bonds on a silicon (100) surface corresponding to a dangling bond density of $5 \times 10^{12}\,\mathrm{cm}^{-2}$, which is a common assumption for the number of bonding defects at the Si-SiO$_2$ interface [20, 23, 45]. The surface silicon atoms are shown in blue, the dangling bonds in red. At this density the average distance between two dangling bonds is $\sim 4.5\,\mathrm{nm}$.
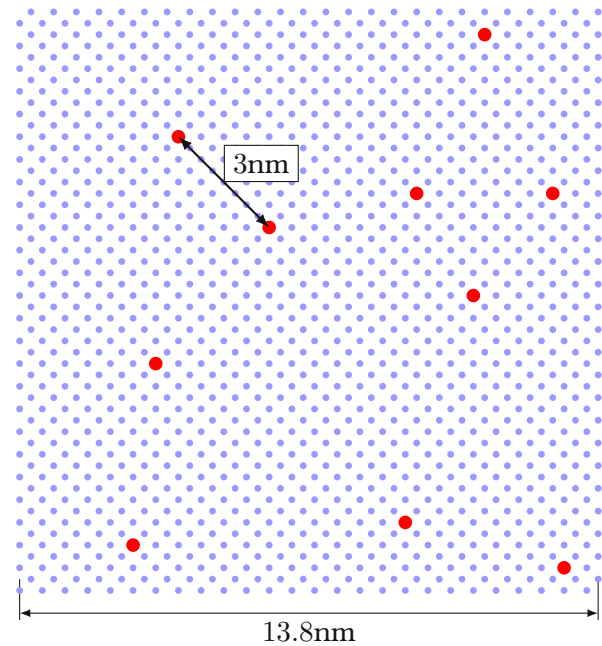
recovery paths, the diffusion coefficients in the macroscopic model are reduced by different factors during recovery and the resulting recovery traces are averaged. Although this approach gives a recovery that proceeds over more time scales, as shown in Fig. 3.2, no derivation for the quasi-three-dimensional description is given and its physical validity is at least questionable. One of our targets is to test the claims of [16] within a firm theoretical framework.

Another motivation for the study of the microscopic limit of the reaction-diffusion model for NBTI is based on general issues with the rate-equation-based description. As a literature study reveals, reaction-diffusion systems have been studied in numerous scientific communities from both the theoretical and the experimental side for more than a century [145–151]. Although the mathematical framework of the RD model (1.4)–(1.6) seems physically sound and the description using densities and rate equations is commonly considered adequate, it is a well known and experimentally confirmed result of theoretical chemistry that the partial differential equation based description of chemical kinetics breaks down for low concentrations [145]. Additionally, in reaction-diffusion systems bimolecular reactions, such as the passivation and the dimerization reaction, require a certain proximity of the reactant species, termed *reaction ra-*

Figure 3.4: An idealized atomic model of an MOS structure and the average dangling bond distance of $4.5\,\mathrm{nm}$, which spans several interstitial positions. It is intuitively clear that an elementary reaction between particles separated by this distance is strongly influenced by diffusion.

dius [146, 151]. Usually the elementary bimolecular reactions happen almost instantaneously and it is the required collision, i.e. the reduction of the distance between two reactants below the reaction radius, which is the rate limiting step [145]. In chemical kinetics, these reactions are called *diffusion-limited* or *diffusion-controlled* reactions [147].

It is easy to show that diffusion must play a dominant role in the bimolecular reactions in the RD model for NBTI. Fig. 3.3 schematically shows a uniform random distribution of dangling bonds on a silicon (100) surface that corresponds to a density of $5 \times 10^{12}\,\mathrm{cm}^{-2}$, which is a usual assumption for N_0 [20, 23, 45] in (1.1) or (1.4). The average distance between two nearest neighbors at this density is $d = N_0^{-1/2} \approx 4.5\,\mathrm{nm}$. An atomic model of the Si-SiO$_2$ interface as in Fig. 3.4 shows that two points separated by this distance have a large number of atoms in between. The assumption of an elementary reaction over this distance is clearly inappropriate, so any reaction between particles of this separation must involve a diffusive step.

Once established by the atomic viewpoint above, the diffusive influence on the bimolecular reactions leads to contradictions in the RD model and its physical interpretation. The predicted degradation of the RD model that is compatible with experimental data is only obtained if the hydrogen atoms that are liberated during stress compete for the available dangling bonds and dimerize at a certain rate. Both requirements involve diffusion over distances much larger than the nearest neighbor distance, which takes about *two seconds* at a commonly assumed diffusion coefficient of $D = 10^{-13}\,\mathrm{cm}^2/\mathrm{s}$ [20, 23]. The reaction radius ρ_H of the dimerization reaction can be estimated from the Smoluchowski theory for irreversible bimolecular reactions [146, 148, 149]

$$\rho_\mathrm{H} = \frac{k_H}{4\pi D}. \tag{3.1}$$

While a reasonable reaction radius is in the regime of the average radius of the oxide interstitials, which is about $4\,\text{\AA}$ [152], the application of (3.1) to published dimerization rates gives values ranging from $70\,\mu\mathrm{m}$ for the parametrization of [23] to thousands of kilometers for other parametrizations [20]. Although both values for ρ_H seem quite unreasonable, they only indicate a limited physical validity of the selected parametrization. An evaluation of the physical validity of the reaction-diffusion model itself requires a more detailed study using a computational model that properly treats the stochastic chemical kinetics involved.

For the present study of the microscopic properties of the RD mechanism we have developed our own atomistic reaction-diffusion simulator based on the considerations of the previous chapter. The microscopic reaction-diffusion picture developed for this purpose also serves as a framework to assess whether a description based on rate-equations is applicable to the physical mechanism behind the RD model.
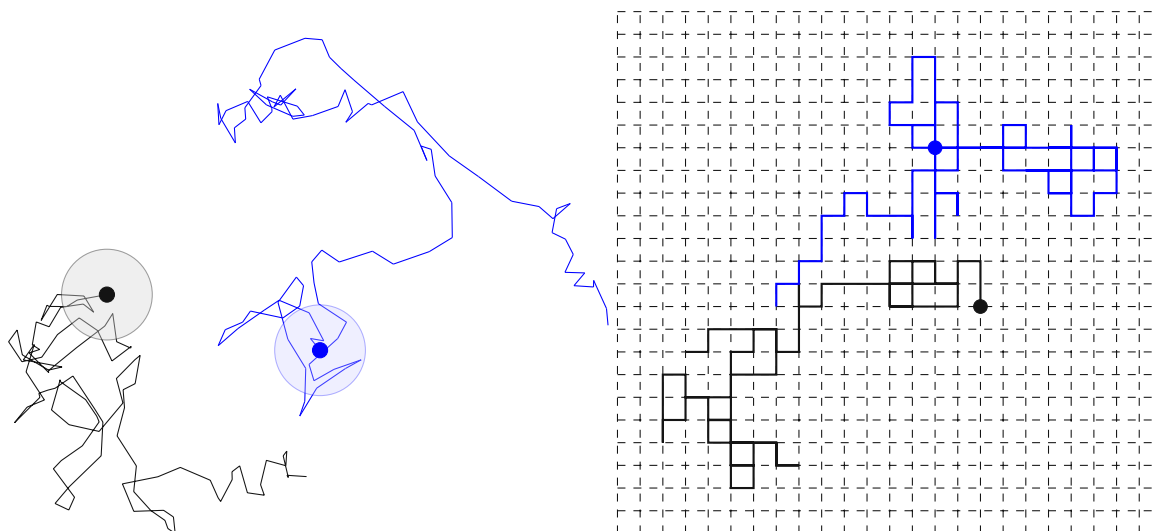
44

Figure 3.5: Schematic illustration of the stochastic modeling approaches to reaction-diffusion systems. **(left)** In grid-less methods, a molecular trajectory is generated from the transient solution of Newton's equations of motion as in molecular dynamics simulation. The interaction with the solvent is modeled by a random force that acts on the diffusors. Bimolecular reactions occur when two particles approach closer than the reaction radius (indicated as circles around the particles) **(right)** In grid-based methods diffusion proceeds as jumps between the sub-domains defined by the grid. Bimolecular reactions occur when two particles occupy the same grid-point.

3.1 The Microscopic RD Model

Our microscopic RD model attempts to mimic the proposed mechanisms of the reaction-diffusion model at a microscopic level. The basic actors are H-atoms, H_2-molecules and the silicon dangling bonds at the interface. The level of physical detail in our model is chosen so that the single-particle effects are captured in a physically meaningful way while still keeping the computational effort manageable even for long-term simulations. Atomic vibrations, i.e. the microstate dynamics, are certainly not of interest here. The present study concerns the RD-process itself and the conclusions therefore do not depend on the microscopic details of the reactions at its basis. The microscopic investigations are thus carried out at the stochastic chemistry level (see Chap. 2).

Several algorithms have been used in the chemical literature for the stochastic simulation of reaction-diffusion systems [148, 149]. The most difficult task in the modeling of these systems is the diffusion of the reactants and several different approaches are available which can roughly be categorized as grid-based methods or grid-less methods [149], see Fig. 3.5. Grid-less methods propagate the coordinates of the diffusing species quite similarly to molecular dynamics methods. Instead of explicitly treating all atoms of the solvent and their effect on the trajectory of the diffusors, the motion of the diffusing particles is perturbed by an empirical random force to generate a Brownian motion. Bimolecular reactions happen at a certain rate as soon as two reaction partners approach closer than a given radius. Although this technique suffers from its sensitivity to the time-step and the specific choice of the random force, it is a popular choice for the simulation of reaction-diffusion processes in liquid solutions where real molecular-dynamics simulations are not feasible [148, 149]. In grid-based methods the simu-
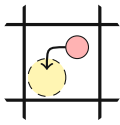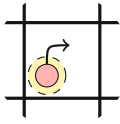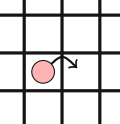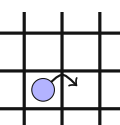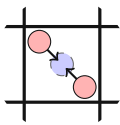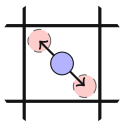
Figure 3.6: Schematic microstate trajectory (blue) of an inert interstitial atom diffusing in a solid-state host material. The potential energy barriers of the host material are indicated as black grid. The diffusion itself proceeds via jumps between the interstitial positions. In between the jumps, the atom vibrates randomly around an energetic minimum.
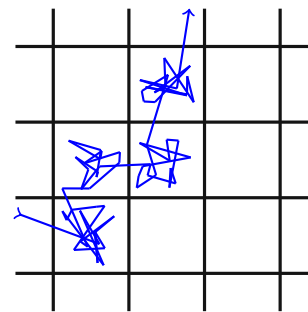
lated volume is divided into small domains and each diffusing particle is assigned to a specific domain. The motion of the diffusors proceeds as hopping between the grid-points. In these models the bimolecular reactions happen at a certain rate as soon as two reactants occupy the same sub-volume. The advantage of this approach is that it can be formulated on top of the chemical master equation (2.20). The master equation can then be solved using the stochastic simulation algorithm (see Sec. 2.11), which does not depend on artificial time-stepping. A problem of the grid-based method that is repeatedly discussed in chemical literature is the choice of the spacial grid as it induces a more or less unphysical motion in liquid solutions. Additionally, the probability to find two particles in the same grid point and in consequence the rate of bimolecular reactions are quite sensitive to the volume of the sub-domains [149].

In the reaction-diffusion model for NBTI, the diffusion of the particles proceeds inside a solid-state solvent. Contrary to diffusion in gases or liquids, the motion of an impurity in a solid-state host material proceeds via jumps between metastable states as illustrated in Fig. 3.6. This hopping diffusion is understood as a barrier-hopping process as explained in Sec. 2.8. In the case of H or H_2, which do not react with the host atoms, the barriers arise from the repelling Coulomb-interaction between the electron clouds of the host lattice and the diffusor. The minima of the potential energy surface are thus the interstitial positions of the host lattice [59, 153]. In between the jumps, the motion of the atom is randomly vibrational rather than diffusive or, in terms of Chap. 2, a microstate trajectory. This discreteness of motion not only strongly suggests the use of a grid-based method, where the grid points are interstitial positions of the host lattice, it also induces a natural discretization into the reaction-diffusion equations. As a consequence, the description based on macroscopic diffusion equations in the RD model (1.5)–(1.6) are only valid at distances that are much larger than the interstitial radius and it has to be assumed that at very short distances a description using hopping diffusion is more accurate.

We conclude that the most appropriate description of the physics considered in the present work is obtained from the reaction-diffusion master equation approach [148–151]. Within the natural lattice of interstitial positions the actors of our RD system exist in well-defined and discrete states. In accord with the considerations of Sec. 2.6, it is now possible to define a state vector $\vec{x}$ that contains the interstitial positions and bonding states of all actors as well as a set of reaction channels which cause transitions between the states of this vector. The RD system then becomes a time-dependent stochastic process $\vec{X}(t)$ that exists in one of a countable set of states $\vec{s}_\omega$ and whose evolution over time can then be described by the chemical master equation (2.20). As explained in Sec. 2.6, the physics behind the reaction channels are contained in the propensity functions a_γ and the state-change vectors $\vec{\nu}_\gamma$, which are given in Fig. 3.7. The reactions employed in our simulations are the hopping transport between interstitial sites, the passivation/depassivation reaction and the dimerization/atomization reaction. The stochastic chemical model is solved using the stochastic simulation algorithm (SSA) explained in Sec. 2.11.

	Reaction	Macroscopic	Microscopic	Illustration
a.	$Si^* + H \rightarrow SiH$	$k_r N_{it} H_{it}$	$\dfrac{k_r}{h^3} n_{DBi} n_{Hi}$	
b.	$SiH \rightarrow Si^* + H$	$k_f (N_0 - N_{it})$	$k_f n_{p,i}$	
c.	$H: I_1 \rightarrow I_2$	$-D\dfrac{\partial^2 H}{\partial x^2}$	$\dfrac{D}{h^2} n_{Hi}$	
d.	$H_2: I_1 \rightarrow I_2$	$-D_2\dfrac{\partial^2 H_2}{\partial x^2}$	$\dfrac{D_2}{h^2} n_{H_2i}$	
e.	$2H \rightarrow H_2$	$k_H H^2$	$2\dfrac{k_H}{h^3} n_{Hi}(n_{Hi} - 1)$	
f.	$H_2 \rightarrow 2H$	$k_{H_2} H_2$	$k_{H_2} n_{H_2i}$	

◌ ...Dangling bond   ⬤ ...H   ⬤ ...H₂

Figure 3.7: Reaction channels and propensities in the microscopic RD model along with their macroscopic counterpart. **(a)** The dangling bonds are represented by special sites at the bottom of the simulation box. Empty dangling bond sites can be passivated by a free hydrogen atom. **(b)** Occupied dangling bond sites do not offer a bonding reaction channel, they can only emit their hydrogen atom. **(c, d)** Within the bulk SiO_2, the atoms or molecules are allowed to jump from an interstitial I_1 to any neighboring site I_2. **(e)** When two hydrogen atoms occupy the same interstitial position, they can undergo a dimerization at rate k_H and form H_2. **(f)** Each hydrogen molecule dissociates at a rate k_{H_2} back into two hydrogen atoms. For interstitial site i, n_{DBi} is the number of (depassivated) dangling bonds, $n_{p,i}$ is the number of passivating hydrogen atoms, n_{Hi} is the number of free hydrogen atoms, and n_{H_2i} is the number of hydrogen molecules. h denotes the step size of the spatial grid.

In the microscopic RD model employed in this work the interstitial sites form a regular and orthogonal three-dimensional grid and the hopping rates for the diffusors are assumed to be constant in accord with the isotropic and non-dispersive diffusion underlying the conventional macroscopic RD model [9]. In a real SiO_2 of a MOS transistor the amorphous structure will of course lead to a random network of interstitial sites [152] with a variety of hopping rates

Figure 3.8: The simulation structure for the microscopic RD model employed in this work is a bounded region of width W and length L and infinite extension in z-direction, i.e. normal to the interface. The silicon dangling bonds are connected to special interstitial positions in the Si-SiO$_2$ interface region at the bottom of the simulation box (blue). The interstitial positions are assumed to form an orthogonal lattice with constant jump-width and constant diffusion coefficients.
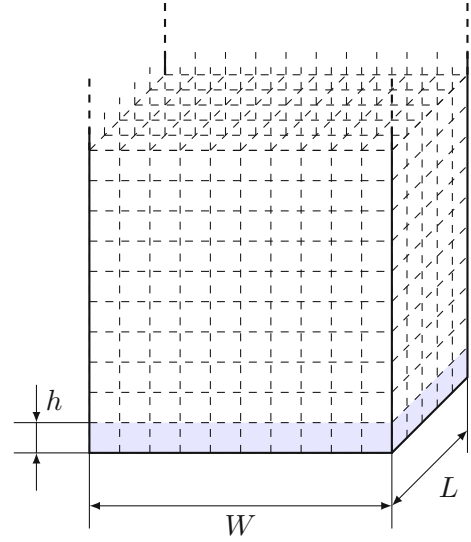
and a more complex topology. However, as the power-law degradation predicted by the macroscopic RD model requires a constant diffusion coefficient, these variations must be assumed unimportant [22] in order to obtain agreement with the established model. As illustrated in Fig. 3.8, the simulation region in our calculations is a rectangular box which extends to infinity normal to the Si-SiO$_2$ interface and has closed lateral boundaries. The Si-SiO$_2$ interface itself is represented by a special region at the bottom of the simulation box where selected interface sites have the ability to bond or release a diffusing hydrogen atom, see Fig. 3.7 and Fig. 3.8. The positions of the dangling bond sites in the interface region are picked randomly, similar to Fig. 3.3.

As mentioned above, the choice of the grid size requires special attention as it determines the probability of the bimolecular reactions. The interstitial size of amorphous silica has been calculated for molecular-dynamics generated atomic structures and is about $4\,\text{Å}$ [152]. We take this value as the physically most reasonable grid size.

Once the microscopic model is defined, the relation to the macroscopic RD model (1.4)–(1.6) has to be established. Using the number of dangling bonds in the simulation box n_{DB}, the number of hydrogen atoms passivating a dangling bond n_{p} and the numbers $n_{\text{H}i}$ of H and $n_{\text{H}_2 i}$ of H$_2$ at interstitial i, this relation is obtained from the discretization induced by the grid [23] as

$$N_0 = \frac{n_{\text{DB}}}{WL}, \tag{3.2}$$

$$N_{\text{it}} = \frac{n_{\text{DB}} - n_{\text{p}}}{WL}, \tag{3.3}$$

$$\text{H}(x_i) = \frac{n_{\text{H}i}}{V_i}, \tag{3.4}$$

$$\text{H}_2(x_i) = \frac{n_{\text{H}_2 i}}{V_i}, \tag{3.5}$$

where W, L and h are illustrated in Fig. 3.8 and V_i is the volume of interstitial i which is $V_i = h^3$ in this work. The relation between the rates of the macroscopic model and the microscopic propensity functions are given in Fig. 3.7. Initially, all hydrogen atoms are passivating silicon dangling bonds

$$n_{\text{p}}(t = 0) = n_{\text{DB}}, \tag{3.6}$$

Reaction	Propensity
Depassivation	$0.5 s^{-1}$
Passivation	$4 \times 10^4 s^{-1}$
Dimerization	$2 \times 10^5 s^{-1}$
Atomization	$5 s^{-1}$
H-hopping	$100 s^{-1}$
H_2-hopping	$100 s^{-1}$

Table 3.1: Parameters of the model system. The parameters have been selected to enable a study of the different regimes of the microscopic RD model at moderate computational expense. The rates are given in terms of the microscopic model as in Fig. 3.7.

in accordance with the assumptions of the macroscopic RD model.

3.2 Results and Discussion

Two different systems have been studied in detail: a model system and a "real-world-example". The model system is used to study the general features of the microscopic reaction-diffusion process. It is parametrized in order to clearly show all relevant features at a moderate computational effort. The parametrization of the real-world system is based on a published parametrization of the modified reaction-diffusion model. This system is used to relate our microscopic model to published data.

3.2.1 General Behavior of the Microscopic RD Model

The parametrization that is used to study the general behavior is given in Tab. 3.1. The number of diffusing particles is a trade-off between accuracy and computational speed. Due to the large computational demand[1] , different regimes of the degradation curve have to be calculated with different numbers of diffusing particles.

The earliest degradation times are dominated by the depassivation of the silicon dangling bonds leading to a linear increase of the degradation, which is equivalent to the initial "reaction limited" degradation of the macroscopic RD model [8]. However, the degradation predicted by the microscopic RD model quickly saturates as an equilibrium forms between depassivation and repassivation *for each dangling bond separately*. In absence of any diffusion the time evolution of the number of hydrogen atoms passivating a silicon dangling bond is given by

$$\frac{\partial n_{\mathrm{p}}}{\partial t}(t) = -k_{\mathrm{f}} n_{\mathrm{p}}(t) + \frac{k_{\mathrm{r}}}{h^3}(n_{\mathrm{DB}} - n_{\mathrm{p}}(t)) \tag{3.7}$$

$$n_{\mathrm{p}}(t=0) = n_{\mathrm{DB}}. \tag{3.8}$$

with the solution

$$n_{\mathrm{p}}(t) = n_{\mathrm{DB}} - \frac{n_{\mathrm{DB}} k_{\mathrm{f}}}{k_{\mathrm{f}} + \frac{k_{\mathrm{r}}}{h^3}}(1 - e^{-(k_{\mathrm{f}} + \frac{k_{\mathrm{r}}}{h^3})t}). \tag{3.9}$$

The main difficulty in the calculation of the early degradation times in the microscopic RD model is the very low degradation level in this regime, which requires a high accuracy, i.e. a large number of particles to obtain smooth results. Fortunately, as reactions between the hydrogen atoms or between hydrogen atoms and neighboring dangling bonds are not happening in this regime, a good parallelization can be obtained by averaging over separate simulation runs, see Fig. 3.9. A comparison of the microscopic RD model and (3.9) is shown in Fig. 3.10.

---

[1]The computational effort of the SSA scales roughly linearly with the simulated time, which means exponential scaling for the logarithmic abscissa that is used for BTI degradation curves. The scaling in the number of particles is also linear.

Figure 3.9: As the interaction between the diffusing particles is small at early degradation times, the computation can be parallelized by averaging over several simulation runs. The figure shows that a calculation with 10^5 particles is equivalent to the average of 100 calculation runs with 10^3 particles. The result of a single 10^3 particle run is shown for comparison. k_f was increased by a factor of 100 for this calculation, in order to obtain smooth curves from the 10^5 particle run.
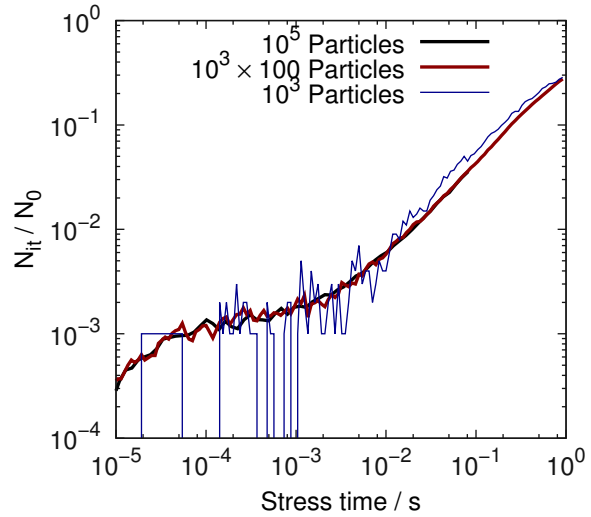
Figure 3.10: Comparison of the microscopic RD model with 25000 particles averaged over 50000 runs to its macroscopic counterpart, the single-particle expressions (3.10)–(3.11) and the isolated dangling-bond equilibration (3.9). The earliest degradation times are dominated by the equilibration between the depassivation and passivation reaction at every dangling bond. Around $1\,\text{ms}$, the departure of the hydrogen atoms from the dangling bond site begins but the interaction between the diffusors is still negligible.
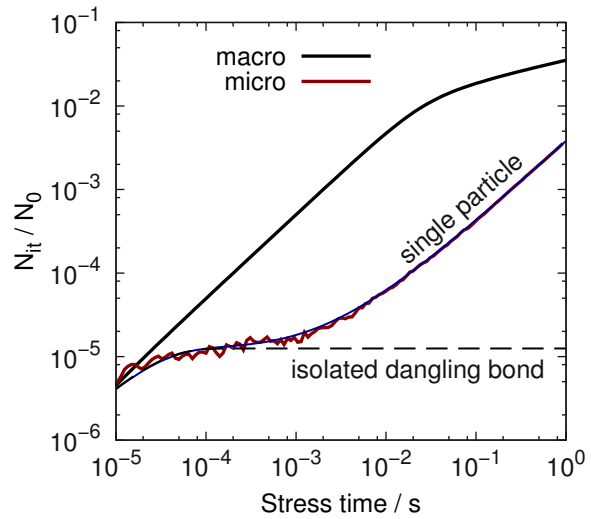
The initial behavior of the microscopic RD model stands in stark contrast to the degradation in the macroscopic model where the linear regime continues until a global equilibrium has formed at the interface.

As this initial behavior takes a central position in our further discussion, it requires a deeper analysis. According to Sec. 2.12 the microscopic single-particle regime can be accurately described using rate equations, as it does not contain any second-order reactions. The required equations are basically those of the RD model, but as every hydrogen atom can be assumed to act independently, the expressions for the hydrogen bonding as well as the competition for dangling bonds are neglected. As the kinetic behavior in this regime is strongly determined by the first diffusive steps of the hydrogen atoms, the diffusion part of this approximation must have the same interstitial topology as the microscopic model. As all hydrogen atoms act independently, only one atom and one dangling bond need to be considered. The interface

Figure 3.11: Long-term simulations can be executed with lower accuracy due to the increased level of degradation. Three microscopic calculations are compared to the macroscopic result. The 25000 particle simulation nicely shows the transition between the single-particle and the macroscopic diffusion-limited regime. The 1000 particle calculation captures the transition region but becomes quite noisy for earlier degradation times. The 90 particle run still captures the macroscopic regime with reasonable accuracy.
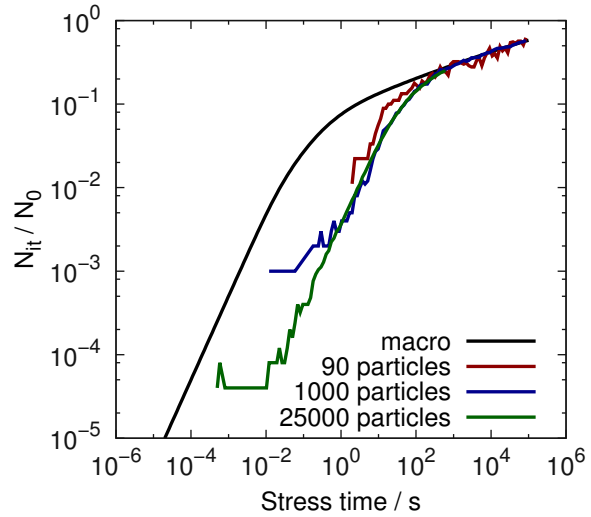
reaction and the diffusion of the hydrogen atom is thus described as

$$\frac{\partial n_{\mathrm{p}}}{\partial t} = -k_{\mathrm{f}} n_{\mathrm{p}} + \frac{k_{\mathrm{r}}}{h^3} n_{\mathrm{DB}} n_{\mathrm{H0}} \quad \text{and} \tag{3.10}$$

$$\frac{\partial n_{\mathrm{H}i}}{\partial t} = \sum_{j \in \mathcal{N}(i)} \frac{D}{h^2} (n_{\mathrm{H}j} - n_{\mathrm{H}i}), \tag{3.11}$$

respectively, where $\mathcal{N}$ denotes the set of neighboring interstitials to i. Fig. 3.10 compares the microscopic RD calculation with the approximations for the different regimes at early degradation times, which shows that the single-particle model perfectly matches the behavior of the atomic model in the initial phase.

After the atoms have traveled sufficiently long distances, the interaction between the particles becomes relevant and the single-particle approximation becomes invalid. In Fig. 3.11 this is visible as a transition away from the single-particle behavior towards the macroscopic solution between 1 s and 1 ks. Due to the relatively large level of degradation, the long-term simulations do not require as much accuracy as the short-term simulations. Consequently the number of particles can be reduced for longer simulation times, which makes the prediction of long-term degradation possible.

Finally, Fig. 3.12 compares the microscopic RD model to the macroscopic version over the course of one complete stress cycle, where the microscopic curve was obtained by combining calculations of different accuracy, as explained above. Instead of the three regions which arise from the macroscopic RD model — reaction-limited, equilibration and diffusion-limited — the H-H$_2$ microscopic description has four to five regimes depending on the particular parametrization.

- The earliest degradation times ($t < 20\,\mu$s in this case) are dominated by the depassivation of dangling bonds. In this regime, the microscopic and the macroscopic model give identical degradation behavior.

- After the passivation and depassivation have reached an equilibrium between k_{f} and k_{r} separately for each Si-H bond, the fraction of depassivated dangling bonds remains constant until the diffusion of the hydrogen atoms becomes dominant. This regime only shows when the individual hydrogen atoms are considered and consequently is not obtained from any model based on rate equations.

Figure 3.12: Comparison of all regimes of the microscopic RD model to the degradation predicted by the macroscopic RD model. Obviously there is a large discrepancy between the two descriptions and the behavior of the physically more reasonable microscopic model is not experimentally observed.
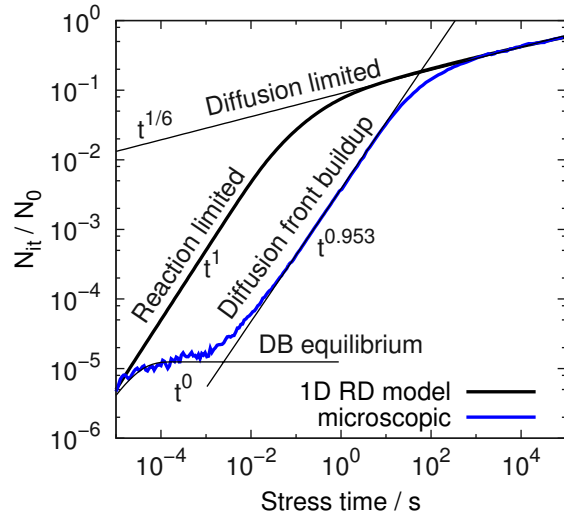
- As more and more hydrogen atoms leave their initial position, the degradation is determined by the buildup of a diffusion front along the Si-SiO_2 interface and the equilibration between the dangling bonds. This regime has a very large power-law exponent of almost one[2] that is not experimentally observed. The stress time range in which this regime is observed depends on the average distance between two dangling bonds, the diffusion coefficient and the interstitial size.

- As the bimolecular reactions become relevant, the macroscopic diffusion-limited regime begins to emerge. For some parametrizations we have observed a time window in which a sufficient amount of H_2 has not formed yet, and thus the initial diffusion-limited regime has the typical $t^{1/4}$-form that arises from the classical RD model without H_2 [25].

The initial single-particle phase of the degradation is a remarkable feature of the microscopic model. As it is incompatible with experimental data and very sensitive to the parametrization, its relevance for real-world reliability projections has to be investigated. For this purpose we have run calculations based on a published parametrization of the reaction-diffusion model for NBTI, see Sec. 3.2.4.

3.2.2 Recovery

In agreement with our investigations on two-dimensional systems [24, 25], the three-dimensional stochastic motion of the hydrogen atoms *does not influence* the recovery behavior of the system after long-term stress, which contradicts the suggestions of [16]. As shown in Fig. 3.13, a longer relaxation transient is only obtained if the foregoing stress phase does not show a power-law regime. As the system comes closer to the macroscopic degradation behavior, the recovery in the microscopic model also approaches the macroscopic version, which is incompatible with experimental data [12, 13, 154]. This behavior is to be expected as the $t^{1/6}$ degradation regime requires an equilibration and thus a quasi-one-dimensional behavior. The recovery proceeds on a timescale that is at least two orders of magnitude longer than the stress time. The lateral search of hydrogen atoms for unoccupied dangling bonds was suggested to dominate at the end of the recovery. However, due to the logarithmic time scale on

---

[2]In our earlier studies on two-dimensional systems this exponent was around 0.8 [25], owing to the topology dependence of this regime.

Figure 3.13: Recovery transients for different stress times. As the degradation transient approaches the macroscopic diffusion limited regime (see inset), the recovery comes closer to the macroscopic recovery, leading to a perfect match as soon as the degradation assumes the experimentally relevant $t^{1/6}$ form.
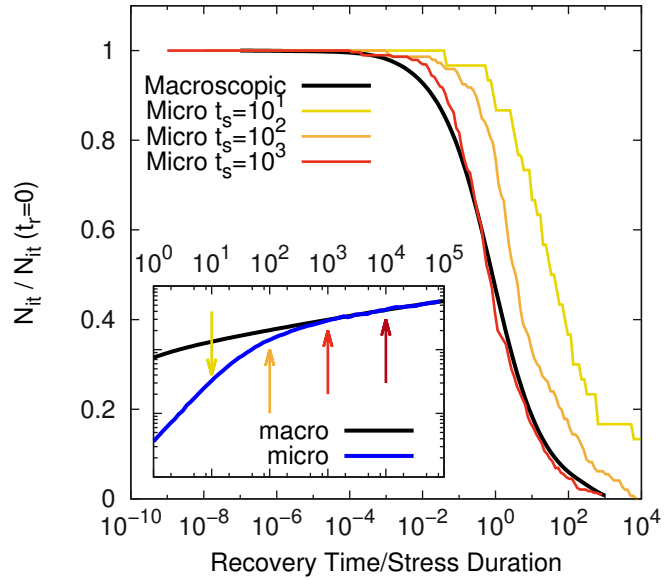
which recovery is monitored, the equilibration along the interface has negligible impact at the end of the recovery trace if this equilibration proceeds about two orders of magnitude faster. Thus, the hovering of hydrogen atoms along the interface does not influence the shape of the recovery transient.

3.2.3 Approximations in the Macroscopic Model

After the microscopic RD theory Fig. 3.7 has been established and its general behavior has been investigated, one can use this framework to analyze the assumptions that are implicit to the macroscopic RD model (1.4)–(1.6), which is still widely considered to be an adequate approximation.

The most obvious approximation in the macroscopic RD model is the one-dimensional description of diffusion. While this may seem to be appropriate as boundary effects in the diffusion of both H and H_2 are negligible, it tacitly introduces the assumption of lateral homogeneity along the interface. This homogeneity includes the following assumptions:

- *All* the liberated hydrogen atoms at the interface (H_{it} in (1.1) and (1.4)) compete instantaneously with *all* the other free interfacial hydrogen atoms for *all* the available dangling bonds.

- *All* the pairs of hydrogen atoms at a certain distance from the Si-SiO_2 interface are equally likely to undergo dimerization and form H_2, independently of their spatial separation.

As was shown above, a hydrogen atom liberated during stress initially stays in the vicinity of its original dangling bond and thus the lateral homogeneity has to be considered a long-term approximation. It is accurate when the diffusion of hydrogen has led to enough intermixing so that there is no significant variability in the concentration of free hydrogen along the interface. Following [115] and the discussion in Sec. 2.12, this condition can be called "lateral well-stirredness" of the system.

The second and more delicate approximation in the macroscopic RD model is the mathematical description using rate- and diffusion-equations. In the microscopic RD model, the rate at

53

Table 3.2: The parameters employed in the real-world simulations. The parameter set is based on the values published in [20] but was slightly modified to give the same degradation behavior with physically more reasonable k_r and k_H.

k_f	$3\,\mathrm{s}^{-1}$
k_r	$6 \times 10^{-13}\,\mathrm{cm}^3\mathrm{s}^{-1}$
k_H	$5.6 \times 10^{-11}\,\mathrm{cm}^3\mathrm{s}^{-1}$
k_{H_2}	$95.4\,\mathrm{s}^{-1}$
D	$10^{-13}\,\mathrm{cm}^2\mathrm{s}^{-1}$
D_2	$1.8126 \times 10^{-14}\,\mathrm{cm}^2\mathrm{s}^{-1}$
N_0	$5 \times 10^{12}\,\mathrm{cm}^{-2}$

which an atom at the interface passivates a dangling bond depends not only on the rate k_r but also on the probability of finding this atom at the position of the dangling bond. In the macroscopic model the precondition of having an unoccupied dangling bond at the interface is described multiplicatively as $k_r N_{it} H_{it}$. At early times during degradation, when each hydrogen atom still resides near its dangling bond, this term introduces an unphysical self-interaction where each hydrogen atom competes with *itself* for its dangling bond. As the root of this problem lies in the assumptions implicit to a formulation based on rate-equations, the error is also present in a macroscopic model with three-dimensional diffusion. As explained in [25], this means that a rate-equation based RD model will not accurately describe the degradation at early times even if higher-dimensional diffusion and discrete dangling bonds are considered.

Similar to the passivation rate, the rate at which H_2 is formed in the microscopic RD model depends on both the dimerization rate k_H and the probability of finding two hydrogen atoms which occupy the same interstitial position. In the macroscopic RD model, this dimerization reaction is modeled as $k_H H^2$. As thoroughly explained in [145], this approximation is only valid for large numbers of particles, as the number of pairs of hydrogen atoms in an interstitial goes as $N(N-1)$ which can only be approximated as N^2 if N is sufficiently large.

All in all, the macroscopic RD model can only be considered a valid approximation of the microscopic RD model for very long stress times and a sufficient amount of liberated hydrogen atoms. The time it takes for the macroscopic approximation to become valid, however, may exceed the time range in which it is usually applied, depending on the parametrization.

3.2.4 A Real-World Example

To study the behavior of the atomistic model for a real-world example, we compare to the measurements of Reisinger et al. [12] using the parametrization of Islam et al. [20] in a modified form, see Tab. 3.2. Fig. 3.14 shows the results of our calculations for several interstitial sizes. While the macroscopic one-dimensional RD model fits the data very well, the kinetic Monte Carlo data shows a completely different behavior. Again, the single-particle regime is clearly present. However, due to the low density of dangling bonds at the interface, the single-particle regime dominates the degradation for a large part of the stress time. For a realistic interstitial size of $4\,\text{Å}$ [152, 155], the onset of the $t^{1/6}$ regime lies far beyond the experimental window of $10^5\mathrm{s}$. When the interstitial size is increased, the onset of the $t^{1/6}$ regime moves to earlier times, which is due to the increase of the reaction radius for the bimolecular reactions as explained above. For the given parameter set, an interstitial size of $h = 2\,\text{nm}$, which is the total thickness of the oxide of the device under consideration [12], is required to at least have the $t^{1/6}$ regime touch the experimental window.

A shift of the onset of the experimentally observed regime to earlier times at a realistic interstitial size requires a dramatic increase of either the hydrogen diffusion coefficient or the availability of free hydrogen near the interface. An increase of the hydrogen diffusion coefficient, however, breaks the dominance of H_2 flux over the flux of atomic hydrogen and changes the

Figure 3.14: The degradation transient predicted by the microscopic RD model for four interstitial sizes compared to the macroscopic one-dimensional model and experimental data. Using the parameters Tab. 3.2, the prediction of the microscopic RD model is completely incompatible with the experimental data as the onset of the $t^{1/6}$ regime is delayed beyond 10^8 s (about three years) for a reasonable interstitial size of $4\,\text{Å}$. Increasing the interstitial size reduces the effect as it increases the effective reaction radius for the bimolecular reactions. However, even for unphysically large interstitial sizes, the onset of the $t^{1/6}$ regime is delayed to 10^4 s ($h = 40\,\text{Å}$) or 10^5 s ($h = 20\,\text{Å}$).
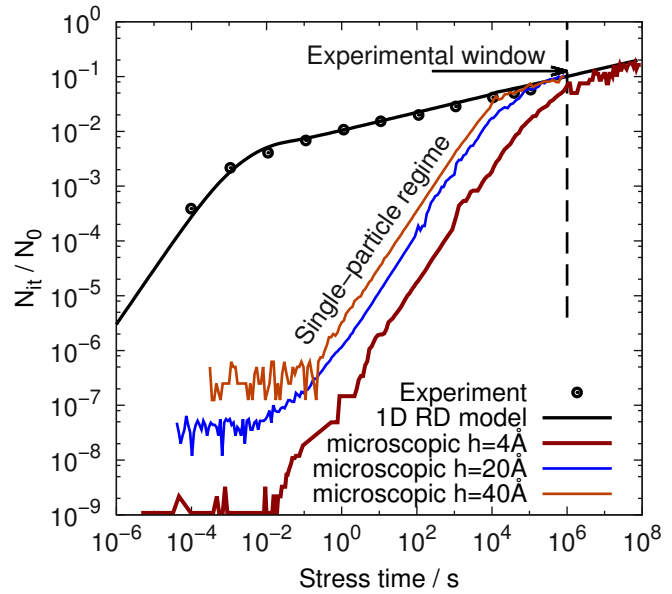
predicted degradation away from the experimentally observed $t^{1/6}$ towards $t^{1/4}$. Increasing the availability of hydrogen at the interface by adjusting the ratio k_f/k_r causes similar problems, as the H_2 diffusion coefficient has to be lowered in order to give the same overall degradation.

This indicates that in the given microscopic model it is impossible to obtain the experimentally observed $t^{1/6}$ degradation within the experimental window at a reasonable interstitial size.

3.2.5 Increased Interface Diffusion

The behavior predicted by the microscopic model is completely incompatible with any experimental data, while the description is much closer to the physical reality than the macroscopic RD model. Only two interpretations are possible to resolve this dilemma. Either the ability of the macroscopic RD model to fit degradation measurements has to be regarded as a mathematical artifact without physical meaning, or the structure of the Si/SiO_2 interface somehow accelerates the lateral equilibration considerably. We investigated the second option more closely by considering first-principles calculations that have shown a lowering of diffusion barriers for hydrogen (molecules) along the Si/SiO_2-interface as compared to the bulk SiO_2 [156]. These findings indicate that the motion of hydrogen might proceed at a much higher rate at the interface. As a higher diffusivity at the interface aids the lateral equilibration, it might be the sought process that makes the one-dimensional RD model physically meaningful. To account for it in our microscopic model, we applied different diffusion coefficients D_I and D_B in the interface region and in the bulk, respectively.

As can be seen in Fig. 3.15, the increase of the interface diffusion coefficient accelerates the degradation during the initial phase as it increases the transport of hydrogen atoms away from their dangling bonds. Interestingly, even if the interface diffusion coefficient is increased by four orders of magnitude there is no $t^{1/6}$ behavior visible, but instead the degradation takes on the typical $t^{1/4}$ behavior of a hydrogen-only reaction-diffusion model. While the competition for dangling bonds sets in earlier for increased interface diffusion coefficients, the formation of H_2 is not accelerated in the same way. Inspection of the atomic diffusion shows that the acceleration of the dimerization is much less pronounced as the liberated hydrogen atoms constantly leave the interface region into the bulk where the diffusion proceeds slower and

Figure 3.15: For increasing D_I, the departure of hydrogen atoms from their dangling bond sites starts earlier, leading to an increased degradation at earlier times. Comparison to the classical RD model without H_2 formation shows that competition for dangling bonds sets in after about $100\,s$, leading to a $t^{1/4}$ degradation. The formation of H_2 is slowly accelerated by the increased D_I and only for $D_I \to \infty$, the macroscopic behavior is obtained.
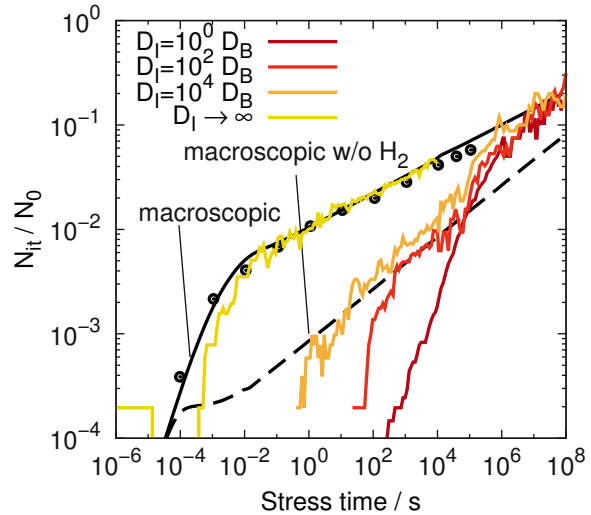
the collision rate is reduced. Only in the limit of $D_I \to \infty$ will the microscopic RD model match the experimentally observed behavior. Although these extremely high interface diffusion coefficients lack any physical justification, this is still closer to the physical reality than the assumption of immediate equilibration along the Si-SiO_2-interface at any depth that is inherent to the usually employed one-dimensional macroscopic RD model.

As a side note we remark that in a real wafer, a nearly infinite diffusion coefficient along the Si/SiO_2-interface would make the hydrogen spread out through the waver during stress. This would again alter the degradation slope and give rise to cross-talk between neighboring devices that would be measurable, but has never been reported.

3.3 Related Work

Three other scientific groups have put forward microscopic RD models recently [23, 157, 158] and interestingly those investigations find a reasonable agreement between their microscopic description and the macroscopic RD model. In the work of Islam et al. [23] the atomic description is basically equivalent to the work presented here but is built upon a one-dimensional foundation which carries the same implicit assumptions as the macroscopic model. Clearly this model cannot capture the effects discussed in this chapter as those are solely due to higher-dimensional effects. From a physical point of view, however, the one-dimensional approximation lacks justification considering the results presented above.

The work of Choi et al. considers the three-dimensional diffusion of the particles based on a grid-less stochastic formulation [158]. Although the degradation in that work seems to match the macroscopic RD model quite well at first sight, also strong discrepancies arise between the two for longer stress times. Interestingly, for situations where the approach presented above predicts a degradation far below the prediction of the macroscopic model, the degradation predicted by Choi et al. overshoots the macroscopic model considerably. Only for an enormous density of dangling bonds or a very large reaction radius the macroscopic behavior is obtained, in accord with our results. The degradation behavior in [158] initially follows $N_{it}(t) = k_f t$, which suggests that the depassivated hydrogen atoms instantly leave the reaction radius of their respective dangling bond. The following excessively high power-law exponent suggests that the repassivation of the silicon dangling bonds is somehow inhibited in this formulation.

The most likely explanation for this behavior is a too low resolution of the time-stepping, in combination with the physically unjustifiable description of the diffusive motion.

The work of Panagopoulos et al. uses a grid-based stochastic RD model that seems to be compatible with our description. The surprisingly good agreement between their results and the macroscopic RD model may be an artifact of the employed method which is based on an adaptive time-stepping [157]. Also, the paper states that the passivation reaction occurs if a hydrogen atom is "close" to a dangling bond. This indicates an artificial capture radius, but this is not explicitly stated. Also, the grid spacing is not given in the paper and its physical relevance is not discussed. However, as shown by our calculations, an unphysically large grid spacing strongly promotes bimolecular reactions and thus induces a degradation behavior that is (falsely) compatible with the macroscopic RD model.

With four parameters
I can fit an elephant,
and with five
I can make him wiggle his trunk.

(John von Neumann (attributed))

4 Atomistic Modeling and the BTI Defect

The defect in the multi-state multi-phonon model for BTI has (at least) two structural and (at least) two electronic configurations, as explained in Sec. 1.5. The structural reorganization of the defect goes largely unnoticed by the rest of the system and it is only the charge state of the defect that acts on the rest of the device via coulombic interaction. The barrier hopping transitions $1 \rightleftharpoons 1'$ and $2 \rightleftharpoons 2'$ appear to proceed independently of the current state of the device. Only the NMP transitions $1 \rightleftharpoons 2'$ and $2 \rightleftharpoons 1'$ need to consider the availability of electrons and holes. All the states and transitions of the BTI defect can be understood within the framework laid out in Chap. 2. The present chapter shows how these transitions can be described using an atomistic model of the defect and a macroscopic model of the device.

4.1 Atomistic Defect Models

An overview of atomistic defect models employed for the calculation of E' defects in the literature is given in Tab. 4.1, including the electronic structure method and the atomic representation employed. The design of the atomic arrangement used to represent the defect directly influences the predictive power of the calculations. Three approaches are widely used in the literature [102], which are illustrated in Fig. 4.1:

- In **isolated cluster** calculations, the defect and its surrounding atoms are represented as an isolated molecule. This method is often used in combination with highly sophisticated quantum chemistry programs which offer highly accurate electronic structure methods.

- **Embedded cluster** methods embed the pseudo-molecules into an atomic host structure which is treated using empirical potentials.

- In **supercell** calculations, the defect is introduced into a periodic cell.

All three approaches have their own benefits and drawbacks. Isolated cluster models are relatively easy to set up and one can choose from the rich pool of quantum chemistry programs for the electronic structure calculation. Isolated clusters offer a simple way to treat defects that are hard to integrate into a full atomic host structure. However, they suffer from the inherent neglect of electrostatic and mechanical long range interactions.

Embedded cluster methods are an approach to improve on these drawbacks. In an embedded cluster calculation the atomistic defect model is split into three nested regions. The inner region surrounds the defect and is treated using a quantum-chemistry method. This quantum region is surrounded by the so-called classical region, which contains a large number of atoms whose interactions are described using empirical potentials [66]. Finally, the quantum-mechanical and classical regions are embedded in an infinite continuum model of the host material. Electrostatic interactions between the quantum region and the classical

58

region are considered using the shell model for polarization on the classical atoms. In structural optimizations an inner sphere of atoms, containing the quantum region and a fraction of the classical region, is moved while the outer shell is held fixed. The atoms at the interface between the quantum region and the classical region need to be included both in the electronic structure part and in the empirical potential part of the calculation. The representation of the interface atoms in the electronic structure method is especially problematic as at least one valence electron of these atoms needs to be replaced by an interaction with the empirical potential. To account for the missing valence electron, the interface atoms are equipped with a parametrizable pseudo-potential that acts on the electrons of the quantum region. Embedded cluster methods improve upon the shortcomings of the isolated cluster calculations at the expense of a dramatically increased complexity. The set-up of an atomistic defect model using the embedded cluster approach requires a lot of fine-tuning of both the empirical potential and the pseudo-potential for the interface atom. For this reason, the embedded cluster approach is not suitable for the original study of defect parameters, but is more appropriate for refining investigations on defects for which reference calculations exist.

Supercell defect calculations have become quite popular in the solid state community. This popularity comes in part from the existence of conduction and valence levels in the calculation, and the increasing availability of plane wave based general purpose codes [102]. In the present work, we employ a supercell approach for exactly these reasons. Issues of the supercell approach include the treatment of charged cells, which will be discussed later, and interactions between the periodic images.

The host materials used in the studies of E'-centers are mostly α-quartz and amorphous SiO_2. Due to its similar density, α-quartz is usually considered a reference system for amorphous silica [57, 59, 163]. Atomistic amorphous silica models are continuous random network structures generated by molecular dynamics melting and quenching [166, 167]. Although an amorphous host structure is closer to the physical reality of the oxide in an MOS transistor, the result of the molecular dynamics generation depends strongly on the parameters of the processing, especially the cooling rate [110]. As the defect parameters strongly depend on the surrounding atoms, the accuracy of a defect study depends on a host structure that accurately represents the material under study. The generation of an amorphous host structure thus requires careful testing of the dependence of the structural properties on the creation process and their evaluation against experimental data. The present work, however, calculates quantities that have not been investigated before. Therefore, it is reasonable to create our defect models upon an α-quartz host structure, in order to build a reference for later studies of defects in amorphous host structures. Due to the vast amount of literature available for this system, α-quartz seems to be best suited for these reference calculations. Our work follows Blöchl [59, 84] and uses an orthogonal 72 atom α-quartz supercell [168]. The employed functional is the gradient-corrected functional of Perdew, Burke, and Ernzerhof [101], the core electrons are represented using the projector augmented wave method as implemented in the Vienna ab-initio simulation program (VASP) [169, 170]. The electronic structure is expanded using a plane-wave basis set, employing periodic boundary conditions for the simulation cell.

4.1.1 Parameters of the DFT Calculations

To be compatible with the work of Blöchl [59], we have constructed an orthogonalized α-quartz supercell for our defect calculations. We use the coordinates given in [168], which reflect the hexagonal symmetry of the α-quartz as a non-orthogonal unit cell, see Fig. 4.2. As two angles of the cell are already $90°$, the orthogonalization of the cell concerns only the plane of the γ

Reference	Electronic Structure	Boundary Condition	Host Structure
[54]	LCLO-MO	isolated cluster	α-quartz
[55]	Tight-Binding	isolated cluster	α-quartz
[56, 57]	MINDO/3, MOPN	isolated cluster	α-quartz
[58]	LSDA	supercell	α-quartz, amorphous
[159]	HF, MP2	isolated cluster	α-quartz
[59]	PBE	supercell	α-quartz
[160, 161]	B3LYP	isolated cluster	α-quartz
[162]	HF, MP2	isolated cluster	Free relaxation
[77]	HF	embedded cluster	α-quartz
[60]	B3LYP	isolated cluster	amorphous
[63, 163]	HF	embedded cluster	α-quartz
[61]	PBE	supercell	amorphous
[64]	LSDA	supercell	α-quartz, amorphous
[65]	PBE	supercell	amorphous
[62]	DFT	supercell	α-quartz
[68, 78]	HF	embedded cluster	amorphous
[69, 164]	B3LYP	embedded cluster	amorphous
[165]	PBE+HF	supercell	α-quartz

Table 4.1: An overview of electronic structure methods and atomistic representations employed in published defect studies. The electronic structure methods are MINDO (modified intermediate neglect of differential overlap), HF (Hartree-Fock), MP2 (second order Møller-Plesset perturbation theory), PBE (DFT with gradient-corrected functional due to Perdew and coworkers), B3LYP (hybrid DFT with gradient-corrected functional due to Becke and coworkers with HF exchange), and PBE+HF (hybrid DFT with PBE functional and HF exchange).

angle. The procedure is described in Fig. 4.3. After the construction the atoms in the cell were relaxed keeping the cell shape and volume constant. The resulting structure is the basis for all following defect calculations and is shown in Fig. 4.4. The energy cut-off for the plane wave expansion is $800\,\mathrm{eV}$ for all calculations in this work. VASP's real space projection is disabled to improve the accuracy. The k space is only sampled at the Γ point. Structures are optimized using the quasi-Newton algorithm [96, 171] until the forces are below $10^{-2}\mathrm{eV/\mathring{A}}$. Optimizations starting far from the optimum were pre-optimized using the more robust conjugate gradient algorithm.

4.1.2 Defect Structures

As explained in Sec. 1.6, the defect structures investigated in this work are the oxygen vacancy and the hydrogen bridge. The oxygen vacancy defect was created by removing one oxygen atom from the cell, the hydrogen bridge by replacing an oxygen atom with a hydrogen atom. Subsequent optimizations led to the dimer configuration for the oxygen vacancy and the closed configuration for the hydrogen bridge, see Fig. 4.6 and Fig. 4.7. The puckered oxygen vacancy and the broken hydrogen bridge were constructed by manual rearrangement of the defects.

Both defects give rise to one occupied state in the SiO_2 band gap. This state is the highest occupied state of the Kohn-Sham spectrum. As the eigenstates of the auxiliary system are occupied from the bottom up, the positively charged defects are easily created by removing an electron from the calculation. Charged defects, however, are problematic in supercell calcula-
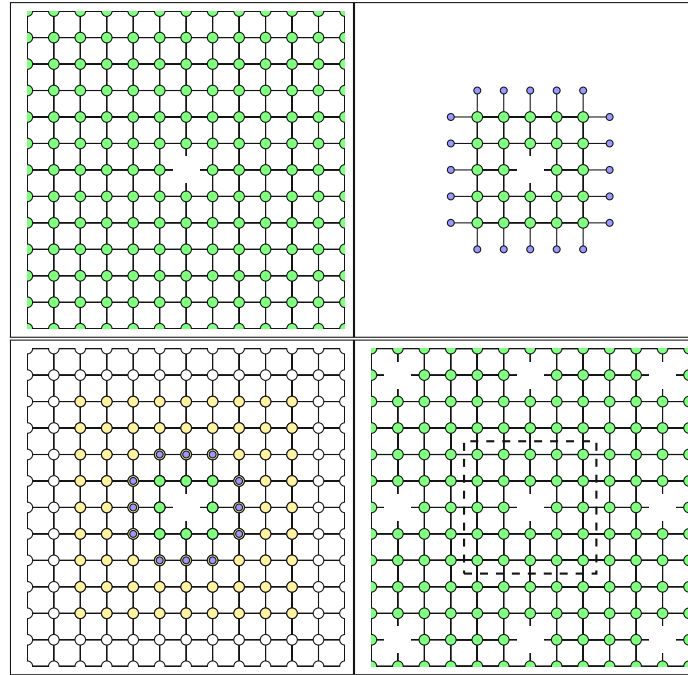
Figure 4.1: Atomistic defect models usually employed in calculations of point defects. All these models attempt to describe a point defect in an otherwise ideal, infinite host structure **(top left)**. In isolated cluster calculations **(top right)**, the defect and its surrounding atoms are represented as a pseudo-molecule (green). The bonds at the boundary of this pseudo-molecule are usually saturated using hydrogen or pseudo-hydrogen atoms (blue). Embedded cluster methods **(bottom left)** surround the pseudo-molecule with atoms that are treated using empirical potentials. These atoms are partially fixed (white) and partially included in structural relaxations (yellow). Supercell methods **(bottom right)** take the defect and its surrounding host atoms and apply periodic boundary conditions.
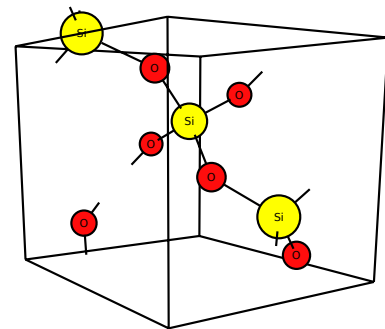
Figure 4.2: The α-quartz unit cell given in [168]. The cell contains nine atoms and the cell angles are $\alpha = \beta = 90°$ and $\gamma = 120°$

tions, as it is not possible to define a meaningful energy for a periodic cell with a net charge. Thus, when an electron is removed from the DFT calculation a compensating background charge is automatically added by VASP [102, 171]. The interaction of the charged defect with this artificial charge background has to be accounted for. In the present work we employ the

(i)

(ii)

$\vec{b}$

$\vec{a}$

(iii)

(iv)
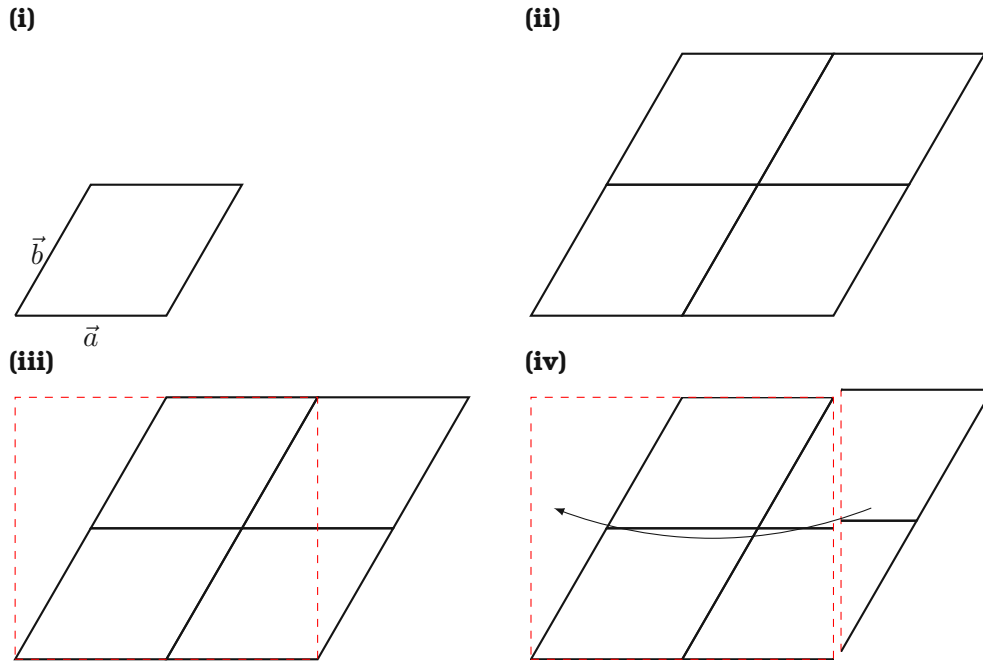
Figure 4.3: Construction of an orthogonalized α-quartz supercell. The unit cell **(i)** is repeated along axes $\vec{a}$ and $\vec{b}$ to give a 2×2 supercell **(ii)**. Due to the geometry of the cell it is possible to change the cell shape as indicated by the red rectangle **(iii)**. Finally, the internals of the cell are adjusted to fit the new shape **(iv)**.
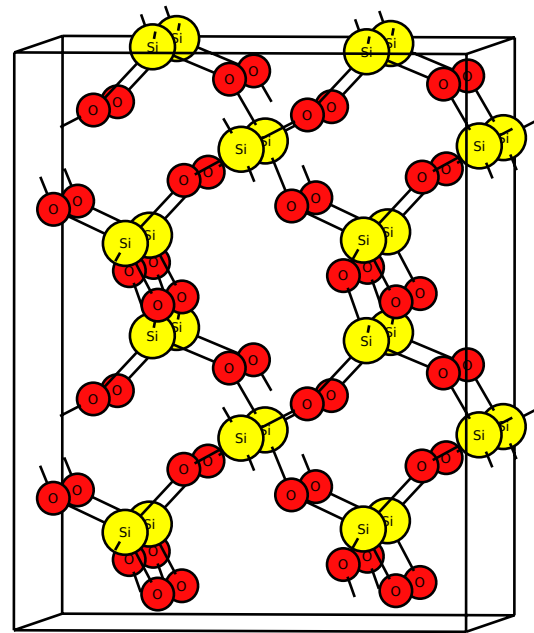
Figure 4.4: The orthogonalized 72 atom α-quartz supercell used in our calculations.

correction used by Blöchl [59], which simply increases the energy for charged cells by $0.48\,\text{eV}$, see the reference for details.

In the neutral state, the dimer configuration of the oxygen vacancy is more stable than the puckered configuration by $2.966\,\text{eV}$. In the positive state, the situation is reversed with the

Figure 4.5: The Kohn-Sham eigenvalue spectrum of the α-quartz host cell. Just as the LDA, the GGA underestimates band gaps. The band gap in the present work amounts to 5.9 eV.
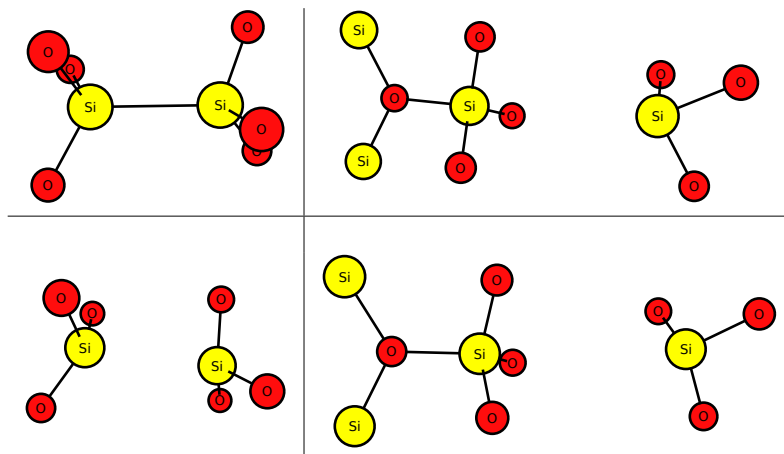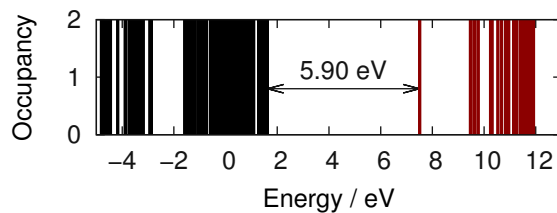
Figure 4.6: Structures of the dimer **(left)** and the puckered **(right)** configuration of the oxygen vacancy as obtained from our DFT calculations. The neutral **(top)** as well as the positive **(bottom)** charge state are shown.

puckered configuration being slightly lower in energy than the dimer configuration by $88\,\mathrm{meV}$. For the neutral hydrogen bridge, the DFT predicts the closed configuration to be $21\,\mathrm{meV}$ more stable than the broken configuration. Similar to the oxygen vacancy, the positive hydrogen bridge is $185\,\mathrm{meV}$ more stable in the broken configuration than in the closed configuration.

The optimized structures for the oxygen vacancy and the hydrogen bridge are shown in Fig. 4.6 and Fig. 4.7, respectively. The geometries obtained from our calculations are in excellent agreement with the literature as shown in Tab. 4.2 and Tab. 4.3.

It is common in defect studies to calculate the "formation energy" of a defect. This energy is an indicator for the abundance of the defect in thermal equilibrium. The structure of the

| | dimer | | puckered | | | |
| | Si-Si distance | | Si-Si distance | | Si-O(3) distance | |
	neutral	positive	neutral	positive	neutral	positive
present work	2.437 Å	2.964 Å	4.026 Å	4.358 Å	1.887 Å	1.841 Å
Blöchl [59]	2.445 Å	3.011 Å	4.052 Å	4.358 Å	1.907 Å	1.852 Å
Boero [58]	2.520 Å	3.050 Å	$\approx 4.37^{\dagger}$ Å	4.46 Å		1.82 Å
Pacchioni [159]	2.530 Å	3.024 Å				

$^{\dagger}\ldots$ sampled from fig. 1

Table 4.2: Comparison of selected structural parameters of the oxygen vacancy defect in our calculations with values from the literature.
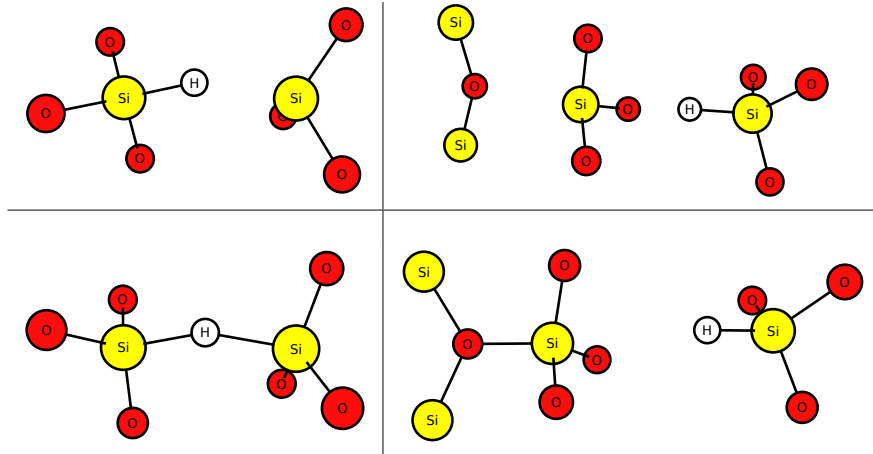
Figure 4.7: Structures of the closed **(left)** and the broken **(right)** hydrogen bridge as obtained from our DFT calculations. The neutral **(top)** as well as the positive **(bottom)** charge state are shown.

		neutral		positive	
		present work	Blöchl [59]	present work	Blöchl [59]
closed	Si-Si distance	3.351 Å	3.368 Å	3.206 Å	3.225 Å
	Si_1-H distance	1.522 Å	1.534 Å	1.641 Å	1.646 Å
	Si_2-H distance	1.985 Å	1.953 Å	1.689 Å	1.710 Å
broken	Si-Si distance	3.948 Å	4.011 Å	4.389 Å	4.394 Å
	Si_1-H distance	1.460 Å	1.460 Å	1.471 Å	1.477 Å
	Si_2-H distance	2.698 Å	2.742 Å	3.171 Å	3.088 Å

Table 4.3: Comparison of selected structural parameters of the hydrogen bridge defect in our calculations with values from the literature.

oxide of an MOS transistor arises from the growth kinetics of the oxidation process. Although the vibrational state of the atoms is in thermal equilibrium with the environment, the bonding structure is not a thermal equilibrium arrangement. Thus, the significance of the formation energies calculated here for the abundance of oxygen vacancies and hydrogen bridges in MOS oxides is limited. We calculate the formation energies here for the purpose of comparison with published work. For the calculation of the formation energies it is necessary to define a "reservoir energy" for each atomic species. The reservoir energy of the atoms is usually defined as the gas phase energy, i.e. an isolated atom calculation [66, 159]. The formation energy of the oxygen vacancy E_{fOV} and the hydrogen bridge E_{fHB} have been calculated with respect to the energies of the isolated oxygen atom E_O and the isolated hydrogen atom E_H as

$$E_{fOV} = E_{OV} - E_{\alpha Q} + E_O \tag{4.1}$$

$$E_{fHB} = E_{HB} - E_{\alpha Q} + E_O - E_H \tag{4.2}$$

where $E_{OV} - E_{\alpha Q}$ and $E_{HB} - E_{\alpha Q}$ are the optimized total energies differences between the DFT calculations with the defect and the ideal crystalline host. The formation energy for the oxygen vacancy in our calculations is $E_{fOV} = 8.468\,\text{eV}$, in agreement with earlier works [59, 159]. Considerably lower formation energies of about $4.6\,\text{eV}$ have been obtained using the embedded

cluster method [66]. This difference partially arises from the neglect of correlation in the Hartree-Fock method used for the quantum region in [66], but also comes from the larger number of relaxing atoms in the embedded cluster approach. This indicates that some strain may remain in the employed supercell and the results of this work should be compared against calculations involving larger supercells at some point. However, this check is not part of the present work. The formation energy of the hydrogen bridge defect in our calculations is $E_{fHB} = 7.802 \, \mathrm{eV}$, in agreement with [59].

4.2 Barrier Hopping Transitions

In terms of Chap. 2, the structural reorganization of the defects, i.e. the transitions $1 \rightleftharpoons 1'$ and $2 \rightleftharpoons 2'$ are barrier hopping transitions. A detailed study of these transitions requires the solution of the thermal integrals of the transition state theory, which gives the barrier hopping transition rates. However, as discussed in Sec. 2.8, one can already gain some insight by just calculating the activation energy for the process, which we consider sufficient for the evaluation of a candidate BTI defect. The calculation of the activation energy requires to find the path of minimum energy between the two potential energy surface minima that correspond to the start- and endpoint of the transition. A popular method to find the reaction path is the nudged elastic band (NEB) method [171, 172], which is also applied in the present work. In the NEB approach, configurations along the reaction path are connected via virtual spring potentials. Then the system of all configurations is optimized with respect to the total energy consisting of the energies of the individual configurations plus the spring potential.

Our NEB calculations use ten points to sample the reaction path. The path is pre-optimized using the conjugate gradient algorithm until forces are below $1 \, \mathrm{eV/\mathring{A}}$. The final optimization to reduce the forces below $0.1 \, \mathrm{eV/\mathring{A}}$ is done using the quasi-Newton algorithm. The resulting energies on the optimized reaction paths for both defects are shown in Fig. 4.8.

4.3 Macroscopic Device Simulation

The charge state transitions $1 \rightleftharpoons 2'$ and $2 \rightleftharpoons 1'$ arise from the interaction of the defect with the semiconductor device. Their theory consequently needs to encompass both the atomistic model of the defect and the macroscopic device model. The atomistic level is the main focus of this thesis and has been described extensively in this document. An in-depth discussion of the fine art of macroscopic device simulation goes beyond the scope of this document and so this topic is only discussed to the extent that is absolutely necessary for the following calculations.

The methods of semiconductor device simulation are used to model the occupation dynamics of the extended electronic states $|k\rangle$ inside a semiconductor [173]. In the ground state some of these states are occupied, and some are unoccupied. The occupied extended states $|k_v\rangle$ form the valence band of the semiconductor, the unoccupied states $|k_c\rangle$ form the conduction band. Their occupation is described by the occupation probability $f_e(k)$ as

$$f_e(k_v) = 1 \quad \text{and} \quad f_e(k_c) = 0. \tag{4.3}$$

The time evolution of the electronic system of the semiconductor is described by the time evolution of the occupancy function $f_e(k)$. On the energy scale, the valence band and the conduction band of a semiconductor are separated by an energy range that has no stationary states, which is called the band gap. In its ground state, the electronic system of the semiconductor is unable to carry electric currents. Only when an electron is removed from the valence band ($f_e(k_v) < 1$),
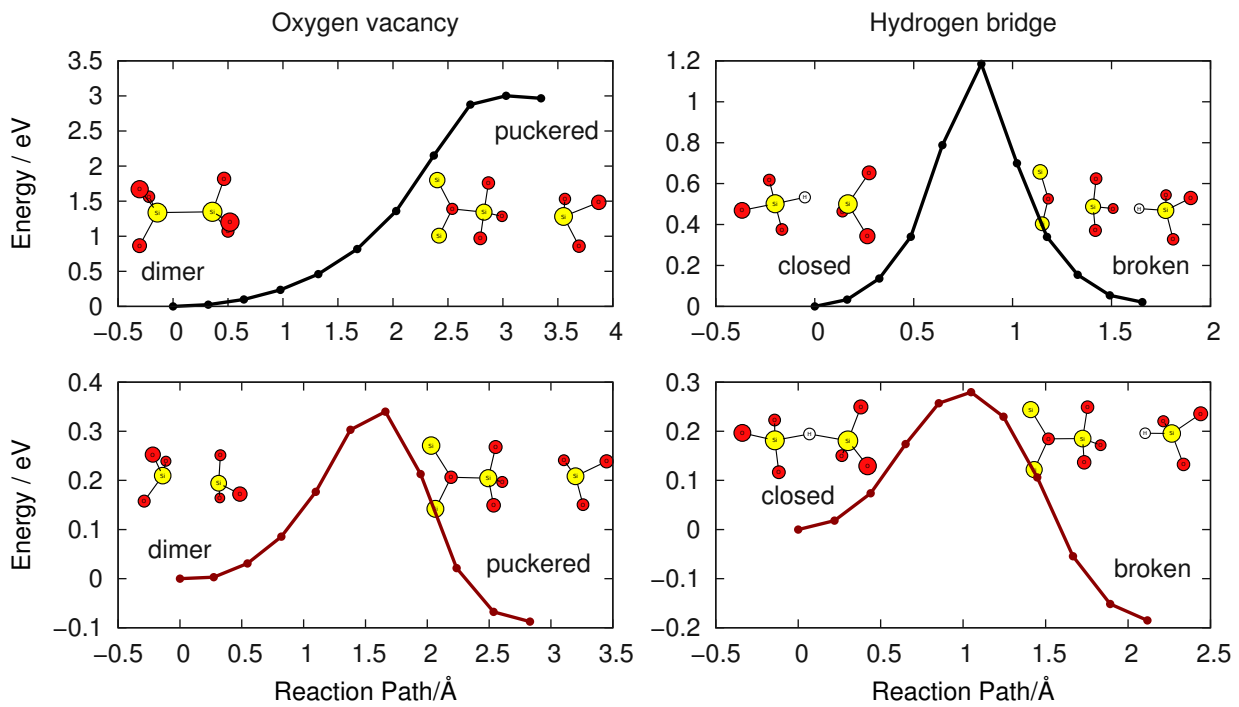
Figure 4.8: Reaction paths calculated using the nudged elastic band method for the oxygen vacancy **(left)** and the hydrogen bridge **(right)** in their neutral **(top)** and positive **(bottom)** charge state. In the positive state, the puckered configuration of the oxygen vacancy is slightly more stable than the dimer configuration. In the neutral state, the situation is reversed with the puckered configuration of the oxygen vacancy being almost $3\,\text{eV}$ higher in energy than the dimer configuration. The two structural configurations of the hydrogen bridge are almost isoenergetic in the neutral state. In the positive state, the broken configuration is more stable than the closed configuration.
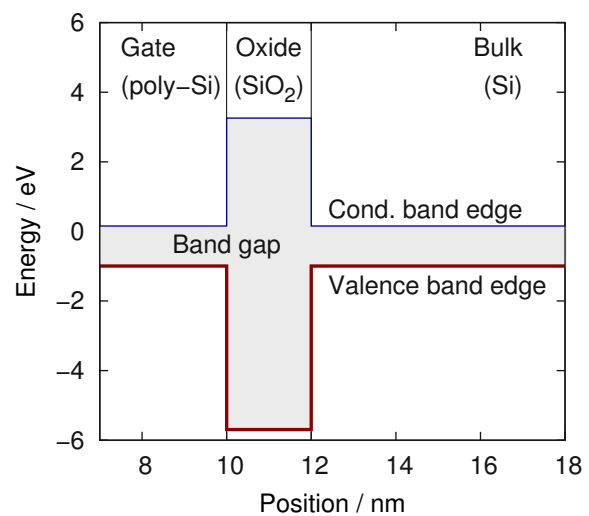
Figure 4.9: In a band diagram, the local values of the conduction and valence band edges are drawn as a function of position. At a material boundary, the band edges abruptly change giving rise to energetic barriers or wells. The shown band diagram corresponds to the situation in an MOS structure.

or added to the conduction band ($f_e(k_c) > 0$), a transport of charge becomes possible. These electronic configurations are inherently many body excitations, which include not only the non-ground-state occupancy but also the response of the electronic system to this occupancy. In the theory of semiconductors, these many body excitations are described as quasi particles [174], where additional electrons in the conduction band are called "excess electrons", or electrons for short, and the unoccupied states are called "holes", or defect electrons. For the excess electrons, the quasi particle states $\{|w_n\rangle\}$ are defined, which correspond to occupied conduction band states $|k_c\rangle$. For the holes, the quasi particle states $\{|w_p\rangle\}$ correspond to unoccupied conduction band states $|k_v\rangle$. The occupancies for the excess electron and hole states are then f_n and f_p, respectively. The physics of the states $\{|w_n\rangle\}$ and $\{|w_p\rangle\}$ is determined by the band structure. This band structure defines the total energy of each quasi particle state as a function of its crystal momentum $\vec{k}$. At material interfaces such as the semiconductor-oxide interface in MOS devices, the band structure abruptly changes, leading to energetic barriers for the carrier gas. It is common to draw the local band edges $E_{c0}(\vec{r})$ (conduction band edge) and $E_{v0}(\vec{r})$ (valence band edge) as a function of position. These graphs are called band diagrams and are a popular tool to illustrate processes in semiconductor devices, see Fig. 4.9.

In semiconductor device modeling, the materials that constitute the semiconductor device are described using their macroscopic properties, e.g. the permittivity [175]. The coulombic interactions in the device are accounted for in a mean field fashion by the potential $\Phi(\vec{r})$, which is obtained from the Poisson equation

$$\nabla^2 \Phi(\vec{r}) = -\frac{q_0}{\epsilon}\left(p(\vec{r}) - n(\vec{r}) + N_D(\vec{r}) - N_A(\vec{r})\right) \tag{4.4}$$

that accounts for the charge arising from the mean density of holes

$$p(\vec{r}) = \int\limits_{w_p} f_p(w'_p) \left|\langle\vec{r}|w'_p\rangle\right|^2 dw'_p, \tag{4.5}$$

the mean density of electrons

$$n(\vec{r}) = \int\limits_{w_n} f_n(w'_n) \left|\langle\vec{r}|w'_n\rangle\right|^2 dw'_n, \tag{4.6}$$

and the ionized dopants $N_D(\vec{r})$ and $N_A(\vec{r})$ [175]. This potential contributes to the energy of the particles, which can be accounted for in the band diagram by replacing the band energies by

$$E_c(\vec{r}) = E_{c0}(\vec{r}) - q_0\Phi(\vec{r}) \quad \text{and} \quad E_v(\vec{r}) = E_{v0}(\vec{r}) - q_0\Phi(\vec{r}). \tag{4.7}$$

The dependence of the local band structure on the electric potential is usually termed "band bending". The band bending as obtained from a device simulation is shown in Fig. 4.10

The quasi particle states $|w_n\rangle$ and $|w_p\rangle$ as well as their occupancies are determined by the carrier model. Depending on the complexity of the device structure, the dynamics of the excess electrons and holes can be described at different levels of physical accuracy. The most common carrier models, which are also employed in state-of-the-art TCAD simulators, are based on semi-classical electrons and holes. These semi-classical particles are pictured as wave packets of Bloch wave functions moving on classical trajectories determined by the local band structure. The time evolution of the carriers is described using the Boltzmann transport equation [176] in various approximations [177, 178]. The state of the carrier gas in this description is fully characterized by the distribution $f_n(\vec{r}, \vec{k})$ of the electrons and the distribution $f_p(\vec{r}, \vec{k})$ of the
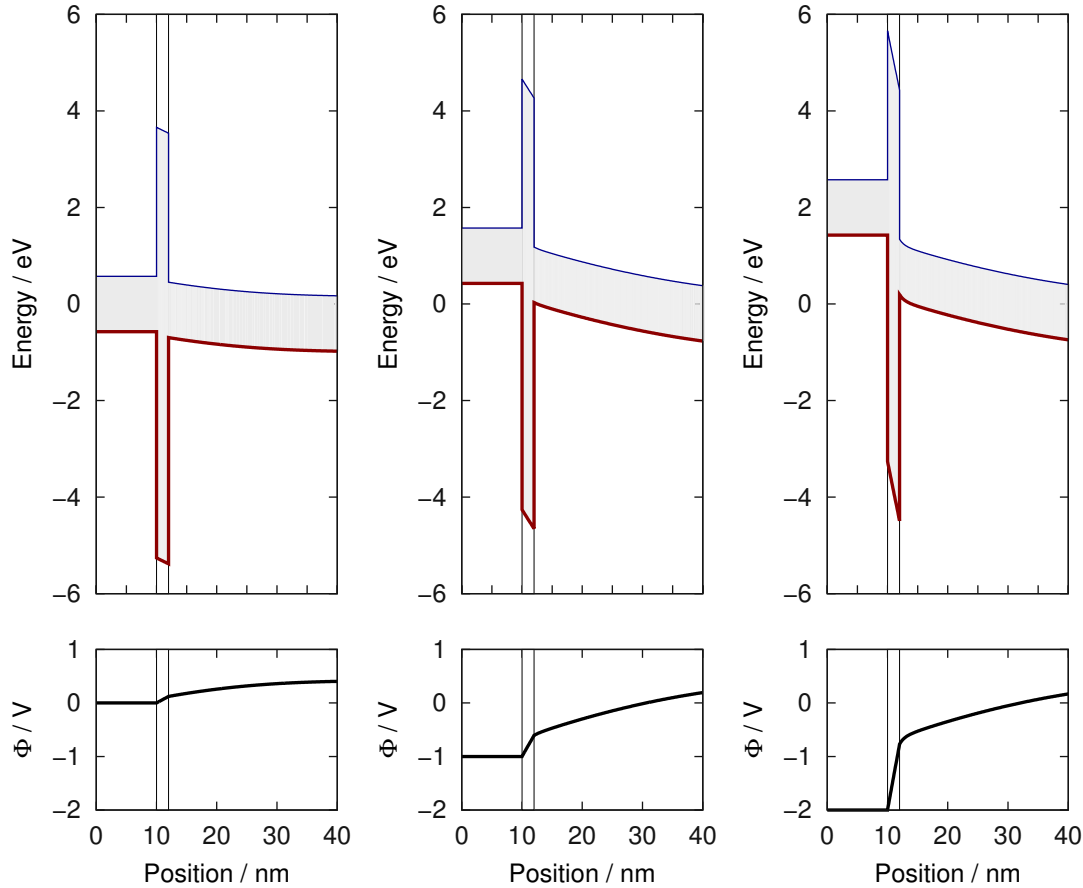
Figure 4.10: The mean potential $\Phi(\vec{r})$, which models the coulomb interactions within the semi-conductor device, can be described as a bending of the band structure. The band bending as obtained from device simulation is shown for three different gate voltages (from left to right $0\,\mathrm{V}$, $-1\,\mathrm{V}$, $-2\,\mathrm{V}$). The bending at zero gate voltage arises from the work function difference between the gate and the substrate.

holes in the phase space $(\vec{r}, \vec{k})$. The current transport in most semiconductor devices can be described very accurately using classical carrier models. For our purposes, however, their applicability is somewhat limited by the inherent neglect of quantum mechanical effects such as the quantization in the inversion channel and the penetration of carriers into the oxide through tunneling. While this quantization has only little effect on the prediction of transport properties, it has a profound effect on the energetics of the carrier system, which strongly influences the carrier trapping, as will be discussed in the next section.

Quantum mechanical carrier models can be loosely categorized into closed and open boundary models. In the former, the Schrödinger equation for the $\{|w_n\rangle\}$ and $\{|w_p\rangle\}$ is solved with Dirichlet boundary conditions. The occupancies of the excess electron and hole states are derived from thermal equilibrium. As before, the carrier model has to be solved self-consistently with the Poisson equation [179], hence these carrier models are sometimes called Schrödinger-Poisson models. Due to the assumed equilibrium occupancy of the particle states these models give good results for non-conducting situations. In bias temperature stress experiments, apart from the switches between stress and recovery voltage, the only currents flowing are the gate

current and the monitoring drain current. As these currents have negligible impact on the states and their occupancies the carriers are typically in thermal equilibrium with the contacts, so a closed boundary description is justified in principle. Schrödinger-Poisson models have been employed in calculations of defect-device interactions to model the quantization in the inversion region of the MOS structure and the penetration of the quasi particle states into the oxide [180–182]. The boundary conditions of the closed boundary quantum mechanical carrier models are of special importance for the calculation of carrier trapping at defects in MOS oxides. As is more deeply discussed below, carrier trapping depends on the ability of the carriers to penetrate into the oxide via quantum mechanical tunneling. The boundaries in Schrödinger-Poisson calculations have to be placed either at the oxide-gate or the oxide-substrate interface and thus potentially influence the tunneling behavior of the carriers and consequently the predicted trapping rates.

Open boundary quantum mechanical carrier models are the most accurate description of the carriers in the device. These models treat the device essentially as a scattering problem. The most popular open boundary transport models are based on the framework of non-equilibrium Green's functions (NEGF) [176]. The biggest advantage of open boundary over closed boundary models is the absence of artificial boundaries inside the device.

Independent of the physical details of the carrier model, the quantities in a semiconductor device simulation are the average potential $\Phi(\vec{r})$, the excess electron and hole states $\{|w_n\rangle\}$ and $\{|w_p\rangle\}$ as well as their occupancies $f_n(w_n)$ and $f_p(w_p)$. As for many applications the most interesting property of an electronic state is its energy, the excess electron and hole states are usually replaced by the corresponding densities of states [176]

$$D_n(x, E) = \int_{w_n} \left|\langle \vec{r}|w_n'\rangle\right|^2 \delta(E - E_{w_n'}) dw_n' \tag{4.8}$$

$$D_p(x, E) = \int_{w_p} \left|\langle \vec{r}|w_p'\rangle\right|^2 \delta(E - E_{w_p'}) dw_n' \tag{4.9}$$

and the corresponding occupation densities $f_n(\vec{r}, E)$ and $f_p(\vec{r}, E)$. These quantities are also of central importance for the calculations of the following section.

4.4 Non-Radiative Transitions in the Device-Defect System

For the calculation of non-radiative transitions between the defect and the device we start from the considerations in Sec. 2.9.2, where the general theory of NMP transitions has been laid out. The transition rates are calculated using (2.102), which requires the determination of the electronic matrix element and the line shape function, where the latter can either be described in the quantum mechanical (2.94) or the classical form (2.109). To describe the phonon mediated capture and emission of electrons and holes, it is necessary to specify the initial electronic state $|i\rangle$ and the final electronic state $|f\rangle$ for the device-defect system. The electronic structure of this system is essentially a quantum mechanical many body problem, which we will formulate upon a basis of single particle states. In the following, $|d\rangle$ is the localized orbit at the defect site, and $|k\rangle$ are the electron states in the semiconductor device, which act as a reservoir for the transition. The defect state as well as the reservoir states can be either unoccupied or occupied by an electron.

The mathematical framework for this is the second quantization formalism [183]. In the following, the creation operators $\hat{c}^\dagger$, the destruction operators $\hat{c}$, and the number operators

$\hat{n} = \hat{c}^\dagger \hat{c}$ are used[1].

In accord with the derivations in Sec. 2.9.2, the electronic basis states for the vibronic transition are Born-Oppenheimer states, which are mixed by the effective non-adiabacity operator $\hat{L}'$. The adiabatic Hamiltonian of the system $\hat{H}$ consists of the Hamiltonian of the defect $\hat{H}_\mathrm{d}$ and of the device $\hat{H}_\mathrm{D}$

$$\hat{H}(\vec{R}) = \hat{H}_\mathrm{D} + \hat{H}_\mathrm{d}(\vec{R}). \tag{4.10}$$

The energy of the device is determined by the occupancy of the free states $|k\rangle$ in the valence band and the conduction band. The energy E_k of these states comes from the employed carrier model and can be understood as a functional of the mean field of the carrier gas, yielding

$$\hat{H}_\mathrm{D} = \sum_k E_k[\Phi(\vec{r})]\hat{n}_k. \tag{4.11}$$

The energy contribution from the electronic structure of the defect is the potential energy surface that we obtain from our atomistic model. In the neutral (occupied) state, the potential energy surface of the defect is $E_\mathrm{d}^0(\vec{R})$ and in the positive (unoccupied) state it is $E_\mathrm{d}^+(\vec{R})$. In addition, we have to consider the interaction of the defect with the mean potential $\Phi(\vec{r})$. As we approximate the defect as a point charge at the position $\vec{r}_\mathrm{d}$, this interaction is just $q_0\Phi(\vec{r}_\mathrm{d})$ in the positive state and zero in the neutral state. The resulting defect Hamiltonian reads

$$\hat{H}_\mathrm{d} = E_\mathrm{d}^+(\vec{R}) + \left(E_\mathrm{d}^0(\vec{R}) - E_\mathrm{d}^+(\vec{R})\right)\hat{n}_\mathrm{d} + q_0\Phi(\vec{r}_\mathrm{d})(1 - \hat{n}_\mathrm{d}). \tag{4.12}$$

The effective non-adiabacity operator mixes the electronic states. In the device-defect system, it annihilates an electron in a reservoir state and creates an electron at the defect state. The corresponding single electron operators are denoted by $\hat{L}''$. The non-adiabacity operator thus reads

$$\hat{L}' = \sum_k \langle \mathrm{d}|\hat{L}''|k\rangle \hat{c}_\mathrm{d}^\dagger \hat{c}_k + \langle k|\hat{L}''|\mathrm{d}\rangle \hat{c}_k^\dagger \hat{c}_\mathrm{d}. \tag{4.13}$$

Now that all the operators are defined, one can calculate the rates for the capture and emission of electrons from the reservoir. At first we consider the capture transition from a reservoir state $|k'\rangle$, which corresponds to the removal of an excess electron from the conduction band or emission of a hole into the valence band of the device. Initially, $|\mathrm{d}\rangle$ is unoccupied, $|k'\rangle$ is occupied, and the occupancy of the other reservoir states is given by f_k. In the second quantization formalism, the wave functions are constructed by applying the creation operators to the vacuum state $|\varnothing\rangle$. The electronic system changes from the initial state

$$|\mathrm{i}\rangle = (\hat{c}_{k'}^\dagger + \sum_{k \neq k'} f_k \hat{c}_k^\dagger)|\varnothing\rangle \tag{4.14}$$

to a state

$$|\mathrm{f}\rangle = (\hat{c}_\mathrm{d}^\dagger + \sum_{k \neq k'} f_k \hat{c}_k^\dagger)|\varnothing\rangle. \tag{4.15}$$

The energies of the initial and final state read

$$E_\mathrm{i}(\vec{R}) = \langle \mathrm{i}|\hat{H}|\mathrm{i}\rangle = \sum_{k \neq k'} f_k E_k[\Phi] + E_\mathrm{d}^+(\vec{R}) + E_{k'}[\Phi] + q_0\Phi(\vec{r}_\mathrm{d}) \tag{4.16}$$

---

[1]As we do not consider direct interactions between the particles, the second quantization formalism is used here only as a bookkeeping method for the energies and matrix elements of the electronic part of the problem.

Figure 4.11: The energy of the reservoir state from which the electron is captured as well as the mean potential in the device simulation contribute to the energetic shift between the potential energy surface of the initial and the final state. Thus, every reservoir state has a different configuration of the potential energy surfaces as indicated by the different red curves. Additionally, a change in the mean potential from the device also leads to an energetic shift, which is indicated as the blue dashed curve.
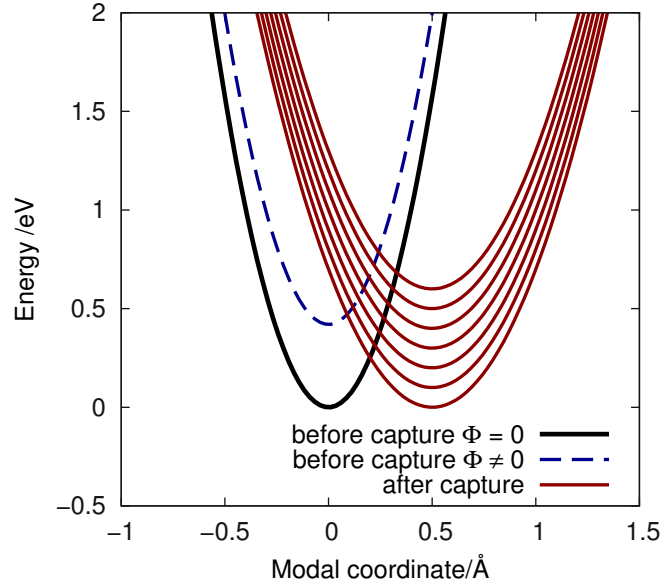
and

$$E_{\mathrm{f}}(\vec{R}) = \langle \mathrm{f}|\hat{H}|\mathrm{f}\rangle = \sum_{k \neq k'} f_k E_k[\Phi] + E_{\mathrm{d}}^0(\vec{R}), \tag{4.17}$$

respectively. Interestingly, the energy of the captured particle as well as the mean potential at the defect enter as an energetic shift between the potential energy surfaces before and after the capture transition. Thus, for every reservoir state, a different configuration of the potentials is obtained leading to a different NMP transition rate, see Fig. 4.11. The dependence of the energy shift on the mean potential is responsible for the large bias dependence of the BTI defect [32, 85] as mentioned briefly in Sec. 1.5. The dependence of the energetic shift between the potential energy surfaces on the potential is a general feature of NMP transitions that is also present at defects within semiconductors [144, 184]. However, for defects in the oxide this effect dominates the field dependence of the transition as the oxide due to the large tunneling distance between the free state and the defect. The shift induced by the oxide field in the limit of a nearly uncharged oxide can be estimated by a simple model [185]. In this case, the potential grows or falls linearly with the distance d from the substrate-oxide interface and with the field F. Neglecting the dependence of the free states E_k on the potential, the shift induced by the oxide field is just $q_0 dF$. This estimate is of course only accurate to first-order. When considering real devices, the potential at the defect site and the dependence of the E_k on the potential have to be taken from a self-consistent calculation.

The capture rate is now calculated from (2.102) as

$$W_{k' \to \mathrm{d}} = \frac{2\pi}{\hbar} \left| \langle \mathrm{f}|\hat{L}'|\mathrm{i}\rangle \right|^2 f, \tag{4.18}$$

with

$$\left| \langle \mathrm{f}|\hat{L}'|\mathrm{i}\rangle \right|^2 = \left| \langle \mathrm{d}|\hat{L}''|k'\rangle \right|^2. \tag{4.19}$$

As mentioned in Sec. 2.9.5, $\hat{L}''$ is not accurately known, and so this term has to be estimated. Different approaches for the estimation of the matrix element exist in the literature, ranging from simple tunneling expressions to model defect wave functions [26, 144, 180]. Due to the

large extent of the free states of the reservoir compared to the extent of the localized state, we approximate the electronic matrix element as [186]

$$\frac{2\pi}{\hbar}\left|\langle \mathrm{d}|\hat{L}''|k'\rangle\right|^2 \approx \lambda \left|\langle \vec{r}_\mathrm{d}|k'\rangle\right|^2, \tag{4.20}$$

where λ is a parameter that needs to be calibrated to experimental data. In essence, this compresses the electronic state of the defect into a Dirac peak and reduces the electronic matrix element to a tunneling expression, which is assumed to be a reasonable approximation. The use of a more natural wave function as is sometimes employed in the literature enables the modeling of crystal momentum dependent coupling to the free states, which is not considered at the moment.

The quantum mechanical line shape is defined as (2.94)

$$f(h\nu) = \operatorname*{avg}_{I} \sum_{F} \left|\langle\!\langle \mathrm{f}F|\mathrm{i}I\rangle\!\rangle\right|^2 \delta(E_{\mathrm{f}F} - E_{\mathrm{i}I} - h\nu) \tag{4.21}$$

The energies $E_{\mathrm{f}F}$ and $E_{\mathrm{i}I}$ are obtained from the solutions of the vibrational Schrödinger equation using the electronic energies $E_\mathrm{f}(\vec{R})$ and $E_\mathrm{i}(\vec{R})$ as potentials,

$$(\hat{T}_\mathrm{N} + \sum_{k \neq k'} f_k E_k[\Phi] + E_\mathrm{d}^+(\vec{R}) + E_{k'}[\Phi] + q_0\Phi(\vec{r}_\mathrm{d}))\big|\mathrm{i}I\big\rangle\!\big\rangle = E_{\mathrm{i}I}\big|\mathrm{i}I\big\rangle\!\big\rangle, \tag{4.22}$$

$$(\hat{T}_\mathrm{N} + \sum_{k \neq k'} f_k E_k[\Phi] + E_\mathrm{d}^0(\vec{R}))\big|\mathrm{f}F\big\rangle\!\big\rangle = E_{\mathrm{f}F}\big|\mathrm{f}F\big\rangle\!\big\rangle. \tag{4.23}$$

In these potentials, the device level quantities only enter as a constant shift of the energies. This shift has no influence on the eigenvectors $\big|\mathrm{i}I\big\rangle\!\big\rangle$ and $\big|\mathrm{f}F\big\rangle\!\big\rangle$, and trivially adds to the eigenvalues. We can thus define the eigensystems

$$(\hat{T}_\mathrm{N} + E_\mathrm{d}^+(\vec{R}))\big|{+}I\big\rangle\!\big\rangle = E_{+I}\big|{+}I\big\rangle\!\big\rangle \tag{4.24}$$

and

$$(\hat{T}_\mathrm{N} + E_\mathrm{d}^0(\vec{R}))\big|0I\big\rangle\!\big\rangle = E_{0I}\big|0I\big\rangle\!\big\rangle, \tag{4.25}$$

which only depend on the quantities of the atomistic model. For electron capture $E_{\mathrm{i}I}$ and $E_{\mathrm{f}F}$ can then be written as

$$E_{\mathrm{i}I} = E_{+I} + \sum_{k \neq k'} f_k E_k[\Phi] + E_{k'}[\Phi] + q_0\Phi(\vec{r}_\mathrm{d}) \tag{4.26}$$

$$E_{\mathrm{f}F} = E_{0F} + \sum_{k \neq k'} f_k E_k[\Phi], \tag{4.27}$$

and the vibrational wave functions are

$$\big|\mathrm{i}I\big\rangle\!\big\rangle = \big|{+}I\big\rangle\!\big\rangle \text{ and } \big|\mathrm{f}F\big\rangle\!\big\rangle = \big|0F\big\rangle\!\big\rangle. \tag{4.28}$$

Inserting these expressions into (4.21) gives

$$f = f^{(+/0)}(E_{k'}[\Phi] + q_0\Phi(\vec{r}_\mathrm{d})), \tag{4.29}$$

with

$$f^{(+/0)}(E) = \operatorname*{avg}_{I} \sum_{F} \left|\langle\!\langle 0F|{+}I\rangle\!\rangle\right|^2 \delta(E_{0F} - E_{+I} - E). \tag{4.30}$$

Figure 4.12: The line shape is referenced to the local band edges. The figure shows the position of a line shape (yellow) relative to the valence band edge (red) and the conduction band edge (blue). Different gate bias voltages lead to different band bendings and different positions of the capture line shape relative to the free quasi-particle states. In the example, the negative bias shifts the line shape maximum closer to the states near the silicon valence band edge, which is the typical NBTI situation.
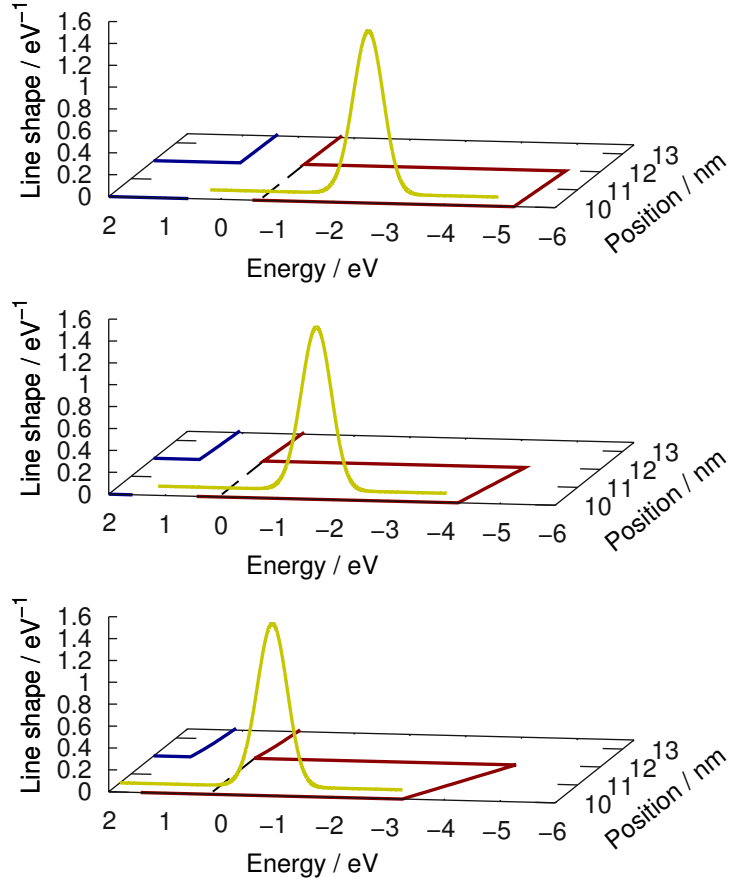
The line shape as a function of energy is determined by the Frank-Condon factors $\langle\langle 0F|+I\rangle\rangle$ as well as $E_{0F} - E_{+I}$. All those quantities are local to the defect and can be extracted from the selected electronic structure method, as shown in Sec. 4.6. The energy conservation expression provides that the energy of the captured particle is counterbalanced by an equivalent increase or decrease of the vibrational energy. The energy of the captured or emitted carrier in non-radiative transitions thus plays the same role as the optical energy in (2.94). For the use of the line shape in a device simulation, it is favorable to reference the energy scale of (4.30) to the carrier energy scale present in the macroscopic device model. We choose the local valence band edge $E_{\mathrm{v}0}(\vec{r}_{\mathrm{d}})$ of the host material of the defect, which is SiO_2 in our case, for this purpose

$$f_{\mathrm{v}}^{(+/0)}(E) = \underset{I}{\mathrm{avg}} \sum_{F} \left| \langle\langle 0F|+I\rangle\rangle \right|^2 \delta(E_{0F} - E_{+I} - E_{\mathrm{v}0}(\vec{r}_{\mathrm{d}}) - E). \tag{4.31}$$

In this case (4.29) becomes

$$f = f_{\mathrm{v}}^{(+/0)}(E_{k'}[\Phi] - E_{\mathrm{v}0}(\vec{r}_{\mathrm{d}}) + q_0\Phi(\vec{r}_{\mathrm{d}})) = f'(E_{k'}[\Phi] - E_{\mathrm{v}}(\vec{r}_{\mathrm{d}})), \tag{4.32}$$

where $E_{\mathrm{v}}(\vec{r}_{\mathrm{d}})$ accounts for the band bending as described above. In essence this means that the line shape follows its local energetic environment and can be referenced to the local band edges at the defect site, as illustrated in Fig. 4.12.

An analogous derivation can be done for the emission of an electron. In this case the elec-

tronic states are

$$|\mathrm{i}\rangle = (\hat{c}_{\mathrm{d}}^\dagger + \sum_{k \neq k'} f_k \hat{c}_k^\dagger)|\varnothing\rangle \tag{4.33}$$

$$|\mathrm{f}\rangle = (\hat{c}_{k'}^\dagger + \sum_{k \neq k'} f_k \hat{c}_k^\dagger)|\varnothing\rangle. \tag{4.34}$$

The relations of the initial and final energies and vibrational wave functions to the defect eigensystem become

$$E_{\mathrm{i}I} = E_{0I} + \sum_{k \neq k'} f_k E_k[\Phi] \text{ and} \tag{4.35}$$

$$E_{\mathrm{f}F} = E_{+F} + \sum_{k \neq k'} f_k E_k[\Phi] + E_{k'}[\Phi] + q_0 \Phi(\vec{r}_{\mathrm{d}}), \tag{4.36}$$

and

$$\big|\mathrm{i}I\big\rangle\!\big\rangle = \big|0I\big\rangle\!\big\rangle \text{ and } \big|\mathrm{f}F\big\rangle\!\big\rangle = \big|+F\big\rangle\!\big\rangle. \tag{4.37}$$

The resulting expressions for the electron trapping and detrapping rates with respect to a state k' are

$$W_{k' \to \mathrm{d}} = \lambda \left|\langle \vec{r}_{\mathrm{d}}|k'\rangle\right|^2 f_{\mathrm{v}}^{(+/0)}(E_{k'}[\Phi] - E_{\mathrm{v}}(\vec{r}_{\mathrm{d}})), \tag{4.38}$$

$$W_{\mathrm{d} \to k'} = \lambda \left|\langle \vec{r}_{\mathrm{d}}|k'\rangle\right|^2 f_{\mathrm{v}}^{(0/+)}(E_{k'}[\Phi] - E_{\mathrm{v}}(\vec{r}_{\mathrm{d}})), \tag{4.39}$$

with

$$f_{\mathrm{v}}^{(0/+)} = \underset{I}{\mathrm{avg}} \sum_F \left|\big\langle\!\big\langle +F|0I\big\rangle\!\big\rangle\right|^2 \delta(E_{0I} - E_{+F} - E_{\mathrm{v}0}(\vec{r}_{\mathrm{d}}) - E). \tag{4.40}$$

The prerequisite for an electron capture from the state k' is that this state is occupied. On the other hand The prerequisite for electron emission into a state k' is that this state is empty. In a semiconductor device at finite temperature, the occupancy of the quasi-particle states fluctuates randomly due to the motion of the particles and the various scattering processes. Therefore, for a real device one has to consider the probability $f_{\mathrm{e}}(k')$ of k' being occupied for electron capture and the probability $1 - f_{\mathrm{e}}(k')$ of k' being unoccupied for emission. Following the explanations of the previous section, these probabilities, along with the probability $\left|\langle \vec{r}|k'\rangle\right|^2$ to find the extended state k' at the defect site, is obtained from the device simulation. The rates for the capture and emission of holes and electrons are then given as

$$k_{n \to \mathrm{d}} = \lambda \int_{-\infty}^{\infty} n(\vec{r}_{\mathrm{d}}, E) f_{\mathrm{v}}^{(+/0)}(E - E_{\mathrm{v}}(\vec{r}_{\mathrm{d}})) dE, \tag{4.41}$$

$$k_{p \to \mathrm{d}} = \lambda \int_{-\infty}^{\infty} p(\vec{r}_{\mathrm{d}}, E) f_{\mathrm{v}}^{(0/+)}(E - E_{\mathrm{v}}(\vec{r}_{\mathrm{d}})) dE, \tag{4.42}$$

$$k_{\mathrm{d} \to n} = \lambda \int_{-\infty}^{\infty} (D_n(\vec{r}_{\mathrm{d}}, E) - n(\vec{r}_{\mathrm{d}}, E)) f_{\mathrm{v}}^{(0/+)}(E - E_{\mathrm{v}}(\vec{r}_{\mathrm{d}})) dE, \tag{4.43}$$

$$k_{\mathrm{d} \to p} = \lambda \int_{-\infty}^{\infty} (D_p(\vec{r}_{\mathrm{d}}, E) - p(\vec{r}_{\mathrm{d}}, E)) f_{\mathrm{v}}^{(+/0)}(E - E_{\mathrm{v}}(\vec{r}_{\mathrm{d}})) dE, \tag{4.44}$$

where the particle densities relate to the density of states as

$$n(\vec{r}, E) = f_n(\vec{r}, E) D_n(\vec{r}, E) \quad \text{and} \quad p(\vec{r}, E) = f_p(\vec{r}, E) D_p(\vec{r}, E). \tag{4.45}$$

Our approach to the calculation of NMP capture or emission rates using both a macroscopic model of the device and an atomic electronic structure model of the defect thus contains the following steps:

1. Calculation of the line shape functions $f^{(+/0)}$ and $f^{(0/+)}$ from the atomistic model.

2. Calculation of $E_{\mathrm{v}}(\vec{r})$, $n(\vec{r}, E)$, $D_n(\vec{r}, E)$, $p(\vec{r}, E)$, and $D_p(\vec{r}, E)$ form the macroscopic device model.

3. Combining the two using the expressions above.

4.5 Energy Levels

Before we can calculate the line shapes (4.67) and (4.68), it is necessary to establish a relation between the potential energy surfaces of the atomistic model and the energy scale of the device model. This is related to the task of energy level calculation from an electronic structure method. As it turns out, there are several ways to define an energy level for a given atomistic defect model, which can be a magnificent source of confusion for the communication between theorists working on atomistic modeling and those working on device modeling. Therefore, we make an attempt here to clarify the relations of the defect levels usually given in publications to each other and to our NMP-transition based approach.

The most commonly published type of energy level calculated from atomistic defect models is the **thermodynamic trap level**. It is also known as thermodynamic transition level in solid state theory and is equivalent to the electron affinity (for reduction) and the ionization potential (for oxidation) in theoretical chemistry [99]. The thermodynamic transition level is an equilibrium property of a defect and comes from viewing the point defect as a thermodynamic system coupled to a reservoir of electrons with a chemical potential μ_{e}. Neglecting the effects of pressure and entropy and identifying the thermodynamic internal energy with the Born-Oppenheimer energy $E_{\mathrm{d}}^q(\vec{R}_q^0)$ at the optimum configuration of the defect $\vec{R}_q^0$ for the charge state q of the system[2], one can define the formation energy [102]

$$E_{\mathrm{d}}^q(\mu_{\mathrm{e}}) = E^q(\vec{R}_q^0) + \mu_{\mathrm{e}} q. \tag{4.46}$$

This formation energy accounts for the average work necessary to exchange an electron with the reservoir. At a certain μ_{e}, the charge state with the lowest E_{d}^q is the dominant charge state in thermal equilibrium. As can be seen from (4.46), the charge state formation energy depends linearly on the electronic chemical potential and different charge states have a different slope q and a different shift. The situation for a hypothetical defect is illustrated in Fig. 4.13. For different intervals of the chemical potential a different charge state has the lowest formation energy, i.e. it dominates in thermal equilibrium. The crossing points of the formation energy lines are the values of the chemical potential where the dominant charge state changes. These are the thermodynamic transition levels. The thermodynamic transition level from charge state q_1 to charge state q_2 is calculated as

$$E_{\mathrm{th}}^{q_1/q_2} = \frac{E^{q_1}(\vec{R}_{q_1}^0) - E^{q_2}(\vec{R}_{q_2}^0)}{q_2 - q_1}. \tag{4.47}$$

---

[2]We use the symbol q here to be compatible with the literature. The charge state here does not denote the excess charge of the system in units of Ampere seconds, but in integral values $\{\ldots, -2, -1, 0, +1, +2, \ldots\}$.

Figure 4.13: Charge state formation energies versus electron chemical potential for a hypothetical defect that has five charge states $++,+,0,-$, and $--$. The crossing points of the formation energy lines corresponding to different charge states are the thermodynamic transition levels.
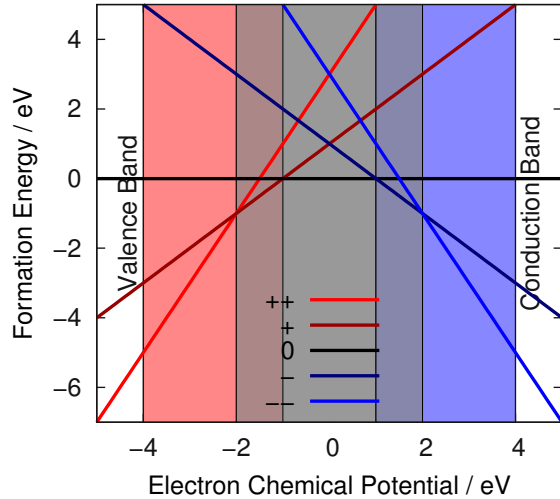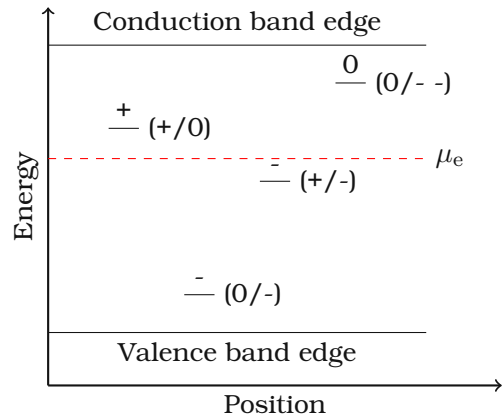

Figure 4.14: The thermodynamic transition level defines the charge state of the defect in thermal equilibrium. If the thermodynamic transition level of a defect is above the chemical potential the defect is more positive, otherwise it is more negative. Shown are different examples of possible defect states relative to a chemical potential μ_e.

In thermal equilibrium, the thermodynamic transition level determines the dominant charge state of a defect, see Fig. 4.14. In semiconductor defect modeling, the chemical potential is commonly replaced by the electronic Fermi level. For defects with vibrational internal states, as considered in the present work, different potential energy surfaces for the various charge states lead to different vibrational spectra. In this case, a change from one charge state to another leads to a difference in the vibrational entropy of the defect [187] and thus the thermodynamic transition level of the defect becomes a Gibbs free energy [188]

$$G_{\mathrm{th}}^{q_1/q_2} = \Delta E^{q_1/q_2} - \Delta S^{q_1/q_2} T. \tag{4.48}$$

The change in the vibrational entropy of the defect thus induces a temperature dependence of the transition level. As usually the entropy change between two charge states is small, the transition level calculated from (4.47) is commonly considered a reasonable approximation. In the present work, we follow the standard approach to neglect entropy for the calculation of transition levels. A special property of the thermodynamic transition levels amongst the defect levels discussed here is that they can describe transitions that involve the exchange of more than one electron with the reservoir. This behavior is found in negative-U defects as illustrated in Fig. 4.15. In SiO_2, a negative-U behavior has been found for the interstitial hydrogen atom [59], which is also of significance for the present work, as discussed below. Chadi [62] has predicted a negative-U behavior with a thermodynamically unstable positive

Figure 4.15: Illustration of a hypothetical negative-U defect. The neutral state of the defect is less stable than the charged states for all values of the chemical potential. At $\mu_e = 0\,\text{eV}$, the negative charge state becomes more stable than the positive charge state, which gives rise to a $E^{+/-}$ transition level.
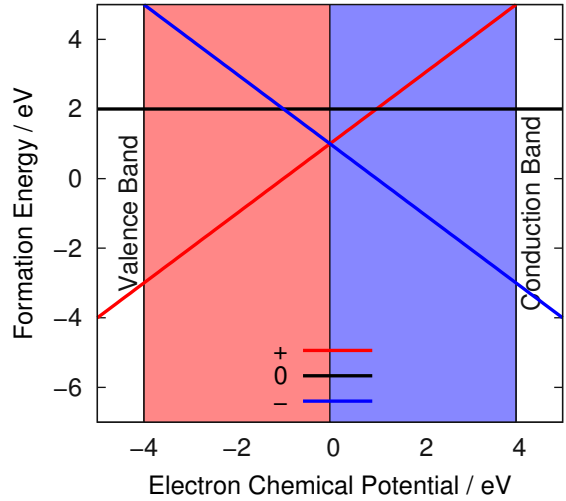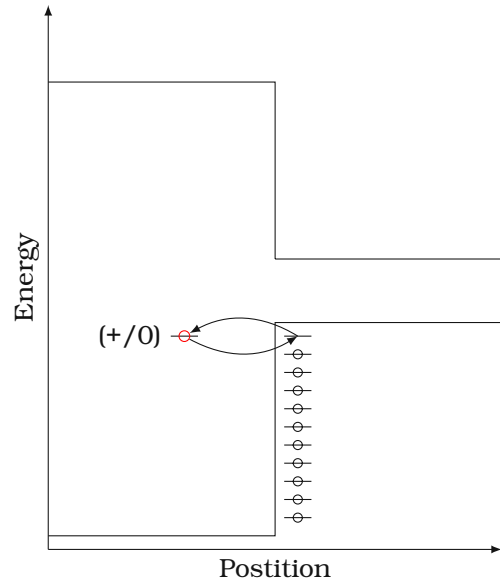

Figure 4.16: The switching trap level describes the energy balance in an elastic capture process. It can be seen as a zero temperature limit of the NMP line shape.

state for the oxygen vacancy. In BTI experiments the thermal equilibrium is only relevant for the initial condition and this equilibrium is broken by the stress. Thus, the thermal instability of the positive state of the oxygen vacancy is not part of the following considerations, as these are concerned with the non-equilibrium behavior of the defect.

In addition to the thermodynamic transition level, which describes the thermal equilibrium of the defect, a so called **switching trap level** or **optical trap level** can be defined. This trap level describes the elastic exchange of an electron between the orbit of the defect and a different state. In accord with the classical Franck-Condon principle these transitions are assumed to take place with the nuclear coordinates fixed [59, 185, 189–191]. Before the transition, the nuclear system is assumed to be in thermal equilibrium, and thus the most dominant configuration is the optimal configuration for the initial charge state. Contrary to the thermodynamic transition level, the switching trap level can only be meaningfully defined for transitions involving the exchange of exactly one electron as it refers to an elementary reaction. Again, the energy of the defect plus the target state have to be considered. However, contrary to the derivation of the thermodynamic transition level the energies here are the actual electronic Born-Oppenheimer

energies instead of thermodynamic potentials. For an elastic transition the total energy before and after the electron exchange are the same. Energy balance gives

$$E_q(\vec{R}_q) = E_{q+1}(\vec{R}_q) + E_{k'} \tag{4.49}$$

for $q/q+1$ transitions and

$$E_q(\vec{R}_q) = E_{q-1}(\vec{R}_{q-1}) - E_{k'} \tag{4.50}$$

for $q/q-1$ transitions involving a state with energy $E_{k'}$. Defining the switching trap level E^{q_1/q_2} from the condition $E_{\mathrm{sw}}^{q_1/q_2} = E_{k'}$, one obtains

$$E_{\mathrm{sw}}^{q/q+1} = E_q(\vec{R}_q) - E_{q+1}(\vec{R}_q) \tag{4.51}$$

for $q/q+1$ transitions and

$$E_{\mathrm{sw}}^{q/q-1} = E_q(\vec{R}_q) - E_{q-1}(\vec{R}_{q-1}) \tag{4.52}$$

for $q/q-1$ transitions. The switching trap level is a special case of a vibronic transition for negligible phonon energy, i.e. $T \to 0$, as can be easily seen from the considerations in Sec. 2.10. As the temperature decreases, the probability density $P(\vec{R}_q^0)$ in (2.104) for the nuclei to reside at the minimum of the potential energy surface E_{d}^q grows without bounds while integral of the probability density is normalized due to the partition function (2.105). Thus, in the zero temperature limit we find

$$\lim_{T\to 0} P(\vec{R}) = \delta(\vec{R} - \vec{R}_q^0). \tag{4.53}$$

In this case, the classical line shape function (2.109) becomes

$$f(h\nu) = \delta\left(h\nu - E_{\mathrm{f}}(\vec{R}_q^0) - E_{\mathrm{i}}(\vec{R}_q^0)\right) \tag{4.54}$$

and via the capture and emission line shapes (4.67) and (4.68), the energy conservation expressions (4.52) and (4.51) are obtained.

The relation of the discussed transition levels to the potential energy surfaces calculated from an atomistic defect model are illustrated in Fig. 4.17. Just as the line shapes, the thermodynamic and the switching levels require the definition of a reference energy in order to set them into relation with the properties of the host material. The density functional calculations in different charge states implicitly contain their own reference level for the electrons. In the calculation of isolated molecules, the removal of an electron from the calculation corresponds to taking the electron infinitely far away from the molecule [99]. Thus, in isolated molecule calculations the reference level is the vacuum level. While this referencing is reasonable for isolated molecules, in an infinite periodic lattice the vacuum level is not a well-defined quantity and it is usually favorable to select as reference energy one of the band edges or the midgap energy. All these energies, however, are absent in the atomic defect models. There are different approaches to obtain reasonable relations between the total energies of the electronic structure method and the band edges. In principle one can use the valence or conduction level from the density functional calculation [189, 192] as the reference. Unfortunately these levels come from the auxiliary system and suffer from the band gap problem. A very popular method for the alignment of the defect levels with the band edges is the so-called marker method [59, 102]. For this approach it is necessary to have a defect with a thermodynamic transition state E_{th} that is known from experiment relative to a reference level, for instance the valence band edge E_{v}

$$E^{\mathrm{exp}} = E_{\mathrm{th}} - E_{\mathrm{v}}^{\mathrm{exp}}. \tag{4.55}$$

Figure 4.17: The relation of the switching and thermodynamic defect levels to the Born-Oppenheimer potential energy surfaces of an atomic model of a point defect. It is assumed that the defect structure is neutral with N electrons.
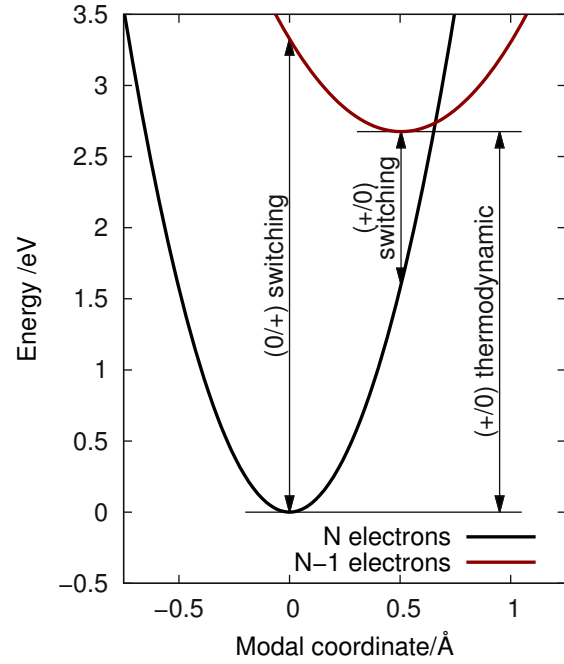
	Oxygen vacancy		Hydrogen bridge	
	Dimer	Puckered	Closed	Broken
(+/0) thermodynamic level	1.761eV	4.814eV	5.161eV	5.366eV
(0/+) switching trap level	1.109eV	3.399eV	3.980eV	3.354eV

Table 4.4: Thermodynamic and switching defect levels for the oxygen vacancy and the hydrogen bridge in both structural configurations, referenced to the SiO_2 valence level.

This defect is called the marker. The same thermodynamic transition level of the marker defect is calculated from the density functional calculation using (4.47). This level will be relative to the DFT zero level

$$E^{DFT} = E_{th} - E_0^{DFT}. \tag{4.56}$$

Assuming that the transition level was measured and calculated accurately, the experimental valence level in the DFT energy scale is then obtained by subtracting the two expressions as

$$E_v^{exp} - E_0^{DFT} = E^{DFT} - E^{exp}. \tag{4.57}$$

In our work we follow Blöchl, who uses the thermodynamic $(+/-)$ transition level of the hydrogen interstitial in SiO_2 as the marker. This level has been experimentally determined to be $0.2\,eV$ above the silicon midgap [59]. Using the Si band gap of $1.14\,eV$ and the Si-SiO_2 valence band offset of $4.4\,eV$, the SiO_2 valence level is placed $0.2\,eV + 1.14/2\,eV + 4.4\,eV = 5.17\,eV$ below the hydrogen interstitial $(+/-)$ transition level.

Tab. 4.4 shows the thermodynamic and switching defect levels in our defect calculations using Blöchl's energy scale alignment scheme. The calculated values are in agreement with results from the literature [59, 65, 190, 193].

As a final remark, it is worthwhile to discuss one further defect level that is sometimes given in the literature. This defect level is the **eigenenergy**, which results from the solution of the Schrödinger equation in the electronic structure model of the defect. For the Hartree-Fock mean
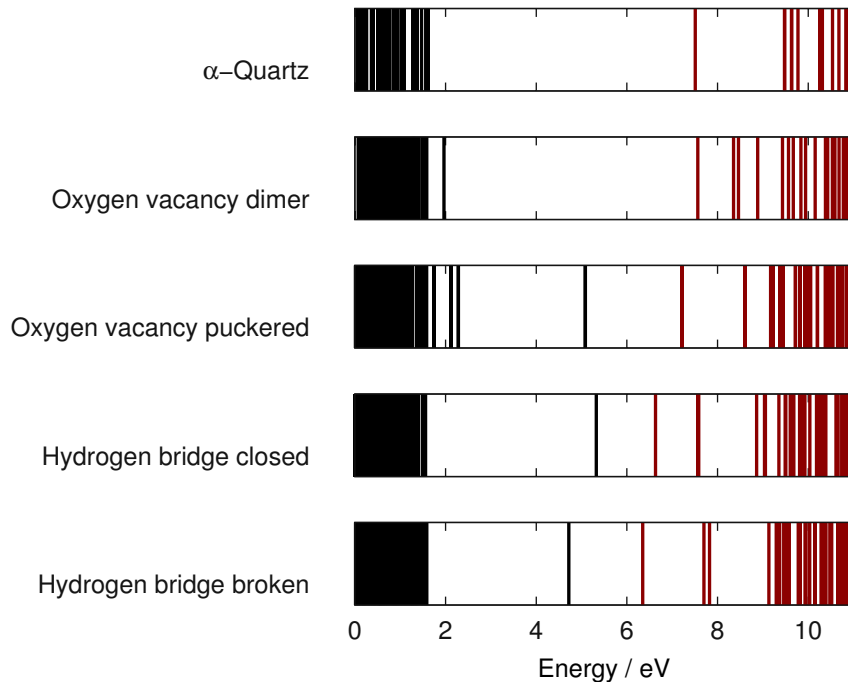
Figure 4.18: Kohn-Sham spectra as obtained from our defect calculations. Comparing the spectra of the defect cells to the spectrum of the ideal α-quartz supercell, two things can be observed. First, both occupied (black) and unoccupied (red) states are introduced into the band gap. Second, the conduction and valence level of the defective cell are perturbed.

field theory, Koopman's theorem [96] states that the orbital energies are an approximation to the change in the total electronic energy upon addition or removal of an electron to an unoccupied state or from an occupied state, respectively. The values are approximate in the sense that they do not consider orbital relaxation. Although Koopman's theorem is specific to the Hartree-Fock theory, similar theorems exist for density functional theory, so the orbital energies can be taken as an approximation to the switching levels described above. Fig. 4.18 shows the Kohn-Sham spectra for the defect structures studied in the present work. Indeed these spectra show the same trends as the calculated switching (0/+) defect levels. The Kohn-Sham eigenlevel of the oxygen vacancy in its dimer state is very close to the valence band edge, all other occupied defect levels are deep in the band gap.

4.6 Extraction of the Quantum Mechanical Line Shape Functions

Once an atomistic defect model and an energy alignment method is selected it is possible to calculate line shape functions $f_\text{v}^{(+/0)}$ and $f_\text{v}^{(0/+)}$ for NMP transitions between the charge states of the defect. In order to calculate the NMP line shape of a defect using (4.31), we need to find the vibrational wave functions $|0I\rangle\!\rangle$ and $|+J\rangle\!\rangle$ and the associated energies. As discussed in Sec. 2.9.2, for a quantum mechanical treatment of the vibronic transitions it is necessary to approximate the potential energy surfaces of the different electronic states as parabolas, see (2.85), which leads to a system of normal modes $\{Q_1, Q_2, Q_3, \ldots\}$. To extract quantum

mechanical line shapes from the density functional calculation we have to approximate the DFT potential energy surfaces $E_\mathrm{d}^0(\vec{R})$ and $E_\mathrm{d}^+(\vec{R})$ as quadratic functions. Due to the inherent anharmonicity of these potential energy surfaces, different harmonic parametrizations can be defined for the same defect, depending on which properties are to be reproduced as accurately as possible [131]. In the present work, we have chosen a parametrization that gives the same thermodynamic and switching defect levels as in the full density functional calculation [85, 86]. Additionally, we assume here that only one mode couples to the transition. While (2.102) is formulated upon an arbitrarily large set of coupling modes, the exact modal spectrum obtained from the electronic structure method will generally include some degree of mode mixing [131, 194], which requires a generalization of the theories this work is based on. The single mode approach must be considered only a first order approximation [144, 195]. However, the application of single effective modes is quite common in the literature [131, 196], and it was shown quite recently that the approximation obtained from our extraction scheme compares well to line shapes including multiple modes [194].

In the following, we denote the nuclear optimum configuration of the neutral charge state with $\vec{R}_0$ and the nuclear optimum configuration of the positive charge state with $\vec{R}_+$. Our single mode approximation defines the direction vector from $\vec{R}_0$ to $\vec{R}_+$ as mode vector of the coupling mode. Based on (2.56), we define

$$\vec{e} = \frac{\vec{R}_+ - \vec{R}_0}{|\vec{R}_+ - \vec{R}_0|}. \tag{4.58}$$

Consequently, the mass M associated with this mode is given by (2.58). For reasons of convenience, we set the modal shift of the neutral state to zero, $Q_0 = 0$, and define

$$Q_+ = Q' = |\vec{R}_+ - \vec{R}_0|. \tag{4.59}$$

The approximate potentials for the coupling mode read

$$E_\mathrm{a}^0(Q) = E_\mathrm{d}^0(\vec{R}_0) + \frac{M\omega_0^2}{2}Q^2 \;\; \text{and} \tag{4.60}$$

$$E_\mathrm{a}^+(Q) = E_\mathrm{d}^+(\vec{R}_+) + \frac{M\omega_+^2}{2}(Q - Q')^2. \tag{4.61}$$

The switching trap levels are defined by the difference between potential energies at the optimum positions. Thus, the parameters ω_0 and ω_+ are obtained from the conditions

$$E_\mathrm{a}^0(Q') = E_\mathrm{d}^0(\vec{R}_+) \text{ and } E_\mathrm{a}^+(0) = E_\mathrm{d}^+(\vec{R}_0), \tag{4.62}$$

which gives the oscillation frequencies as

$$\omega_0 = \sqrt{2\frac{E_\mathrm{d}^0(\vec{R}_+) - E_\mathrm{d}^0(\vec{R}_0)}{MQ'^2}} \;\; \text{and} \tag{4.63}$$

$$\omega_+ = \sqrt{2\frac{E_\mathrm{d}^+(\vec{R}_0) - E_\mathrm{d}^+(\vec{R}_+)}{MQ'^2}}. \tag{4.64}$$

The resulting vibrational wave functions are harmonic oscillator wave functions (2.78)

$$\big|0I\big\rangle\!\big\rangle = \big|I, M\omega_0, 0\big\rangle\!\big\rangle \text{ and } \big|+J\big\rangle\!\big\rangle = \big|J, M\omega_+, Q'\big\rangle\!\big\rangle, \tag{4.65}$$

	M/amu	ω_0/s^{-1}	ω_+/s^{-1}	$Q'/\text{Å}$
Oxygen vacancy dimer	24.662	7.018×10^{13}	$4.476 \times 10^{13}(-36\%)$	0.504
Oxygen vacancy puckered	25.644	5.974×10^{13}	$7.931 \times 10^{13}(+33\%)$	0.411
Hydrogen bridge closed	16.329	3.884×10^{13}	$4.043 \times 10^{13}(+4\%)$	0.923
Hydrogen bridge broken	17.928	2.227×10^{13}	$2.736 \times 10^{13}(+23\%)$	1.700

Table 4.5: Parameters of the extracted potential energy surfaces.

where $\left|I, \lambda, Q\right\rangle\!\rangle$ is the I-th eigenvector of the harmonic oscillator of normalized frequency λ, displaced by Q, see (2.78). The associated energies are

$$E_{0I} = \hbar\omega_0 \left(I + \frac{1}{2} \right) \text{ and } E_{+J} = \hbar\omega_+ \left(J + \frac{1}{2} \right). \tag{4.66}$$

The line shapes of the defect are now calculated by inserting (4.65) and (4.66) into (4.31) as

$$f_{\text{v}}^{(+/0)}(E) = \underset{I}{\text{avg}} \sum_F \left| \left\langle\!\left\langle F, M\omega_0, 0 | I, M\omega_+, Q' \right\rangle\!\right\rangle \right|^2$$
$$\delta\left(\hbar\omega_0(F + 1/2) - \hbar\omega_+(I + 1/2) + E_{\text{th}}^{(+/0)} - E \right), \tag{4.67}$$

$$f_{\text{v}}^{(0/+)}(E) = \underset{I}{\text{avg}} \sum_F \left| \left\langle\!\left\langle F, M\omega_+, Q' | I, M\omega_0, 0 \right\rangle\!\right\rangle \right|^2$$
$$\delta\left(\hbar\omega_0(I + 1/2) - \hbar\omega_+(F + 1/2) + E_{\text{th}}^{(+/0)} - E \right), \tag{4.68}$$

with the thermodynamic transition level

$$E_{\text{th}}^{(+/0)} = E_{\text{d}}^0(\vec{R}_0) - E_{\text{d}}^+(\vec{R}_+) - E_{\text{v}}^{\text{SiO}_2} \tag{4.69}$$

as defined in Sec. 4.5. The Franck-Condon factors $\left\langle\!\left\langle F, M\omega_0, 0 | I, M\omega_+, Q' \right\rangle\!\right\rangle$ and $\left\langle\!\left\langle F, M\omega_+, Q' | I, M\omega_0, 0 \right\rangle\!\right\rangle$ are overlaps of harmonic oscillator wave functions [127]

$$\left\langle\!\left\langle F, M\omega_0, 0 | I, M\omega_+, Q' \right\rangle\!\right\rangle = \int_{-\infty}^{\infty} h_{M\omega_0}^F(Q) h_{M\omega_+}^I(Q - Q') dQ \tag{4.70}$$

$$\left\langle\!\left\langle F, M\omega_+, Q' | I, M\omega_0, 0 \right\rangle\!\right\rangle = \int_{-\infty}^{\infty} h_{M\omega_+}^F(Q - Q') h_{M\omega_0}^I(Q) dQ. \tag{4.71}$$

Several analytic solutions for this integral can be found in the literature [197–200]. In our defect studies, we have compared several different methods. Our initial calculations employed the expressions of Zapol [198], which give a direct solution for any combination of oscillation frequencies and for any quantum numbers. However, for quantum numbers I and F larger than about 80, the factorials in the overlap expressions are numerically problematic as they lead to overflow and roundoff errors. Numerical integration of the harmonic oscillator wave functions allows the calculation of overlaps at higher quantum numbers. However for quantum numbers larger than about 120 this method suffers from the large roundoff errors in the summation. The best results were obtained using the recurrence relations published recently by Schmidt [200], which are computationally efficient and numerically stable up to very high quantum numbers [201], see Fig. 4.19.

Fig. 4.20 illustrates the approximate potential energy surfaces for our atomistic models of the oxygen vacancy and the hydrogen bridge. The parameters with respect to (4.60) and (4.61) are

Figure 4.19: Comparison of the harmonic oscillator overlaps calculated by numerical integration to the recurrence relations of Schmidt [200]. For large quantum numbers the roundoff errors in the numerical integration become dominant, while the recurrence relations are numerically stable.
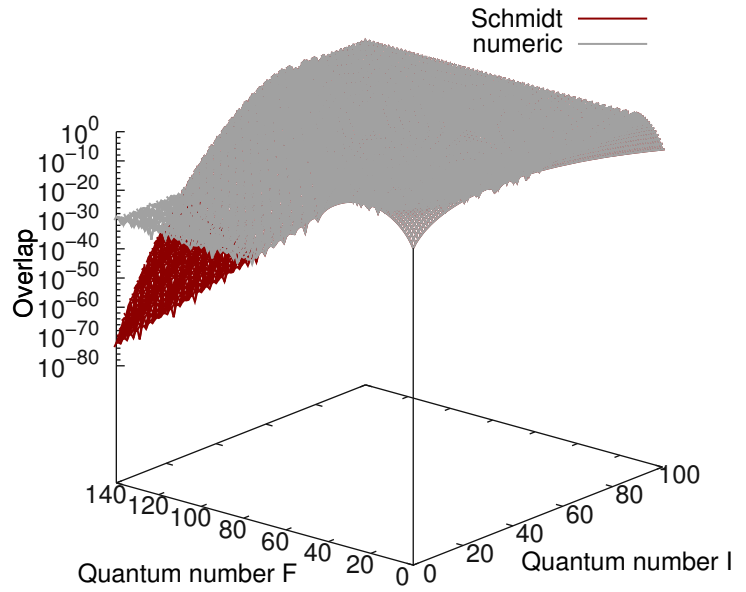
given in Tab. 4.5. As explained in Sec. 4.4, the relative energetic position of these potentials depends on the reservoir state E_k which is involved in the transition. The reservoir state for the potentials in Fig. 4.20 is the silicon valence band edge, which corresponds to the energetic situation for hole capture and emission at zero oxide field. A general feature of the extracted potentials is the difference in oscillator frequency between the neutral and the positive state. This is an important finding, as the expressions that are usually used to fit experimental data are derived assuming linear coupling modes, i.e. $\omega_i = \omega_f$ [180, 181, 202].

To check the validity of our line shape calculation method, we compare our numerically calculated line shapes to the popular formula of Huang and Rhys [127]. The Huang-Rhys line shape is derived for linear coupling, which means that the oscillation frequency before and after the transition are the same, $\omega_+ = \omega_0 = \omega$, see Sec. 2.9.2. The electron emission line shape for this case reads [117]

$$f_{\mathrm{v}}^{(0/+)}(E) = \sum_{p=-\infty}^{\infty} W_p \delta(E_{\mathrm{th}}^{(+/0)} - \hbar\omega p - E), \tag{4.72}$$

with

$$W_p = e^{-S(2\bar{n}+1)} \frac{\bar{n}+1}{\bar{n}}^{p/2} I_p(2S\sqrt{\bar{n}(\bar{n}+1)}),$$

$$\bar{n} = \frac{1}{e^{\hbar\omega/k_{\mathrm{B}}T}-1}, \qquad S = \frac{Q'M\omega}{2\hbar}.$$

Two results of this comparison are shown in Fig. 4.21 for the parameters extracted for the oxygen vacancy dimer and the closed hydrogen bridge. Due to the limitation of the Huang-Rhys formula, we have set $\omega_+ = \omega_0$ for both defects, to make a direct comparison possible. Both methods give identical results, which we take as an indication of the validity of our approach.
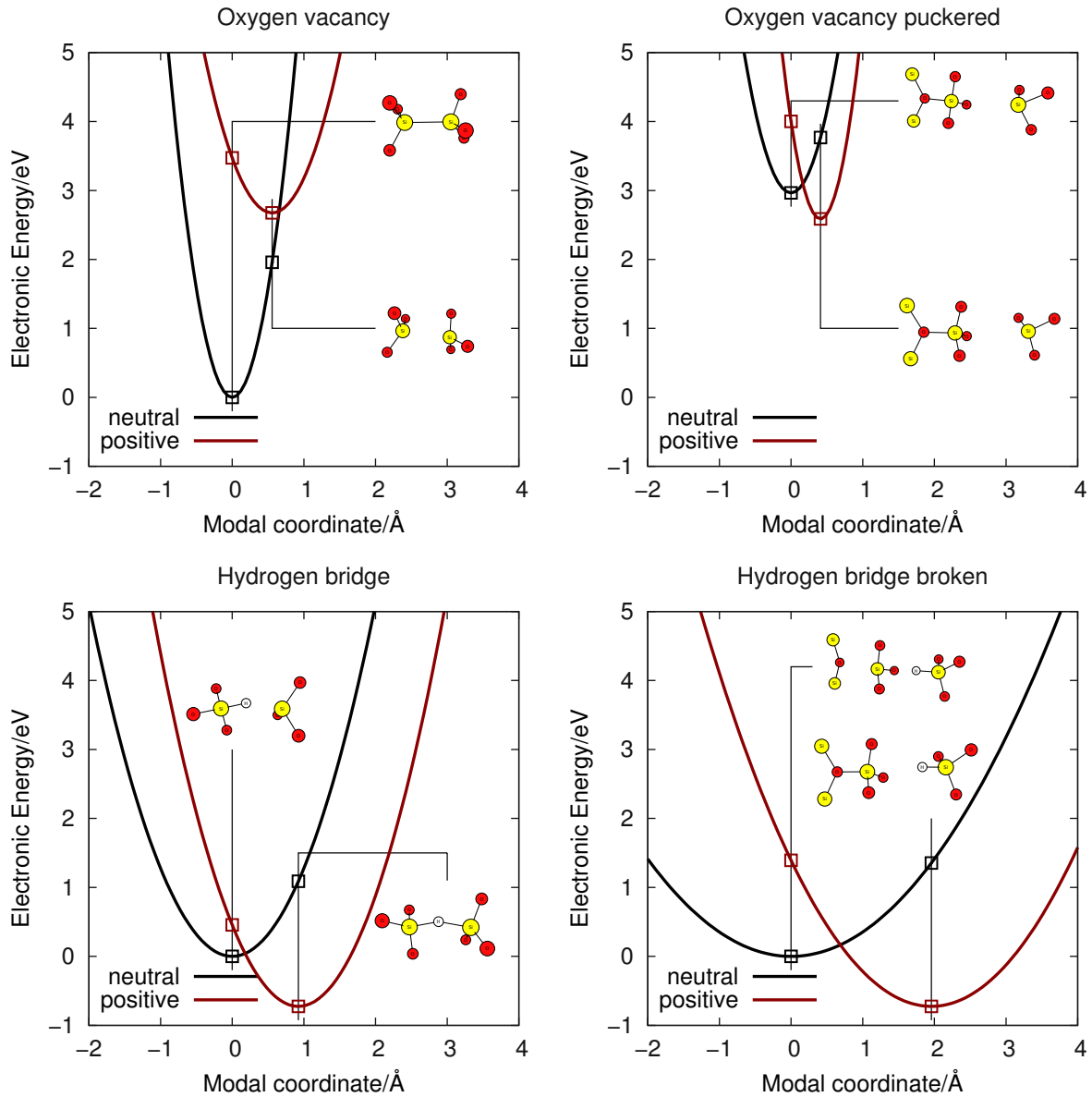
Figure 4.20: Potentials for the oxygen vacancy and the hydrogen bridge (reservoir state is the silicon valence band edge). Symbols indicate the actual DFT calculations which are used to parametrize the parabolas. All defect configurations show a shift in the oscillator frequency between the two charge states, see also Tab. 4.5.

For the calculation of the line shapes we have considered 200 neutral and 200 positive states. The line shape functions as calculated by (4.67) and (4.68) are a series of weighted Dirac impulses, see Fig. 4.22. These Dirac peaks, however, are artifacts of the time dependent perturbation theory that is used to calculate the rates. This approach assumes that at $t = 0$ the perturbation operator is "switched on" and then the system evolves freely for very long time. This clearly is not the case here, as one can expect that the time range during which the defect evolves without perturbation from the environment is rather short. For shorter times the Dirac peaks are widened [98] leading to smoother resonances. Additional spreading of the

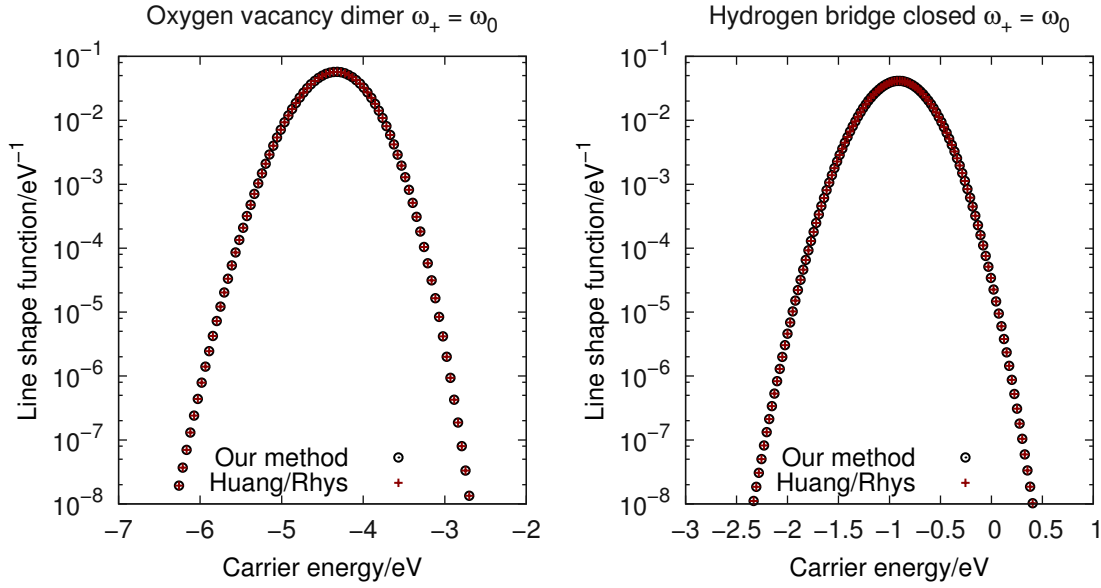**Figure 4.21:** Comparison of our line shape calculation method that is based on harmonic oscillator overlaps and the formula of Huang and Rhys (4.72). The energy scale is referenced to the silicon midgap energy. The Huang-Rhys formula is limited to linear coupling, i.e. the oscillation frequencies before and after the transition are the same. In this example we use ω_0 for both parabolas.

peaks arises from the non-orthogonality of the selected coupling mode, the neglect of other coupling modes and the neglect of the energetic contribution of the perturbation operator. Unfortunately, all these effects are impossible to model rigorously. In the literature, it is common to account for this "life time broadening" by moving from integral phonon numbers to fractional ones [117, 127]. Our results are corrected to give continuous line shapes by smearing with a normal distribution of standard deviation $k_\mathrm{B}T$, see Fig. 4.22. As long as the distributions drop sharper than the weights of the Dirac peaks, the results are not very sensitive on the smearing parameter. The application of a temperature dependent smearing parameter is also disputable, Alkauskas et al. have used a fixed smearing value of $10\mathrm{meV}$ [194]. A more rigorous description of the smearing requires experimental input, possibly from transitions at low temperatures, that is not available at the moment.

The line shape functions for all transitions are shown in Fig. 4.23, which shows that stronger bonds in the initial state lead to sharper line shape peaks. The bond of the oxygen vacancy dimer is weakened by hole capture, so the $f_\mathrm{v}^{(+/0)}$ line shape is wider than the $f_\mathrm{v}^{(0/+)}$ line shape. The electron in the occupied defect state of the hydrogen bridge has a fraction of anti-binding [59], so the bond that forms over the hydrogen atom is stronger when this electron is removed and the $f_\mathrm{v}^{(+/0)}$ line shape is slightly sharper than the $f_\mathrm{v}^{(0/+)}$ line shape.

Fig. 4.24 shows the temperature behavior of the $(0/+)$ and the $(+/0)$ line shape of the oxygen vacancy dimer, both before and after the smearing. An increase in the temperature increases the weight of the peaks that correspond to higher energy initial states. Especially in the unsmeared line shape of the oxygen vacancy dimer, one can see a main comb of Dirac peaks that is only weakly temperature dependent, which corresponds to the initial vibrational states of lower energy. The gaps between the peaks of the main comb are filled by smaller peaks
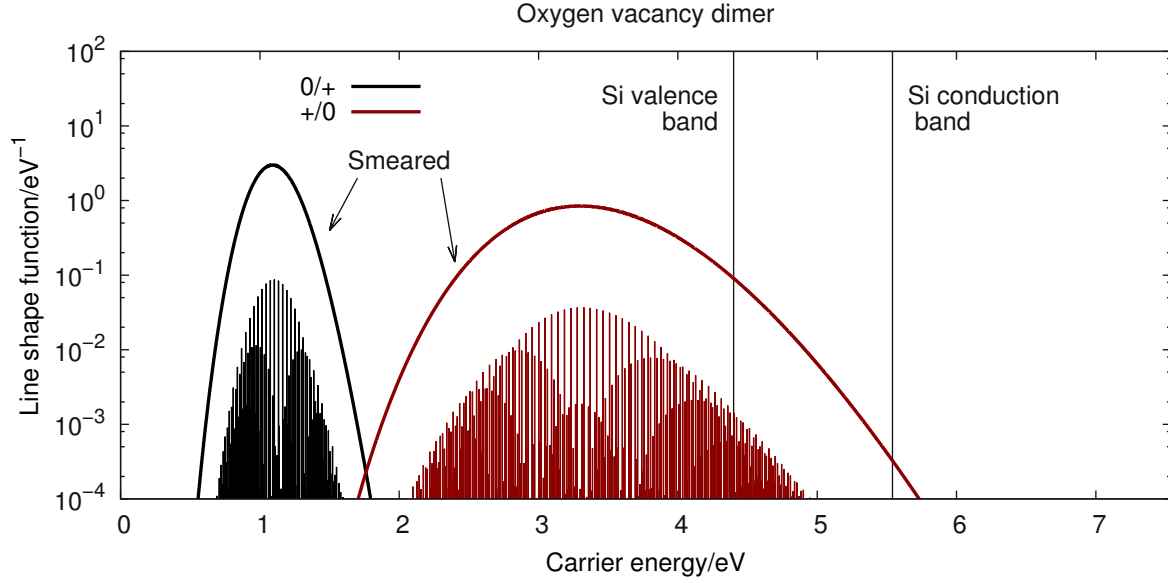
Figure 4.22: Line shapes $f_\mathrm{v}^{(0/+)}$ and $f_\mathrm{v}^{(+/0)}$ for the oxygen vacancy in the dimer configuration. The plain solution of (4.67) and (4.68) is a series of weighted Dirac-peaks, indicated in the figure as impulses whose length corresponds to the weight. To obtain smooth line shapes, we smear these peaks with a Gaussian distribution of width $k_\mathrm{B}T$.

at higher temperatures. The oscillations in the smeared line shapes for $100\,\mathrm{K}$ are partly due to the gaps of the main comb not being filled up and partly due to the temperature dependent smearing parameter used in this work.

4.7 Extraction of the Classical Line Shapes

As discussed in Sec. 2.10, line shapes can also be calculated based on classical statistical physics. In the defect-device system, the shift induced by the mean field and the free state enters directly into the energy conservation expression. Again we can define the defect line shapes

$$f_\mathrm{v}^{(+/0)}(E) = \int\limits_{\mathbb{R}^N} Z_0^{-1} e^{-\frac{E_\mathrm{d}^+(\vec{R})}{k_\mathrm{B}T}} \delta\left(E_\mathrm{d}^0(\vec{R}) - E_\mathrm{d}^+(\vec{R}) - E_\mathrm{v0}^{\mathrm{SiO_2}} - E\right) d\vec{R}, \tag{4.73}$$

$$f_\mathrm{v}^{(0/+)}(E) = \int\limits_{\mathbb{R}^N} Z_+^{-1} e^{-\frac{E_\mathrm{d}^0(\vec{R})}{k_\mathrm{B}T}} \delta\left(E_\mathrm{d}^0(\vec{R}) - E_\mathrm{d}^+(\vec{R}) - E_\mathrm{v0}^{\mathrm{SiO_2}} - E\right) d\vec{R}, \tag{4.74}$$

with the partition functions

$$Z_0 = \int\limits_{\mathbb{R}^N} e^{-\frac{E_\mathrm{d}^0(\vec{R})}{k_\mathrm{B}T}} d\vec{R}, \tag{4.75}$$

$$Z_+ = \int\limits_{\mathbb{R}^N} e^{-\frac{E_\mathrm{d}^+(\vec{R})}{k_\mathrm{B}T}} d\vec{R}. \tag{4.76}$$
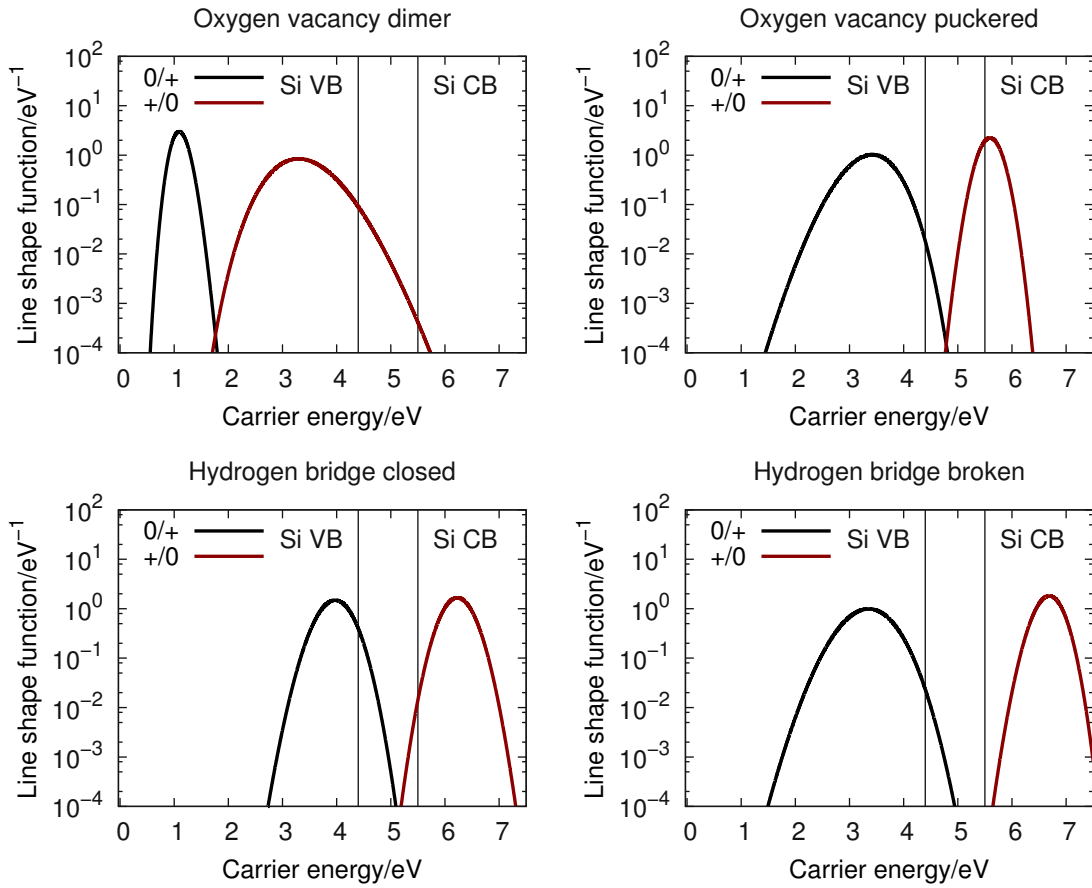
Figure 4.23: Emission and capture line shape functions at $300\,\mathrm{K}$ for the oxygen vacancy and the hydrogen bridge. Two hundred eigenstates in both the neutral and the positive defect state have been considered for the calculation of the line shapes. The energy scale is referenced to the $\mathrm{SiO_2}$ valence band edge.

In these expressions, the integration runs over all nuclear degrees of freedom. For our 72 atom defect structures, the direct numerical solution would require the evaluation of an integral in 216 dimensions, which is clearly beyond our computational capacity. Nevertheless, there are atomistic modeling methods for the evaluation of thermal integrals and we will come back to this below. At first, it is interesting to see how strong the nuclear quantum effects are for the defects under investigation. For this purpose, we calculate the classical line shapes for the approximate one-dimensional potential energy surfaces.

Inserting the one dimensional potentials (4.60) and (4.61) into (4.73) and (4.74) yields

$$f_{\mathrm{v}}^{(+/0)}(E) = \int\limits_{-\infty}^{\infty} Z_+^{-1} e^{-\frac{M\omega_+^2(Q-Q')^2}{2k_{\mathrm{B}}T}} \delta\left(E_{\mathrm{th}}^{(+/0)} + \frac{M\omega_0^2}{2}Q^2 - \frac{M\omega_+^2}{2}(Q-Q')^2 - E \right) dQ' \quad (4.77)$$

$$f_{\mathrm{v}}^{(0/+)}(E) = \int\limits_{-\infty}^{\infty} Z_0^{-1} e^{-\frac{M\omega_0^2 Q^2}{2k_{\mathrm{B}}T}} \delta\left(E_{\mathrm{th}}^{(+/0)} + \frac{M\omega_0^2}{2}Q^2 - \frac{M\omega_+^2}{2}(Q-Q')^2 - E \right) dQ, \quad (4.78)$$
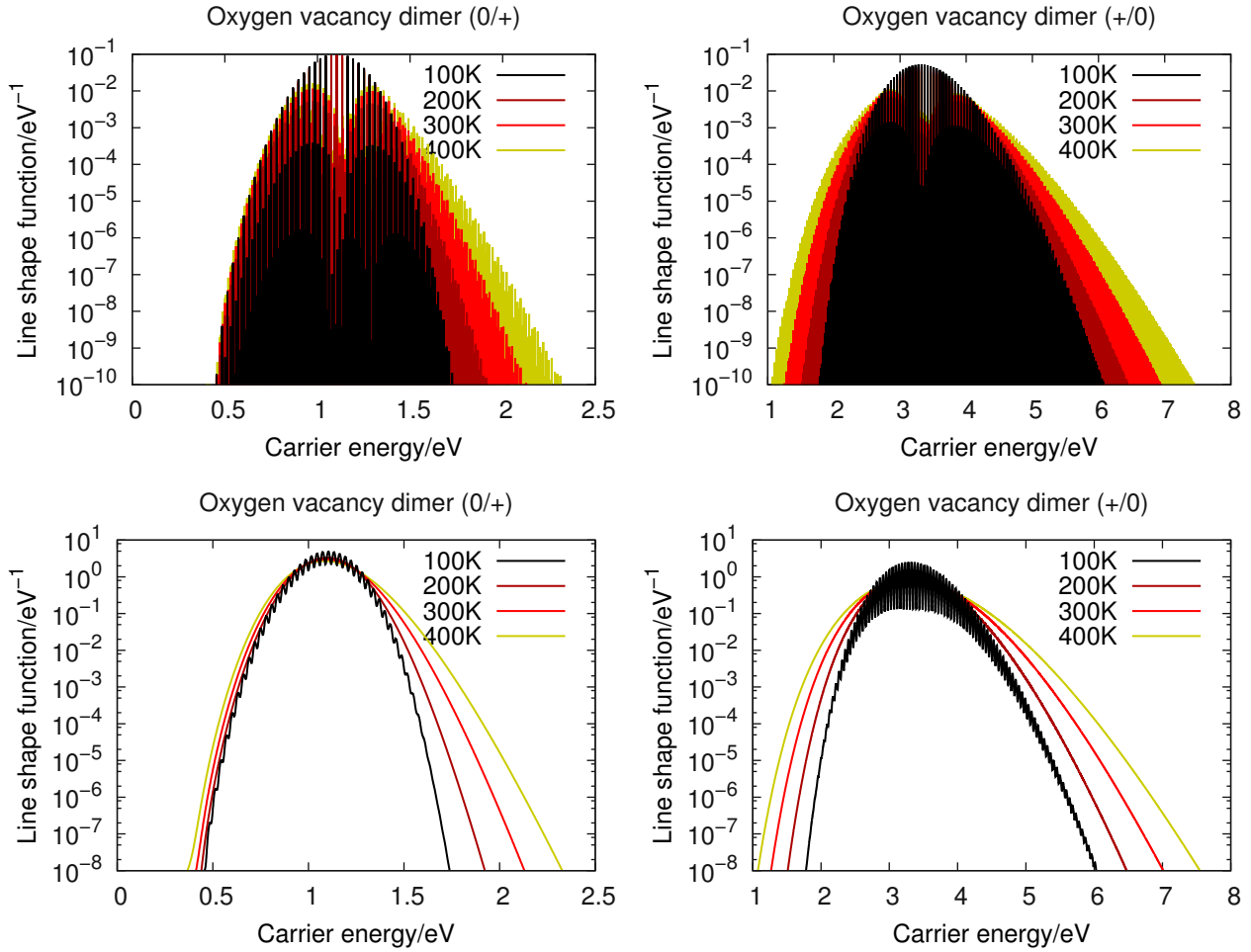
Figure 4.24: Quantum mechanical line shapes of the oxygen vacancy dimer both before **(top)** and after **(bottom)** smearing for different temperatures. With increasing temperature, the probability of finding the vibrational system in energetically higher states increases, increasing the weight of the corresponding Dirac-peaks. In the smeared line shape this shows as a broadening. For low temperatures, the smeared line shapes show oscillations.

with the partition functions

$$Z_+ = \int_{-\infty}^{\infty} e^{-\frac{M\omega_+^2 (Q-Q')^2}{2k_\mathrm{B}T}} dQ = \sqrt{\frac{2\pi k_\mathrm{B} T}{M\omega_+^2}} \tag{4.79}$$

$$Z_0 = \int_{-\infty}^{\infty} e^{-\frac{M\omega_0^2 Q^2}{2k_\mathrm{B}T}} dQ = \sqrt{\frac{2\pi k_\mathrm{B} T}{M\omega_0^2}}. \tag{4.80}$$

For the solution of the integrals above we use

$$\int_{-\infty}^{\infty} F(Q)\delta(G(Q))dQ = \sum_i \frac{F(Q_i)}{\left|\frac{\partial G(Q_i)}{\partial Q}\right|}, \tag{4.81}$$

where the Q_i are the zeros of $G(Q)$. The Dirac distributions thus reduce the line shape integrals to a summation over the two points

$$Q_{1,2}(E) = \frac{\omega_+^2 Q' \pm \sqrt{\omega_0^2 \omega_+^2 Q' + 2\frac{\omega_0^2 - \omega_+^2}{M}(E - (E_{\text{th}}^{(+/0)} - E_{\text{v0}}^{\text{SiO}_2}))}}{\omega_+^2 - \omega_0^2},$$ (4.82)

which are exactly the crossing points of the two parabolas defined by (4.60) and (4.61). The final expressions for the line shapes read

$$f_{\text{v}}^{(0/+)}(E) = Z_0^{-1}\left(\frac{e^{-\frac{M\omega_0 Q_1(E)^2}{k_{\text{B}}T}}}{|M\omega_0^2 Q_1(E) + M\omega_+^2(Q_1(E) - Q')|} + \frac{e^{-\frac{M\omega_0 Q_2(E)^2}{k_{\text{B}}T}}}{|M\omega_0^2 Q_2(E) + M\omega_+^2(Q_2(E) - Q')|}\right)$$
(4.83)

$$f_{\text{v}}^{(+/0)}(E) = Z_+^{-1}\left(\frac{e^{-\frac{M\omega_+(Q_1(E)-Q')^2}{k_{\text{B}}T}}}{|M\omega_0^2 Q_1(E) + M\omega_+^2(Q_1(E) - Q')|} + \frac{e^{-\frac{M\omega_+(Q_2(E)-Q')^2}{k_{\text{B}}T}}}{|M\omega_0^2 Q_2(E) + M\omega_+^2(Q_2(E) - Q')|}\right)$$
(4.84)

These line shapes have the typical Arrhenius form of a thermally activated process. The activation energies in this case are the crossing points of the potential energy surfaces [123]. The classical line shapes are simple analytic expressions, which can be easily implemented into a device simulator. Due to the Boltzmann terms in the classical line shapes, the crossing point that is lower in energy dominates the transition. As discussed before, the crossing points themselves depend on the energy of the free state.

The classical $f_{\text{v}}^{(+/0)}$ line shapes are compared to their quantum mechanically calculated counterparts in Fig. 4.25 for the oxygen vacancy dimer and the closed hydrogen bridge. The classical formula underestimates the transition rate at low temperatures and for energies that are below the maximum of the line shape. This energy range corresponds to the weak coupling regime of the defect [37]. These underestimations are due to the neglect of tunneling in the classical model. For strong coupling, which is especially relevant for the exchange of holes with the silicon valence band, good agreement between the classical and the quantum mechanical version is already given at room temperature. We take this result as an indication that the quantum mechanical nature of the nuclei does not have a strong influence on the line shapes in the temperature ranges that are of interest to BTI.

When quantum effects are negligible, however, it is also possible to calculate line shapes with the full potential energy surfaces from the density functional calculations. Quite generally, the integrals of a function $X(\vec{R})$ of the form

$$\int_{\mathbb{R}^N} Z^{-1} e^{-\frac{E(\vec{R})}{k_{\text{B}}T}} X(\vec{R}) d\vec{R}$$ (4.85)

are called "thermal averages" of the canconical (N, V, T) ensemble and are written as $\langle X \rangle$. As the potential $E(\vec{R})$ that determines the weighting factor for the averaging is usually a function of low symmetry in $\mathbb{R}^N$, these integrals are impossible to evaluate from a simple numerical integration based on discretization. The calculation methods that are applied to this type of problems are *Metropolis Monte Carlo* and *molecular dynamics*. The Metropolis Monte Carlo method moves through the configuration space on a random trajectory. This trajectory is steered such that the regions with the highest occupation probability are most densely sampled. Denoting the trajectory of the Metropolis Monte Carlo algorithm as $\vec{R}_1, \vec{R}_2, \vec{R}_3, \ldots, \vec{R}_I$, the

Oxygen vacancy dimer
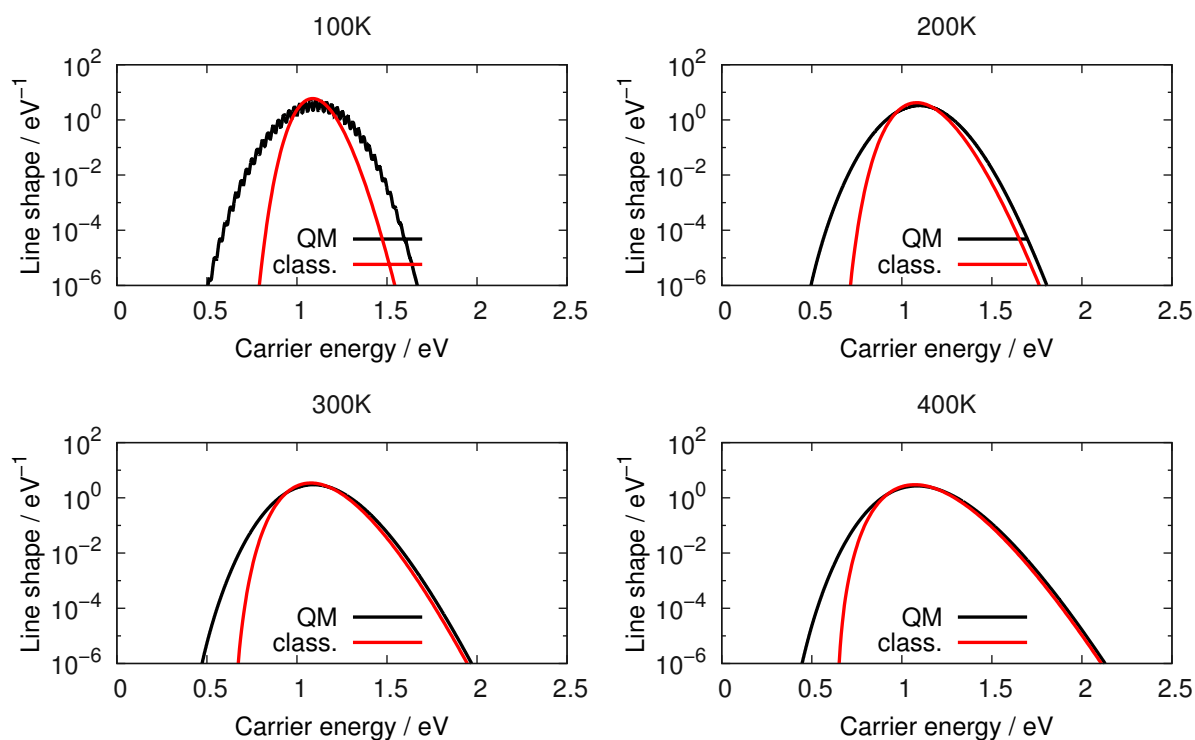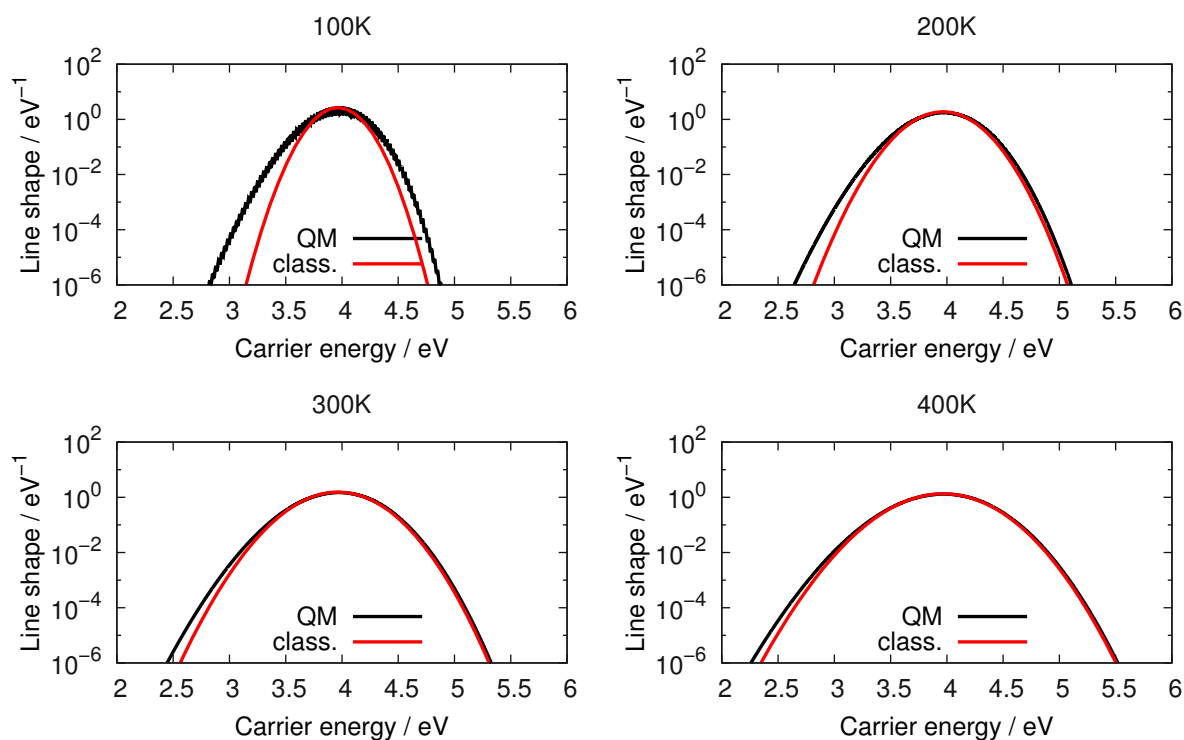
Figure 4.25: Comparison of the classical line shapes from (4.84) to their quantum mechanical counterparts that were calculated numerically from (4.68) at the indicated temperatures for the dimer configuration of the oxygen vacancy and the closed hydrogen bridge. Deviations between the two versions arise at low temperatures and in the weak coupling regime (energies below the peak of the line shape) due to the absence of tunneling in the classical version.

average of the function $X(\vec{R})$ over the set of sample points will approach the true average of the canonical ensemble

$$\lim_{I \to \infty} \frac{1}{I} \sum_{K=1}^{I} X(\vec{R}_K) = \langle X \rangle \tag{4.86}$$

The Metropolis Monte Carlo algorithm is broadly applied in atomistic modeling to calculate thermally influenced properties as bond lengths, free energies, etc. and its general formulation makes it possible to include a particle reservoir and pressure in addition to a thermal reservoir [112, 120, 203].

The molecular dynamics method on the other hand tries to describe the dynamics of the molecular system by propagating the positions of the nuclei according to Newton's equations of motion [119, 120]. In its pure form, the method just generates the constant energy trajectory of an atomic system from a given starting point in phase space [119], which corresponds to the microcanonical (N, V, E) ensemble of statistical physics [112]. As this ensemble has very limited practical relevance, there are extensions to the method for the coupling to a heat bath, which results in a canonical (N, V, T) ensemble, and the inclusion of pressure, which results in an isothermal-isobaric (N, p, T) ensemble [112, 120]. These extensions are sometimes referred to as thermostats and barostats, respectively. Similar to the Monte Carlo Method, the temperature and pressure control are designed so as to give the correct thermal averages in the long time limit,

$$\lim_{t \to \infty} \frac{1}{t} \int_{0}^{t} X(\vec{R}(t'))dt' = \langle X \rangle . \tag{4.87}$$

(N, V, T) and (N, p, T) molecular dynamics simulations are routinely used to compute the dynamics of frequent events such as the hopping of fast diffusors or reactions at high temperatures [153]. However, it has to be mentioned here that strictly speaking the trajectories generated in those runs are not 'physical' trajectories, as the thermostats and barostats are only designed to give the right *averages*, rather than nuclear dynamics.

The classical line shapes can also be written as thermal averages

$$f^{(+/0)}(E) = \left\langle \delta(E_{\mathrm{sw}}(\vec{R}) - E) \right\rangle_{+} \tag{4.88}$$

$$f^{(0/+)}(E) = \left\langle \delta(E_{\mathrm{sw}}(\vec{R}) - E) \right\rangle_{0}, \tag{4.89}$$

with

$$E_{\mathrm{sw}}(\vec{R}) = E_{\mathrm{d}}^{+}(\vec{R}) - E_{\mathrm{d}}^{0}(\vec{R}) - E_{\mathrm{v0}}^{\mathrm{SiO_2}} \tag{4.90}$$

As mentioned in Sec. 2.10, these averages give the probability that for a given carrier energy E an elastic capture or emission transition is possible. In the terminology of Sec. 4.5, the line shape can be seen as a thermally broadened switching trap level $E_{\mathrm{d}}^{+}(\vec{R}) - E_{\mathrm{d}}^{0}(\vec{R}) - E_{\mathrm{v0}}^{\mathrm{SiO_2}}$. In a numerical calculation, we can approximate this distribution as a normalized histogram over the sample points drawn from a Metropolis Monte Carlo or molecular dynamics trajectory.

We have tested this calculation method for the closed hydrogen bridge. For the generation of the trajectory, we use the molecular dynamics implementation of VASP, which implements a Nosé thermostat [112]. Due to the large computational demand of the molecular dynamics calculation, the accuracy of the density functional calculation is reduced here, using a plane wave cut-off of $500\,\mathrm{eV}$ and the real space projection feature of VASP. We calculate the $f_{\mathrm{v}}^{(0/+)}$ line shape from the molecular dynamics trajectory in the neutral state of the defect as a histogram of the switching trap levels of all configurations in the trajectory. The structure is equilibrated for $3\,\mathrm{ps}$, then the line shape is extracted from a $10\,\mathrm{ps}$ simulation.

Figure 4.26: Comparison of the line shapes for the closed hydrogen bridge as calculated from the approximate harmonic potential energy surface in the classical and quantum mechanical form to the line shapes calculated from molecular dynamics. Excellent agreement between the different calculation methods is found around the maximum of the line shape.
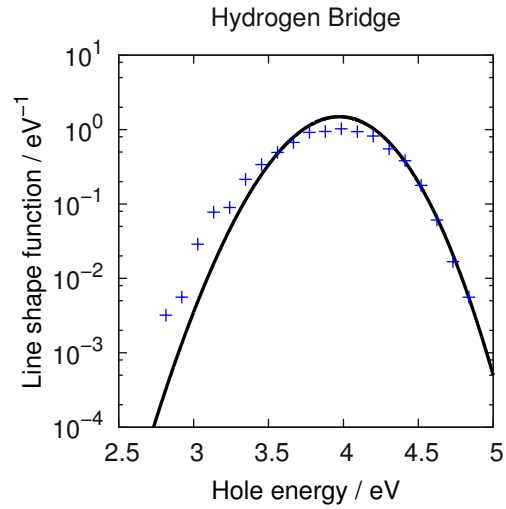
The result is shown in Fig. 4.26. Excellent agreement is found between the line shapes calculated from molecular dynamics and from the approximate potentials around the maximum and above. We take this result as an indication for the validity of the harmonic approximation. The calculation of line shapes from molecular dynamics or Metropolis Monte Carlo is undoubtedly an appealing approach as it includes all features of the density functional potential energy surfaces. Its applicability to the calculation of line shapes for BTI, however, is limited by the long trajectories that have to be calculated in order to get smooth line shapes further away from the maximum. The line shape in Fig. 4.26 is only smooth to about $0.7\,\mathrm{eV}$ above the maximum. As shown below, the hole capture in BTI happens at about $1.2\,\mathrm{eV}$ above the maximum, which due to the squared-exponential drop of the line shape we estimate to require about a billion molecular dynamics steps. Unfortunately, this is again far beyond our patience. As for the barrier hopping transitions, however, an approach similar to the nudged elastic band method could be developed to find the lowest energy crossing point of the two potential energy surface, in order to estimate the activation energy of the transition process.

4.8 Density Functional Dependence

The PBE gradient corrected functional we employ in our work is quite popular in solid state theory. However, adding a fraction of Hartree-Fock exchange to the density functional calculation improves the description of band gaps and other properties of many atomic systems [99, 192]. We have checked the dependence of the calculated line shapes on the employed functional by comparing our PBE results with calculations using the PBE0 hybrid functional. Due to the high computational effort that is required with hybrid functionals, we only investigated the primary states of our model defects, i.e. the oxygen vacancy in its dimer configuration and the closed hydrogen bridge. A comparison between the PBE and PBE0 prediction of the defect levels for the model defects considered here has been done by Alkauskas et al. [204]. This comparison found that the defect levels were largely shifted by about $1.45\,\mathrm{eV}$, but the relative positions were almost the same. The findings of Alkauskas and coworkers agree well with our results shown in Fig. 4.27, except for the strong shift which is absent in our work due to the marker based alignment.
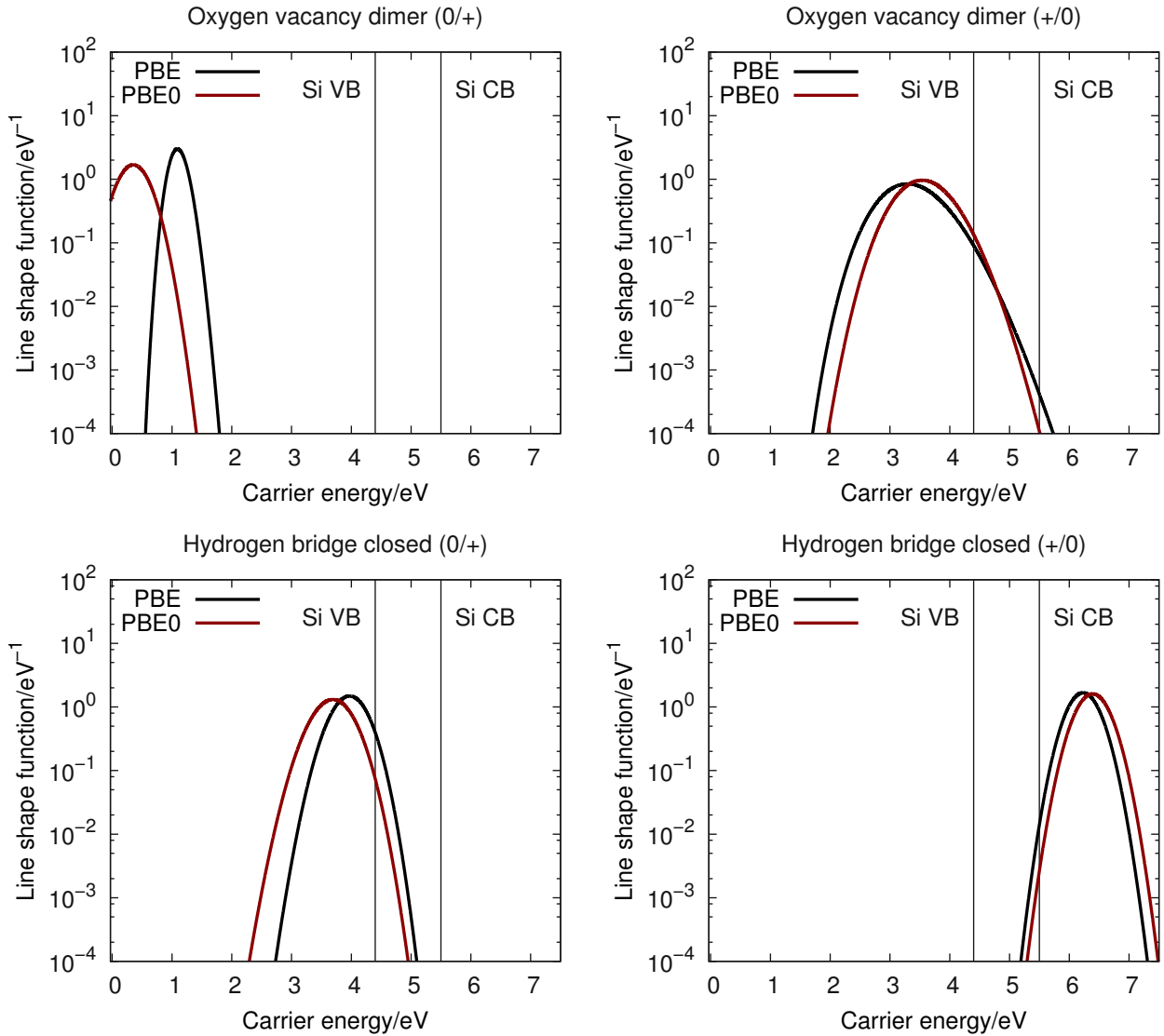
Figure 4.27: Comparison of the line shapes extracted from density functional theory based on the PBE functional and the PBE0 functional. Except for the $(0/+)$ line shape of the oxygen vacancy in the dimer configuration, the line shapes calculated using PBE0 agree well with the PBE results.

4.9 Energy Alignment

The biggest uncertainty in our calculations comes from the alignment of the energy scales between the atomistic defect model and the free charge carrier states in the semiconductor device. Although the marker method performs well for defects that are sufficiently similar to the marker defect [102], the accuracy of the alignment depends heavily on the accuracy of the experimental reference values. Blöchl's placement of the $(+/-)$ transition level $0.2\,\mathrm{eV}$ above the silicon midgap is based on CV measurements of MOS structures after hydrogen exposure [59, 81]. However, the distribution of the states which have been measured in [81] spans from $0.1\,\mathrm{eV}$ below silicon midgap to $0.3\,\mathrm{eV}$ above, and the assignment of this transition

	$1 \rightarrow 1'$	$1' \rightarrow 1$	$2 \rightarrow 2'$	$2' \rightarrow 2$
Oxygen vacancy	$3.00\,\mathrm{eV}$	$36.0\,\mathrm{meV}$	$0.43\,\mathrm{eV}$	$0.34\,\mathrm{eV}$
Hydrogen bridge	$1.18\,\mathrm{eV}$	$1.16\,\mathrm{eV}$	$0.46\,\mathrm{eV}$	$0.18\,\mathrm{eV}$
BTI defect [206]	$\approx 1.00\,\mathrm{eV}$	$\approx 1.2\,\mathrm{eV}$	$\approx 0.7\,\mathrm{eV}$	$\approx 0.3\,\mathrm{eV}$

Table 4.6: Activation energies for the structural reconfigurations as calculated from the atomistic defect models using the nudged elastic band method.

level to the hydrogen interstitial is debatable. As an alternative one can take the band edges of the Kohn-Sham system as reference levels. This leads to large differences in our calculations as the SiO_2 valence band edge of the Kohn-Sham system lies $1.53\,\mathrm{eV}$ above the level estimated from Blöchl's alignment scheme. Interestingly, this difference is reduced to $149\,\mathrm{meV}$ for the PBE0 functional. Another uncertainty concerns the Si-SiO_2 valence band offset. Different values have been given in the literature, ranging from $4.2\,\mathrm{eV}$ to $4.8\,\mathrm{eV}$ [205]. Considering all these uncertainties, in a future comparison of model defects to experimental data it may thus be favorable to leave some freedom to optimize the energy alignment between the energy scale of the line shapes and the device.

4.10 Discussion of the DFT Results in the Context of BTI

In the multi-state multi-phonon model for BTI, the more stable configurations in the neutral state and the positive state are 1 and 2, the metastable configurations are $1'$ and $2'$, respectively. Based on the energy differences of the configurations given in Sec. 4.1.2, the configurations 1 and $2'$ correspond to the neutral and positive state of the dimer configuration for the oxygen bridge and the closed configuration of the hydrogen bridge. Consequently, the puckered/broken configurations are assigned $1'$ in the neutral state and 2 in the positive state.

The reaction paths for the $1 \rightleftharpoons 1'$ and $2 \rightleftharpoons 2'$ transitions are shown in Fig. 4.8, the extracted barriers are compared to estimates for the BTI defect in Tab. 4.6. The hydrogen bridge shows reasonable agreement with the BTI defect values both in the neutral and the positive state. For the oxygen vacancy, the $2 \rightleftharpoons 2'$ barriers are also close to the experimental estimates, but a strong discrepancy arises for the $1 \rightleftharpoons 1'$ barriers. The barrier of about $36\,\mathrm{meV}$ for the transition from the puckered to the dimer configuration is much too small for BTI, as the experiments show defects that can be switched several times between the positive and the neutral state in the secondary configuration [37]. A $1' \rightarrow 1$ barrier as small as the oxygen vacancy value would be overcome instantaneously after neutralization of the defect. However, this issue may be a feature of the crystalline host structure, as higher barriers have been reported [64] for the oxygen vacancy in amorphous silica.

For the discussion of the charging and discharging reactions $1 \rightleftharpoons 2'$ and $2 \rightleftharpoons 1'$, we first take a look at the $f_v^{(0/+)}$ and $f_v^{(+/0)}$ line shapes in Fig. 4.23. One can see a striking difference in the hole capture (electron emission, $f_v^{(0/+)}$) behavior of the dimer and the puckered state of the oxygen vacancy, while this difference is much less pronounced for the closed and broken hydrogen bridge. The position of the $f_v^{(0/+)}$ maximum of the oxygen vacancy dimer is close to the SiO_2 valence level, in agreement with the switching trap level for that transition given in Tab. 4.4. A $f_v^{(0/+)}$ line shape at this energetic position makes a hole capture from the Si valence level very unlikely, even under large bias. Gös et al. have calculated switching trap

levels for oxygen vacancies in amorphous silica [193] and have found a very small spread in the distribution of these levels for the investigated samples. One can thus assume that the low position of the hole capture line shape is only weakly influenced by the surrounding atoms. This makes the oxygen vacancy dimer position a very unlikely candidate for the state 1 of the BTI defect.

The maximum of the hole capture line shape of the closed hydrogen bridge on the other hand is too close to the silicon valence band to show the BTI behavior. The widening due to an increase in the temperature as well as the bias dependence are stronger for carriers further away from the line shape maximum. In the shown configuration, both the bias and the temperature dependence are weak, which unfortunately does not match the properties of the BTI defect. However, the calculations in [193] showed a spread for the $(0/+)$ switching trap level of the hydrogen bridge in amorphous silica that is larger compared to the same level of the oxygen vacancy. Thus, there may be hydrogen bridges which match the hole capture properties of the BTI defect in amorphous silica.

While the line shape of a defect includes the quantum mechanical effects, and the dependence on the reservoir state energy and the band bending, it does not give any information about the temperature behavior. However, as mentioned in Sec. 4.7, the activation barrier for the charge state transition can be estimated from the intersection of the potential energy surfaces. The parabolic approximations extracted from our density functional calculations are shown in Fig. 4.20, where the energy of the involved free state is placed at the silicon valence level. This corresponds to the most dominant energetic configuration for hole capture with no field in the oxide. It can be seen that in the primary (dimer) state, the oxygen vacancy has to overcome a large thermal barrier to capture a hole from the silicon valence band edge, which corresponds to the small value of the line shape at this energy. The temperature activation of the $1 \rightarrow 2'$ transition determines the temperature activation of the BTI degradation, which is in the 0.2 – $0.3\,\mathrm{eV}$ regime. The initial hole capture barrier of the oxygen vacancy is $\approx 2.7\,\mathrm{eV}$ at zero bias, and a reduction to the experimental BTI activation energy requires a field induced shift of $\approx 2.6\,\mathrm{eV}$. At a typical NBTI field of $7\,\mathrm{MV/cm}$, this requires a distance of about $3.7\,\mathrm{nm}$ between the defect and the interface, which is beyond the thickness of most state-of-the-art MOS oxides. The hydrogen bridge on the other hand shows a transition barrier of $\approx 35\,\mathrm{meV}$ for the initial hole capture. This value is too low compared to experimental BTI data, considering that this value is without any applied field.

Only minor changes to the line shapes are observed when moving from the PBE to the PBE0 functional, except for the $(0/+)$ line shape of the oxygen vacancy in the dimer configuration. This line shape is moved further down on the energy scale, which makes a hole capture from the silicon valence band even more unlikely. The predicted charge transition properties depend strongly on the selected alignment scheme. Using the Kohn-Sham valence level of our density functional calculations as a reference instead of the $(+/-)$ transition level of the hydrogen interstitial shifts all trap levels and line shapes down by more than $1.5\,\mathrm{eV}$. The line shape of the oxygen vacancy in this case is moved into the $\mathrm{SiO_2}$ valence band, making its hole capture behavior even less compatible with the BTI defect. The hydrogen bridge, on the other hand, assumes an energetic configuration that corresponds well with the BTI experiments. Judging from the good agreement between the $\mathrm{SiO_2}$ valence level in Blöchl's marker method and the prediction of the PBE0 functional, the PBE valence level does not seem to be a reasonable reference. Nevertheless, in the next section we take the line shapes referenced to the PBE valence level as they give better results for the hole capture rate in this case. The rate calculations presented here thus have to be considered a proof-of-concept of the calculation method rather than a presentation of rigorously calculated results.
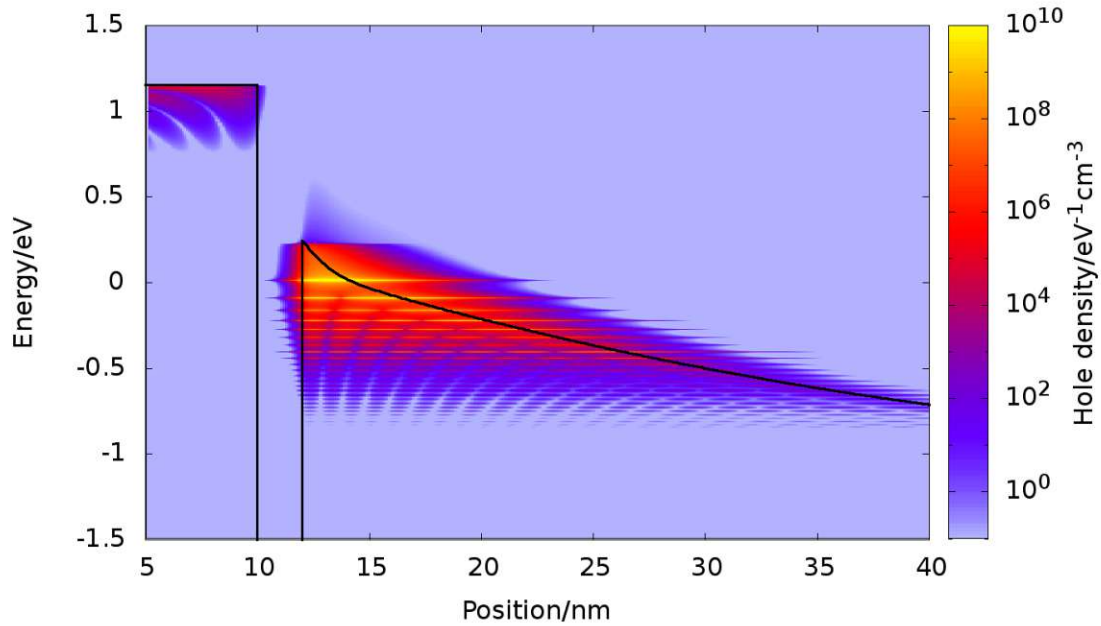
Figure 4.28: The spatially and energetically distributed hole density as calculated using the NEGF method. Thermal equilibrium in the gate and the silicon bulk is induced via an optical potential. The quantization of the hole states and their penetration into the oxide can be clearly seen.

4.11 Hole Capture Rates

Once the line shapes are calculated and an accurate device simulation method is selected, one can proceed to calculate capture and emission rates using (4.41)–(4.44). In the present work, the carrier concentration of the MOS structure has been calculated self-consistently using the non-equilibrium Green's function method [207]. The densities $n(\vec{r}, E)$, $p(\vec{r}, E)$, $D_n(\vec{r}, E)$ and $D_p(\vec{r}, E)$ are readily obtained from the non-equilibrium Green's functions [208][3]. The formalism assumes thermal equilibrium in the gate and bulk region where level broadening due to scattering is modeled using an optical potential [207]. The oxide is treated as a non-equilibrium domain with ballistic quantum transport. Fig. 4.28 shows the hole density in the band diagram as obtained from the NEGF method. The device calculations are done by the Vienna Schrödinger-Poisson software package (VSP2) [179]. The device structure consists of a poly-Si gate and an n-doped bulk separated by a $2\,\mathrm{nm}$ $\mathrm{SiO_2}$ layer. For electrons the unprimed and primed valleys with $0.19m_\mathrm{e}$ and $0.91m_\mathrm{e}$ electron mass are included. Holes were considered with $0.49m_\mathrm{e}$ effective mass.

We have implemented the rate calculation directly into the VSP2 simulator. The calculation of the NMP hole capture rates proceeds in a two step process. First, the band bending is calculated by solving the Poisson- and the NEGF equations self-consistently. Secondly, the NEGF problem is again solved non-self-consistently on a different energy grid that accounts for high energy holes as these contribute considerably to the NMP transitions. The integration is implemented as a post-processing step using the numerical NEGF and line shape data.

---

[3]The densities $n(\vec{r}, E)$, $p(\vec{r}, E)$, $D_n(\vec{r}, E)$ and $D_p(\vec{r}, E)$ can also be obtained from a classical device simulation. In this case, the penetration of the free states into the oxide is commonly modeled using a Wentzel-Kramers-Brillouin (WKB) expression [26].

Figure 4.29: Illustration of the bias induced shift of the relative position of the line shape and the free hole states. The $f_v^{(0/+)}$ line shape of the closed hydrogen bridge is used, the defect position is 2 Å from the Si-SiO$_2$ interface. With more negative gate voltage, the overlap between $f_v^{(0/+)}(E - E_v(\vec{r}_d))$ and $h(\vec{r}_d, E)$, and in consequence the transition rate, strongly increase.
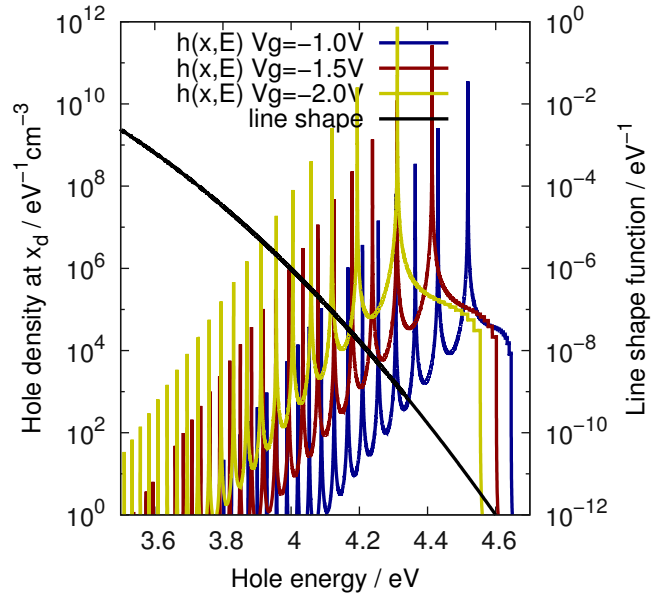
At the time this thesis is written, the transition rate calculations involving unoccupied states in the device, corresponding to hole emission and excess electron emission, is still work in progress. Of the transitions involving occupied states, corresponding to carrier capture, the hole capture transition is most important for the present work. For this reason we concentrate on the calculation of hole capture rates using (4.42). Due to the empirical factor λ in (4.42), all capture rates can be calculated up to a constant factor, therefore all computed time constants in this section are given in arbitrary units.

First, we investigate the effect of the bias induced shift of the relative positions of the line shape and the hole states. As mentioned in Sec. 4.4, this shift is especially relevant for the trapping behavior of oxide defects. Application of a gate voltage induces the largest electric field, and in consequence the largest band bending, in the oxide due to the absence of native carriers there. As illustrated in Fig. 4.29, the dependence of the line shape on the value of the reference energy at the defect site plays a crucial role for the transition kinetics, as the band bending energetically shifts the relative position of the line shape and the spectrum of the hole states, leading to large changes in the capture rate.

In semiconductor device modeling, defects are primarily considered as recombination centers and described using the Shockley-Read-Hall (SRH) theory [209], which characterizes a defect via the capture cross section σ and the (thermodynamic) trap level E_T. The capture of particles is modeled as a flux through the cross section at the speed v_{th}, which is the "thermal velocity"

$$k_{n \to d} = \sigma v_{th} n(\vec{r}_d). \tag{4.91}$$

The emission of an electron into a state of energy E is calculated based on the occupancy in thermal equilibrium as

$$k_{d \to E} = k_{n \to d} e^{-\frac{E_T - E}{k_B T}}. \tag{4.92}$$

The temperature and bias dependence of the capture transition in the classic SRH model comes solely from the density of carriers at the defect site. NMP capture can be modeled within the framework of the SRH theory as an energy dependent capture cross section $\sigma(E)$ [117]. We compare the capture rates calculated from the NMP line shapes to SRH-type rates that only
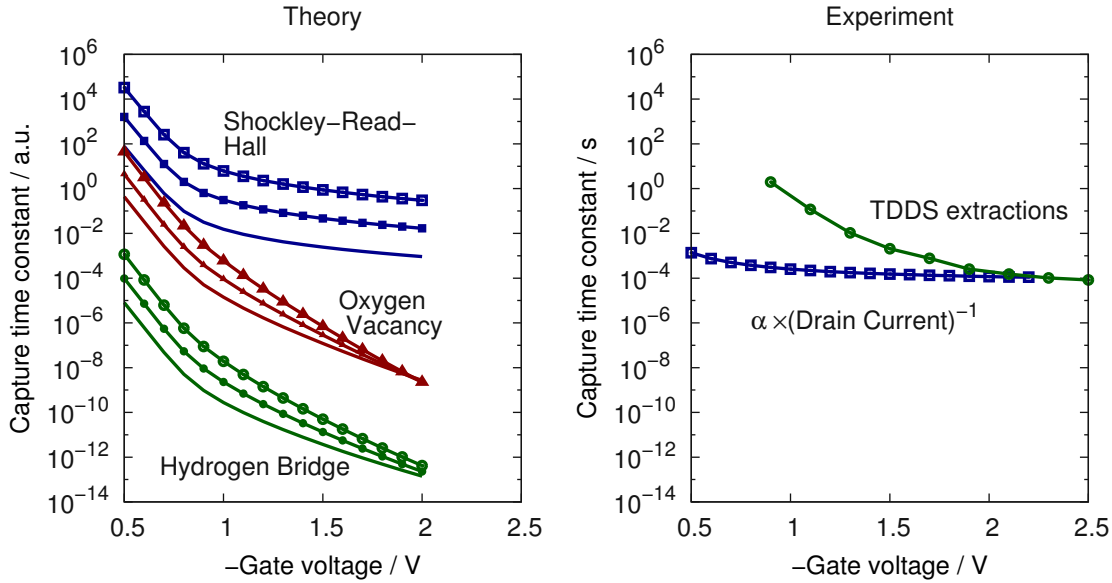
Figure 4.30: (left) Gate voltage dependence of the hole capture time constant for the hydrogen bridge and the puckered oxygen vacancy. The calculated time constants are in arbitrary units to account for the empirical factor λ from (4.42). The NMP capture rates are compared to a Shockley-Read-Hall like capture model, which shows much weaker gate voltage dependence in deep inversion. The calculation temperature is $400\,\mathrm{K}$ and the defect position is $2\,\mathrm{\AA}$ (no symbols), $4\,\mathrm{\AA}$ (medium sized symbols) and $6\,\mathrm{\AA}$ (large symbols) from the silicon bulk. **(right)** Capture time constants extracted using the TDDS technique [32] are compared with the inverse of the drain current, which is proportional to what would be seen for Shockley-Read-Hall-like defects.

depend on the density of holes at the defect site to illustrate the impact of the vibrational influence on the transition rate.

Fig. 4.30 left shows the gate voltage dependence of the NMP hole capture time constants for the two model defects. The gate voltage dependence predicted from the NMP theory is much stronger than the prediction of th SRH-like model. Further, the gate voltage dependence increases with the distance of the defect from the silicon bulk. Both of these strong dependencies are caused primarily by the energetic shift of the line shape functions relative to the holes in the inversion layer, as illustrated in Fig. 4.29. This behavior is in qualitative agreement with the capture rates observed in TDDS measurements. As explained in the previous section, the agreement would not be as good in the originally selected energy alignment scheme.

The temperature dependence of the hole capture is shown in Fig. 4.31. The calculation of NMP hole capture rates for the given defects becomes numerically challenging for low temperatures. As the temperature decreases, the line shapes become increasingly narrow, thus making high energy holes the dominantly captured particles. Accurate representation of high energy holes in the NEGF algorithm requires an improved refinement strategy for the energy grid, which is currently under development. To overcome this limitation, the hole distribution over energy was calculated from a classical density of states for the Arrhenius plot, taking only the total hole concentration at the defect site from the NEGF calculation.

NMP defects show a strong temperature activation, in contrast to capture rates whose temperature dependence comes from the total carrier density alone, as in the SRH description. The calculated activation energies for the hole capture are in excellent agreement with the activa-

Figure 4.31: Arrhenius plots of the capture rates for the defect types comparing the quantum mechanical NMP capture rates (4.68) for the puckered oxygen vacancy and the closed hydrogen bridge to the capture rates calculated using classical atoms (4.84) and to a SRH like model. The indicated activation energies are obtained by fitting to an Arrhenius law.
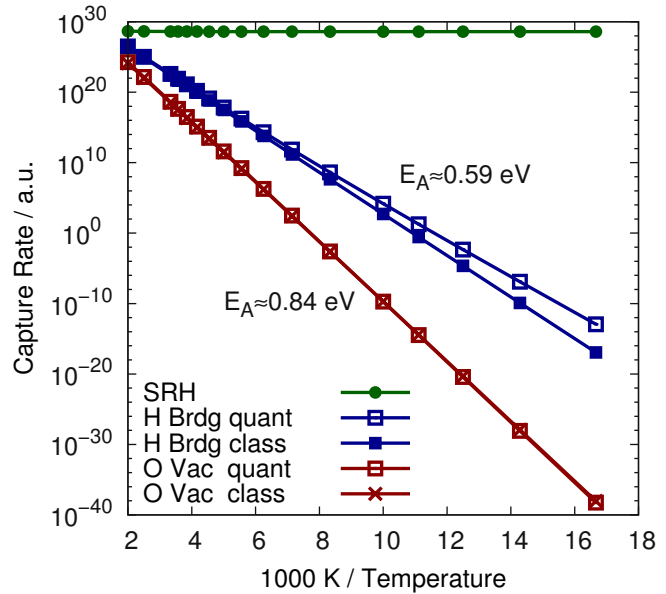
tion energies obtained from TDDS experiments in [32], which is again strongly influenced by the selected alignment scheme. The difference in temperature activation between line shapes calculated using the quantum mechanical formula of (4.68) and those calculated based on classical statistical physics (4.84) are also compared in Fig. 4.31. For the closed hydrogen bridge, this difference becomes visible only below $140\,\mathrm{K}$. For the puckered oxygen vacancy, the classical formula reproduces the quantum mechanical behavior over the complete temperature range investigated. Again, we take this as an indication that the quantum mechanical effects of the nuclei are negligible for the calculation of rates of typical BTI experiments.

4.12 Related Work

NMP theory has been used by several authors in the context of semiconductor devices [32, 144, 180–182, 202]. The transition rate formulas employed are usually based on linear electron-phonon coupling. As shown in Fig. 4.20, this assumption is not fulfilled for our density functional based defect models. Purely quadratic coupling has been investigated in the literature [128, 129], but a linear-quadratic coupling that changes both the equilibrium position and the frequency of the coupling mode has not been considered up to now.

With respect to the modal spectrum, it is either assumed that the transition couples to an infinite number of phonon modes — all having the same oscillator strength — where each can contribute only one phonon [127, 181, 202], or that the transition couples to only one effective mode which receives or emits an arbitrary number of phonons [117, 131, 144]. Interestingly, for linear coupling modes both assumptions lead to essentially the same expression for the capture rates. For the situation we find in the bias temperature instability, in our opinion it is more reasonable to assume that the NMP kinetics are determined by a small number of local modes at the defect site. A coupling to a large number of modes does not seem reasonable for the defects involved in BTI and RTN considering the large variations in transition rates between the defects that are observed in measurements. These variations can only be explained by differences in the local environment of the defect structure which can only hold a small number of vibrational modes.

Abschied nimmt die bunte Welt,
die so lieb mir ward.
Hab ich auch das Ziel verfehlt,
kühn war doch die Fahrt.

(Hermann Hesse)

5 Conclusion and Outlook

This chapter summarizes the main results of the previous chapters and gives an outlook on our future plans to refine those results.

5.1 The Microscopic Limit of the RD model for NBTI

The work presented in Chap. 3 shows that the reaction-diffusion model for the negative bias temperature instability, which has been used for nearly forty years to interpret experimental data, has a number of inherent assumptions on the underlying physics that lack any physical justification. Those are:

1. **Continuous diffusion in the sub-nm regime.** Diffusion of neutral hydrogen atoms and H_2 proceeds via jumps between the interstitial sites of the host material. Positional changes that are smaller than about $4\,\text{Å}$ are atomic vibrations around an equilibrium position and thus not diffusive in nature. This is especially relevant as in the macroscopic modified H-H_2 RD model, the onset of the power-law regime is quite discretization dependent.

2. **Instantaneous well-stirredness along the interface.** The one-dimensional macroscopic RD model, which gives the experimentally relevant $t^{1/6}$ behavior inherently assumes that all hydrogen atoms that are liberated during stress instantaneously compete with other hydrogen atoms at the interface for available dangling bonds or dimerize with each other. However, at typically assumed dangling bond densities of $5 \times 10^{12}\,\text{cm}^{-2}$, the distance between two dangling bonds will be about $4.5\,\text{nm}$. At a depassivation level of $1\,\%$ this means that the average initial distance between two hydrogen atoms is even in the range of $45\,\text{nm}$. The reduction of this distance to the typical H_2 bonding distance of $0.7\,\text{Å}$ [59] needs to be overcome by a diffusion step, which takes about $200\,\text{s}$ at a diffusion coefficient of $10^{-13}\,\text{cm}^2/\text{s}$.

3. **Rate-equation-based description.** It is well established in chemical literature that bimolecular reactions are not sufficiently described by reaction rate equations if the particle numbers are small. In a reaction rate equation system it is for instance possible for $0.5\,H$ atoms to form $0.25\,H_2$, which is physically meaningless. An accurate description in the limit of small particle numbers is only obtained from an atomistic description.

We have implemented a stochastic three-dimensional modified reaction-diffusion model for NBTI to study the degree to which a more realistic description changes the predicted behavior. The model is theoretically well-founded on the theory of stochastic chemical kinetics and is understood as a consequent realization of the physical picture behind the reaction-diffusion theory.

100

The degradation predicted by the microscopic model features a unique new initial regime in which the motion of each hydrogen atom is completely independent from the others. This regime features a strongly increased power-law exponent that is not observed experimentally, yet it is a necessary consequence of the liberation of hydrogen during stress. Application of the atomic RD model to a real-world example shows that for a realistic jump width it is impossible to obtain the experimentally observed behavior due to the apparent diffusion limitation of the dimerization and passivation rates. The match of the microscopic model with the macroscopic version and experimental data can be improved by using an increased diffusion coefficient at the interface. However, the required diffusion coefficients are many orders of magnitude above $10^{-9}\,\mathrm{cm^2/s}$ which leads to diffusion lengths way beyond the dimensions of individual microelectronic devices during stress. Consequently, interface diffusion coefficients of this magnitude would lead to cross-talk and a dramatically increased degradation due to the loss of hydrogen.

The recovery predicted by the microscopic model matches the macroscopic counterpart as soon as the previous degradation has entered the classical diffusion-limited regime. This behavior is due to the prerequisite that the system has to be equilibrated along the interface before the $t^{1/6}$ regime can emerge. As the recovery happens on much larger time-scales than the stress duration, lateral equilibration effects are invisible in recovery traces. A distribution of arrival times as predicted by the simple estimate using different diffusion coefficients during recovery as in [16] could not be found.

In summary, our study of the microscopic limit points out severe problems in the traditional mathematical formulation of the reaction diffusion model for NBTI, rendering all variants that are based on partial differential equations physically meaningless. In a physically meaningful microscopic version of the model, no experimental feature remains that can be accurately predicted. The apparent match of the RD models with experimental data must therefore be considered a mathematical artifact without any physical background. In the author's opinion, the only way to add physical meaning to the reaction-diffusion model is to abandon the assumption that the power-law arises from the out-flux of the diffusing particles and move to a dispersive-hopping formulation. This path was taken by our group years ago and led us to the multi-state multi-phonon models we use today.

5.2 Atomistic Modeling and the BTI Defect

The work presented in Chap. 4 shows how the number of free parameters of the multi-state multi-phonon model for BTI can be reduced using a density functional theory based atomistic defect model. As examples, we investigate two well studied model defect structures, the hydrogen bridge and the oxygen vacancy in α-quartz. Both of these defects feature two stable structural configurations both in the neutral and the positive state, which are called dimer and puckered state for the oxygen bridge, and closed and broken state for the hydrogen bridge.

The activation barriers for the structural reconfiguration of the defect are calculated using the nudged elastic band method. The reconfiguration barrier of the hydrogen bridge is in agreement with the extracted parameters of the BTI defect. The predicted reconfiguration barrier of the oxygen vacancy for the $1' \rightarrow 1$ transition is about $36\,\mathrm{meV}$, which is to too low for the BTI defect as it would be overcome instantaneously in the typical temperature range of BTI experiments.

The charging and discharging rates are calculated using the non-radiative multi-phonon theory. We have developed a method to calculate the NMP transition rates for the charging and discharging of a defect from an atomistic defect model and a macroscopic device simulation. For

this purpose, we model the non-radiative transitions as quasi-optical transitions with negligible photonic energy. The derived expressions for carrier capture and emission rates consist of a tunneling expression, a line shape, and an empirical factor. For the rate calculation, the tunneling probability is taken from a macroscopic device simulation and the line shape is calculated from the atomistic model of the defect. Three approaches for the calculation of line shapes from the atomistic model are presented:

1. A quantum mechanical line shape based on Franck-Condon factors for approximate one dimensional parabolic potential energy surfaces in the different charge states. These line shapes are taken as the quantum mechanical reference calculations. They include nuclear quantization and tunneling. To get smooth lines it is necessary to introduce an empirical spread of the Dirac peaks. Our Franck-Condon-factor-based line shapes compare well with published analytic expressions. However, our method goes beyond previously published calculation methods as it allows to include a frequency change of the coupling mode. As our potential energy surface extractions show, this frequency change is a relevant feature of the atomistic defect models.

2. A line shape derived from classical statistical mechanics based on the same approximate potential energy surfaces. These line shapes are simple analytic expressions that can be easily implemented into a device simulator. For the temperature range in which typical BTI experiments are executed, these classical line shapes are a good approximation to the quantum mechanical line shapes.

3. A classical line shape based on molecular dynamics simulation. These line shapes consider the full potential energy surfaces obtained from the density functional calculations. Unfortunately, reasonably smooth line shapes require long molecular dynamics runs. For regions that are far ($>1\,\mathrm{eV}$) away from the line shape maximum, this method quickly becomes unfeasible. For the region around the maximum, however, good agreement is found between the line shapes based on molecular dynamics and the approximate potentials.

For the evaluation of our model defects as candidates for the BTI, we concentrate on the initial hole capture transition. The calculated line shapes for this transition are energetically too low for the oxygen vacancy and too high for the hydrogen bridge. This leads to a much too high initial charging barrier for the oxygen vacancy and a too weak temperature dependence for the hydrogen bridge. However, these results heavily depend on the selected energy alignment scheme, which itself bears large uncertainties.

To illustrate how the line shapes obtained from the atomistic models can be employed to calculate rates, we calculate the hole capture rate using the density functional line shapes and an open boundary non-equilibrium Green's functions device simulation. The presented results are meant as a proof-of-concept for extracting NMP parameters for device modeling from DFT and also serve as a benchmark for computationally less expensive approximations. The calculations have been compared qualitatively to experimental data obtained using the time dependent defect spectroscopy method on small area MOSFETs. The gate voltage dependence of the calculated capture time constants shows good qualitative agreement with experiment. Also, the reported strong temperature activation can be explained by the NMP model and good agreement is found for the temperature activation of hole capture rates based on classical and quantum mechanical line shapes down to very low temperatures.

The good agreement between the predicted and measured hole capture rates, however, is only made possible by a modification to the alignment scheme and is therefore of limited significance

for the evaluation of the defects as candidates for the BTI. A method for the definitive alignment of the energy scales of the defect line shapes and the states in the device is not in sight at the time this document is written. However, for the search of the BTI defect it is expected that if both charging and discharging kinetics are taken into consideration, this will compensate the uncertainty in the energy alignment. Judging from the results presented here, the hydrogen bridge seems to be the more promising candidate for the BTI defect.

The work presented here is the fundament for future efforts to find the defect responsible for the bias temperature instability. The next steps on this path are the study of the reconfiguration barriers and line shapes of oxygen vacancies and hydrogen bridges in more realistic host structures, such as amorphous silica and Si-SiO_2 interface structures. Different approaches to this target are tested at the moment as part of the EU project "Modelling of the reliability and degradation of next generation nanoelectronic devices" (MORDRED). The results of our α-quartz based calculations will also serve as a reference for these studies. For this purpose, however, our results have to be checked against larger supercells or embedded cluster calculations, to exclude artificial strain effects.

The inclusion of the calculation of emission rates into the device simulator VSP2 is being worked on heavily at the moment and first results are expected to be published soon. For a future inclusion of the non-radiative capture and emission model into standard TCAD simulation, it is necessary to find a compromise between physical accuracy and computational efficiency. Therefore, different levels of approximations will be compared for the NMP capture and emission rates, concerning both the tunneling expression and the line shape functions. In this context, the good agreement between the capture rates computed from the classical and the quantum mechanical line shapes provides a quite promising result.

Bibliography

[1] D. K. Schroder and J. A. Babcock, "Negative bias temperature instability: Road to cross in deep submicron silicon semiconductor manufacturing," *J.Appl.Phys.*, vol. 94, no. 1, pp. 1–18, 2003.

[2] D. K. Schroder, "Negative bias temperature instability: What do we understand?," *Microelectronics Reliability*, vol. 47, pp. 841–852, 2007.

[3] A. Goetzberger and H. Nigh, "Surface charge after annealing of Al-SiO$_2$-Si structures under bias," *Proc.IEEE*, vol. 54, no. 10, pp. 1454–1454, 1966.

[4] Y. Miura and Y. Matukura, "Investigation of silicon-silicon dioxide interface using MOS structure," *Jap.J.Appl.Phys.*, vol. 5, p. 180, 1966.

[5] G. Groeseneken, R. Degraeve, B. Kaczer, and K. Martens, "Trends and perspectives for electrical characterization and reliability assessment in advanced CMOS technologies," in *Proc. ESSDERC*, pp. 64–72, 2010.

[6] A. Kerber and W. McMahon, "Front end of line (FEOL) reliability in CMOS technologies," in *IEEE Int. Reliab. Phys. Symp. Tutorial Notes*, 2012.

[7] K. Jeppson and C. Svensson, "Negative bias stress of MOS devices at high electric fields and degradation of MNOS devices," *J.Appl.Phys.*, vol. 48, no. 5, pp. 2004–2014, 1977.

[8] H. Kufluoglu and M. Alam, "Theory of interface-trap-induced NBTI degradation for reduced cross section MOSFETs," *IEEE Trans.Electron Devices*, vol. 53, pp. 1120 – 1130, May 2006.

[9] T. Grasser, W. Goes, and B. Kaczer, "Dispersive transport and negative bias temperature instability: Boundary conditions, initial conditions, and transport models," *IEEE Trans.Device and Materials Reliability*, vol. 8, pp. 79 –97, March 2008.

[10] S. Ogawa and N. Shiono, "Generalized diffusion-reaction model for the low-field charge build up instability at the Si/SiO$_2$ interface," *Physical Review B*, vol. 51, no. 7, pp. 4218–4230, 1995.

[11] B. Kaczer, V. Arkhipov, R. Degraeve, N. Collaert, G. Groeseneken, and M. Goodwin, "Disorder-controlled-kinetics model for negative bias temperature instability and its experimental verification," in *Proc. Intl.Rel.Phys.Symp.*, pp. 381–387, 2005.

[12] H. Reisinger, O. Blank, W. Heinrigs, A. Mühlhoff, W. Gustin, and C. Schlünder, "Analysis of NBTI degradation- and recovery-behavior based on ultra fast V_{th}-measurements," in *Proc. Intl.Rel.Phys.Symp.*, pp. 448–453, 2006.

[13] T. Grasser, W. Goes, V. Sverdlov, and B. Kaczer, "The universality of NBTI relaxation and its implications for modeling and characterization," in *Proc. Intl.Rel.Phys.Symp.*, pp. 268 –280, April 2007.

[14] T. Grasser, B. Kaczer, W. Gös, H. Reisinger, T. Aichinger, P. Hehenberger, P.-J. Wagner, F. Schanovsky, J. Franco, P. J. Roussel, and M. Nelhiebel, "Recent advances in understanding the bias temperature instability," in *Proc. Intl.Electron Devices Meeting*, pp. 82 – 85, 2010.

[15] S. Mahapatra, V. D. Maheta, A. E. Islam, and M. A. Alam, "Isolation of NBTI stress generated interface trap and hole-trapping components in PNO p-MOSFETs," *IEEE Trans.Electron Devices*, vol. 56, pp. 236–242, Feb. 2009.

[16] S. Mahapatra, A. Islam, S. Deora, V. Maheta, K. Joshi, A. Jain, and M. Alam, "A critical re-evaluation of the usefulness of R-D framework in predicting NBTI stress and recovery," in *Proc. Intl.Rel.Phys.Symp.*, pp. 6A.3.1 –6A.3.10, April 2011.

[17] S. Mahapatra, A. Islam, S. Deora, V. Maheta, K. Joshi, and M. Alam, "Characterization and modeling of NBTI stress, recovery, material dependence and AC degradation using R-D framework," in *Proc. Intl.Symp. on Physical and Failure Analysis of Integrated Circuits*, pp. 1–7, July 2011.

[18] K. Joshi, S. Mukhopadhyay, N. Goel, and S. Mahapatra, "A consistent physical framework for N and P BTI in HKMG MOSFETs," in *Proc. Intl.Rel.Phys.Symp.*, pp. 5A.3.1–10, 2012.

[19] A. Islam, H. Kufluoglu, D. Varghese, S. Mahapatra, and M. Alam, "Recent issues in negative-bias temperature instability: Initial degradation, field dependence of interface trap generation, hole trapping effects, and relaxation," *IEEE Trans.Electron Devices*, vol. 54, pp. 2143 –2154, Sept. 2007.

[20] A. E. Islam, H. Kufluoglu, D. Varghese, and M. A. Alam, "Critical analysis of short-term negative bias temperature instability measurements: Explaining the effect of time-zero delay for on-the-fly measurements," *Appl.Phys.Lett.*, vol. 90, no. 8, p. 083505, 2007.

[21] H. Kufluoglu and M. Alam, "A generalized reaction-diffusion model with explicit H-H_2 dynamics for negative-bias temperature-instability (NBTI) degradation," *IEEE Trans.Electron Devices*, vol. 54, pp. 1101 – 1107, May 2007.

[22] A. Islam, H. Kufluoglu, D. Varghese, and M. Alam, "Temperature dependence of the negative bias temperature instability in the framework of dispersive transport," *Appl.Phys.Lett.*, vol. 90, no. 1, pp. 083505–1–083505–3, 2007.

[23] A. Islam and M. Alam, "Analyzing the distribution of threshold voltage degradation in nanoscale transistors by using reaction-diffusion and percolation theory," *J.Comp.Elect.*, pp. 1–11, 2011. 10.1007/s10825-011-0369-4.

[24] F. Schanovsky and T. Grasser, "On the microscopic limit of the reaction-diffusion model for negative bias temperature instability," in *Proc. Intl.Integrated Reliability Workshop*, pp. 17–21, 2011.

[25] F. Schanovsky and T. Grasser, "On the microscopic limit of the modified reaction-diffusion model for negative bias temperature instability," in *Proc. Intl.Rel.Phys.Symp.*, pp. XT.10.1–6, 2012.

[26] T. Grasser, B. Kaczer, W. Goes, T. Aichinger, P. Hehenberger, and M. Nelhiebel, "A two-stage model for negative bias temperature instability," in *Proc. Intl.Rel.Phys.Symp.*, pp. 33–44, 2009.

[27] T. Grasser, B. Kaczer, and W. Gös, "An energy-level perspective of bias temperature instability," in *Proc. Intl.Rel.Phys.Symp.*, pp. 28–38, 2008.

[28] T. Grasser, W. Gös, and B. Kaczer, "Modeling bias temperature instability during stress and recovery," in *Proc. Simu.Semicond.Proc.Dev.*, pp. 65–68, 2008.

[29] T. Grasser, B. Kaczer, T. Aichinger, W. Gös, and M. Nelhiebel, "Defect creation stimulated by thermally activated hole trapping as the driving force behind negative bias temperature instability in SiO_2, SiON and high-k gate stacks," in *Proc. Intl.Integrated Reliability Workshop*, pp. 91–95, 2008.

[30] A. Lelis and T. Oldham, "Time dependence of switching oxide traps," *IEEE Trans.Nucl.Science*, vol. 41, pp. 1835 –1843, dec. 1994.

[31] T. Grasser, H. Reisinger, P. Wagner, and B. Kaczer, "Time-dependent defect spectroscopy for characterization of border traps in metal-oxide-semiconductor transistors," *Physical Review B*, vol. 82, pp. 245318–1, 2010.

[32] T. Grasser, H. Reisinger, P.-J. Wagner, and B. Kaczer, "The time dependent defect spectroscopy (TDDS) for the characterization of the bias temperature instability," in *Proc. Intl.Rel.Phys.Symp.*, pp. 16–25, 2010.

[33] M. Toledano-Luque, B. Kaczer, P. J. Roussel, M. Cho, T. Grasser, and G. Groeseneken, "Temperature dependence of the emission and capture times of SiON individual traps after positive bias temperature stress," *J.Vac.Sci.Technol.B*, vol. 29, pp. 01AA04–1 – 01AA04–5, 2011.

[34] M. Kirton and M. Uren, "Capture and emission kinetics of individual $Si:SiO_2$ interface states," *Appl.Phys.Lett.*, vol. 48, pp. 1270–1272, 1986.

[35] D. Fleetwood, H. Xiong, Z.-Y. Lu, C. Nicklaw, J. Felix, R. Schrimpf, and S. Pantelides, "Unified model of hole trapping, 1/f noise, and thermally stimulated current in mos devices," *IEEE Trans.Nucl.Sci.*, vol. 49, no. 6, pp. 2674–2683, 2002.

[36] P. Wagner, T. Aichinger, T. Grasser, M. Nelhiebel, and L. Vandamme, "Possible correlation between flicker noise and bias temperature stress," in *Proc. Int. Conf. on Noise and Fluctuations*, pp. 621 – 624, 2009.

[37] T. Grasser, "Stochastic charge trapping in oxides: From random telegraph noise to bias temperature instabilities," *Microelectronics Reliability*, vol. 52, no. 1, pp. 39 – 70, 2012.

[38] P. M. Lenahan and J. J. F. Conley, "What can electron paramagnetic resonance tell us about the Si/SiO_2 system?," *J.Vac.Sci.Technol.B*, vol. 16, no. 4, pp. 2134–2153, 1998.

[39] C. R. Helms and E. H. Poindexter, "The silicon-silicon dioxide system: Its microstructure and imperfections," *Rep.Prog.Phys.*, vol. 57, no. 8, p. 791, 1994.

[40] S. P. Karna, H. A. Kurtz, A. C. Pineda, W. M. Shedd, and R. D. Pugh, *Point Defects in Si-SiO_2 systems: Current Understanding*, pp. 699–615. Kluwer Academic Publishers, 2000.

[41] P. M. Lenahan, *Defects in Microelectronic Materials and Devices*, ch. Dominating Defects in the MOS System P_b and E' Centers, pp. 163–214. CRC Press, 2009.

[42] J. Ryan, P. Lenahan, T. Grasser, and H. Enichlmair, "Recovery-free electron spin resonance observations of NBTI degradation," in *Proc. Intl.Rel.Phys.Symp.*, pp. 43–49, 2010.

[43] P. M. Lenahan and P. V. Dressendorfer, "An electron spin resonance study of radiation-induced electrically active paramagnetic centers at the Si/SiO_2 interface," *J.Appl.Phys.*, vol. 54, no. 3, pp. 1457–1460, 1983.

[44] E. H. Poindexter, G. J. Gerardi, M.-E. Rueckel, P. J. Caplan, N. M. Johnson, and D. K. Biegelsen, "Electronic traps and P_b centers at the Si/SiO_2 interface: Band-gap energy distribution," *Journal of Applied Physics*, vol. 56, no. 10, pp. 2844–2849, 1984.

[45] A. Stesmans, B. Nouwen, and V. V. Afanas'ev, "P_{b1} interface defect in thermal $(100)Si/SiO_2$: ^{29}Si hyperfine interaction," *Phys. Rev. B*, vol. 58, pp. 15801–15809, Dec 1998.

[46] P. Lenahan and J. Conley, J.R., "A comprehensive physically based predictive model for radiation damage in MOS systems," *IEEE Trans.Nucl.Science*, vol. 45, pp. 2413 –2423, December 1998.

[47] P. M. Lenahan and P. V. Dressendorfer, "Hole traps and trivalent silicon centers in metal/oxide/silicon devices," *J.Appl.Phys.*, vol. 55, no. 10, pp. 3495–3499, 1984.

[48] P. M. Lenahan, W. L. Warren, D. T. Krick, P. V. Dressendorfer, and B. B. Triplett, "Interaction of molecular hydrogen with trapped hole E' centers in irradiated and high field stressed metal/oxide/silicon oxides," *J.Appl.Phys.*, vol. 67, no. 12, pp. 7612–7614, 1990.

[49] V. V. Afanas'ev, J. M. M. de Nijs, P. Balk, and A. Stesmans, "Degradation of the thermal oxide of the $Si/SiO_2/Al$ system due to vacuum ultraviolet irradiation," *J.Appl.Phys.*, vol. 78, no. 11, pp. 6481–6490, 1995.

[50] E. H. Pointdexter and W. L. Warren, "Paramagnetic point defects in amorphous thin films of SiO_2 and Si_3N_4: Updates and additions," *J.Electrochem.Soc.*, vol. 142, pp. 2508–2516, 1995.

[51] P. E. Bunson, M. D. Ventra, S. T. Pantelides, D. M. Fleetwood, and R. D. Schrimpf, "Hydrogen-related defects in irradiated SiO_2," *IEEE Trans.Nucl.Sci.*, vol. 47, pp. 2289–2296, 2000.

[52] V. Afanas'ev and A. Stesmans, "Leakage currents induced in ultrathin oxides on (100)Si by deep-UV photons," *Mat.Sci.Eng.B*, vol. 71, no. 1-3, pp. 56 – 61, 2000.

[53] V. V. Afanas'ev and A. Stesmans, "Proton nature of radiation-induced positive charge in SiO_2 layers on Si," *Eur.Phys.Lett.*, vol. 53, no. 2, p. 233, 2001.

[54] K. L. Yip and W. B. Fowler, "Electronic structure of E'$_1$ centers in SiO$_2$," *Physical Review B*, vol. 11, pp. 2327–2338, 1975.

[55] E. P. O'Reilly and J. Robertson, "Theory of defects in vitreous silicon dioxide," *Physical Review B*, vol. 27, pp. 3780–3795, Mar 1983.

[56] J. K. Rudra, W. B. Fowler, and F. J. Feigl, "Model for the E'$_2$ center in alpha quartz," *Physical Review Letters*, vol. 55, pp. 2614–2617, 1985.

[57] J. K. Rudra and W. B. Fowler, "Oxygen vacancy and the E$'_1$ center in crystalline SiO$_2$," *Physical Review B*, vol. 35, no. 15, pp. 8223–8230, 1987.

[58] M. Boero, A. Pasquarello, J. Sarnthein, and R. Car, "Structure and hyperfine parameters of E'_1 centers in α-quartz and in vitreous SiO$_2$," *Physical Review Letters*, vol. 78, pp. 887–890, Feb 1997.

[59] P. E. Blöchl, "First-principles calculations of defects in oxygen-deficient silica exposed to hydrogen," *Physical Review B*, vol. 62, pp. 6158–6178, September 2000.

[60] T. Uchino, M. Takahashi, and T. Yoko, "E' centers in amorphous SiO$_2$ revisited: A new look at an old problem," *Physical Review Letters*, vol. 86, pp. 5522–5525, 2001.

[61] A. Stirling and A. Pasquarello, "First-principles modeling of paramagnetic Si dangling-bond defects in amorphous SiO$_2$," *Physical Review B*, vol. 66, p. 245201, Dec 2002.

[62] D. J. Chadi, "Negative-U property of the oxygen vacancy defect in SiO$_2$ and its implication for the E'_1 center in alpha-quartz," *Appl.Phys.Lett.*, vol. 83, no. 3, pp. 437–439, 2003.

[63] M. Busso, S. Casassa, C. Pisani, and V. B. Sulimov, "Ab initio simulation of the oxygen vacancy bistability in pure and Ge-doped α-quartz," *Modelling and Simulation in Materials Science and Engineering*, vol. 10, no. 1, p. 21, 2002.

[64] Z.-Y. Lu, C. J. Nicklaw, D. M. Fleetwood, R. D. Schrimpf, and S. T. Pantelides, "Structure, properties, and dynamics of oxygen vacancies in amorphous SiO$_2$," *Physical Review Letters*, vol. 89, p. 285505, Dec 2002.

[65] C. J. Nicklaw, Z.-Y. Lu, D. Fleetwood, R. Schrimpf, and S. Pantelides, "The structure, properties, and dynamics of oxygen vacancies in amorphous SiO$_2$," *IEEE Trans.Nucl.Sci.*, vol. 49, pp. 2667–2673, 2002.

[66] V. B. Sulimov, P. V. Sushko, A. H. Edwards, A. L. Shluger, and A. M. Stoneham, "Asymmetry and long-range character of lattice deformation by neutral oxygen vacancy in α-quartz," *Physical Review B*, vol. 66, p. 024108, Jul 2002.

[67] L. Martin-Samos, Y. Limoge, N. Richard, J. P. Crocombette, G. Roma, E. Anglada, and E. Artacho, "Oxygen neutral defects in silica: Origin of the dirstribution of the formation energies," *Eur.Phys.Lett.*, vol. 66, pp. 680–686, 2004.

[68] S. Mukhopadhyay, P. V. Sushko, A. M. Stoneham, and A. L. Shluger, "Modeling of the structure and properties of oxygen vacancies in amorphous silica," *Physical Review B*, vol. 70, p. 195203, Nov 2004.

[69] S. Mukhopadhyay, P. V. Sushko, A. M. Stoneham, and A. L. Shluger, "Correlation between the atomic structure, formation energies, and optical absorption of neutral oxygen vacancies in amorphous silica," *Physical Review B*, vol. 71, p. 235204, Jun 2005.

[70] P. Sushko, S. Mukhopadhyay, A. Stoneham, and A. Shluger, "Oxygen vacancies in amorphous silica: structure and distribution of properties," *Microelectronic Engineering*, vol. 80, no. 0, pp. 292 – 295, 2005.

[71] P. V. Sushko, S. Mukhopadhyay, A. S. Mysovsky, V. B. Sulimov, A. Taga, and A. L. Shluger, "Structure and properties of defects in amorphous silica: new insights from embedded cluster calculations," *J.Phys.:Condensed Matter*, vol. 17, no. 21, p. S2115, 2005.

[72] A. Kimmel, P. Sushko, A. Shluger, and G. Bersuker, "Positive and negative oxygen vacancies in amorphous silica," *ECS Trans.*, vol. 19, pp. 3–17, 2009.

[73] D. M. Fleetwood and J. H. Scofield, "Evidence that similar point defects cause $1/f$ noise and radiation-induced-hole trapping in metal-oxide-semiconductor transistors," *Physical Review Letters*, vol. 64, pp. 579–582, Jan 1990.

[74] D. Fleetwood, "Fast and slow border traps in mos devices," *IEEE Trans.Nucl.Science*, vol. 43, pp. 779 –786, jun 1996.

[75] A. Yokozawa, A. Oshiyama, Y. Miyamoto, and S. Kumashiro, "Oxygen vacancy with large lattice distortion as an origin of leakage currents in SiO_2," in *Proc. Intl.Electron Devices Meeting*, pp. 703 –706, December 1997.

[76] J. W. McPherson and H. C. Mogul, "Underlying physics of the thermochemical E model in describing low-field time-dependent dielectric breakdown in SiO_2 thin films," *J.Appl.Phys.*, vol. 84, no. 3, pp. 1513–1523, 1998.

[77] A. Edwards, P. Sushko, A. Shluger, and V. Sulimov, "Embedding techniques for irradiation-induced defects in crystalline SiO_2," in *Radiation and Its Effects on Components and Systems, 2001. 6th European Conference on*, pp. 98 – 104, sept. 2001.

[78] S. Mukhopadhyay, P. V. Sushko, A. H. Edwards, and A. L. Shluger, "Calculation of relative concentrations of E' centres in amorphous silica," *Journal of Non-Crystalline Solids*, vol. 345-346, no. 0, pp. 703 – 709, 2004.

[79] R. A. Weeks and M. Abraham, "Electron spin resonance of irradiated quartz: Atomic hydrogen," *J.Chem.Phys.*, vol. 42, no. 1, pp. 68–71, 1965.

[80] E. H. Poindexter, "Chemical reactions of hydrogenous species in the $SiSiO_2$ system," *Journal of Non-Crystalline Solids*, vol. 187, no. 0, pp. 257 – 263, 1995.

[81] E. Cartier and J. Stathis, "Atomic hydrogen-induced degradation of the $SiSiO_2$ structure," *Microelectronic Engineering*, vol. 28, no. 1-4, pp. 3 – 10, 1995.

[82] M. Nelhiebel, J. Wissenwasser, T. Detzel, A. Timmerer, and E. Bertagnolli, "Hydrogen-related influence of the metallization stack on characteristics and reliability of a trench gate oxide," *Microelectronics Reliability*, vol. 45, no. 9-11, pp. 1355 – 1359, 2005.

[83] V. V. Afanas'ev and A. Stesmans, "H-complexed oxygen vacancy in SiO_2: Energy level of a negatively charged state," *Appl.Phys.Lett.*, vol. 71, no. 26, pp. 3844–3846, 1997.

[84] P. E. Blöchl and J. H. Stathis, "Hydrogen electrochemistry and stress-induced leakage current in silica," *Physical Review Letters*, vol. 83, pp. 372–375, July 1999.

[85] F. Schanovsky, W. Goes, and T. Grasser, "Multi-phonon hole-trapping from first principles," *J.Vac.Sci.Technol.B*, vol. 29, pp. 01A201–1, 2011.

[86] F. Schanovsky, W. Goes, and T. Grasser, "An advanced description of oxide traps in MOS transistors and its relation to DFT," *J.Comp.Elect.*, vol. 9, pp. 135–140, 2010.

[87] B. Kaczer, T. Grasser, J. Martin-Martinez, E. Simoen, M. Aoulaiche, P. Roussel, and G. Groeseneken, "NBTI from the perspective of defect states with widely distributed time scales," in *Proc. Intl.Rel.Phys.Symp.*, pp. 55–60, 2009.

[88] M. Born and R. Oppenheimer, "Zur quantentheorie der molekeln," *Ann.Phys.*, vol. 84, pp. 457–484, 1927.

[89] J. J. Markham, "Electron-nuclear wave functions in multiphonon processes," *Physical Review*, vol. 103, no. 3, pp. 588–597, 1956.

[90] M. Born and K. Huang, *Dynamical Theory of Crystal Lattices*. Oxford University Press, 1954.

[91] A. M. Stoneham, *Theory of Defects in Solids*. Oxford University Press, 1975.

[92] M. Born, "Kopplung der Elektronen- und Kernbewegung in Molekeln und Kristallen," *Gött. Nachr. math. phys.*, 1951.

[93] D. R. Hartree, "The wave mechanics of an atom with a non-coulomb central field. part I. theory and methods," *Proc. Cambridge Philosoph. Society*, vol. 24, pp. 89–110, 1928.

[94] D. R. Hartree, "The wave mechanics of an atom with a non-coulomb central field. part II. some results and discussion," *Mathematical Proceedings of the Cambridge Philosophical Society*, vol. 24, pp. 111–132, 0 1928.

[95] D. R. Hartree, "The wave mechanics of an atom with a non-coulomb central field. part III. term values and intensities in series in optical spectra," *Mathematical Proceedings of the Cambridge Philosophical Society*, vol. 24, pp. 426–437, 6 1928.

[96] R. M. Martin, *Electronic Structure: Basic Theory and Practical Methods*. Cambridge University Press, 2004.

[97] I. N. Levine, *Quantum Chemistry*. Person Prentice Hall, 2009.

[98] C. Cohen-Tannoudji, B. Diu, and F. L. V. . 2, *Quantenmechanik*. deGruyter, 2009.

[99] J. B. Foresman and A. Frisch, *Exploring Chemistry with Electronic Structure Methods*. Gaussian, Inc., 1996.

[100] R. G. Parr and W. Yang, *Density-Functional Theory of Atoms and Molecules*. Oxford University Press, 1989.

[101] J. P. Perdew, K. Burke, and M. Ernzerhof, "Generalized gradient approximation made simple," *Physical Review Letters*, vol. 77, pp. 3865–3868, 1996.

[102] R. M. Nieminen, *Theory of Defects in Semiconductors*, ch. Supercell Methods for Defect Calculations, pp. 29–67. Springer, 2010.

[103] P. Deák, L. C. Snyder, R. K. Singh, and J. W. Corbett, "Evaluation of semiempirical quantum-chemical methods in solid-state applications. I. molecular-cluster calculations of defects in silicon," *Physical Review B*, vol. 36, pp. 9612–9618, Dec 1987.

[104] P. Deák and L. C. Snyder, "Evaluation of semiempirical quantum-chemical methods in solid-state applications. II. cyclic-cluster calculations of silicon," *Physical Review B*, vol. 36, pp. 9619–9627, Dec 1987.

[105] K. C. Snyder and W. B. Fowler, "Oxygen vacancy in α-quartz: A possible bi- and metastable defect," *Phys. Rev. B*, vol. 48, pp. 13238–13243, Nov 1993.

[106] D. E. Boucher and G. G. DeLeo, "Tight-binding quantum molecular-dynamics simulations of hydrogen in silicon," *Physical Review B*, vol. 50, pp. 5247–5254, August 1994.

[107] M. Tang, L. Colombo, J. Zhu, and T. Diaz de la Rubia, "Intrinsic point defects in crystalline silicon: Tight-binding molecular dynamics studiesof self-diffusion, interstitial-vacancy recombination, and formation volumes," *Physical Review B*, vol. 55, pp. 14279–14289, Jun 1997.

[108] R. Biswas, L. Qiming, B. C. Pan, and Y. Yoon, "Mechanism for hydrogen diffusion in amorphous silicon," *Physical Review B*, vol. 57, pp. 2253–2256, January 1998.

[109] M. Schaible, "Empirical molecular dynamics modeling of silicon and silicon dioxide: A review," *Crit. Rev. Solid State Mat. Sci.*, vol. 24, pp. 265–323, 1999.

[110] K. Vollmayr, W. Kob, and K. Binder, "Cooling-rate effects in amorphous silica: A computer-simulation study," *Physical Review B*, vol. 54, pp. 15808–15826, 1996.

[111] R. M. van Ginhoven, H. Jonsson, and L. R. Corrales, "Silica glass structure generation for ab initio calculations using small samples of amorphous silica," *Physical Review B*, vol. 71, pp. 024208–1, 2005.

[112] M. Tuckerman, *Statistical Mechanics: Theory and Molecular Simulation*. Oxford University Press, 2010.

[113] R. Biswas, Y.-P. Li, and B. Pan, "Isotopic effect between hydrogen and deuterium emission in silicon," *Journal of Non-Crystalline Solids*, vol. 266-269, pp. 176–179, 2000.

[114] D. Gillespie, "A general method for numerically simulating the stochastic time evolution of coupled chemical reactions," *J.Comp.Phys.*, vol. 22, pp. 403–434, 1976.

[115] D. T. Gillespie, "Simulation methods in systems biology," in *Proc. Int. Conf. Form. Meth. Sys. Bio.*, SFM'08, (Berlin, Heidelberg), pp. 125–167, Springer-Verlag, 2008.

[116] H. Sumi, "Phonon-kick mechanism for defect reactions enhanced by electronic excitation," *J.Phys.:Condensed Matter*, vol. 17, no. 34, p. 6071, 1984.

[117] C. H. Henry and D. V. Lang, "Nonradiative capture and recombination by multiphono emission in gaas and gap," *Physical Review B*, vol. 15, pp. 989–1016, January 1977.

[118] T. Grasser, T. Aichinger, G. Pobegen, H. Reisinger, P. Wagner, J. Franco, M. Nelhiebel, and B. Kaczer, "The 'permanent' component of NBTI: Composition and annealing," in *Proc. Intl.Rel.Phys.Symp.*, pp. 6A.2.1 –6A.2.9, April 2011.

[119] J. M. Haile, *Molecular Dynamics Simulation.* Wiley, 1997.

[120] D. Frenkel and B. Smit, *Understanding Molecular Simulation.* Academic Press, 2002.

[121] A. F. Voter, F. Montalenti, and T. C. Germann, "Extending the time scale in atomistic simulation of materials," *Ann.Rev.Mater.Res.*, vol. 32, pp. 321–346, 2002.

[122] K. Mikkelsen and M. Ratner, "Electron tunneling in solid-state electron-transfer reactions," *chemrev*, vol. 87, pp. 113–153, 1987.

[123] V. Abakumov, V. Perel, and I. Yassievich, *Nonradiative recombination in semiconductors.* North-Holland, 1991.

[124] M. D. Newton, "Quantum chemical probes of electron-transfer kinetics: the nature of donor-acceptor interactions," *Chem.Rev.*, vol. 91, pp. 767–792, 1991.

[125] D. M. Adams, L. Brus, C. E. D. Chidsey, S. Creager, C. Creutz, C. R. Kagan, P. V. Kamat, M. Lieberman, S. Lindsay, R. A. Marcus, R. M. Metzger, M. E. Michel-Beyerle, J. R. Miller, M. D. Newton, D. R. Rolison, O. Sankey, K. S. Schanze, J. Yardley, and X. Zhu, "Charge transfer on the nanoscale: Current status," *J.Phys.Chem.B*, vol. 107, no. 28, pp. 6668–6697, 2003.

[126] P. E. S. Wormer and A. van der Avoird, *Theory and Applications of Computational Chemistry: The First Forty Years*, ch. Forty Years of Ab Initio Calculations on Intermolecular Forces, pp. 1047–1091. Elsevier, 2005.

[127] K. Huang and A. Rhys, "Theory of light absorption and non-radiative transitions in f-centers," *Proc. Roy. Soc. A*, vol. 204, pp. 406–423, 1950.

[128] R. Kubo, "Thermal ionization of trapped electrons," *Physical Review*, vol. 86, pp. 929–937, 1952.

[129] T. H. Keil, "Shapes of impurity absorption bands in solids," *Physical Review*, vol. 140, pp. A601–A617, 1965.

[130] B. K. Ridley, "Multiphonon, non-radiative transition rate for electrons in semiconductors and insulators," *J.Phys.:Condensed Matter*, vol. 11, pp. 2323–2341, 1978.

[131] A. M. Stoneham, "Non-radiative transitions in semiconductors," *Rep.Prog.Phys.*, vol. 44, pp. 1251–1295, 1981.

[132] K. Huang, "Adiabatic approximation theory and static coupling theory of nonradiative transition," *Scientia Sinica*, vol. 24, pp. 27–34, 1981.

[133] K. Peuker and A. Schenk, "Grundlagen der Theorie der strahlungslosen Multi-Phonon-Rekombination," *Wiss. Z. d. Humboldt-Univ. Berlin*, vol. 31, pp. 267–270, 1982.

[134] G. Helmis, "Zur Theorie der Störstellenelektronen. I Optische Übergänge," *Ann.Phys.*, vol. 452, no. 6-8, pp. 356–370, 1956.

[135] G. Helmis, "Zur Theorie der Störstellenelektronen. II Strahlungslose Übergänge," *Ann.Phys.*, vol. 454, no. 1-2, pp. 41–54, 1956.

[136] E. Gutsche, "Non-condon approximations and the static approach in the theory of non-radiative multiphonon transitions," *Phys.stat.sol.(b)*, vol. 109, no. 2, pp. 583–597, 1982.

[137] M. G. Burt, "On the relation between static and adiabatic coupling schemes for calculating non-radiative multiphonon transition rates," *J.Phys.C:Solid State Phys.*, vol. 15, pp. L381–L384, 1982.

[138] M. G. Burt, "The relation between various coupling schemes for calculating non-radiative multiphonon transition rates," *J.Phys.C:Solid State Phys.*, vol. 16, pp. 4137–4149, 1983.

[139] A. F. J. Levi, *Applied Quantum Mechanics Second Edition.* Cambridge, 2006.

[140] F. Schanovsky, O. Baumgartner, V. Sverdlov, and T. Grasser, "A multi scale modeling approach to non-radiative multi phonon transitions at oxide defects in MOS structures," *J.Comp.Elect.*, vol. 11, pp. 218–224, 2012.

[141] M. Lax, "The franck-condon principle and its application to crystals," *J.Chem.Phys.*, vol. 20, pp. 1752–1760, 1952.

[142] A. Schenk, K. Irmscher, D. Suisky, R. Enderlein, F. Bechstedt, and H. Klose, "(Mo-P-10) field dependence of the emission rate at deep centers in Si and GaAs," *Act.Phys.Polon.*, vol. A67, pp. 73–76, 1985.

[143] S. Makram-Ebeid and M. Lannoo, "Electric-field-induced phonon-assisted tunnel ionization from deep levels in semiconductors," *Physical Review Letters*, vol. 48, pp. 1281–1284, May 1982.

[144] S. Makram-Ebeid and M. Lannoo, "Quantum model for phonon-assisted tunnel ionization of deep levels in a semiconductor," *Physical Review B*, vol. 25, pp. 6406–6424, May 1982.

[145] D. A. McQuarrie, "Stochastic approach to chemical kinetics," *J.Appl.Prob.*, vol. 4, no. 3, pp. 413–478, 1967.

[146] P. Hänggi, P. Talkner, and M. Borkovec, "Reaction-rate theory: fifty years after Kramers," *Rev.Mod.Phys*, vol. 62, no. 2, pp. 251–342, 1990.

[147] S. Torquato and C. L. Y. Yeong, "Universal scaling for diffusion-controlled reactions among traps," *J.Chem.Phys.*, vol. 106, pp. 8814–8820, 1997.

[148] S. S. Andrews and D. Bray, "Stochastic simulation of chemical reactions with spatial resolution and single molecule detail," *Phys.Biol.*, vol. 1, pp. 137–151, 2004.

[149] R. Erban and S. J. Chapman, "Stochastic modelling of reaction-diffusion processes: algorithms for bimolecular reactions," *Phys.Biol.*, vol. 6, p. 046001, 2009.

[150] S. A. Isaacson and D. Isaacson, "Reaction-diffusion master equation, diffusion-limited reactions, and singular potentials," *Physical Review E*, vol. 80, p. 066106, 2009.

[151] D. Fange, O. G. Berg, P. Sjöberg, and J. Elf, "Stochastic reaction-diffusion kinetics in the microscopic limit," *Proc.Nat.Acad.Sci.*, vol. 107, no. 46, pp. 19820–19825, 2010.

[152] G. Malavasi, M. C. Menziani, A. Pedone, and U. Segre, "Void size distribution in MD-modelled silica glass structures," *Journal of Non-Crystalline Solids*, vol. 352, no. 3, pp. 285 – 296, 2006.

[153] A. Bongiorno, L. Colombo, and F. Cargnoni, "Hydrogen diffusion in crystalline SiO_2," *Chem.Phys.Lett.*, vol. 264, pp. 435–440, 1997.

[154] V. Huard, M. Denais, and C. Parthasarathy, "NBTI degradation: From physical mechanisms to modelling," *Microelectronics Reliability*, vol. 46, no. 1, pp. 1–23, 2006.

[155] B. Tuttle, "Energetics and diffusion of hydrogen in SiO_2," *Physical Review B*, vol. 61, pp. 4417–4420, February 2000.

[156] S. T. Pantelides, L. Tsetseris, S. Rashkeev, X. Zhou, D. Fleetwood, and R. Schrimpf, "Hydrogen in MOSFETs - a primary agent of reliability issues," *Microelectronics Reliability*, vol. 47, no. 6, pp. 903 – 911, 2007.

[157] G. Panagopoulos and K. Roy, "A physics-based three-dimensional analytical model for RDF-induced threshold voltage variations," *IEEE Trans.Electron Devices*, vol. 58, pp. 392 –403, Feb. 2011.

[158] S. Choi, Y. Park, C.-K. Baek, and S. Park, "An improved 3D Monte Carlo simulation of reaction diffusion model for accurate prediction on the NBTI stress/relaxation," in *Proc. Simu.Semicond.Proc.Dev.*, pp. 185–188, 2012.

[159] G. Pacchioni and G. Ieranò, "*Ab initio* formation energies of point defects in pure and Ge-doped SiO_2," *Physical Review B*, vol. 56, pp. 7304–7312, Sep 1997.

[160] N. Lopez, F. Illas, and G. Pacchioni, "Mechanisms of proton formation from interaction of H_2 with E' and oxygen vacancy centers in SiO_2: Cluster model calculations," *J.Phys.Chem.B*, vol. 104, no. 23, pp. 5471–5477, 2000.

[161] M. Vitiello, N. Lopez, F. Illas, and G. Pacchioni, "H_2 cracking at SiO_2 defect centers," *J.Phys.Chem.A*, vol. 104, no. 20, pp. 4674–4684, 2000.

[162] A. H. Edwards, W. Shedd, and R. Pugh, "Theory of H in SiO_2," *Journal of Non-Crystalline Solids*, vol. 289, no. 1â"3, pp. 42 – 52, 2001.

[163] A. S. Mysovsky, P. V. Sushko, S. Mukhopadhyay, A. H. Edwards, and A. L. Shluger, "Calibration of embedded-cluster method for defect studies in amorphous silica," *Physical Review B*, vol. 69, no. 8, p. 085202, 2004.

[164] S. Mukhopadhyay, P. V. Sushko, V. A. Mashkov, and A. L. Shluger, "Spectroscopic features of dimer and dangling bond E' centres in amorphous silica," *J.Phys.:Condensed Matter*, vol. 17, no. 8, p. 1311, 2005.

[165] A. Alkauskas and A. Pasquarello, "Effect of improved band-gap description in density functional theory on defect energy levels in α-quartz," *Physica B*, vol. 401â"402, no. 0, pp. 670 – 673, 2007.

[166] J. Sarnthein, A. Pasquarello, and R. Car, "Structural and electronic properties of liquid and amorphous SiO$_2$: An *Ab Initio* molecular dynamics study," *Physical Review Letters*, vol. 74, pp. 4682–4685, Jun 1995.

[167] J. Sarnthein, A. Pasquarello, and R. Car, "Model of vitreous SiO$_2$ generated by an *ab initio* molecular-dynamics quench from the melt," *Physical Review B*, vol. 52, pp. 12690–12695, Nov 1995.

[168] E. Calabrese and W. Fowler, "Electronic energy-band structure of α quartz," *Physical Review B*, vol. 18, no. 6, pp. 2888–2896, 1978.

[169] G. Kresse and J. Furthmüller, "Efficient iterative schemes for ab initio total-energy calculations using a plane-wave basis set," *Physical Review B*, vol. 54, no. 11, pp. 11169–11186, 1996.

[170] G. Kresse and D. Joubert, "From ultrasoft pseudopotentials to the projector augmented-wave method," *Physical Review B*, vol. 59, p. 1758, 1999.

[171] G. Kresse, M. Marsman, and J. Furthmüller, *VASP Manual.* Universität Wien, Sensengasse 8, A-1130 Wien, Austria, 2009.

[172] G. Henkelman, B. P. Uberuaga, and H. Jónsson, "A climbing image nudged elastic band method for finding saddle points and minimum energy paths," *J.Chem.Phys.*, vol. 113, no. 22, pp. 9901–9904, 2000.

[173] E. H. Nicollian and J. R. Brews, *MOS (Metal Oxide Semiconductor) Physics and Technology.* Wiley, 1982.

[174] R. D. Mattuck, *A Guide to Feynman Diagrams in the Many-Body Problem.* McGraw-Hill, 1992.

[175] K. M. Kramer and W. N. G. Hitchon, *Semiconductor Devices: A Simulation Approach.* Prentice Hall, 1997.

[176] M. Anantram, M. Lundstrom, and D. Nikonov, "Modeling of nanoscale devices," *Proc.IEEE*, vol. 96, pp. 1511 –1550, sept. 2008.

[177] A. Schenk, *Advanced Physical Models for Silicon Device Simulation.* Springer, 1998.

[178] T. Ayalew, T. Binder, J. Cervenka, K. Dragosits, R. Entner, A. Gehring, T. Grasser, M. Gritsch, R. Klima, M. Knaipp, H. Kosina, R. Mlekus, V. Palankovski, R. Rodriguez-Torres, M. Rottinger, G. Schrom, S. Selberherr, M. Stockinger, and S. Wagner, *Minimos-NT device and circuit simulator Release 2.0.* Nanochemistry Research Institute, Department of Applied Chemistry, Curtin University of Technology, P.O. Box U1987, Perth 6845, Western Australia, 2004.

[179] M. Karner, A. Gehring, S. Holzer, M. Pourfath, M. Wagner, W. Goes, M. Vasicek, O. Baumgartner, C. Kernstock, K. Schnass, G. Zeiler, T. Grasser, H. Kosina, and S. Selberherr, "A multi-purpose schrödinger-poisson solver for tcad applications," *J.Comp.Elect.*, vol. 6, pp. 179–182, 2007.

[180] A. Palma, A. Godoy, J. A. Jemènez-Tejada, J. E. Carceller, and J. A. Lòpez-Villanueva, "Quantum two-dimensional calculation of time constants of random telegraph signals in metal-oxide-semiconductor structures," *Physical Review B*, vol. 56, pp. 9565–9574, October 1997.

[181] D. Garetto, Y. M. Randiamihaja, D. Rideau, E. Dornel, W. F. Clark, A. Schmid, V. Huard, H. Jaouen, and Y. Leblebic, "Small signal analysis of electrically-stressed oxides with poisson-schroedinger based multiphonon capture model," in *Proc. Intl.Worksh.Comput.Electron.*, pp. 327–330, 2010.

[182] P. Hehenberger, W. Gös, O. Baumgartner, J. Franco, B. Kaczer, and T. Grasser, "Quantum-mechanical modeling of NBTI in high-k SiGe MOSFETs," in *Proc. Simu.Semicond.Proc.Dev.*, pp. 11 – 14, 2011.

[183] G. D. Mahan, *Many-Particle Physics*. Plenum Press, 1990.

[184] A. Schenk, K. Irmscher, D. Suisky, R. Enderlein, F. Bechstedt, and H. Klose, "Electric field effect on multiphonon transitions at deep centers," in *Proc. Intl. Conf. Phys. Semi.*, 1985.

[185] W. B. Fowler, J. K. Rudra, M. E. Zvanut, and F. J. Feigl, "Hysteresis and franck-condon relaxation in insulator-semiconductor tunneling," *Physical Review B*, vol. 41, no. 12, pp. 8313–8317, 1990.

[186] F. Schanovsky, "Ab-initio calculation of the vibrational influence on hole-trapping," in *Proc. Intl.Worksh.Comput.Electron.*, pp. 163 – 166, 2010.

[187] O. Engstrom and H. G. Grimmeiss, "Vibronic states of silicon-silicon dioxide interface traps," *Semicond.Sci.Technol.*, vol. 4, no. 12, p. 1106, 1989.

[188] O. Engström, "Influence of entropy properties on measured trap energy distributions at insulator-semiconductor interfaces," *Appl.Phys.Lett.*, vol. 55, no. 1, pp. 47–49, 1989.

[189] C. G. Van de Walle and J. Neugebauer, "First-principles calculations for defects and impurities: Applications to III-nitrides," *J.Appl.Phys.*, vol. 95, no. 8, pp. 3851–3879, 2004.

[190] W. Gös and T. Grasser, "First-principles investigation on oxide trapping," in *Simulation of Semiconductor Processes and Devices 2007* (T. Grasser and S. Selberherr, eds.), pp. 157–160, Springer Vienna, 2007.

[191] W. Goes, M. Karner, V. Sverdlov, and T. Grasser, "A rigorous model for trapping and detrapping in thin gate dielectrics," in *Proc. Intl.Symp. on Physical and Failure Analysis of Integrated Circuits*, pp. 1 –6, july 2008.

[192] A. Alkauskas, P. Broqvist, and A. Pasquarello, "Defect energy levels in density functional calculations: Alignment and band gap problem," *Physical Review Letters*, vol. 101, p. 046405, Jul 2008.

[193] W. Goes, M. Karner, V. Sverdlov, and T. Grasser, "Charging and discharging of oxide defects in reliability issues," *Device and Materials Reliability, IEEE Transactions on*, vol. 8, pp. 491 –500, sept. 2008.

[194] A. Alkauskas, J. L. Lyons, D. Steiauf, and C. G. Van de Walle, "First-principles calculations of luminescence spectrum line shapes for defects in semiconductors: The example of gan and zno," *Physical Review Letters*, vol. 109, p. 267401, Dec 2012.

[195] A. Schenk, "(Mo-P-22) field-dependent emission rate at deep centers in GaAs by using a two-phonon mode model," *Act.Phys.Polon.*, vol. A69, no. 5, pp. 813–815, 1986.

[196] A. Schenk, "A model for the field and temperature dependence of Shockley-Read-Hall lifetimes in silicon," *Solid-State Electron.*, vol. 35, pp. 1585–1596, 1992.

[197] F. Ansbacher, "A note on the overlap integral of two harmonic oscillator wave functions," *Z.Naturforschg*, vol. 14a, pp. 889–892, 1959.

[198] B. Zapol, "New expressions for the overlap integral of two linear harmonic oscillator wavefunctions," *Chem.Phys.Lett.*, vol. 93, no. 6, pp. 549–552, 1982.

[199] F. Iachello and M. Ibrahim, "Analytic and algebraic evaluation of Franck-Condon overlap integrals," *J.Phys.Chem.A*, vol. 102, pp. 9427–9432, 1998.

[200] P. P. Schmidt, "Computationally efficient recurrence relations for one-dimensional franck-condon overlap integrals," *Molecular Physics*, vol. 108, pp. 1513–1529, 2010.

[201] M. Wastl, "Berechnung eindimensionaler Überlappintegrale des harmonischen Oszillators," bakkalaureatsarbeit, TU Wien, 2011.

[202] J. H. Zheng, H. S. Tan, and S. C. Ng, "Theory of non-radiative capture of carriers by multiphonon processes for deep centers in semiconductors," *J.Phys.:Condensed Matter*, vol. 6, pp. 1695–1706, 1994.

[203] J. D. Gale, *General Utility Lattice Program*. Nanochemistry Research Institute, Department of Applied Chemistry, Curtin University of Technology, P.O. Box U1987, Perth 6845, Western Australia, 2003.

[204] A. Alkauskas and A. Pasquarello, "Alignment of hydrogen-related defect levels at the interface," *Physica B*, vol. 401-402, no. 0, pp. 546 – 549, 2007.

[205] B. R. Tuttle, "Theoretical investigation of the valence-band offset between si(001) and SiO_2," *Physical Review B*, vol. 70, p. 125322, Sep 2004.

[206] T. Grasser, H. Reisinger, K. Rott, M. Toledano-Luque, and B. Kaczer, "On the microscopic origin of the frequency dependence of hole trapping in pMOSFETs," in *Proc. Intl.Electron Devices Meeting*, 2012.

[207] O. Baumgartner, M. Karner, and H. Kosina, "Modeling of high-k-metal-gate-stacks using the non-equilibrium Green's function formalism," in *Proc. Simu.Semicond.Proc.Dev.*, pp. 353–356, 2008.

[208] S. Datta, *Electronic Transport in Mesoscopic Systems*. Cambridge, 1995.

[209] W. Shockley and W. T. Read, "Statistics of the recombinations of holes and electrons," *Physical Review*, vol. 87, pp. 835–842, 1952.

Own Publications

[1] F. Schanovsky, O. Baumgartner, V. Sverdlov, and T. Grasser, "A multi scale modeling approach to non-radiative multi phonon transitions at oxide defects in MOS structures," *Journal of Computational Electronics*, vol. 11, no. 3, pp. 218–224, 2012.

[2] F. Schanovsky and T. Grasser, "On the microscopic limit of the modified reaction-diffusion model for the negative bias temperature instability," in *Conference Proceedings of International Reliability Physics Symposium (IRPS 2012)*, 2012. poster: International Reliability Physics Symposium (IRPS), Californi, USA; 2012-04-17 – 2012-04-19.

[3] F. Schanovsky and T. Grasser, "Bias temperature instabilities in highly-scaled MOSFETs." invited; talk: 2012 CMOS Emerging Technologies, Vancouver, BC Canada; 2012-07-18 – 2012-07-21, 2012.

[4] W. Gös, F. Schanovsky, H. Reisinger, B. Kaczer, and T. Grasser, "Bistable defects as the cause for NBTI and RTN," *Solid State Phenomena*, vol. 178-179, pp. 473–482, 2011. invited.

[5] T. Grasser, B. Kaczer, W. Gös, H. Reisinger, T. Aichinger, P. Hehenberger, P.-J. Wagner, F. Schanovsky, J. Franco, M. Toledano-Luque, and M. Nelhiebel, "The paradigm shift in understanding the bias temperature instability: From reaction-diffusion to switching oxide traps," *IEEE Transactions on Electron Devices*, vol. 58, no. 11, pp. 3652–3666, 2011. invited.

[6] F. Schanovsky, W. Gös, and T. Grasser, "Multiphonon hole trapping from first principles," *Journal of Vacuum Science & Technology B*, vol. 29, no. 1, pp. 01A201–1–01A201–5, 2011.

[7] H. Ceric, R. Orio, F. Schanovsky, W. Zisser, and S. Selberherr, "Multilevel simulation for the investigation of fast diffusivity paths," in *Proceedings of the 16th International Conference on Simulation of Semiconductor Processes and Devices*, pp. 135–138, 2011. talk: International Conference on Simulation of Semiconductor Processes and Devices (SISPAD), Osaka, Japan; 2011-09-08 – 2011-09-10.

[8] W. Gös, F. Schanovsky, T. Grasser, H. Reisinger, and B. Kaczer, "Advanced modeling of oxide defects for random telegraph noise," in *Proceedings of the 21st International Conference on Noise and Fluctuations*, 2011. talk: International Conference on Noise and Fluctuations (ICNF), Toronto, Canada; 2011-06-12 – 2011-06-16.

[9] W. Gös, F. Schanovsky, H. Reisinger, B. Kaczer, and T. Grasser, "Bistable defects as the cause for NBTI and RTN," in *GADEST 2011: Abstract Booklet*, p. 153, 2011. invited; talk: Gettering and Defect Engineering in Semiconductor Technology, Loipersdorf, Austria; 2011-09-25 – 2011-09-30.

[10] F. Schanovsky, O. Baumgartner, and T. Grasser, "Multi scale modeling of multi phonon hole capture in the context of NBTI," in *Proceedings of the 16th International Conference on Simulation of Semiconductor Processes and Devices*, pp. 15–18, 2011. talk: International Conference on Simulation of Semiconductor Processes and Devices (SISPAD), Osaka, Japan; 2011-09-08 – 2011-09-10.

[11] F. Schanovsky and T. Grasser, "On the microscopic limit of the reaction-diffusion model for the negative bias temperature instability," in *Final Report of IEEE International Integrated Reliability Workshop (IIRW 2011)*, pp. 17–21, 2011. talk: IEEE International Integrated Reliability Workshop, South Lake Tahoe, USA; 2011-10-16 – 2011-10-20.

[12] F. Schanovsky, W. Gös, and T. Grasser, "An advanced description of oxide traps in MOS transistors and its relation to DFT," *Journal of Computational Electronics*, vol. 9, no. 3-4, pp. 135–140, 2010. invited.

[13] W. Gös, F. Schanovsky, P. Hehenberger, P.-J. Wagner, and T. Grasser, "Charge trapping and the negative bias temperature instability," in *Physics and Technology of High-k Materials 8*, pp. 565–589, ECS Transactions, 2010. invited.

[14] W. Gös, F. Schanovsky, P. Hehenberger, P.-J. Wagner, and T. Grasser, "Charge trapping and the negative bias temperature instability," in *Meet. Abstr. - Electrochem. Soc. 2010*, 2010. talk: 218th ECS Meeting, Las Vegas, USA; 2010-10-10 – 2010-10-15.

[15] T. Grasser, B. Kaczer, W. Gös, H. Reisinger, T. Aichinger, P. Hehenberger, P.-J. Wagner, F. Schanovsky, J. Franco, P. J. Roussel, and M. Nelhiebel, "Recent advances in understanding the bias temperature instability," in *Proceedings of the 2010 IEEE International Electron Devices Meeting (IEDM)*, pp. 82–85, 2010. invited; talk: International Electron Devices Meeting (IEDM), San Francisco; 2010-12-06 – 2010-12-08.

[16] T. Grasser, H. Reisinger, P. Wagner, B. Kaczer, F. Schanovsky, and W. Gös, "The time dependent defect spectroscopy (TDDS) for the characterization of the bias temperature instability," in *Proceedings of the International Reliability Physics Symposium*, pp. 16–25, 2010. talk: International Reliability Physics Symposium (IRPS), Anaheim; 2010-05-02 – 2010-05-06.

[17] F. Schanovsky, W. Gös, and T. Grasser, "Ab-initio calculation of the vibrational influence on hole-trapping," in *Proceedings of the 14th International Workshop on Computational Electronics (IWCE)*, pp. 163–166, 2010. talk: International Workshop on Computational Electronics (IWCE), Pisa; 2010-10-26 – 2010-10-29.

[18] F. Schanovsky, W. Gös, and T. Grasser, "Hole capture into oxide defects in MOS structures from first principles," in *Abstract Book*, p. 435, 2010. poster: Ψ_k - 2010 Conference, Berlin; 2010-09-12 – 2010-09-16.

[19] F. Schanovsky, W. Gös, and T. Grasser, "Mulit-phonon hole-trapping from first-principles," in *Book of Abstracts*, p. 54, 2010. talk: Workshop on Dielectrics in Micro-electronics (WODIM), Bratislava; 2010-06-28 – 2010-06-30.

[20] T. Grasser, H. Reisinger, P.-J. Wagner, W. Gös, F. Schanovsky, and B. Kaczer, "The time dependent defect spectroscopy (TDDS) for the characterization of the bias temperature instability." invited; talk: European Symposium on Reliability of Electron Devices, Failure Physics and Analysis (ESREF), Gaeta; 2010-10-11, 2010.

[21] V. Sverdlov, T. Windbacher, F. Schanovsky, and S. Selberherr, "Mobility modeling in advanced MOSFETs with ultra-thin silicon body under stress," *Journal Integrated Circuits and Systems*, vol. 4, no. 2, pp. 55–60, 2009.

[22] V. Sverdlov, O. Baumgartner, H. Kosina, S. Selberherr, F. Schanovsky, and D. Esseni, "The linear combination of bulk bands-method for electron and hole subband calculations in strained silicon films and surface layers," in *13th International Workshop on Computational Electronics*, pp. 49–52, 2009. talk: International Workshop on Computational Electronics (IWCE), Beijing; 2009-05-27 – 2009-05-29.

[23] V. Sverdlov, O. Baumgartner, T. Windbacher, F. Schanovsky, and S. Selberherr, "Impact of confinement and stress on the subband parameters in ultra-thin silicon films," in *Proceedings Intl.Symposium on Microelectronics Technology and Devices (SBMicro)*, pp. 389–396, 2009. talk: Intl. Symposium on Microelectronics Technology and Devices (SBMicro), Natal; 2009-08-31 – 2009-09-03.

[24] V. Sverdlov, O. Baumgartner, T. Windbacher, F. Schanovsky, and S. Selberherr, "Impact of confinement of semiconductor and band engineering on future device performance," in *Proceedings 215th Meeting of the Electrochemical Society, Silicon-on-Insulator Technology and Devices*, (19/4), pp. 15–26, 2009. invited; talk: 215th Meeting of the Electrochemical Society, Silicon-on-Insulator Technology and Devices, San Francisco; 2009-05-24 – 2009-05-29.

[25] V. Sverdlov, O. Baumgartner, T. Windbacher, F. Schanovsky, and S. Selberherr, "Thickness dependence of the effective masses in a strained thin silicon film," in *Proceedings of the International Conference on Simulation of Semiconductor Processes and Devices*, pp. 51–54, 2009. talk: International Conference on Simulation of Semiconductor Processes and Devices (SISPAD), San Diego; 2009-09-09 – 2009-09-11.

[26] V. Sverdlov, T. Windbacher, O. Baumgartner, F. Schanovsky, and S. Selberherr, "Valley splitting in thin silicon films from a two-band $k \cdot p$ model," in *Proceedings of the 10th International Conference on Ultimate Integration of Silicon*, pp. 277–280, 2009. poster: International Conference on Ultimate Integration of Silicon (ULIS), Aachen; 2009-03-18 – 2009-03-20.

[27] F. Schanovsky, "Dispersive transport modeling within the multiple trapping framework," Master's thesis, Institut für Mikroelektronik, 2008.

[28] T. Grasser, W. Gös, O. Triebl, P. Hehenberger, P.-J. Wagner, P. Schwaha, R. Heinzl, S. Holzer, R. Entner, S. Wagner, and F. Schanovsky, "3 year report 2005-2007," tech. rep., E360 - Institut für Mikroelektronik; Technische Universität Wien, 2007.

Curriculum Vitae

Personal Information

28.6.1981	Born in Linz, Austria
4.3.2005	Birth of my daughter Lena
2.7.2007	Marriage with Nicole Rausch
14.6.2011	Birth of my daughter Margarete

Primary Education:

VS Garsten 1987-1991, HS Garsten 1991-1995

Further Education:

1995-2000	HTL Steyr - Ausbildungszweig Elektronik/Informatik
Jun 2000	Passed the matura exams (with honors)
Oct 2000	Enrolled in electrical engineering at the TU Wien
Jun 2002 - May 2003	Alternative civilian service at the Viennese Red Cross
Oct 2006	Received degree *Bakkalaureus der Technik* (BSc. equivalent) Bakkalaureatsarbeiten: *Blutdruckmessung mittels Elektrischer Feldplethysmographie* *Visualisierung einer Brückenmessung* Enrolled in microelectronics at TU Wien
Mar 2008	Received degree *Diplomingenieur* (MSc. equivalent): Diploma thesis: *Dispersive Transport Modeling within the Multiple Trapping Framework* Entered PhD program at the Institute for Microelectronics, TU Wien

Work Experience

1998-2000	Summer internships as programmer (internet traffic analysis software) at pLANet (later Karrer&Partner)
2002 - 2004	Programmer for web applications and technical support for Linux and MacOS at Fa. Alexander Biedermann `http://homepage-designer.com/`
winter term 2004/05	Tutor for object oriented programming at the Institute of Computer Technology, TU Wien
summer term 2005	Tutor for signal and system analysis at the Institute for Telecommunication, TU Wien
2005 - 2007	Service technician at ELVG-Bentlage `http://www.elvg.at`